Computational design for the wire and arc additive manufacturing process

Mishra, V.

DOI
10.4233/uuid:a8092558-5d07-4a15-828b-91f624afdc45

Publication date
2023

Document Version
Final published version

Citation (APA)
Mishra, V. (2023). *Computational design for the wire and arc additive manufacturing process*. [Dissertation (TU Delft), Delft University of Technology]. https://doi.org/10.4233/uuid:a8092558-5d07-4a15-828b-91f624afdc45

COMPUTATIONAL DESIGN FOR THE WIRE AND ARC ADDITIVE MANUFACTURING PROCESS

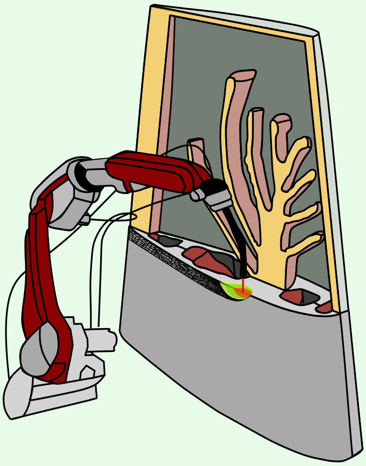

Vibhas MISHRA

COMPUTATIONAL DESIGN FOR THE
WIRE AND ARC ADDITIVE MANUFACTURING PROCESS

Vibhas MISHRA

COMPUTATIONAL DESIGN FOR THE WIRE AND ARC ADDITIVE MANUFACTURING PROCESS

Vibhas MISHRA

COMPUTATIONAL DESIGN FOR THE WIRE AND ARC ADDITIVE MANUFACTURING PROCESS

Dissertation

for the purpose of obtaining the degree of doctor
at Delft University of Technology
by the authority of the Rector Magnificus prof.dr.ir. T.H.J.J. van der Hagen
chair of the Board for Doctorates
to be defended publicly on
Monday 25 September 2023 at 12:30 o'clock

by

Vibhas MISHRA
Master of Science in Aerospace Engineering, Delft University of Technology, the Netherlands
born in Lakhimpur-Kheri, Uttar Pradesh, India.

This dissertation has been approved by the promotors

Composition of the doctoral committee:

Rector Magnificus,	chairperson
Prof. dr. ir. A. van Keulen,	Delft University of Technology, promoter
Prof. dr. ir. M. Langelaar,	Delft University of Technology, promoter
Dr. C. Ayas,	Delft University of Technology, copromoter

Independent members:

Prof. dr. J. Hensel	Chemnitz University of Technology, Germany
Prof. dr. ing. M. Bruggi	Polytechnic University of Milan, Italy
Prof. dr. M. J. Santofimia Navarro	Delft University of Technology
Prof. dr. ir. M. A. N. Hendriks	Delft University of Technology
Prof. dr. ir. J. L. Herder	Delft Univeristy of Technology, reserve member

Keywords: Metal Additive Manufacturing, Topology Optimization, Microstructure
Printed by: Gildeprint
Cover by: Vibhas Mishra.

ISBN 978-94-6384-441-3

An electronic version of this dissertation is available at
http://repository.tudelft.nl/.

Dedicated to my parents and my wife, Richa.

CONTENTS

SUMMARY

The world has seen industrial revolutions with advancements in manufacturing technologies. The advancements in Additive Manufacturing (AM) technologies will bring another revolution sooner rather than later. Nowadays, the Wire and Arc Additive Manufacturing (WAAM) process is already used to manufacture large-scale structures such as ship propellers, pedestrian bridges, aircraft components, and heavy-lifting structures. These structures are critical load-bearing structures during operations. WAAM has high material deposition rate which is unique within the entirety of metal AM processes. Moreover, WAAM reduces lead time and material waste compared to conventional manufacturing processes such as milling and casting.

Though WAAM has remarkable benefits, the lack of fundamental understanding of the process and its effects on the mechanical properties of the manufactured parts limits its utilization in the industry. The impact of the process conditions on the mechanical properties of the manufactured parts is relatively complex. The mechanical properties are dependent upon the microstructure formation during the WAAM process. Various aspects of the WAAM part's microstructure are influenced by the complex thermal conditions the part endures during WAAM. These thermal conditions depend on the part design, process design, and post-processing steps. Therefore, a highly complex correlation exists between the different stages of the WAAM process flow and the resultant properties. It is imperative to understand this particular correlation and to generate WAAM parts with the required mechanical properties. The goal of this thesis is to understand the complex correlation between process stages and mechanical properties to optimize the design and process for WAAM. The focus of the dissertation is on two types of steel that have a wide variety of structural applicability and show excellent weldability, which is required for WAAM. These steels are stainless steels and high strength low alloy steels.

For the optimization of AM parts, a computational design method is often used, namely, *Topology Optimization* (TO). TO is an iterative design tool that generates designs with high stiffness (or other desired properties) using a given amount of material. TO designs are often geometrically complex and therefore difficult to produce by conventional manufacturing, but AM offers a means to realize these high-performance TO parts. Therefore, TO and AM complement each other. Still, specific limitations, particularly for WAAM, need to be considered to ensure manufacturability.

At the WAAM design stage, an important consideration is to reduce the geometrical complexity of the design. Specifically, thin intersections in designs should be avoided as these locations are sites for defects. A TO-based optimization method is presented in this thesis to identify the intersections thereby generating designs suitable for WAAM with minimum thin intersections. Moreover, WAAM-manufactured stainless steel structures show an anisotropic elastic response. The Youngs moduli of the material are reported to be higher at a specific angle from the deposition direction. The elastic anisotropy and the flexibility of the WAAM process are exploited in this thesis to generate simultaneously optimized design layout and deposition directions for WAAM. Furthermore, for high strength low alloy steels, it is identified that the cooling rates experienced by the part during WAAM are responsible for its local mechanical strength. The cooling rates are highly dependent upon the design layout and process design. A novel TO-based strategy is devised and demonstrated in this thesis to control the cooling rates through design optimization such that required properties are realized during the WAAM process.

With these new approaches, this thesis presents several new TO methods for WAAM that help alleviate current bottlenecks and enable engineers to exploit the strengths and potential of WAAM. In this way, this research brings the (WA)AM revolution several steps closer.

SAMENVATTING

De wereld heeft industriële revoluties gezien met vooruitgang in productietechnologieën. De vooruitgang in Additive Manufacturing (AM) technologieën zal eerder vroeger dan later een nieuwe revolutie teweegbrengen. Tegenwoordig wordt het Wire and Arc Additive Manufacturing (WAAM) proces al gebruikt voor de vervaardiging van grootschalige structuren zoals scheepsschroeven, voetgangersbruggen, vliegtuigonderdelen en zware hefconstructies. Deze structuren zijn in gebruik als kritieke dragende structuren. WAAM heeft een hoge materiaaldepositiesnelheid die uniek is binnen alle AM-metaalprocessen. Bovendien vermindert WAAM de doorlooptijd en materiaalverspilling in vergelijking met conventionele fabricageprocessen zoals frezen en gieten.

Hoewel WAAM opmerkelijke voordelen heeft, beperkt het gebrek aan fundamenteel inzicht in het proces en de effecten ervan op de mechanische eigenschappen van de vervaardigde onderdelen het gebruik ervan in de industrie. Het effect van de procescondities op de mechanische eigenschappen van de vervaardigde onderdelen is relatief complex. De mechanische eigenschappen zijn afhankelijk van de microstructuurvorming tijdens het WAAM-proces. Verschillende aspecten van de microstructuur van een WAAM-onderdeel worden beïnvloed door de complexe thermische omstandigheden waaraan het tijdens WAAM wordt blootgesteld. Deze thermische omstandigheden zijn afhankelijk van het ontwerp, het procesontwerp en de nabewerkingsstappen. Daarom bestaat er een zeer complexe correlatie tussen de verschillende stadia van het WAAM-proces en de resulterende eigenschappen. Het is absoluut noodzakelijk deze specifieke correlatie te begrijpen en WAAM-onderdelen te genereren met de vereiste mechanische eigenschappen. Het doel van dit proefschrift is de complexe correlatie tussen processtappen en mechanische eigenschappen te begrijpen om het ontwerp en het proces voor WAAM te optimaliseren. De nadruk van het proefschrift ligt op twee staalsoorten die een grote verscheidenheid aan structurele toepasbaarheid hebben en een uitstekende lasbaarheid vertonen, hetgeen vereist is voor WAAM. Deze staalsoorten zijn roestvrij staal en laag gelegeerd hoogsterktestaal.

Voor de optimalisatie van AM-onderdelen wordt vaak een computergebaseerde ontwerpmethode gebruikt, namelijk Topologie Optimalisatie (TO). TO is een iteratief ontwerpinstrument dat met een bepaalde hoeveelheid materiaal ontwerpen genereert met een hoge stijfheid (of andere gewenste eigenschappen). TO-ontwerpen zijn vaak geometrisch complex en daarom moeilijk te produceren door conventionele fabricage, maar AM biedt een middel om deze hoogwaardige TO-onderdelen te realiseren. Daarom vullen TO en AM elkaar aan. Toch moet rekening worden gehouden met specifieke beperkingen, met name voor WAAM, om de maakbaarheid te waarborgen.

In het WAAM-ontwerpstadium is de vermindering van de geometrische complexiteit van het ontwerp een belangrijk aspect. Met name dunne kruispunten in ontwerpen moeten worden vermeden, omdat deze punten locaties voor defecten zijn. In dit proefschrift wordt een TO-gebaseerde optimalisatiemethode gepresenteerd om de kruispun-

ten te identificeren en zo voor WAAM geschikte ontwerpen te genereren met een minimum aan dunne kruispunten. Bovendien vertonen WAAM-gefabriceerde roestvrijstalen constructies een anisotrope elastische respons. De Young's moduli van het materiaal blijken hoger onder een specifieke hoek ten opzichte van de depositie richting. De elastische anisotropie en de flexibiliteit van het WAAM-proces worden in dit proefschrift benut om tegelijkertijd de geoptimaliseerde ontwerp-lay-out en depositie-richtingen voor WAAM te genereren. Verder is voor laag gelegeerd hoogsterktestaal vastgesteld dat de koelsnelheden die het onderdeel tijdens WAAM ondergaat, verantwoordelijk zijn voor de lokale mechanische sterkte. De koelsnelheden zijn sterk afhankelijk van het ontwerp en het procesontwerp. In dit proefschrift wordt een nieuwe, op TO gebaseerde strategie ontwikkeld en gedemonstreerd om de koelsnelheden door middel van ontwerpoptimalisatie zodanig te beheersen dat de vereiste eigenschappen tijdens het WAAM-proces worden gerealiseerd.

Met deze nieuwe benaderingen presenteert dit proefschrift verschillende nieuwe TO-methoden voor WAAM die de huidige knelpunten helpen verlichten en ingenieurs in staat stellen de sterke punten en het potentieel van WAAM te benutten. Op deze manier brengt dit onderzoek de (WA)AM-revolutie enkele stappen dichterbij.

1

INTRODUCTION

1.1. BACKGROUND

Additive Manufacturing (AM) is a manufacturing process in which material is deposited sequentially to generate a part. The AM process is popular primarily because complex shaped designs can be realized with it, which is difficult or impossible with conventional manufacturing processes such as casting and milling. AM processes find their application in industries such as aerospace, maritime, medical, and architecture. Currently, through AM processes, parts composed of materials such as ceramics, polymers, and metals can be realized (Bikas et al., 2016; Frazier, 2014; Wong and Hernandez, 2012). Various AM processes can also be employed to produce parts ranging from a millimeter to several meters.

Metal AM processes can be broadly classified as powder bed-based processes and direct energy deposition processes (DebRoy et al., 2018). In powder bed-based processes, a thin layer of metal powder is dispensed uniformly across a build area and a high-energy beam is used to melt and fuse the powder particles selectively. The process is repeated until the part's completion. However, powder bed-based AM is limited to small-scale parts, which are constrained by the size of the build chamber with an inert atmosphere and manufacturing speed. For large-scale parts, rapid direct energy deposition processes such as Laser Cladding (Koch and Mazumder, 1993) and Laser Metal Deposition (Gu et al., 2012) have been developed. These processes still provide relatively high dimensional accuracy, however, the heat transfer efficiency of the high-energy laser beam is low, which makes these processes expensive. A more energy-efficient process has emerged for manufacturing large parts, namely, Wire and Arc Additive Manufacturing (WAAM) (Almeida and Williams, 2010). In the WAAM process, metal wire is melted through an electric arc and deposited simultaneously along a pre-defined deposition path by a robotic arm. By careful selection of the process parameters the material volume deposited per unit time by WAAM can be twice that of the material volume scanned during powder bed-based processes (Shi et al., 2017). Unlike the powder bed-based processes (McMillan et al., 2017), continuous deposition can be achieved in the WAAM (Wu et al., 2018). Therefore, due to this particular advantage, the material deposition rate becomes 10 – 20 times higher than the powder bed-based processes. A disadvantage of WAAM is the higher surface roughness and lower resolution of the WAAM parts compared to powder bed-based processes. Therefore, post-processing of WAAM parts is typically required. However, the gain in material deposition rate makes the WAAM process attractive and an ideal choice for manufacturing large-scale parts. A few examples of real-life structures manufactured by WAAM are shown in Fig. 1.1.

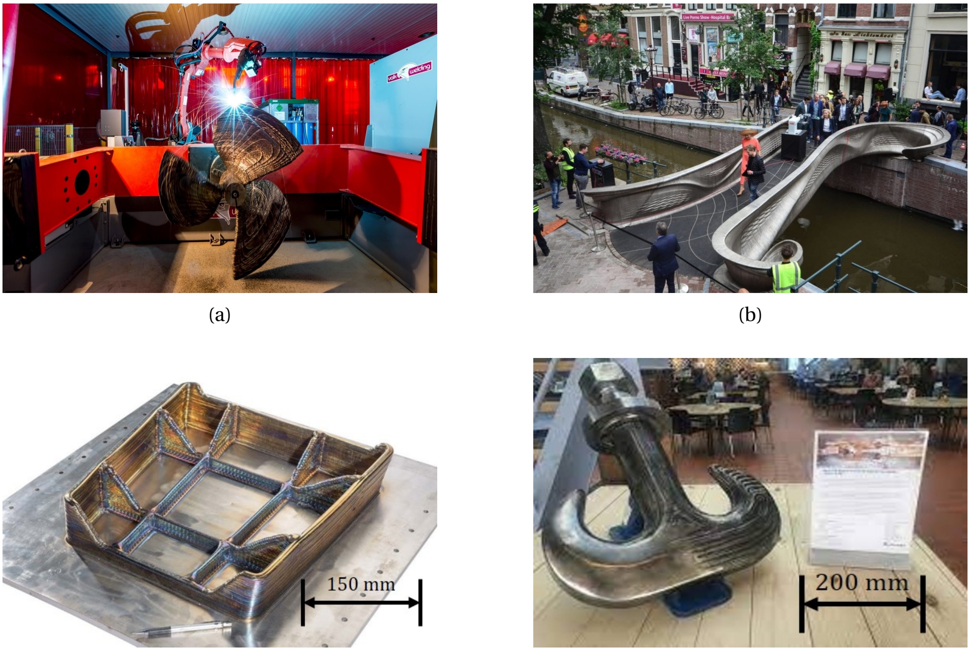

(a) (b)

(c) (d)

Figure 1.1: WAAM Applications : (a) Ship propeller, (b)Pedestrian bridge in Amsterdam, (c) Landing gear rib, and (d) Mechanical hook manufactured by WAAM.

The capability of AM to realize complex shaped designs opens up the possibility to optimize the geometric layout of the structure to improve its mechanical performance. It ensures optimal use of the material thereby reducing the structure's weight. A computational design method, Topology Optimization (TO) is typically used to optimize design layouts for improved mechanical performance. In TO, a design space is identified in which a limited amount of material is distributed to achieve the best performance of choice. In density-based TO, the design space is discretized with finite elements. Each finite element is then associated with a design variable indicating the amount of material present at that location, ranging from 0 (void) to 1 (solid) as shown in Fig. 1.2 (Bendsoe and Sigmund, 2013).

TO is an iterative process in which the finite element analysis of an evolving design is performed at every iteration, making it computationally extensive. To reduce the num-

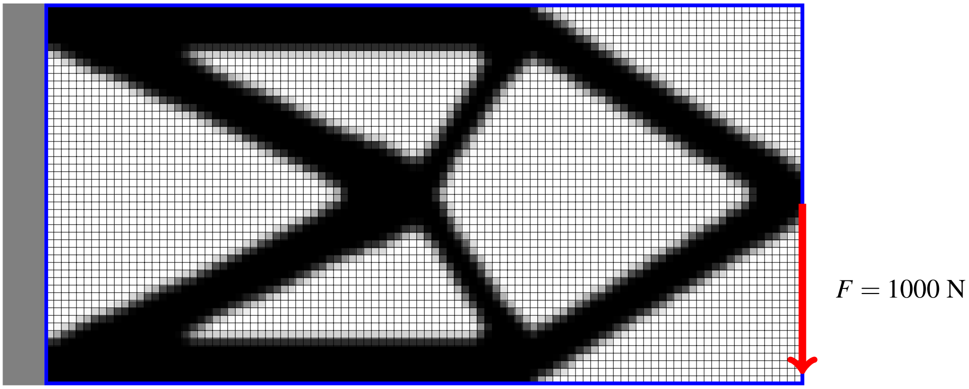

Figure 1.2: Density-based Topology Optimization for Cantilever loadcase: The area encompassed by the blue rectangle is the design domain, which is discretized with quadrilateral finite elements. Loading and boundary conditions are applied to the finite element mesh. Each quadrilateral finite element is associated with a continuous design variable. The design variable is 0 and 1 for the void and solid material, respectively. For the optimized design, the black regions represent the solid material and the white regions are the voids.

ber of iterations and achieve fast convergence to an optimal design solution, gradient-based optimization techniques are used to obtain optimal design solutions. This requires evaluation of the sensitivities of the objectives and constraints with respect to design variables. TO generates often organic and complex shapes that require AM to be realized.

However, AM also has form limitations, and these limitations are more pronounced for WAAM than for other metal AM processes. WAAM in general is suitable for parts with less geometrical complexity and can not be applied to generate parts with very intricate geometrical features. These geometrical features are very common in TO designs. This restricts the use of TO for WAAM leaving an untapped potential for WAAM design performance.

Besides manufacturability, other commonly observed problems in WAAM are part distortion, residual stresses, and local overheating which directly impact the mechanical performance and dimensional tolerances of WAAM parts. These problems arise because WAAM parts experience high local temperatures during the process. The thermal history, that is the spatial and temporal dependence of the temperatures experienced by the AM parts, is complex and difficult to monitor. Moreover, the thermal history of the AM parts affects the microstructure development. The microstructure development in metal AM impacts the material properties such as elastic modulus, hardness, and yield strength (Callister Jr and Rethwisch, 2020) crucial for the mechanical performance of the parts produced by WAAM. The thermal history also depends on the geometric layout of the part and the deposition strategy to manufacture the part. It is open-ended how TO can be used to optimize the geometrical layout and deposition strategy such that the required microstructure during the AM process can be achieved.

Accounting for the WAAM-related challenges in a TO framework is not trivial, since it requires formulating the physical phenomenon of interest to be modeled efficiently in a mathematical framework where the shape of the part is not clearly defined during the optimization process. This mathematical framework provides input for the objectives and constraints of the optimization problem. Therefore, these formulations need to be continuous and differentiable with respect to the design variables so that the gradient-based optimization approaches can be used. The aim of this thesis is therefore to develop TO procedures specific to WAAM and in general for AM. Before specifying the exact research questions this thesis focuses on, a more detailed introduction to the WAAM process and the associated design considerations is needed.

1.2. DESIGN FOR WAAM

In this section, the WAAM process description is given in Section 1.2.1, and design considerations for WAAM are discussed. In Section 1.2.2, the geometrical design considerations for WAAM are listed. The considerations are essential to improve the manufacturability of a part using WAAM. Also, the research gap for including manufacturing-related aspects of TO for WAAM is discussed. In Section 1.2.3, the relation between the geometrical design, WAAM process, resultant thermal history, and consequently its effect on the material properties is discussed. The focus is on Stainless steels and High Strength Low Alloy (HSLA) steels, which are ideal for WAAM printing due to their excellent weldability properties and their widespread applications in the industry. The relation between geometry and material properties is necessary to understand for the required mechanical performance. Here also, the research gaps in the literature are identified.

1.2.1. WAAM - PROCESS DESCRIPTION

In WAAM, the CAD geometry is sliced into typically hundreds of layers. Thereafter, the deposition paths and process parameters such as wire feed rate and travel speed of the robotic arm are described for each layer. Generally, the deposition happens on a large metal block called the substrate or base plate. An electrical arc is established between the substrate plate and the metal wire, which facilitates the melting and deposition of the wire on the substrate. The metal wire melts simultaneously with the substrate surface. The arc moves away from the molten material and the deposited metal fuses with the substrate before solidification. Cooling happens through heat transfer mechanisms: conduction, convection, and radiation. The same process for material deposition is continuously repeated layer-by-layer on the previously deposited material to generate the complete part. A schematic representation of the WAAM process is given in Fig. 1.3. A list of typical process parameters used in the WAAM process is given in Table 1.1.

Manufacturing of a part by WAAM is followed by two prior stages: Part Design and Process Design. The part design can be generated by CAD modeling or using more advanced computational design methods such as TO. At the process design stage, the build direction of a part is selected. Based on the build direction the slicing is performed and for each layer, the deposition patterns are designed along with the process parameters such as current, voltage, wire feed rate, and travel speed of the robot arm. After WAAM manufacturing, the as-deposited part goes through the post-processing stage. Here the part is subjected to milling and grinding operations for the required surface finish. The

Table 1.1: WAAM process characteristics.

WAAM Process Variants	Gas Metal Arc Welding Gas Tungsten Arc Welding Plasma Arc Welding
Input Power	Voltage - 22V Current - 150A Power - 3kW
Materials	Steels, Titanium, Inconel, Tungsten, and others.
Travel Speed	6 – 12 mm/s
Wire Feed Rate	85 – 120 mm/s
Wire Diameter	1.2 mm
Layer Thickness	1.5 mm
Surface Roughness	500 μm
Heat transfer efficiency	upto 80 – 90%

part is also subjected to heat treatments to relieve residual stresses. The process flow of manufacturing of a part by WAAM is shown in Fig. 1.4.

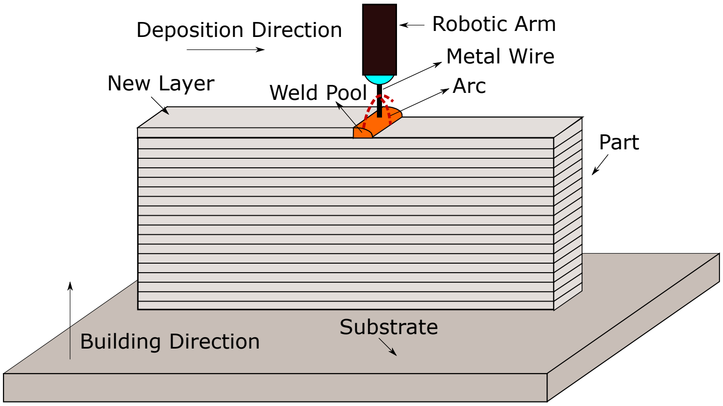

Figure 1.3: Schematic representation of the WAAM process.

1.2.2. GEOMETRICAL DESIGN CONSIDERATIONS FOR WAAM

The following considerations should be accounted for at an early design stage to improve the manufacturability of a design through WAAM:

1. **Feature Size**: Generally, the material is deposited along a path, and the deposited material along a line is termed a bead. The size of the bead is the minimum deposited feature size in WAAM. The feature size less than the bead size is attainable

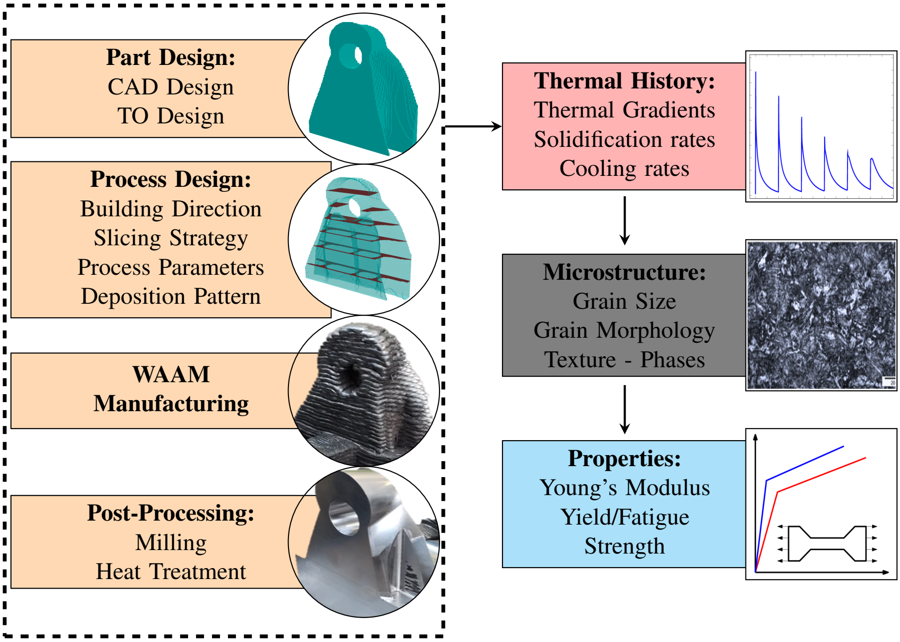

Figure 1.4: Process flow of the WAAM process and relation with the mechanical properties.

in a part, however, it involves the post-processing operations such as milling after WAAM. The dimension of the bead depends on the wire feed rate and travel speed. The variation in bead size with respect to the heat input is shown in Fig. 1.5. The wire feed rate and the travel speed are generally selected based on the slicing of the part design. When using a uniform slicing strategy, part design can be decimated into many layers with equal thickness. Consequently, a single set of process parameters can be selected for each layer. However, a uniform slicing strategy cannot be employed for parts with complex designs(Jafari et al., 2021). Therefore, the part design is decimated into layers with varying layer thicknesses. In WAAM, the process parameter can be varied along the build directions to generate parts with varying layer thicknesses by depositing beads of corresponding thicknesses.

2. **Overhangs**: Overhanging features are problematic to be manufactured by powder bed-based AM processes without support structures. However, it is shown by Mehnen et al., 2014 that even shallow overhang features can be manufactured by WAAM, see Fig. 1.6. The overhanging features do require adjustment of the local build direction during the WAAM process. The local build direction can be changed by rotating the part. For instance, the ship propeller shown in Fig. 1.1a has overhanging edges. To manufacture these overhanging edges the shaft on which the deposition started is turned so that the overhanging edges can be produced. The video of the manufacturing process is available here[1].

---

[1] Offline readers please refer to the online version of the thesis or visit www.ramlab.com

3. **Minimum number of Start and Stop Points:** The locations at which the deposition process starts and stops are called the start and stop points, respectively. At the start and stop points, the electrical current ramps up and ramps down, respectively. Therefore, the deposited material forms uneven bead shapes at these locations. The uneven beads can accumulate over the layers and may lead to non-uniform deposited heights. The uneven deposition at the start and stop locations can be compensated by choosing the alternate deposition strategy as shown in Fig. 1.7. The material deposited at the start and stop locations also has poor material quality. Therefore, these points should be at locations from where they can be easily machined and removed from the part. It is also required to have continuous material deposition for the parts to avoid these points in the structure.

4. **Intersections**: WAAM is preferred to manufacture Thin-walled structures which generally find applications in the aerospace industry. The near-net shape can be achieved by WAAM and it improves the buy-to-fly ratio of thin-walled structures (Lockett et al., 2017). These structures do not exhibit any variation in design along the building directions. Moreover, intersections at which two or more members intersect are often observed in these structures. Manufacturing these intersections in thin-walled structures is problematic with a continuous material deposition as extra material is deposited at these locations every time a robotic arm passes above it. This leads to non-uniformity of the deposited heights or deposition failures. Examples of defects at intersections produced by the WAAM process are shown in Fig. 1.8. To tackle the problem related to intersections, path-planning strategies are suggested to reduce the height error at intersections (Li et al., 2020; Song et al., 2021). The process parameters, such as deposition rate, can be locally modified at intersections to mitigate the deposition errors in heights (Gudeljevic and Klein, 2021). However, considering the WAAM of intersections at the part design stage is missing from the literature.

Several of the geometrical design considerations mentioned above can be included in TO to generate optimized designs for WAAM. Numerous formulations to include geometrical designs consideration related to minimum feature size (Zhou et al., 2015) and overhangs (Gaynor et al., 2014; Langelaar, 2017; Qian, 2017; van de Ven et al., 2018) for AM in TO are already present in the literature. These formulations can be used to generate designs for WAAM. However, a research gap exists to control the start and stop points and intersections features in TO.

1.2.3. DESIGN - PROCESS - MECHANICAL PERFORMANCE RELATIONSHIP

As mentioned in Section 1.1, the thermal history impacts the residual stresses, part distortion, overheating, and microstructure development. The thermal history experienced by the WAAM part depends on the geometrical layout, the deposition pattern, and process parameters.

Part design features can either facilitate or prohibit heat transfer which impacts the local transient thermal history experienced by the part (Gudeljevic and Klein, 2021). For intersections, at the junction, the amount of material is more than the amount of material away from the junctions. This increases the local conductance of the junction which

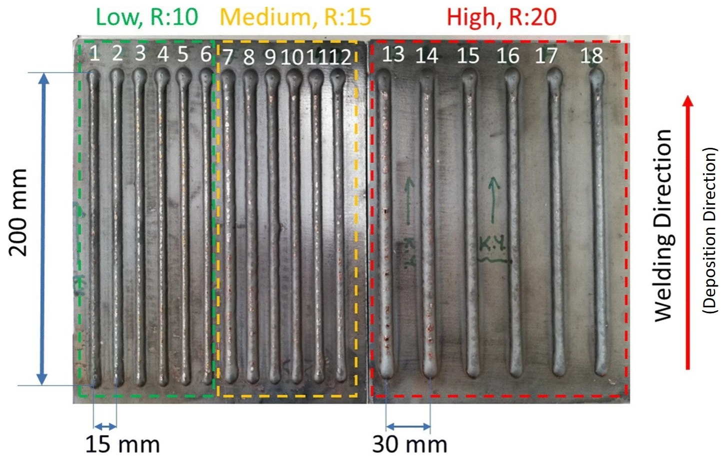

Figure 1.5: Variation of the bead size with respect to the heat input (Yildiz et al., 2020).

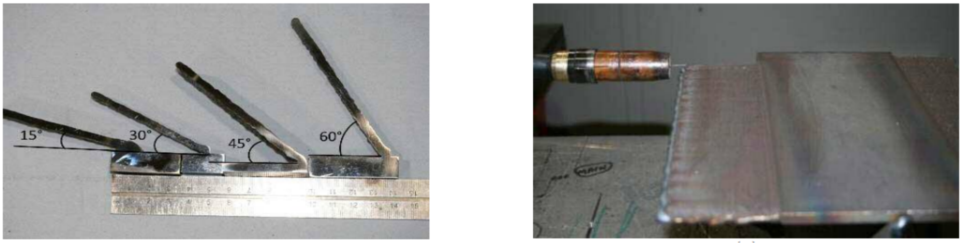

(a)

(b)

Figure 1.6: Overhanging features produced by the WAAM process (Mehnen et al., 2014).

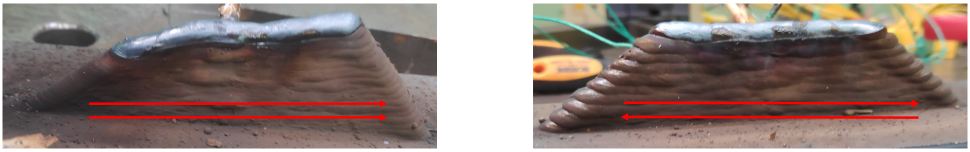

(a)

(b)

Figure 1.7: A tapered wall manufactured by two deposition strategies as indicated by the arrows. (a) shows the non-uniform deposition heights at the start and stop locations. (b) shows the uniform material deposition at the start and stop locations. The uniform deposition is due to the compensation at the start and stop locations achieved by employing the alternate deposition pattern.

facilitates high cooling rates at junctions. Moreover, the number of times the heat source passes over the material at the junction is more than for regions away from the junction. These two combined effects may impact the mechanical properties of the material at the junction and away from it differently. Heat transfer also depends on the overhanging

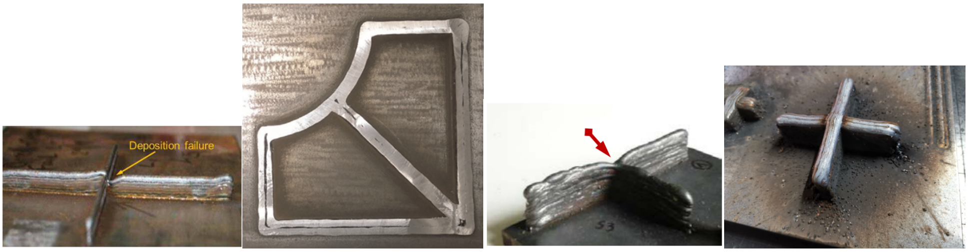

(a) (b) (c) (d)

Figure 1.8: Defects encountered at the intersections during WAAM.(a) Mehnen et al., 2014 (b) Ding et al., 2015 (c) Venturini et al., 2016 (d) Courtesy: RAMLAB.

angles in a design. Features with low overhanging angles may lead to heat accumulation and do not facilitate rapid heat transfer in the part. This leads to slow cooling rates, contrary to design features with high overhanging angles which may show a higher cooling rate. Thus, the overhanging angle can affect the material properties.

The process design stage of a part during WAAM involves the build direction selection, slicing of a part into layers, process parameter selection, and deposition strategy in each layer. Once the part is manufactured the post-processing steps are employed to reduce the surface roughness and relieve residual stresses through heat treatment (Goviazin et al., 2023; Vazquez et al., 2021). All the steps directly impact the thermal history experienced by the manufactured part. Various aspects of thermal history such as solidification rate, cooling rate, and thermal gradients affect the part performance. A considerable amount of research focused on residual stresses, part distortion, and overheating in AM parts exists (Akhtar et al., 2022; Barath Kumar and Manikandan, 2022; Bartlett and Li, 2019; Srivastava et al., 2021; Xie et al., 2022). Moreover, TO-related strategies to generate optimized designs for AM to minimize residual stresses and part distortions are also present in the literature (Cheng et al., 2019; Miki and Yamada, 2021; Misiun et al., 2021; Xu et al., 2022). These strategies can be extended to the WAAM process to minimize residual stresses and distortion. However, thus far, research on influencing part performance while altering the microstructure in metal AM through TO is missing in the literature.

The metal microstructure has various aspects such as grain size, grain morphology, texture, and solid-state phases. All of these aspects affect the mechanical properties such as Young's modulus and yield strength of the metal (Callister Jr and Rethwisch, 2020). WAAM parts comprised of stainless steels show anisotropy in Young's modulus and strength due to the textured microstructure (Belotti et al., 2023; Kyvelou et al., 2020; van Nuland et al., 2021). Unlike stainless steels, High Strength Low Alloy (HSLA) steels show no significant anisotropy due to negligible texture in the microstructure. However, the cooling rates during the process affect the solid-state phase fractions which impact the yield strength of the HSLA material (Babu et al., 2023; Huang et al., 2022).

In conclusion, the thermal history of the AM part can be influenced by design, processing steps, and post-processing such that microstructure development in the part

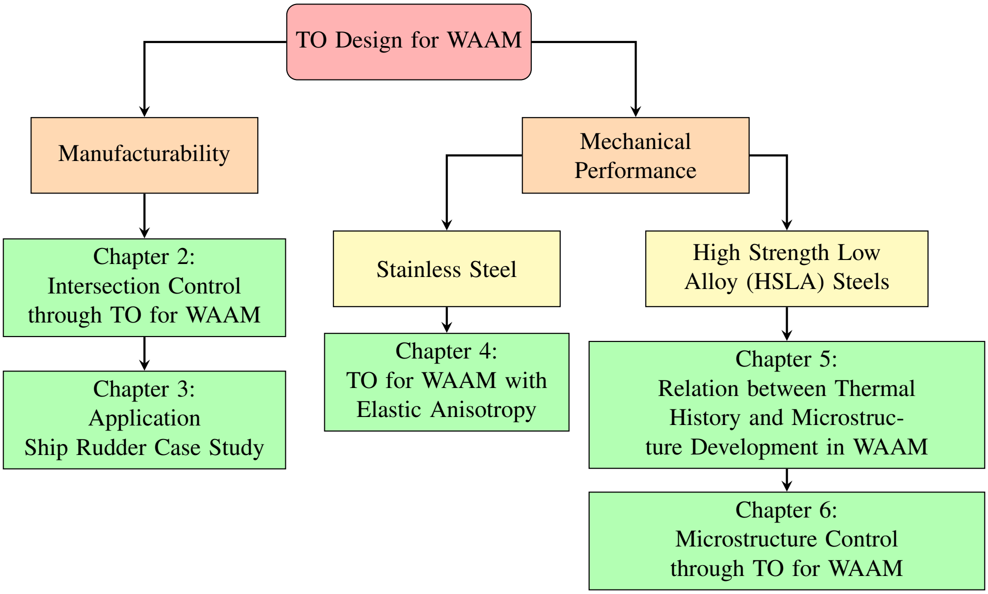

Figure 1.9: Outline of the thesis

during AM can be influenced. This offers new opportunities to create parts with improved properties. To exploit the complex relationship between geometry, process, and final properties, dedicated novel computational design methods are required.

1.3. RESEARCH QUESTIONS AND THESIS OUTLINE

Design for WAAM using TO has an aspect related to manufacturability, which is directly related to geometrical design. Another aspect is related to geometrical design, process, and mechanical properties. In this thesis, both aspects are explored and mathematical formulations are proposed to design for WAAM using TO. The thesis outline is shown in Fig. 1.9.

In Chapter 2, a novel methodology is developed to identify and control intersections during TO. It is previously emphasized that intersections are important design features that are susceptible to WAAM specific manufacturing defects. The research question essential to answer is:

1. *How to identify and control intersections that are susceptible to WAAM defects in TO?*

In Chapter 3, a ship rudder is redesigned using TO which will be manufactured by WAAM. The ship rudder is redesigned to achieve the equivalent mechanical performance of the original rudder design while reducing weight. There are also various design and manufacturing requirements for the ship rudder which are required to be satisfied during TO.

In Chapter 4, the elastic anisotropy exhibited by WAAM parts of stainless steel structures (Belotti et al., 2023; Kyvelou et al., 2020; van Nuland et al., 2021) due to microstructural texture is integrated into a TO framework. The elastic anisotropy is exploited to optimize the geometrical design and deposition directions simultaneously to generate optimized structural designs and deposition paths for WAAM with high stiffness. To integrate elastic anisotropy in TO the following research question is essential to explore:

2. *How to account and exploit for the elastic anisotropy in a TO framework?*

In Chapter 5, the relationship between the thermal history experienced by the WAAM part of HSLA steels and the solid-state phase transformations is established. The research question essential to explore is:

3. *How to model and validate the thermal history and phase transformations experienced by WAAM parts and their effect on the resulting microstructure and mechanical properties?*

In Chapter 6, the relationship developed in Chapter 5 is integrated into TO and used to optimize the geometric layout such that required solid-state phases are obtained for a desired local yield strength at specific part locations during the WAAM process. The pertinent research question addressed in this chapter is:

4. *How to account for the effect of the thermal history in a TO framework to obtain the desired microstructure and mechanical properties during WAAM?*

Finally, in Chapter 7 major conclusions of the conducted research are outlined.

BIBLIOGRAPHY

Akhtar, W., Lazoglu, I., & Liang, S. Y. (2022). Prediction and control of residual stress-based distortions in the machining of aerospace parts: A review. *Journal of Manufacturing Processes*, *76*, 106–122.

Almeida, P., & Williams, S. (2010). Innovative process model of ti-6al-4v additive layer manufacturing using cold metal transfer (cmt). *2010 International Solid Freeform Fabrication Symposium*.

Babu, A., Ebrahimi, A., Wu, K.-H., Richardson, I. M., & Hermans, M. J. (2023). Local control of microstructure and mechanical properties of high-strength steel in electric arc-based additive manufacturing. *Journal of Materials Research and Technology*.

Barath Kumar, M., & Manikandan, M. (2022). Assessment of process, parameters, residual stress mitigation, post treatments and finite element analysis simulations of wire arc additive manufacturing technique. *Metals and Materials International*, *28*(1), 54–111.

Bartlett, J. L., & Li, X. (2019). An overview of residual stresses in metal powder bed fusion. *Additive Manufacturing*, *27*, 131–149.

Belotti, L. P., van Nuland, T., Geers, M., Hoefnagels, J., & van Dommelen, J. (2023). On the anisotropy of thick-walled wire arc additively manufactured stainless steel parts. *Materials Science and Engineering: A*, *863*, 144538.

Bendsoe, M. P., & Sigmund, O. (2013). *Topology optimization: Theory, methods, and applications*. Springer Science & Business Media.

Bikas, H., Stavropoulos, P., & Chryssolouris, G. (2016). Additive manufacturing methods and modelling approaches: A critical review. *The International Journal of Advanced Manufacturing Technology*, *83*(1), 389–405.

Callister Jr, W. D., & Rethwisch, D. G. (2020). *Callister's materials science and engineering*. John Wiley & Sons.

Cheng, L., Liang, X., Bai, J., Chen, Q., Lemon, J., & To, A. (2019). On utilizing topology optimization to design support structure to prevent residual stress induced build failure in laser powder bed metal additive manufacturing. *Additive Manufacturing*, *27*, 290–304.

DebRoy, T., Wei, H., Zuback, J., Mukherjee, T., Elmer, J., Milewski, J., Beese, A. M., Wilson-Heid, A. d., De, A., & Zhang, W. (2018). Additive manufacturing of metallic components–process, structure and properties. *Progress in Materials Science*, *92*, 112–224.

Ding, D., Pan, Z., Cuiuri, D., & Li, H. (2015). A practical path planning methodology for wire and arc additive manufacturing of thin-walled structures. *Robotics and Computer-Integrated Manufacturing*, *34*, 8–19.

Frazier, W. E. (2014). Metal additive manufacturing: A review. *Journal of Materials Engineering and performance*, *23*(6), 1917–1928.

Gaynor, A. T., Meisel, N. A., Williams, C. B., & Guest, J. K. (2014). Topology optimization for additive manufacturing: Considering maximum overhang constraint. *15th AIAA/ISSMO multidisciplinary analysis and optimization conference*, 2036.

Goviazin, G., Rittel, D., & Shirizly, A. (2023). Achieving high strength with low residual stress in waam ss316l using flow-forming and heat treatment. *Materials Science and Engineering: A*, *873*, 145043.

Gu, D. D., Meiners, W., Wissenbach, K., & Poprawe, R. (2012). Laser additive manufacturing of metallic components: Materials, processes and mechanisms. *International materials reviews*, *57*(3), 133–164.

Gudeljevic, M., & Klein, T. (2021). Investigation of material characteristics of intersections built by wire and arc additive manufacturing using locally varying deposition parameters. *The International Journal of Advanced Manufacturing Technology*, *116*, 2021–2029.

Huang, C., Kyvelou, P., Zhang, R., Britton, T. B., & Gardner, L. (2022). Mechanical testing and microstructural analysis of wire arc additively manufactured steels. *Materials & Design*, *216*, 110544.

Jafari, D., Vaneker, T. H., & Gibson, I. (2021). Wire and arc additive manufacturing: Opportunities and challenges to control the quality and accuracy of manufactured parts. *Materials & Design*, *202*, 109471.

Koch, J., & Mazumder, J. (1993). Rapid prototyping by laser cladding. *International Congress on Applications of Lasers & Electro-Optics*, *1993*(1), 556–565.

Kyvelou, P., Slack, H., Mountanou, D. D., Wadee, M. A., Britton, T. B., Buchanan, C., & Gardner, L. (2020). Mechanical and microstructural testing of wire and arc additively manufactured sheet material. *Materials & Design*, *192*, 108675.

Langelaar, M. (2017). An additive manufacturing filter for topology optimization of print-ready designs. *Structural and multidisciplinary optimization*, *55*(3), 871–883.

Li, R., Zhang, H., Dai, F., Huang, C., & Wang, G. (2020). End lateral extension path strategy for intersection in wire and arc additive manufactured 2319 aluminum alloy. *Rapid Prototyping Journal*, *26*(2), 360–369.

Lockett, H., Ding, J., Williams, S., & Martina, F. (2017). Design for wire+ arc additive manufacture: Design rules and build orientation selection. *Journal of Engineering Design*, *28*(7-9), 568–598.

McMillan, M., Leary, M., & Brandt, M. (2017). Computationally efficient finite difference method for metal additive manufacturing: A reduced-order dfam tool applied to slm. *Materials & Design*, *132*, 226–243.

Mehnen, J., Ding, J., Lockett, H., & Kazanas, P. (2014). Design study for wire and arc additive manufacture. *International Journal of Product Development 20*, *19*(1-3), 2–20.

Miki, T., & Yamada, T. (2021). Topology optimization considering the distortion in additive manufacturing. *Finite Elements in Analysis and Design*, *193*, 103558.

Misiun, G., van de Ven, E., Langelaar, M., Geijselaers, H., van Keulen, F., van den Boogaard, T., & Ayas, C. (2021). Topology optimization for additive manufacturing with distortion constraints. *Computer Methods in Applied Mechanics and Engineering*, *386*, 114095.

Qian, X. (2017). Undercut and overhang angle control in topology optimization: A density gradient based integral approach. *International Journal for Numerical Methods in Engineering, 111*(3), 247–272.

Shi, X., Ma, S., Liu, C., Wu, Q., Lu, J., Liu, Y., & Shi, W. (2017). Selective laser melting-wire arc additive manufacturing hybrid fabrication of ti-6al-4v alloy: Microstructure and mechanical properties. *Materials Science and Engineering: A, 684*, 196–204.

Song, G.-H., Lee, C.-M., & Kim, D.-H. (2021). Investigation of path planning to reduce height errors of intersection parts in wire-arc additive manufacturing. *Materials, 14*(21), 6477.

Srivastava, S., Garg, R. K., Sharma, V. S., & Sachdeva, A. (2021). Measurement and mitigation of residual stress in wire-arc additive manufacturing: A review of macro-scale continuum modelling approach. *Archives of Computational Methods in Engineering, 28*, 3491–3515.

van de Ven, E., Maas, R., Ayas, C., Langelaar, M., & van Keulen, F. (2018). Continuous front propagation-based overhang control for topology optimization with additive manufacturing. *Structural and Multidisciplinary Optimization, 57*(5), 2075–2091.

van Nuland, T. F., van Dommelen, J., & Geers, M. G. (2021). Microstructural modeling of anisotropic plasticity in large scale additively manufactured 316l stainless steel. *Mechanics of Materials, 153*, 103664.

Vazquez, L., Rodriguez, M. N., Rodriguez, I., & Alvarez, P. (2021). Influence of post-deposition heat treatments on the microstructure and tensile properties of ti-6al-4v parts manufactured by cmt-waam. *Metals, 11*(8), 1161.

Venturini, G., Montevecchi, F., Scippa, A., & Campatelli, G. (2016). Optimization of waam deposition patterns for t-crossing features. *Procedia Cirp, 55*, 95–100.

Wong, K. V., & Hernandez, A. (2012). A review of additive manufacturing. *International scholarly research notices, 2012*.

Wu, B., Pan, Z., Ding, D., Cuiuri, D., Li, H., Xu, J., & Norrish, J. (2018). A review of the wire arc additive manufacturing of metals: Properties, defects and quality improvement. *Journal of Manufacturing Processes, 35*, 127–139.

Xie, D., Lv, F., Yang, Y., Shen, L., Tian, Z., Shuai, C., Chen, B., & Zhao, J. (2022). A review on distortion and residual stress in additive manufacturing. *Chinese Journal of Mechanical Engineering: Additive Manufacturing Frontiers*, 100039.

Xu, S., Liu, J., & Ma, Y. (2022). Residual stress constrained self-support topology optimization for metal additive manufacturing. *Computer Methods in Applied Mechanics and Engineering, 389*, 114380.

Yildiz, A. S., Davut, K., Koc, B., & Yilmaz, O. (2020). Wire arc additive manufacturing of high-strength low alloy steels: Study of process parameters and their influence on the bead geometry and mechanical characteristics. *The International Journal of Advanced Manufacturing Technology, 108*(11), 3391–3404.

Zhou, M., Lazarov, B. S., Wang, F., & Sigmund, O. (2015). Minimum length scale in topology optimization by geometric constraints. *Computer Methods in Applied Mechanics and Engineering, 293*, 266–282.

2

A STRESS-BASED CRITERION TO IDENTIFY AND CONTROL INTERSECTIONS IN 2D COMPLIANCE MINIMIZATION TOPOLOGY OPTIMIZATION

Topology optimization typically generates designs that exhibit significant geometrical complexity, which can pose difficulties for manufacturing and assembly. The number of occurrences of an important design feature, in particular intersections, increases with geometrical complexity. Intersections are essential for load transfer in many engineering structures. For certain upcoming manufacturing processes, such as direct metal deposition, the size of an intersection plays a role. During metal deposition, slim intersections are more prone to manufacturing defects than bulkier ones. In this study, a computationally tractable methodology is proposed to both control occurrence and size of intersections in topology optimization. To identify intersections, a stress-based quantity is proposed, denoted as Intersection Indicator. This quantity is based on the local degree of multi-axiality of the stress state, and identifies material points at intersections. The proposed intersection indicator can identify intersections in both single as well as multi-load case problems. To detect the relative size of intersections, the average density in the vicinity of an intersection is used to penalize or promote intersection sizes of interest. The corresponding sensitivity analysis involves solving a set of adjoint equations for each load case. Numerical 2D experiments demonstrate a controllable reduction of penalized slim intersections compared to the designs obtained from conventional compliance minimization. The overall geometrical complexity of the design is reduced due to the promotion of bulkier intersections which leads to an increase in compliance. The designs obtained are more suitable for manufacturing processes such as direct metal deposition.

2.1. INTRODUCTION

Topology Optimization (TO) is an effective method to generate early phase designs in a variety of engineering applications such as aerospace, biomedical, optics and maritime (Bendsoe and Sigmund, 2013). Designs obtained by TO, although having a superior mechanical performance, can be difficult or impossible to manufacture due to their geometrical complexity (Lazarov et al., 2016). Additional manufacturing constraints are hence usually integrated into TO to generate designs which are suitable for processes such as casting (Xia et al., 2010; L. Zhou and Zhang, 2019), machining (Langelaar, 2019; Sigmund, 2009) and Additive Manufacturing (AM) (Gaynor and Guest, 2016; Langelaar, 2016; Van de Ven et al., 2020). Many other studies have also provided methods to specifically reduce the geometrical complexity of TO designs. For instance, controlling minimum length scale in material and void regions. Length scale control can be achieved by filters or projection methods (Bourdin, 2001; Guest et al., 2004; M. Zhou et al., 2015) and skeleton-based methods (Xia and Shi, 2015; Zhang et al., 2016; Zhang, Liu, et al., 2017; Zhang et al., 2014). Moreover, geometrical complexity can also be controlled by restricting the number of structural components, in, e.g., the moving morphable component framework (Wein et al., 2020; Zhang, Zhou, et al., 2017). In all mentioned methods a certain amount of mechanical performance is typically sacrificed in order to achieve a manufacturable design.

Here we focus on generating designs by TO while controlling an important geometrical aspect of a structural design, namely *intersections*. The number of occurrences of intersections increase with the increase in geometrical complexity. Intersections are critical from both a performance and manufacturing point of view. However, how to explicitly control intersections is an open question in the literature. An *intersection* is a connection between two or more structural members in a design where a major change in the stress state occurs (Ambrozkiewicz and Kriegesmann, 2018). Consequently, a multiaxial stress state is encountered at intersections (M. Bendsøe and Haber, 1993). Intersections can be susceptible to failure due to stress multi-axiality (Clausmeyer et al., 1991). Moreover, from a manufacturing perspective, intersections can be associated with high cost. For structures produced by assembly operations, intersections may imply joining through riveting, bolting or welding operations (Megson, 2019). Consequently, reducing the number of intersections in designs will lead to less joining operations, and lower cost. Intersections also pose a problem in certain AM methods. A prominent example is Direct Metal Deposition (DMD). DMD is a metal AM variant which is rapidly maturing and used currently to produce large functional structures such as ship propellers and aircraft components (Lockett et al., 2017). In DMD, simultaneous material melting and deposition occurs along the deposition lines. It is difficult to avoid overlapping of the deposition paths at intersections. This leads to extra material deposition at intersections which in turn cause geometrical deviations (Mehnen et al., 2014). However, when the size of an intersection is sufficiently large, overlapping of the deposition paths can be avoided. Hence, it is of interest to control not only the number but also the size of intersections.

Intersection detection in density based TO problem has been investigated through an image-based method (Gamache et al., 2018) and a stress-based method (Ambrozkiewicz and Kriegesmann, 2018). In the image-based method, the skeleton of the structure is used to identify the structural members intersecting at nodes. These nodes are considered as intersections. However, the algorithm used for detection is not differentiable and therefore design sensitivities can not be calculated. This poses a problem in using this approach in gradient-based optimization (Gamache et al., 2018). Detection of intersections through a stress-based parameter provides a possibility for design sensitivity calculation. Stresses and sensitivities of stress-based quantities are readily computable for mechanical TO problems. Ambrozkiewicz and Kriegesmann, 2018 used principal stress ratios to detect intersections and straight members connected to it, in order to evaluate the load path in the design. However, specific control on intersections during optimization was not performed and the use of these ratios was limited to detection in single load case problem.

In this paper, the control of intersections is studied using stress-state information in the context of the classical density based TO problem of compliance minimization (M. P. Bendsøe, 1989). Controlling the number and/or size of intersections that are typically generated in TO may lead to major topological changes. To illustrate this, consider the schematic of a structural baseline design, shown in Fig. 2.1a. The intersections are marked by red dashed circles. The designs shown in Fig. 2.1b and Fig. 2.1c have the same material volume as the baseline design, but the intersections are larger and fewer. A significant reduction in the geometrical complexity is observed from Fig. 2.1a to Fig. 2.1b and from Fig. 2.1b to Fig. 2.1c. The aim of this paper is to present a computationally tractable approach for identifying and controlling intersections as a function of their size, in 2D density-based compliance minimization for single and multi load case problems. 2D problems are relevant for industrial DMD applications, because most of the structural components produced by DMD are manufactured by stacking 2D layers on top of each other. A discussion on challenges to extend the method to 3D is given at the end of the paper. Note that controlling intersections is shown for compliance minimization TO problems, however, the stress multi-axiality at intersections can also be used in many other applications.

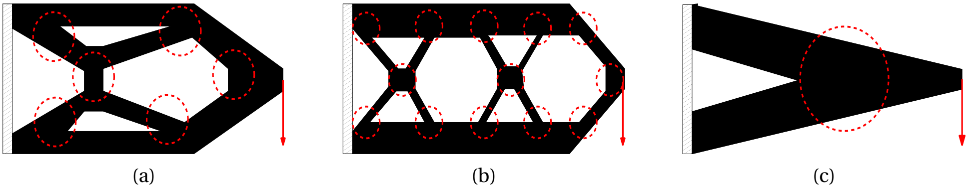
(a) (b) (c)

Figure 2.1: Schematic representation : (a) Complex baseline design with marked intersections (red dashed circles). (b) Design modification with reduced geometrical complexity and relatively thicker intersections than the baseline design. (c) Design modification with further reduced geometrical complexity and an even thicker intersection than in (b).

In order to achieve the above mentioned aim, a mathematical formulation is developed to identify the intersections in the density based minimum compliance TO. There are two aspects to consider: detection and discriminating intersections depending on their relative size. In order to detect intersections, the stress state generated in the design due to the applied loads and boundary conditions is evaluated. The key idea is that at an intersection, the stress state exhibits an higher level of multi-axiality compared to uniaxially loaded design features. Therefore, a stress-based parameter is defined to measure the local degree of stress multi-axiality, making use of the principal stress ratios. An absolute value of this ratio close to 1 indicates a multi-axial state that occurs typically in the vicinity of an intersection. The stress-based parameter is selected because the sensitivity with respect to the design variables can be calculated easily. The mathematical description of the proposed Intersection Indicator is given for both single load and multi load problems. The latter is more challenging, because stress fields produced in response to each load system are different.

Once the intersections can be identified, a further step is to control the occurrence as a function of the relative size of the intersections. In order to identify relative size, the average density in a local circular domain at the location of an intersection is used as a measure of the size of the intersection. Consequently, intersections slimmer (or bulkier) in size can be penalized more, whereas bulkier (or slimmer) can be allowed in the design domain using a weight function. To illustrate how these measures can be combined, we propose an objective function aiming to minimize relatively slim intersections, as this is of particular interest for the DMD process.

During optimization, if the objective is dominated equally by compliance and intersection reduction, then black and white design will be realized. However, if the objective is dominated by intersection minimization, designs with considerable gray regions may result. This problem arises because, the intersection identification is indifferent to the magnitude of the local stress but solely depends on the local principal stress ratio. For this, a threshold stress level is introduced to distinguish between elements with similar principal stress ratios but different stress levels. Moreover, since the intersection indicator is a function of the principal stress ratio, if one or both principal stresses vanish during optimization the intersection indicator will be ill-defined. By introducing the threshold stresses into the formulation, this problem is also resolved. In general for stress-based TO, problems related to the local nature of the stresses and possible stress singularity are of concern (Bruggi, 2008; Duysinx and Bendsøe, 1998; Kirsch, 1990). However, these problems are encountered when the stresses are constrained in the design domain. In our case, no constraints are imposed on the stresses, hence, reported problems are not encountered in our work. The effectiveness of our formulation is demonstrated, and the influence of various numerical parameters is studied based on several 2D compliance minimization problems.

The remainder of the paper is organized as follows: Section 2.2 presents the formulation of the Intersection Indicator, influence of threshold stress levels and intersection size estimation. The topology optimization problem formulation to minimize slim intersections and influence of threshold stress during optimization are presented in Section 2.3. Description of the numerical examples and resulting optimized designs and discussion are given in Section 2.4. A brief discussion on challenges to extend the method to 3D problems are outlined in Section 2.5. Finally, Section 2.6 provides the final conclusions.

Table 2.1: Default Parameters for the optimization

Finite Element Model and Material Properties		Optimization parameters	
Element size	1 mm × 1 mm	p	3
Element Type	Plane stress Q4 element	μ	0.02
E_0 (Material)	210 GPa (Chen et al., 2016)	V_0	50% of design domain
$E_{\min}$ (Void)	$E_0 \times 10^{-9}$	Initial state	$\rho_e = 0.5 \ \forall e \in \Omega_N$
ν	0.3	Stopping Criterion	$\|\|\Delta\boldsymbol{\rho}\|\|_\infty \leq 0.01$
Stress calculation	At centroid	Move limit	0.2
Thickness of domain	1 mm (Plane stress condition)	$r_{\min}$	2.5 mm

2.2. INTERSECTION INDICATOR

2.2.1. OPTIMIZATION PROBLEM

For completeness, we briefly summarize the optimization problem considered:

$$\min_{\boldsymbol{\rho}} \quad c = \sum_{e=1}^{N} E_e(\tilde{\rho}_e)\mathbf{u}_e^{\mathrm{T}}\mathbf{k}_0\mathbf{u}_e, \tag{2.1}$$

$$\text{where} \quad \tilde{\rho}_e = \frac{\sum_{i\in\Omega_e^{\min}} t_i(\mathbf{x}_i)v_i\rho_i}{\sum_{i\in\Omega_e^{\min}} t_i(\mathbf{x}_i)v_i}, \tag{2.2}$$

$$t_i(\mathbf{x}_i) = r_{\min} - ||\mathbf{x}_i - \mathbf{x}_e||. \tag{2.3}$$

$$\text{s.t.} \quad \mathbf{Ku} = \mathbf{f}. \tag{2.4}$$

$$g = \frac{\sum_{\Omega_N} v_e\tilde{\rho}_e}{V_0} - 1 \leq 0. \tag{2.5}$$

$$0 \leq \rho_e \leq 1, \quad \forall e \in \Omega_N. \tag{2.6}$$

In Eq. (2.1), c is the structural compliance, $\mathbf{u}_e$ represents the element nodal degrees of freedom, $\mathbf{k_0}$ is the element stiffness matrix, and E_e is the Young's modulus which is scaled using the filtered density $\tilde{\rho}_e$ as

$$E_e(\tilde{\rho}_e) = E_{\min} + \tilde{\rho}_e^p(E_0 - E_{\min}). \tag{2.7}$$

E_0 and $E_{\min}$ are the Young's modulus of material and void, respectively, p is the SIMP penalization exponent and N is the total number of elements in design domain Ω_N. Eq. (2.2) defines the density filter applied to the design variable ρ_e at position $\mathbf{x_e}$ with element volume v_e (Bruns and Tortorelli, 2001). Eq. (2.3) represents the weight (t_i) calculation for the density filter. $\Omega_e^{\min}$ is the local circular region in which the filter is effective with a radius $r_{\min}$. Eq. (2.4) is the linear elastic state equation, where $\mathbf{K}$ is the global

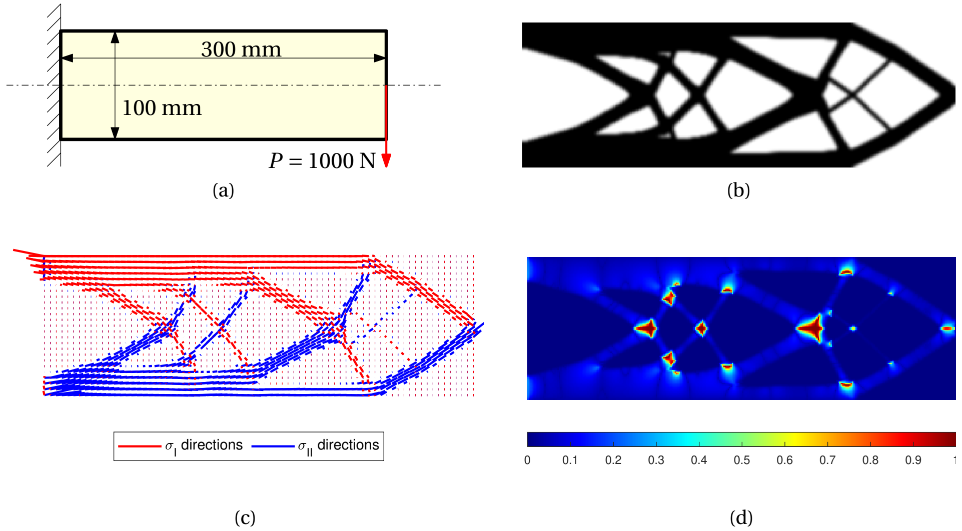

Figure 2.2: Load case Cantilever Beam : (a) design domain with dimensions discretized with 300 × 100 quadrilateral finite elements, loading and boundary conditions indicated, (b) design ($\tilde{\rho}_e$) obtained upon solving the standard compliance minimization problem (c) vector plot of dominant principal stress directions scaled with the magnitude dominant principal stress. Red and Blue are the representation of principal stresses σ_I and σ_{II}, respectively. (d) Intersection indicator (ξ_e) field of the corresponding design which indicates biaxiality of the stress state within the structure when it is approximately one (red regions).

stiffness matrix and, **u** and **f** are the global nodal degrees of freedom and nodal loads, respectively. Eq. (2.5) represents the volume constraint, and Eq. (2.6) bounds the density variable for all elements in the design domain Ω_N. The 2D problem is solved using gradient-based optimization (Svanberg, 1987) following the nested analysis and design approach (Amir et al., 2010).

2.2.2. INTERSECTION DETECTION

SINGLE LOAD CASE

In order to identify intersections in compliance minimization TO, multi-axiality of the stress state is exploited. In compliance optimization the TO generates structural features typically under uniaxial stress to bear the load, such that the principal stress direction align in accordance with the orientation of a member (Ambrozkiewicz and Kriegesmann, 2018; M. Bendsøe and Haber, 1993). Since an intersection is where members with different orientation meet, the stress tensor should exhibit a multi-axial characteristic for single load case. This notion is illustrated using an optimized cantilever beam layout shown in Fig. 2.2. The optimization is carried out using the default parameters shown in Table 2.1, for the design domain depicted in Fig. 2.2a along with loading and boundary conditions. For the design obtained by standard compliance minimization, as depicted in Fig. 2.2b, two principal stresses σ_I and σ_{II} are calculated and the directions of the dominant principal stresses, i.e. either σ_I or σ_{II}, for the material region are realized by line segments in Fig. 2.2c. The length of the line segments in Fig. 2.2c are scaled with the magnitude of the principal stresses. As expected, the stress state is primarily uniaxial in the members except at the intersections.

It remains to quantify stress multi-axiality in a design. The stresses in each element can be computed as follows:

$$\boldsymbol{\sigma}_e = \tilde{\rho}_e^p \mathbf{D}_e \mathbf{B}_e \mathbf{u}_e. \tag{2.8}$$

Note that the displacement field is already calculated in each optimization iteration. Stresses can therefore be obtained for a low computational cost. Here, $\boldsymbol{\sigma}_e$ is the stress state of element e calculated at its centroid, $\mathbf{B}_e$ is the strain-displacement matrix and $\mathbf{D}_e$ is the constant constitutive matrix for isotropic linear elasticity. A plane stress condition is considered, i.e. $\boldsymbol{\sigma}_e$ is given by $[\sigma_{xx}, \sigma_{yy}, \tau_{xy}]^T$ using Voigt notation. Next, the principal stresses for element e are calculated using:

$$\begin{aligned}
\sigma_I &= \frac{\sigma_{xx}+\sigma_{yy}}{2} + \sqrt{\left(\frac{\sigma_{xx}-\sigma_{yy}}{2}\right)^2 + \tau_{xy}^2},\\
\sigma_{II} &= \frac{\sigma_{xx}+\sigma_{yy}}{2} - \sqrt{\left(\frac{\sigma_{xx}-\sigma_{yy}}{2}\right)^2 + \tau_{xy}^2}.
\end{aligned} \tag{2.9}$$

To measure stress biaxiality, we introduce a quantity R_e composed of the ratios of these principal stresses

$$R_e = \frac{\sigma_I^2}{\sigma_{II}^2} + \frac{\sigma_{II}^2}{\sigma_I^2}. \tag{2.10}$$

The above function is chosen because it involves both ratios σ_I/σ_{II} and σ_{II}/σ_I. The stresses are squared because principal stresses could be both negative as well as positive and here we are only interested in the magnitude of stresses. For a biaxial stress state with principal stresses of roughly equal magnitude we obtain $R_e \approx 2$. In cases where the magnitude of the principal stresses differ significantly, including uniaxial stress states, it follows that $R_e >> 2$. In the void regions, where the magnitude of the principal stresses is relatively small, R_e may give false positives. Therefore, the filtered design variables $\tilde{\rho}_e$ can be used to avoid incorrect intersection detection in void regions. Thus, an Intersection Indicator (ξ_e) is proposed as:

$$\xi_e = \frac{\tilde{\rho}_e^p}{\log_2\left(R_e\right)}. \tag{2.11}$$

The operation $1/\log_2(.)$ is applied on R_e to map the value of ξ_e between 0 and 1. As a result, three distinct settings can be identified: biaxial stress states in the solid ($\xi_e \approx 1$), uniaxial stress states in the solid ($0 < \xi_e \ll 1$) and void regions ($\xi_e \approx 0$). Contours of this Intersection Indicator of the cantilever beam presented in Fig. 2.2b, are shown in Fig. 2.2d. It is clearly visible that the indicator reaches values near unity at intersections and does not lead to false positive in void regions. Thus, through exploiting biaxiality of the stress state intersections can be accurately identified.

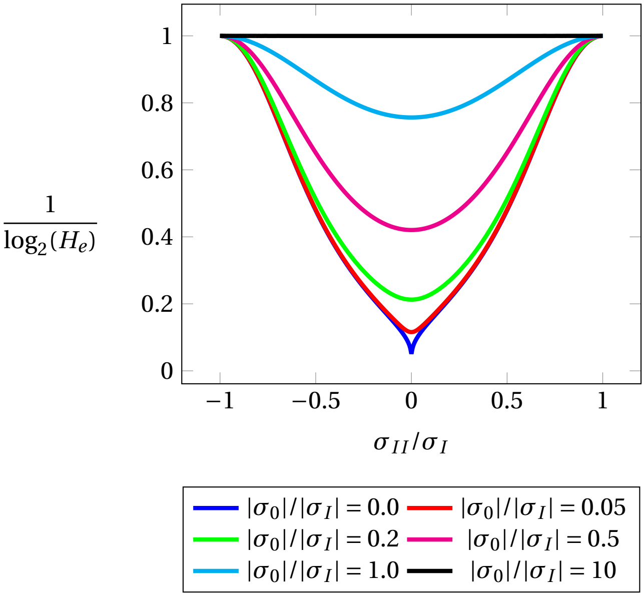

Figure 2.3: The effect of the threshold stress on the multi-axiality criterion. The x-axis represent the stress ratios assuming $|\sigma_{II}| \leq |\sigma_I|$, and y-axis represent the corresponding value of the multi-axiality criterion. The multi-axiality criterion is plotted for various ratios of threshold stress and first principal stress.

INFLUENCE OF THRESHOLD STRESS ON INTERSECTION INDICATOR

As mentioned previously, ξ_e is the intersection indicator which is a function of filtered density variable $\tilde{\rho}_e$ and stress multiaxiality measure R_e. The intersection indicator is used for optimization but when the design focus is primarily on intersection reduction, gray regions in mildly stressed regions remain. This is because the multi-axiality criterion R_e is indifferent to stress levels. Therefore, the optimizer tends to reduce the multi-axiality of the local stress state instead of reducing the density of the element. Two elements which are at different stress levels but with comparable principal stress ratios will give a similar value of R_e. Therefore, it is desirable to distinguish between elements at different stress levels during optimization. Although void regions that are not load bearing are filtered out by the $\tilde{\rho}_e$ dependence of Eq. (2.11), the indifference of stress multi-axiality to differing stress levels can result in gray densities remaining in the design.

We introduce a threshold stress to distinguish between points at different stress levels to mitigate the complications discussed above. Moreover, to define intersection indicator for the cases where principal stresses may vanish, i.e., $\sigma_I \approx 0$ or $\sigma_{II} \approx 0$ or both, the threshold stress is used. The multi-axiality criterion, R_e, is thus modified to account for multi-axiality of the stress state only above a threshold stress level σ_0:

$$H_e = \frac{\sigma_I^2 + \sigma_0^2}{\sigma_{II}^2 + \sigma_0^2} + \frac{\sigma_{II}^2 + \sigma_0^2}{\sigma_I^2 + \sigma_0^2}. \tag{2.12}$$

For $\sigma_0 = 0$, H_e is equal to R_e. The effect of threshold stresses on the multi-axiality criterion is shown in Fig. 2.3. For a non-zero σ_0, the multi-axiality criterion will behave

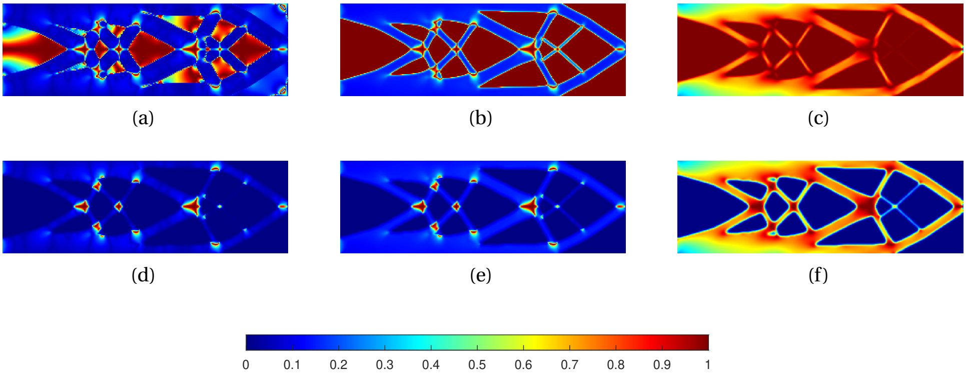
(a) (b) (c)

(d) (e) (f)

Figure 2.4: Effect of the threshold stresses : (a), (b) and (c) shows the effect on multiaxiality criterion ($1/\log_2(H_e)$) and, (d), (e) and (f) shows the effect on Intersection Indicator I_e for $\sigma_0 = 0$ MPa, 10 MPa and 100 MPa, respectively. The average and maximum value of $|\sigma_I|$ and $|\sigma_{II}|$ in the domain are 25.05 MPa and 618.16 MPa, respectively.

almost identical for points in the domain where stress levels are significantly above σ_0 (compare cases $|\sigma_0/\sigma_I| = 0.05$ and $|\sigma_0/\sigma_I| = 0$). However, regions where both principal stresses are significantly smaller than the threshold stress level (see for example the case $|\sigma_0/\sigma_I| = 10$) will be considered artificially as biaxially stressed regions even when $|\sigma_{II}|$ is very different from $|\sigma_I|$. Consequently, for mildly stressed areas the multi-axiality criterion becomes insensitive to the modification of the stress state. Replacing R_e with H_e in Eq. (2.11) provides the modified Intersection Indicator (I_e):

$$I_e = \frac{\tilde{\rho}_e^p}{\log_2\left(H_e\right)}. \tag{2.13}$$

The effect of σ_0 is demonstrated in Fig. 2.4. In this figure, $1/\log_2(H_e)$ and I_e are plotted for values of threshold stresses equal to 0, 10 MPa and 100 MPa for the design shown in Fig. 2.2b. The average and maximum value of both $|\sigma_I|$ and $|\sigma_{II}|$ in the domain are 25 MPa and 618 MPa, respectively. For $\sigma_0 = 0$, in Fig. 2.4a it can be seen that the low-stressed regions, which are the void regions, exhibit both uniaxiality as well as biaxiality of the stress state. Since the stress levels are insignificant in these regions, the notion of multi-axiality of the stress state does not signify presence of any relevant design features at these locations. However, in the solid region the multiaxiality parameter clearly identifies the straight members and intersections via an uniaxial or biaxial stress state, respectively. Note that the magnitude of principal stresses in the void areas are orders of magnitude smaller than those in the solid area, but still the multiaxiality criterion does not differentiate between them. Scaling the multiaxiality criterion with the local density yields the intersection indicator shown in Fig. 2.4d. For the case $\sigma_0 = 10$ MPa, the multiaxiality criterion is shown in Fig. 2.4b. It can be observed that the void regions in which the stress levels are negligible are now artificially identified as being in the biaxial stress state. Scaling with the filtered design variable removes these artificial biaxial regions. The resulting intersection indicator plot shown in Fig. 2.4e, shows no sign of artificial biaxial regions and no effect in the material regions. Hence, through the introduction of the threshold stresses, for mildly stressed regions multi-axiality becomes constant and thus cannot be influenced by the optimizer. The effect of threshold stress during optimization for intersection minimization of the same problem is discussed in detail in Section 2.3.2. More importantly, most solid regions experience stress levels far above the threshold stress levels, thus the effect of the threshold stress is not visible in the solid region. This observation will be used in Section 2.3.2 to select the threshold stress for different considered problems. A higher threshold stress value, like $\sigma_0 = 100$ MPa, affects both the multiaxiality criterion and the intersection indicator, such that the material regions are also considered in the artificial biaxial stress state as shown in Fig. 2.4c and Fig. 2.4f, which should be avoided. Therefore, threshold stresses should be lower than the principal stresses in the solid region.

MULTI-LOAD CASE

The Intersection Indicator defined above can be easily extended to multi-load case problems. First, a slight modification in notation is required for a multi-load case problem. Analogous to Eq. (2.10), for a total of M load cases with $m = 1\ldots M$, biaxiality in the design due to the m^{th} load case is determined via

$$R_e^{(m)} = \frac{\left(\sigma_I^{(m)}\right)^2}{\left(\sigma_{II}^{(m)}\right)^2} + \frac{\left(\sigma_{II}^{(m)}\right)^2}{\left(\sigma_I^{(m)}\right)^2}. \tag{2.14}$$

Substituting, $R_e^{(m)}$ in Eq. (2.11) provides the intersection indicator for the m^{th} load case, denoted as $\xi_e^{(m)}$.

Multiple threshold stress values should be selected, one $\sigma_0^{(m)}$ corresponding to each load case m because loads can be of differing magnitude. Therefore, Eq. (2.14) becomes

$$H_e^{(m)} = \frac{\left(\sigma_I^{(m)}\right)^2 + \left(\sigma_0^{(m)}\right)^2}{\left(\sigma_{II}^{(m)}\right)^2 + \left(\sigma_0^{(m)}\right)^2} + \frac{\left(\sigma_{II}^{(m)}\right)^2 + \left(\sigma_0^{(m)}\right)^2}{\left(\sigma_I^{(m)}\right)^2 + \left(\sigma_0^{(m)}\right)^2}. \tag{2.15}$$

Substituting $H_e^{(m)}$ in Eq. (2.13) gives the intersection indicator ($I_e^{(m)}$) corresponding to the m^{th} load case. Fig. 2.5a shows the design domain of a cantilever beam with prescribed boundary and loading conditions. Note that, P_1 and P_2 are applied as separate load cases, corresponding to $m = 1$ and $m = 2$, respectively. Through standard topology optimization for multi-load case problem, the design shown in Fig. 2.5b is obtained. The default parameters used for optimization are given in Table 2.1. The average $|\sigma_I|$ and $|\sigma_{II}|$ in the domain corresponding to only load P_1 are 26 MPa and 24 MPa, respectively, and corresponding to only load P_2 are 9 MPa and 7 MPa, respectively. Therefore, the threshold stresses $\sigma_0^{(m)}$ corresponding to only load P_1 and P_2 are selected as 10 MPa and 3 MPa, respectively, which are lower than both average principal stress values. The biaxiality criterion $1/\log_2(H_e^{(m)})$ for load case $m = 1$ and 2 are shown in Fig. 2.5c and Fig. 2.5d, respectively. The corresponding intersection indicator $I_e^{(m)}$ for load case $m = 1$ and 2 are shown in Fig. 2.5e and Fig. 2.5f, respectively. It is evident that through $I_e^{(1)}$ all intersections of the design can be identified. However, $I_e^{(2)}$ shows several false positives in the structural members (for example, Point d_2 in Fig. 2.5f). This is due to the fact that part of

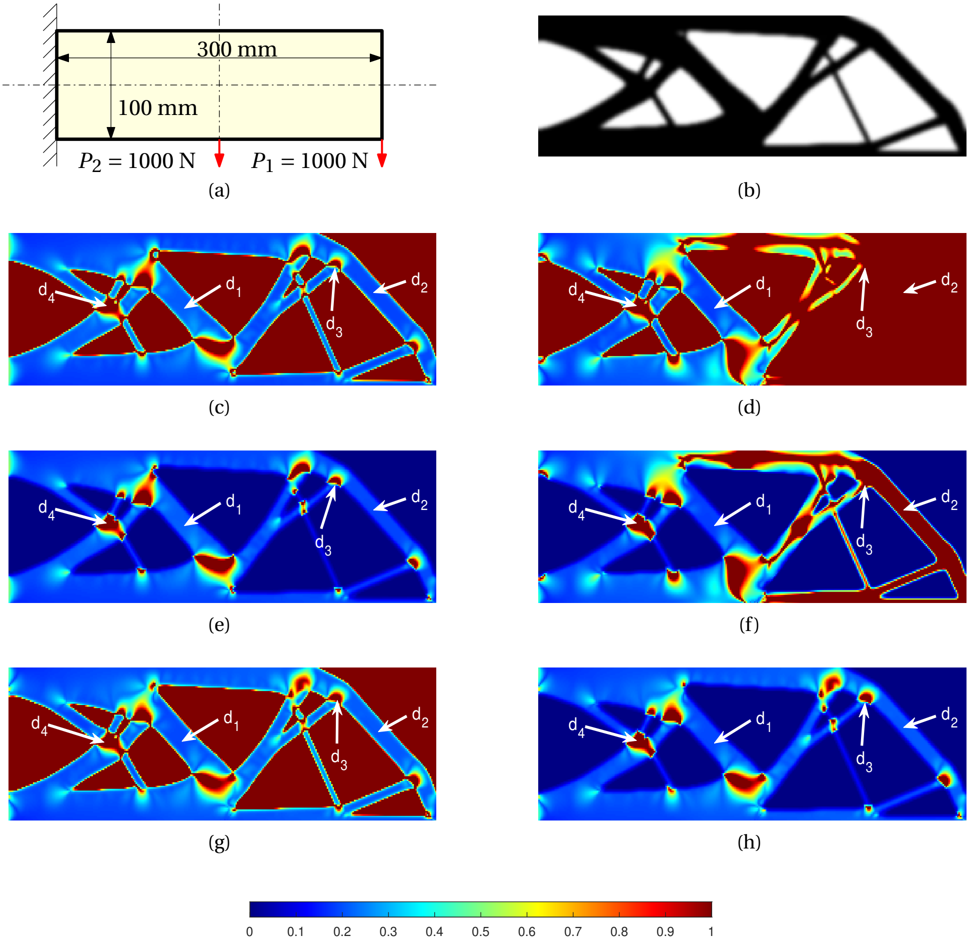

Figure 2.5: Multi-load case Cantilever Beam : (a) design domain with specified size, loading and boundary conditions, (b) design $(\tilde{\rho}_e)$ obtained by solving standard topology optimization compliance minimization problem, (c) and (d) represents the biaxiality criterion $(1/\log_2(H_e^{(m)}))$ for each load P_1 and P_2, respectively. (e) and (f) shows the Intersection Indicator $(I_e^{(m)})$ field of the corresponding design considering load case P_1 and P_2, respectively. (g) represents the aggregated biaxiality criterion $(1/\log_2(H_e))$. H_e is calculated using Eq. (2.16). (h) is the corresponding intersection indicator field obtained by aggregating the biaxiality of the stress state experienced by the structure by load P_1 and P_2.

the structure on the right side of the load P_2 is not load-bearing for the load case with P_2 only. Therefore, the stresses generated on the right side are negligible. Thus, false multiaxiality is detected in the unloaded part of the structure. To account for all the load cases and mitigate false positives, an aggregation scheme is applied considering the following statements:

- If an Element e has an uniaxial stress state and is load bearing in all load cases, then for all load cases, $|\sigma_I^{(m)}| \gg |\sigma_{II}^{(m)}|$ or vice versa, leading to high $H_e^{(m)}$ values in each case. In the example problem depicted in Fig. 2.5, Point d_1 is load bearing for both load P_1 and P_2. The values of $H_e^{(m)}$ for Point d_1 in both load cases are considerably higher than 2 which can be inferred by Fig. 2.5c–2.5d. Another case would be an Element e loaded in a uniaxial stress state for several loadcases which is not load bearing in other loadcases. Then, for loadcases in which it is load bearing $|\sigma_I^{(m)}| \gg |\sigma_{II}^{(m)}|$ or vice versa, again leading to high $H_e^{(m)}$ values in each case. However, for loadcases in which it is not loaded $|\sigma_I^{(m)}| \approx |\sigma_{II}^{(m)}| \approx 0$. Therefore, $H_e^{(m)}$ will be approximately equal to 2. In the example problem, Point d_2 is uniaxially loaded for loadcase P_1 but is not loaded for P_2. Therefore, the value of $H_e^{(1)}$ is high and $H_e^{(2)} \approx 2$ as shown in Fig. 2.5c-2.5d. Thus, all Elements e which are uniaxially loaded in at least one loadcase will exhibit at least one $H_e^{(m)}$ which is $\gg 2$. It implies that aggregating the individual $H_e^{(m)}$ for an uniaxially loaded element across all loadcases will result into values $\gg 2$.

- Similarly, if an Element e is biaxially loaded and is load bearing in all load cases then $|\sigma_I^{(m)}| \approx |\sigma_{II}^{(m)}|$. In the example problem, Point d_4 is biaxially load-bearing for both loads P_1 and P_2. The $H_e^{(m)}$ values for both loadcases is approximately 2. Another case occurs when Element e is biaxially loaded in certain load cases and not loaded in other cases. Then for load cases in which the Element is biaxially loaded, $|\sigma_I^{(m)}| \approx |\sigma_{II}^{(m)}|$. However, for the case in which it is not loaded, $|\sigma_I^{(m)}| \approx |\sigma_{II}^{(m)}| \approx 0$. Note, for both sets, $H_e^{(m)} \approx 2$ is obtained. Point d_3 is biaxially load-bearing for load P_1 only but not load-bearing for P_2. The values of $H_e^{(m)}$ in both load cases are approximately 2 which can be inferred by Fig. 2.5c–2.5d. Thus, for elements which are biaxially loaded in at least one load case and not load bearing in other cases results with $H_e^{(m)}$ approximately 2 for all load cases. Aggregating $H_e^{(m)}$ over all the loadcases will hence result into a value approximately equal to $2M$.

Motivated by above observations to formulate the intersection indicator for multi load case problems, the biaxiality in the structure is aggregated as follows:

$$H_e = \frac{1}{M}\sum_{m=1}^{M} H_e^{(m)}. \tag{2.16}$$

Through this definition the uniaxially loaded elements in at least one loadcase will exhibit value of $H_e \gg 2$. Moreover, the biaxially loaded elements at least in one loadcase will exhibit value of $H_e \approx 2$. Now, substituting Eq. (2.16) in Eq. (2.13) provides intersection indicator (I_e) for the multi-load case problem. For the example problem, the plot of $1/\log_2(H_e)$ and corresponding intersection indicator is shown in Fig. 2.5g and Fig. 2.5h, respectively. It can be observed in Fig. 2.5g that through aggregation the uniaxially and biaxially loaded elements in the solid are clearly identified. The void regions are considered in artificially biaxial state which are then filtered out through filtered density as shown in corresponding intersection indicator plot Fig. 2.5h. This formulation is also applied to problems with more than 2 load cases to check the scope of the approach. It is observed that through proposed aggregation, intersections can be detected in multi-load case problems with more than two load cases. We note in passing, for $M = 1$, Eq. (2.16) reduces to Eq. (2.12).

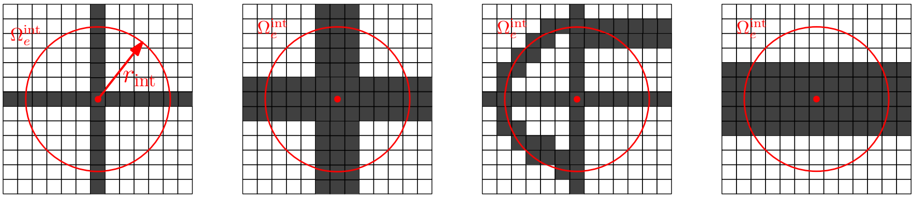

(a) (b) (c) (d)

Figure 2.6: Schematic illustration of various design features such as (a) a slim intersection (b) a bulky intersection (c) a slim intersection with extra material around and (d) a straight member.

2.2.3. INTERSECTION SIZE

As discussed in the Introduction, in certain applications one may require to control the occurrence of intersections depending on their sizes. Consider the two intersections, shown in Fig. 2.6a and Fig. 2.6b. To evaluate the intersection size, assume a circular domain, Ω_e^{int}, centered at Element e (indicated by a red dot in Fig. 2.6). Averaging the filtered densities in this local domain provides information on the size of the intersection at Element e. For a relatively bulky intersection, shown in Fig. 2.6b, the average filtered density is higher than in case of a relatively slim intersection, shown in Fig. 2.6a. However, the intersection shown in Fig. 2.6c, which happens to be an intersection as slim as the intersection depicted in Fig. 2.6a, has a higher average density in the local region Ω_e^{int} compared to that of the intersection shown in Fig. 2.6a. Note that, the farther the material is located from the center of the circular domain at Element e, the lower the probability this material is part of the intersection. To account for this, a weighted averaging scheme is proposed, such that the contribution of the filtered density of a particular element to the local averaged density at a point of interest depends on the distance between the element and the point of interest. The weighted density filter (Bruns and Tortorelli, 2001) is used to calculate the local weighted average of the filtered density($\hat{\tilde{\rho}}_e$):

$$\begin{aligned} \hat{\tilde{\rho}}_e &= \frac{\sum_{i\in\Omega_e^{\text{int}}} w_i(\mathbf{x}_i)\, v_i\, \tilde{\rho}_i}{\sum_{i\in\Omega_e^{\text{int}}} w_i(\mathbf{x}_i)\, v_i}, \\ w_i(\mathbf{x}_i) &= r_{\text{int}} - ||\mathbf{x}_i - \mathbf{x}_e||. \end{aligned} \tag{2.17}$$

Here, r_{int} is the radius of the local circular domain Ω^{int}.

A straight member, as shown in Fig. 2.6d, has values of $\hat{\tilde{\rho}}_e$ equivalent to that of a bulky intersection. To distinguish between a straight member and an intersection, this size measure $\hat{\tilde{\rho}}_e$ must be combined with the Intersection Indicator (I_e).

Inspired by the requirements in the DMD process, we consider the case of allowing bulky intersections, while suppressing slim ones. Thus, to penalize slim intersections, weight factors are calculated as function of intersection size

$$\hat{s}_e = 1 - \hat{\hat{\rho}}_e, \tag{2.18}$$

$$S_e = \hat{s}_e I_e. \tag{2.19}$$

Here, $\hat{s}_e$ is the weight assigned to the intersections at Element e and S_e is the weighted intersection indicator that is higher for slim intersections in a design. These weights are chosen as an example for the DMD application, however, the weights can be chosen in other ways to target different intersection sizes for other applications.

Recall that the minimum member size in TO is set to be $2r_{\text{min}}$ therefore, the minimum intersection size is $2\sqrt{2}r_{\text{min}}$. Thus, to detect the size of an intersection, we require $r_{\text{int}} > \sqrt{2}r_{\text{min}}$. Consequently, intersections larger than the chosen value r_{int} are not detected. To illustrate this with an example, we revisit the cantilever problem shown in Fig. 2.2. The filter given in Eq. (2.17) is applied to the filtered density field shown in Fig. 2.2b for three different β values, where $\beta = r_{int}/r_{min}$, as shown in Fig. 2.7. The chosen values of β are 2, 4 and 6. As observed from Fig. 2.7a–2.7c, increasing the radius increases $\hat{s}_e$ in entire domain, and thus, a greater number of thin intersections are identified below the domain size Ω_e^{int}. This is evident from Fig. 2.7d–2.7f. Note that the weighted averaging in the local domain provides a relative size measure which can distinguish between bulky and slim intersections.

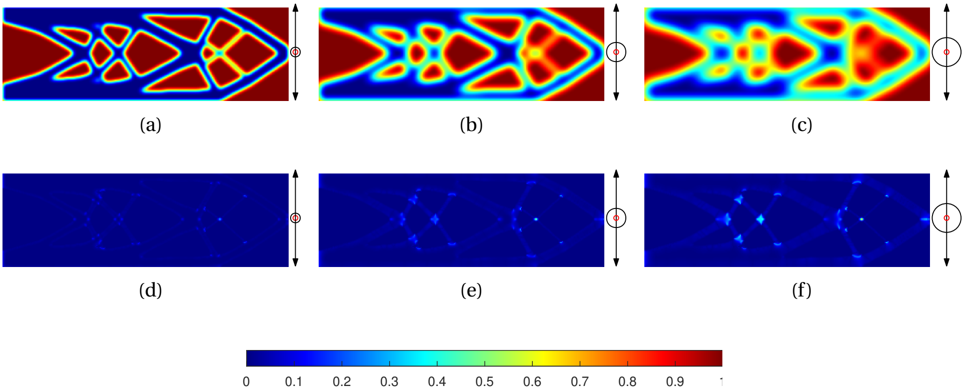
(a) (b) (c)
(d) (e) (f)

Figure 2.7: Load case Cantilever Beam : (a), (b) and (c) show the intersection weight factors, $\hat{s}_e$, for $\beta = r_{int}/r_{min} = 2$, 4 and 6, respectively. (d), (e) and (f) represent the corresponding weighted intersection indicator $S_e = \hat{s}_e I_e$ representing the intersections smaller than the threshold defined by r_{int}. The red and black circles represent the size of the r_{min} and r_{int}, respectively. As radius r_{int} increases more number of intersecting features are identified.

2.3. PROBLEM DESCRIPTION AND THRESHOLD STRESS SELECTION

2.3.1. MULTI-OBJECTIVE FORMULATION : COMPLIANCE AND INTERSECTION OBJECTIVE

So far it has been established that the presence of intersections can be identified and their relative size can be determined. It remains to control the occurence of intersections in TO. The intersection indicator defined in the previous section only gives an indication of intersection presence. It does not provide insight on the actual number of intersections. Moreover, as stated in the Introduction, intersections facilitate load transfer, therefore their presence is paramount for mechanical performance. However, from a manufacturing point of view, such as for DMD, slim intersections are problematic. Therefore, the number of slim intersections should be restricted to improve manufacturability of through DMD. Therefore, there is a trade off between performance and manufacturability. Consequently, for optimization we adopt a multi-objective approach where a total objective function is defined as a combination of compliance of the structure and a function suppressing slim intersections.

Firstly, we define the function that will be minimized to achieve fewer slim intersections for DMD application. The proposed function which is also termed as intersection objective I is defined as:

$$I = \frac{\sum_{\Omega_N} S_e}{\frac{1}{V_0}\sum_{\Omega_N} v_e \tilde{\rho}_e}. \tag{2.20}$$

The numerator of the intersection objective I is the summation of the weighted intersection indicator S_e over the entire domain. Given Eq. (2.18), the contribution from relatively slim intersections will be higher, whereas bulky intersections and straight members will only contribute marginally. Thus, minimizing the numerator will minimize thin intersections and promote bulky intersections or straight members in a design. The denominator of the intersection objective is the design volume normalized by the allowed volume in the design domain V_0. Upon omitting the term, the optimizer removes material from the intersection location and the optimization tends towards a trivial solution of no material. Therefore, the denominator term promotes material in the design domain.

Finally, the standard compliance minimization problem, given in Eq. (2.1)–(2.6) is extended to a multi-objective problem as described below:

$$\min_{\rho} \quad O = \frac{1}{\mu}\left(\theta \frac{c}{c^*} + (1-\theta)\frac{I}{I^*}\right). \tag{2.21}$$

$$\text{s.t.} \quad \mathbf{Ku} = \mathbf{f}. \tag{2.22}$$

$$g = \frac{\sum_{\Omega_N} v_e \tilde{\rho}_e}{V_0} - 1 \leq 0. \tag{2.23}$$

$$0 \leq \rho_e \leq 1, \quad \forall e \in \Omega_N. \tag{2.24}$$

In Eq. (2.21), O is the total objective function, θ is the weight assigned to the compliance objective, consequently, $(1-\theta)$ is the weight assigned to the intersection objective. The parameter θ is a tuning parameter which can be reduced to emphasis on manufacturability of the design through DMD. Both the objectives are normalized by their respective values of the compliance (c^*) and intersection (I^*) calculated for the design obtained by the standard compliance minimization problem. Superscripts $(*)$ are used to indicate values that are calculated on the converged standard compliance minimization design. The constant factor μ is introduced to scale the value of the objective such that it ranges between 1 and 100 for the stability of the MMA optimizer, see Svanberg, 1987. The sensitivity analysis of the objective and constraint functions are determined using the adjoint method and detailed in A.1.

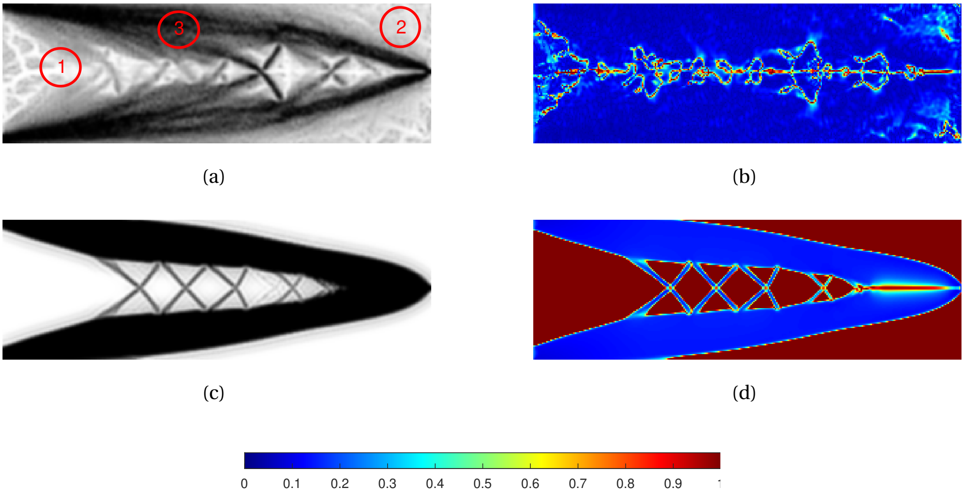

(a) (b)

(c) (d)

Figure 2.8: Effect of threshold stress levels on intersection minimization results for Problem 1: (a) Design at 100^{th} iteration for $\sigma_0 = 0$ MPa. (b) is the corresponding multi-axiality criterion $1/\log_2(H_e)$. (c) and (d) Design and corresponding multi-axiality criteria at 100^{th} iteration step for $\sigma_0 = 10$ MPa. The threshold stress is selected from the reference compliance minimization design shown in Fig. **??**. For the reference case, the average and maximum value of both $|\sigma_I|$ and $|\sigma_{II}|$ in the domain are 25 MPa and 618 MPa. The threhold stress, $\sigma_0 = 10$ MPa, is below the average stress value in the reference case.

2.3.2. EFFECT OF THRESHOLD STRESS LEVELS ON INTERSECTION MINIMIZATION AND SELECTION STRATEGY

As mentioned in Section 2.2.2, the effect of the chosen threshold stress during optimization is crucial. To demonstrate its effect, initially the threshold stress is assumed to be zero $(\sigma_0 = 0)$. The multi-objective formulation is applied to Problem 1 with $\theta = 0.2$, i.e, the contribution of intersection objective I is dominant. The pure compliance minimization design previously shown in Fig. 2.2b is chosen as the reference case for the calculation of c^* and I^*. The value of $\beta = 6$ is chosen because it targets every intersection in a compliance minimization design, shown in Fig. 2.7f. The results obtained after 100 iterations are presented in Fig. 2.8. In the design shown in Fig. 2.8a, it can be observed gray regions are present at locations which experience low stress levels, such as Region 1 and 2 (indicated by red circles) and an arch shaped design feature is observed with high material density in Region 3. The corresponding objective values are $c/c^* = 2.01$, $I/I^* = 0.44$ and $O/O^* = 0.75$, see Eq. (2.21). It shows that the intersection objective and total objective have reduced, as desired. However, the obtained result does not represent a desired, manufacturable geometry. The features formed in the low stresses regions demonstrate that the effect of reducing the local multi-axial stress state dominates removal of local densities in these regions, as shown in Fig. 2.8b, leading to the depicted undesired result. In order to facilitate only removal of local densities from low stresses regions, the effect of reducing local multi-axial stress state should be nullified.

To avoid generation of the design features in regions where the stress is negligible during optimization, the threshold stress, mentioned in Section 2.2.2, is introduced. The stress response from the pure compliance minimization reference design is used to aid in the selecting the threshold stress level. Recalling that for the compliance minimization design in Fig. 2.2b average and maximum value of both $|\sigma_I|$ and $|\sigma_{II}|$ in the domain are 25 MPa and 618 MPa, respectively. Also, it is shown previously that for σ_0 = 10 MPa, which is below the average stress value, does not affect the intersection indicator of the converged compliance design (see Fig. 2.4d and Fig. 2.4e). Therefore, for the intersection minimization problem, σ_0 = 10 MPa is selected because in the reference compliance minimization case, the stresses in the solid region are significantly above 10 MPa. The result of intersection minimization after 100 optimization iterations considering σ_0 = 10 MPa is shown in Fig. 2.8c. The design does not contain gray design features in the lowly stressed region, as they are artificially considered in the biaxial stress state which can be observed in Fig. 2.8d. Since, there is no possibility to reduce the local multi-axial stress state in the low stressed region, the intersection objective is reduced by removing the local densities in these regions, which promotes convergence to a manufacturable designs. The corresponding objective values are $c/c^* = 1.34$, $I/I^* = 0.35$ and $O/O^* = 0.55$.

It remains to determine the value of the threshold stress for general cases. The key aspect is that low-stressed regions should be discouraged to affect the detection of stress multi-axiality. Since the intersection minimization problem is solved simultaneously with the compliance minimization problem, the stress levels found in the solid regions of the compliance minimization design are considered as representative. Therefore, the threshold stress value should be selected such that it is smaller than the stress levels present in the solid regions of the compliance minimization design. Now, the stress levels in the solid regions are either dictated by σ_I, σ_{II} or both. Thus, the measure of stress levels should be combination of the individual principal stress components. This motivates the selection of Von Mises stresses as a measure of stress levels in solid regions and the threshold stress should be smaller than the Von Mises stress field in the solid regions of compliance minimization design.

The compliance minimization design consists of void (white) and material (black) regions separated by interface (gray) regions. The stress levels experienced by interface (gray) regions fall between those in void and material regions. In this paper, the following procedure is adopted to select the threshold stresses for single and multi loadcase problems:

1. Apply the load and boundary conditions to the converged design obtained from the standard compliance minimization problem and determine the principal stresses at each element in the domain using Eq. (2.8) and Eq. (2.9).
2. Calculate the Von Mises stress ($\sigma_{(\mathrm{vm})}$) at each element in the domain using $\sqrt{\sigma_I^2 - \sigma_I \sigma_{II} + \sigma_{II}^2}$.
3. To identify the Von Mises stress in the gray regions, stresses which corresponds to filtered design variables $0.1 < \tilde{\rho}_e < 0.5$ are selected. Due to SIMP penalization, the stress levels corresponding to the value of $\tilde{\rho}_e = 0.1$ and $\tilde{\rho}_e = 0.5$ will be in the order of 0.1% and 12.5% compared to the stress levels in the solid region ($\tilde{\rho}_e = 1$), respectively. Therefore, the stress levels in the selected range will be significantly lower than the stresses in the solid region.
4. To select the threshold stresses as low as possible, sort the Von Mises stresses of the selected filtered density range in ascending order. Pick the stress value found at an index closest to 90% of the length of the array. The 90% value is selected as threshold so that most of the lowly stressed regions in a design are artificially considered in biaxial stress state.

The proposed algorithm used to systematically select threshold stresses presented a good performance distinguishing between the lowly and significantly stressed regions during optimization for all problems discussed in this paper. Nevertheless, note that the proposed algorithm is only one option and choosing the best algorithm is beyond the scope of this work.

2.4. RESULTS

In this section, results obtained by applying the proposed multi-objective formulation on various single and multi load problems are presented. The design domains and boundary conditions of the 5 considered test problems are given in Fig. 2.9. Each problem is labeled with a problem number for reference. All the design domains have equal dimensions. Recall that the default optimization settings are given in Table 2.1. Optimization results of all the problems and effect of different parameters on the designs are shown in Section 2.4.1. An overall discussion is given in Section 2.4.2.

2.4.1. DESIGNS

EFFECT OF θ

The designs obtained for all of the test problems defined in Fig. 2.9 are shown in Fig. 2.10. Results obtained for $\beta = 6$ are shown. Here, r_{int} is chosen to be sufficiently large to target every intersection in the respective compliance minimization design, further effects of r_{int} on the design are discussed in Section 2.4.1. Converged designs obtained for different values of θ and their corresponding intersection and compliance objective values are shown in Fig. 2.10. Designs for $\theta = 1.0$ correspond to standard compliance minimization, the reference design for each of the problems. It is evident from the designs that, as

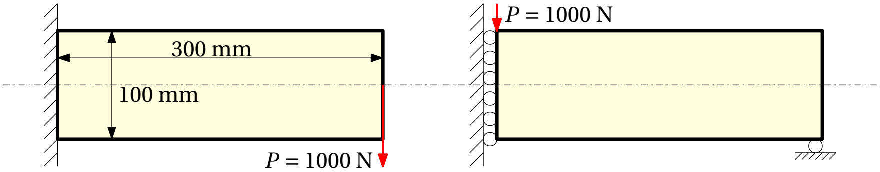

(a) Problem 1 (b) Problem 2

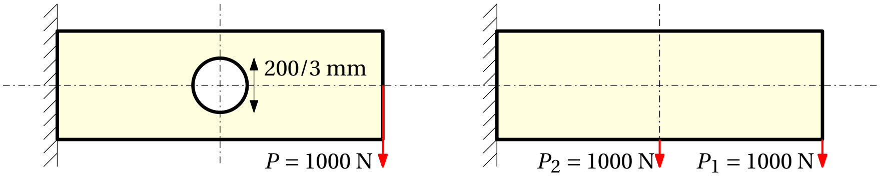

(c) Problem 3 (d) Problem 4

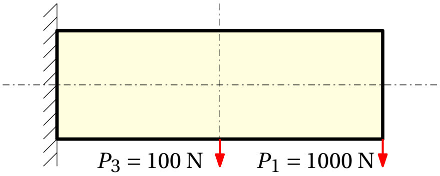

(e) Problem 5

Figure 2.9: Test problems: (a) Cantilever beam; (b) MBB Beam; (c) Cantilever beam with a hole; (d) Multi load case beam problem with equal loads (e) Multi load case beam problem with different loading. The dimensions of the design domain of all the test problems are 300 mm × 100 mm.

the weight on the intersection objective increases, the number of intersections reduces in the design. Consistently the compliance objective is increasing while the intersection objective is decreasing. In all the problems, it is observed that the minimization of intersections comes at the cost of inferior stiffness performance.

EFFECT OF r_{MIN} AND r_{INT}

Recall that the proposed method utilizes two local circular domains, determined by the radii, r_{min} and r_{int}, that are anticipated to affect the optimized design. Increasing r_{min} leads to an increase in the minimum member size and, thus, leading to fewer intersections. In order to isolate the effect of r_{int}, r_{min} is kept constant and r_{int} is varied. In Fig. 2.11, designs for Problem 1 are illustrated for three selected values of $\beta = r_{\text{int}}/r_{\text{min}}$ equal to 2 ,4 and 6, while keeping $r_{\text{min}} = 2.5$ mm and $\theta = 0.6$. The values of compliance and intersection objective given in Fig. 2.11 are normalized by the reference design shown in Fig. 2.2b. For all the designs, the intersections are clearly identified by the intersection indicator as shown in the corresponding plot of I_e, see Fig. 2.11.

During optimization, if an intersection size reaches the size of the local domain with radius r_{int}, then the contribution of that intersection to the intersection objective will be negligible and therefore, the intersection will not be reduced. This effect is clearly visible in the design for $\beta = 2$, as shown in Fig. 2.11. The weights $\hat{s}_e$, which is inversely proportional to intersection size (see Eq. (2.18)), corresponding to each intersection are close to 0. It suggests that the intersection size is equivalent to the local domain with

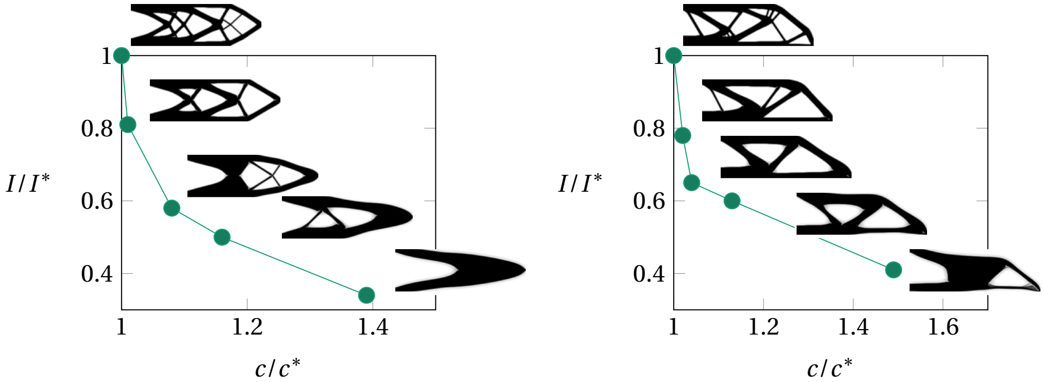

(a) Problem 1

(b) Problem 2

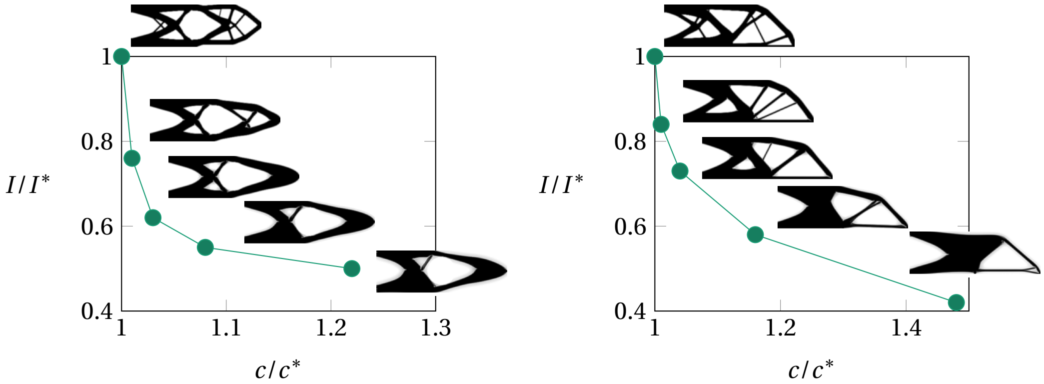

(c) Problem 3

(d) Problem 4

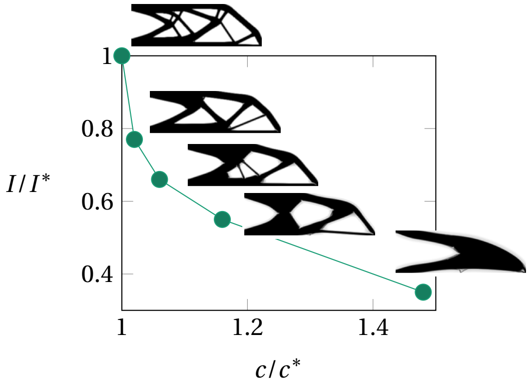

(e) Problem 5

Figure 2.10: Designs obtained after applying compliance and intersection minimization for considered problems. Arrows indicate designs for the corresponding data point. The parameter θ associated to a design is given below the design. In all the test problems, as the weight on the intersection objective increases slim intersections are reduced and bulky intersections are preferred, consequently, geometrical complexity is reduced.

radius r_{int}. Also the contribution of the intersections in the intersection objective is close to 0 as evident from the S_e plots.

As r_{int} increases, bulkier intersections are preferred which can be seen in the design for $\beta = 4$, see Fig. 2.11. The weight $\hat{s}_e$ corresponding to the bulky intersection is close to 0 as can be seen in the $\hat{s}_e$ plots. Furthermore, the contribution from bulky intersections to the intersection objective is also close to 0 as shown in the S_e plots.

Further increasing r_{int}, i.e. for $\beta = 6$, relatively thicker intersections are observed than for $\beta = 2$. However, a slim intersection is also observed which is not removed during optimization. Plot of weight $\hat{s}_e$ shows that the bulky intersection has relatively lower value of $\hat{s}_e$ than the slim intersection. The contribution from slim intersection to the intersection objective is also higher as shown in S_e plot. It means that the slim intersections are detected, however, it is not removed during optimization. This happens because, firstly, the slim intersections are minimized which does not mean that slim intersections can not exist in a design. Secondly, using $\theta = 0.6$ means that the compliance objective function has a greater influence, therefore, the slim feature is not removed completely.

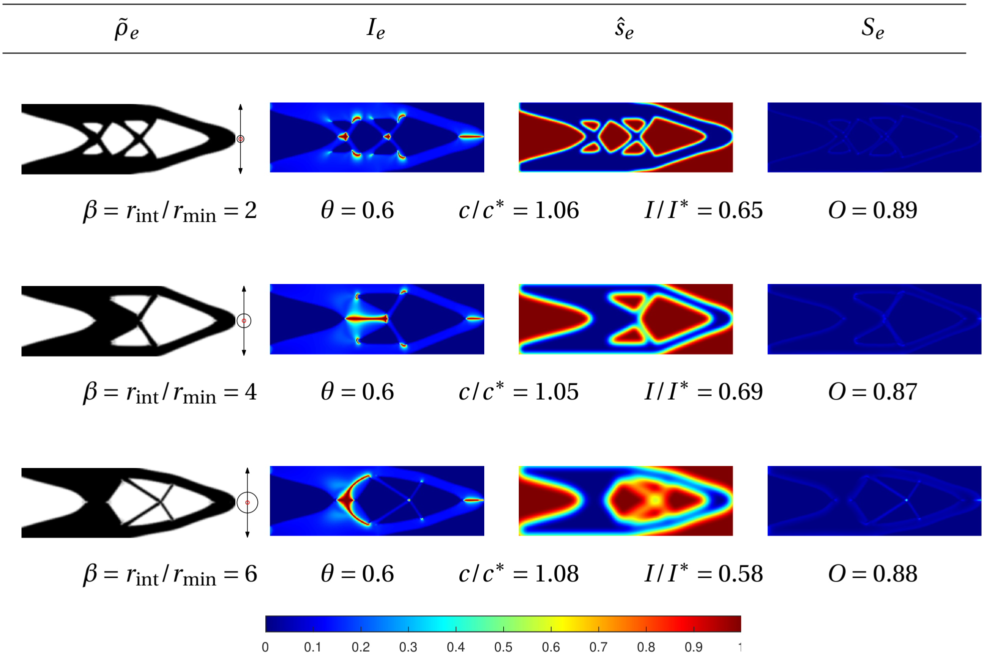

Figure 2.11: Effect of r_{int} on Problem 1 : Cantilever Beam. The red and black circles indicate the size of the local circular domain with radius r_{min} and r_{int}, respectively. As the radius r_{int} increases the size of the intersections promoted in the design domain increases. Therefore, the size of the intersections also increases in the converged designs with increase of r_{int}.

2.4.2. Discussions on Results

The results show that by minimizing the slim intersections, the topology of the compliance minimization design has been simplified. Moreover, calculation of the intersection indicator is computationally efficient because at every iteration step displacement information is available, and calculation of stresses based on this requires only element level linear operations (see Eq. (2.8)). However, for minimizing the intersection objective an additional set of adjoint equations has to be solved which increases its computational cost. For the multi-load case problem, the number of adjoint equations scales with the number of load cases in a single problem because stress fields from different load cases are aggregated together. The convergence behavior of normalized compliance and intersection objective with respect to iteration step of Problem 1 with $\beta = 6$ are shown in Fig. 2.12 and Fig. 2.13, respectively. The convergence plots show smooth convergence. However, the number of iterations required was quite high compared to standard compliance minimization problem. This is due to the fact that the sensitivity of the compliance minimization problem is always negative with respect to every design variable, but for the intersection objective it is not the case, thus the convergence gets slower compared to compliance minimization.

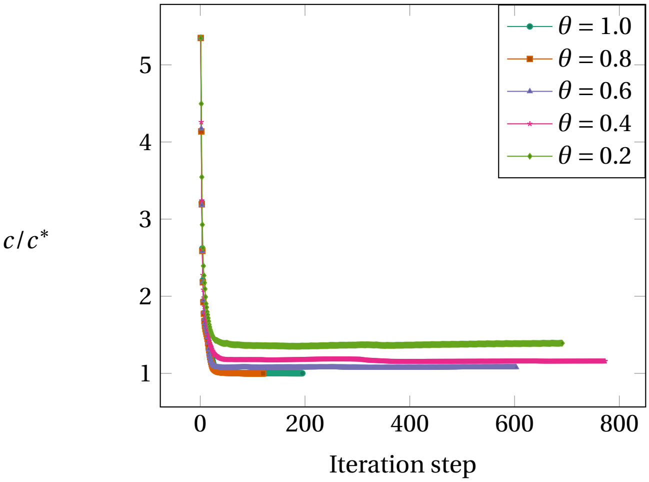

Figure 2.12: Convergence of compliance objective of cantilever beam (Problem 1)

2.5. Extension to 3D Problems

For 3D problems, again there are two aspects to be considered, identification and control of 3D intersections. In contrast to the 2D problems, it was observed, by examining 3D TO results, one may identify following types of intersections:

- Straight beams intersecting with each other.
- Straight beams intersecting with a plate type structure.
- Two or more plate like structures intersecting with each other.

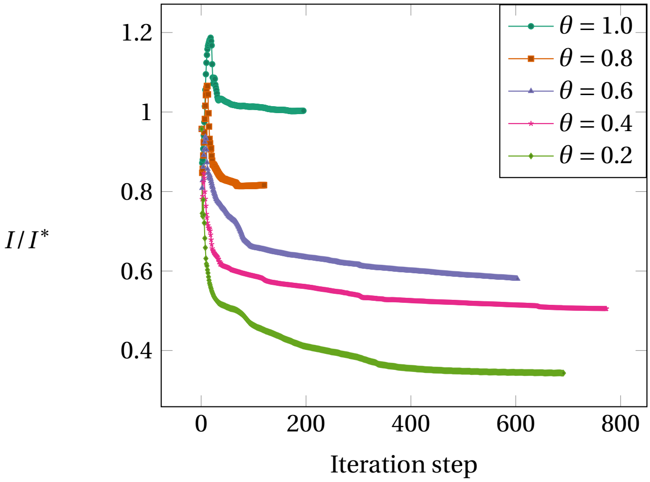

Figure 2.13: Convergence of intersection objective of cantilever beam (Problem 1)

To identify above mentioned 3D intersections certain ‘signatures’ in terms of principal stress ratios have been recognized. However, defining an indicator, similar to the 2D case, to reliably identify these features proves more challenging due to the larger variety of intersection types. Further investigation is needed to develop an intersection indicator for 3D problems.

Moreover, controlling 3D intersections to generate designs for certain manufacturing process such as DMD have two important aspects. Firstly, 3D intersections need not be problematic for the DMD process because mostly the production happens in a layer-by-layer manner. Thus, it is possible that within the deposition layer intersections are not encountered and the part could be produced easily. A rather challenging problem left for future research is to identify the intersections within the deposition layers and then minimize them for DMD related applications. This could be achieved by projecting the stress components to the plane of deposition. Secondly, for DMD processes, designs with high geometric complexity could also pose a problem during manufacturing. Hence, once a reliable 3D intersection indicator is developed, then, based on their relative size, intersections can be controlled to achieve minimal geometric complexity, similar to the 2D case.

2.6. CONCLUSIONS

In this study a novel approach to reduce geometric complexity of designs in 2D compliance minimization topology optimization is presented. The reduction in the geometric complexity is attained through identifying and controlling intersections by means of the local stress state for single and multi load case problems. The reduction of geometric complexity of a design improves manufacturability through both conventional as well as additive manufacturing processes, such as DMD.

The proposed Intersection Indicator is a function of the ratio of local principal stresses.

Therefore, the design sensitivities of the indicator can be easily evaluated by solving a set of adjoint equations per loadcase. This renders the indicator suitable for gradient-based optimization. To prevent convergence problems due to spurious stress ratios in low-stressed regions, a threshold stress is introduced as well as a procedure to select an appropriate value. To control intersections, a multi-objective formulation is proposed comprising of a compliance and intersection objective. A provision to emphasize intersections according to their size has also been presented, and demonstrated in the context of the DMD process, where slim intersections are to be avoided. Controlled by the relative weight of the intersection objective, different levels of design simplification are achieved, both for single as well as multi-load problems. As expected, increasing restrictions on design complexity leads to increased compliance.

Smooth convergence is observed without a continuation scheme. However, the number of iterations required for convergence increases when the relative weight of the intersection objective increases. Implementing the proposed formulation in an existing topology optimization framework, such as the 88-line MATLAB TO code presented by Andreassen et al., 2011, is straightforward. It involves calculation of principal stresses, threshold stresses and sensitivities of intersection objective.

Although the proposed approach proved effective in various test problems, it has limitations. First, it does not provide control on the exact number of intersections. Second, the stress-based indicator relies on characteristics of optimal designs obtained in compliance minimization. Its extension to other problems such as compliant mechanism or thermal optimization will require developing a relation between geometrical aspects of intersections and the 'physics' observed at intersections. Currently, the presented intersection indicator is therefore restricted to 2D compliance minimization problems. Extension to a 3D setting is a topic for future work, where stress-based recognition of the variety of intersection types that can occur in 3D is the main challenge.

BIBLIOGRAPHY

Ambrozkiewicz, O., & Kriegesmann, B. (2018). Adaptive strategies for fail-safe topology optimization. *International Conference on Engineering Optimization*, 200–211.

Amir, O., Stolpe, M., & Sigmund, O. (2010). Efficient use of iterative solvers in nested topology optimization. *Structural and Multidisciplinary Optimization*, *42*(1), 55–72.

Andreassen, E., Clausen, A., Schevenels, M., Lazarov, B. S., & Sigmund, O. (2011). Efficient topology optimization in matlab using 88 lines of code. *Structural and Multidisciplinary Optimization*, *43*(1), 1–16.

Bendsøe, M. P. (1989). Optimal shape design as a material distribution problem. *Structural optimization*, *1*(4), 193–202.

Bendsoe, M. P., & Sigmund, O. (2013). *Topology optimization: Theory, methods, and applications*. Springer Science & Business Media.

Bendsøe, M., & Haber, R. (1993). The michell layout problem as a low volume fraction limit of the perforated plate topology optimization problem: An asymptotic study. *Structural optimization*, *6*(4), 263–267.

Bourdin, B. (2001). Filters in topology optimization. *International journal for numerical methods in engineering*, *50*(9), 2143–2158.

Bruggi, M. (2008). On an alternative approach to stress constraints relaxation in topology optimization. *Structural and multidisciplinary optimization*, *36*(2), 125–141.

Bruns, T. E., & Tortorelli, D. A. (2001). Topology optimization of non-linear elastic structures and compliant mechanisms. *Computer methods in applied mechanics and engineering*, *190*(26-27), 3443–3459.

Chen, Z., Gandhi, U., Lee, J., & Wagoner, R. (2016). Variation and consistency of young's modulus in steel. *Journal of Materials Processing Technology*, *227*, 227–243.

Clausmeyer, H., Kussmaul, K., & Roos, E. (1991). Influence of Stress State on the Failure Behavior of Cracked Components Made of Steel. *Applied Mechanics Reviews*, *44*(2), 77–92.

Duysinx, P., & Bendsøe, M. P. (1998). Topology optimization of continuum structures with local stress constraints. *International journal for numerical methods in engineering*, *43*(8), 1453–1478.

Gamache, J.-F., Vadean, A., Noirot-Nérin, É., Beaini, D., & Achiche, S. (2018). Image-based truss recognition for density-based topology optimization approach. *Structural and Multidisciplinary Optimization*, *58*(6), 2697–2709.

Gaynor, A. T., & Guest, J. K. (2016). Topology optimization considering overhang constraints: Eliminating sacrificial support material in additive manufacturing through design. *Structural and Multidisciplinary Optimization*, *54*(5), 1157–1172.

Guest, J. K., Prévost, J. H., & Belytschko, T. (2004). Achieving minimum length scale in topology optimization using nodal design variables and projection functions. *International journal for numerical methods in engineering*, *61*(2), 238–254.

Kirsch, U. (1990). On singular topologies in optimum structural design. *Structural optimization*, *2*(3), 133–142.

Langelaar, M. (2016). Topology optimization of 3D self-supporting structures for additive manufacturing. *Additive Manufacturing, 12*, 60–70.

Langelaar, M. (2019). Topology optimization for multi-axis machining. *Computer Methods in Applied Mechanics and Engineering, 351*, 226–252.

Lazarov, B. S., Wang, F., & Sigmund, O. (2016). Length scale and manufacturability in density-based topology optimization. *Archive of Applied Mechanics*, *86*(1-2), 189–218.

Lockett, H., Ding, J., Williams, S., & Martina, F. (2017). Design for wire+ arc additive manufacture: Design rules and build orientation selection. *Journal of Engineering Design*, *28*(7-9), 568–598.

Megson, T. H. G. (2019). *Structural and stress analysis*. Butterworth-Heinemann.

Mehnen, J., Ding, J., Lockett, H., & Kazanas, P. (2014). Design study for wire and arc additive manufacture. *International Journal of Product Development 20*, *19*(1-3), 2–20.

Sigmund, O. (2009). Manufacturing tolerant topology optimization. *Acta Mechanica Sinica*, *25*(2), 227–239.

Svanberg, K. (1987). The method of moving asymptotes—a new method for structural optimization. *International journal for numerical methods in engineering, 24*(2), 359–373.

Van de Ven, E., Maas, R., Ayas, C., Langelaar, M., & van Keulen, F. (2020). Overhang control based on front propagation in 3D topology optimization for additive manufacturing. *Computer Methods in Applied Mechanics and Engineering, 369*, 113169.

Wein, F., Dunning, P. D., & Norato, J. A. (2020). A review on feature-mapping methods for structural optimization. *Structural and multidisciplinary optimization*, *62*(4), 1597–1638.

Xia, Q., & Shi, T. (2015). Constraints of distance from boundary to skeleton: For the control of length scale in level set based structural topology optimization. *Computer Methods in Applied Mechanics and Engineering, 295*, 525–542.

Xia, Q., Shi, T., Wang, M. Y., & Liu, S. (2010). A level set based method for the optimization of cast part. *Structural and Multidisciplinary Optimization, 41*(5), 735–747.

Zhang, W., Li, D., Zhang, J., & Guo, X. (2016). Minimum length scale control in structural topology optimization based on the moving morphable components (mmc) approach. *Computer Methods in Applied Mechanics and Engineering, 311*, 327–355.

Zhang, W., Liu, Y., Wei, P., Zhu, Y., & Guo, X. (2017). Explicit control of structural complexity in topology optimization. *Computer Methods in Applied Mechanics and Engineering, 324*, 149–169.

Zhang, W., Zhong, W., & Guo, X. (2014). An explicit length scale control approach in simp-based topology optimization. *Computer Methods in Applied Mechanics and Engineering, 282*, 71–86.

Zhang, W., Zhou, J., Zhu, Y., & Guo, X. (2017). Structural complexity control in topology optimization via moving morphable component (mmc) approach. *Structural and Multidisciplinary Optimization*, *56*(3), 535–552.

Zhou, L., & Zhang, W. (2019). Topology optimization method with elimination of enclosed voids. *Structural and Multidisciplinary Optimization*, *60*(1), 117–136.

Zhou, M., Lazarov, B. S., Wang, F., & Sigmund, O. (2015). Minimum length scale in topology optimization by geometric constraints. *Computer Methods in Applied Mechanics and Engineering*, *293*, 266–282.

3

CASE STUDY: WAAM RUDDER

3.1. INTRODUCTION

In this chapter, a ship rudder case study is presented to showcase the potential application of the developed TO methods and the WAAM process in the industry. A ship rudder is a part of a ship for steering that is subjected to hydrodynamic pressures during operation. When the rudder is steered a pressure difference due to the unbalanced hydrodynamic pressure load generates thrust to steer the ship.

The ship rudder discussed in this chapter is originally designed by Damen as shown in Fig. 3.1. The rudder has a skin with a particular thickness that envelops several plates positioned approximately equidistant from each other. The plates are shaped as aerofoils according to the cross-section of the skin. A shaft runs through the plates that connect the rudder and the ship. The cross-section of the rudder is tapered along the shaft.

The weight of this type of ship rudder is generally a few hundred kilograms. Reducing the weight of the rudder will improve the fuel efficiency. It would also require less material processing during the manufacturing of the ship rudder. Moreover, the original rudder design requires a series of joining operations between plates, shaft, and skin. These joining operations are costly and will be completely eliminated if the rudder is manufactured in an automated manner by WAAM.

TO is used to reduce the weight of the ship rudder while maintaining the equivalent mechanical performance as the original design TO is used. Here the outer hydrodynamic surface is kept fixed, and TO is applied to redesign the interior. The redesigning of the ship rudder is considering multiple hydrodynamic loading scenarios. Certain design and manufacturing requirements are enforced during the TO process so that the rudder can be easily manufactured through WAAM. Moreover, a few conditions are also posed by Damen so that the design is compatible with its standards. The design and manufacturing requirements are fulfilled by applying an extension of the novel concepts discussed in the previous chapter and existing formulations in TO. The requirements and TO formulations used are given in Section 3.2. The optimized design obtained by TO considering the manufacturing and design requirements is presented in Section 3.3. Finally, the conclusions based on this particular case study are outlined in Section 3.4.

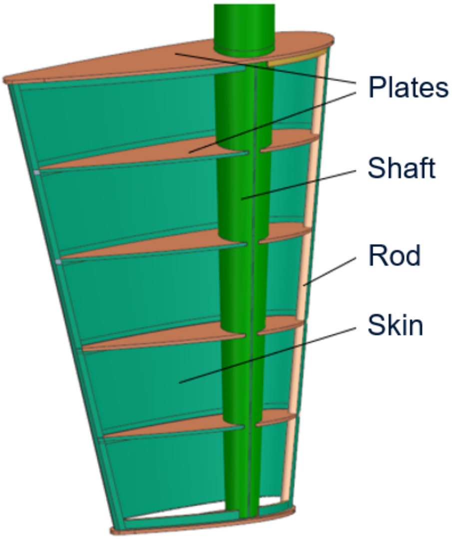

Figure 3.1: The original ship rudder designed by Damen Holding B.V.

3.2. DESIGN AND MANUFACTURING REQUIREMENTS

To redesign the ship rudder, a 3D TO code written in MATLAB is used as a basis (Liu and Tovar, 2014). One of the main challenges in redesigning the rudder is performing TO on the actual size of the rudder, which is in the order of meters while maintaining sufficient resolutions. The bounding box of the actual rudder, shown in Fig. 3.2 is discretized with a structured mesh comprising 3D eight-node hexahedron elements. The length of the edges of the 3D elements is 10 mm. Furthermore, this case study was executed under a tight time constraint. For this reason, simplifications and practical approximations were applied in geometry and load representation. This is justified by the fact that the TO result was intended as a starting point for further design iterations, as discussed in the next section. The design and manufacturing requirements to redesign the rudder posed by Damen and the methods applied to fulfill these approaches are listed as follows:

1. *The aerofoil shape of the skin remains the same*: To maintain the same aerofoil profile of the skin, the CAD geometry of the skin from the original design is used to identify whether an element is inside the skin, using the ray intersection method (Adam, 2023). The elements inside the enclosed volume of the skin, comprise the design domain to be optimized. The interface of the inside and outside elements follows the shape of the aerofoil which is the design requirement.

2. *The thickness of the skin can be reduced*: In order to model the thickness of the skin, the elements which are inside the skin and share nodes with the elements outside the skin are extracted. These elements are chosen to be the non-design domain and represent the skin of the ship rudder. The TO density-based design variable is fixed to 1 for these elements. The skin thickness of the original design

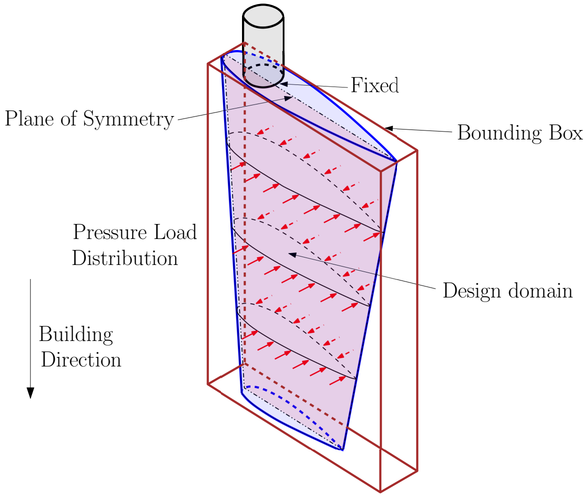

Figure 3.2: Schematic of Ship Rudder Optimization Problem: The bounding box encompassing the rudder is represented by the brown region. The volume enclosed by the skin indicated by the blue region is the design domain. The domain is fixed completely where it connects with the shaft. The symmetry of the design is imposed with respect to the indicated plane of symmetry. The red arrow indicates the pressure load distribution along the skin.

is equal to 10 mm, which is equivalent to the element size. To model the reduction in the thickness of the rudder skin, the stiffness matrix corresponding to the finite elements associated with the rudder skin is scaled. This coarse approximation was chosen as the time for implementation of an actual shell geometry was not available for this case study, and using smaller elements would result in excessive computation time. However, more accurate modeling of the rudder strength and stiffness is required after the TO phase because of this approximation.

3. *Multiple hydrodynamic pressure loads*: The ship rudder is subjected to hydrodynamic pressure during operation. The pressure distribution over the outer skin of the rudder depends on many variables such as the angle at which the rudder is oriented, the velocity of the ship, and the physical properties of the fluid. Three critical orientations were identified by Damen and the pressure distribution at these orientations was evaluated at a particular Reynolds number. The pressure distribution for a particular orientation is evaluated numerically through Computational Fluid Dynamics (CFD) analysis at multiple 2D cross-sections of the skin as schematically shown in Fig. 3.2. The pressure distribution data is then used to estimate the pressure load for the optimization model. The pressure distribution is interpolated spatially at the centroid of the 3D finite elements which represent the skin of the rudder. To evaluate the pressure load from the pressure distribution, the corresponding surface normal vectors and area at which the pressure is applied, are evaluated at the centroid of the 3D finite elements representing the rudder

skin. The normal vectors are evaluated from the CAD file of the rudder and then spatially interpolated at the centroid of the 3D finite elements. The area at which the pressure is applied is the area inscribed by the plane in the 3D finite element that is perpendicular to the interpolated normal vector. After the calculations of the corresponding normals and area of the inscribed plane, the load direction and magnitude are calculated at the centroid of the 3D finite elements. The load at the centroid is then equally distributed at the nodes of each 3D finite element and then assembled into a load array.

4. *Symmetry*: Symmetry of the internal design with respect to the plane which passes through the chord line of each plate in the original design as shown in Fig. 3.2. Symmetry is imposed since the rudder must operate similarly in both directions. Moreover, symmetry is helpful to ensure symmetrical deposition paths and reduce distortion after the WAAM of the rudder. To ensure the symmetry of the design along the plane of symmetry the finite elements which are symmetric to each other are identified. A symmetry filter is applied to these elements by calculating the average of the density variable associated with the pair of symmetric finite elements and then assigning the average value to each symmetric element. Note that the pressure loads on the rudder are not symmetric, therefore full model was considered during optimization.

5. *Minimum feature size*: For the WAAM process, a minimum feature size is required as discussed in the introduction. The density filter (Bruns and Tortorelli, 2001) ensures the minimum feature size in the rudder design. Each finite element is assigned a weighted average of the density variable around the finite element. The number of finite elements used for averaging depends on the size of the filter. In this study, the filter size is 1.5 times the size of the 3D finite element.

6. *Reducing Geometrical Complexity*: A design requirement for the ship rudder is to have no enclosed holes. With no enclosed holes the geometrical complexity of the design will reduce. This requirement is essential as the rudder will be subjected to a pressure test in which the rudder is filled with fluid. The reduction in the geometrical complexity of a design is also suitable for WAAM. For instance, during layer-by-layer WAAM along the deposition direction indicated in Fig. 3.2, with a reduction in the enclosed volume the number of thin intersections encountered in the layers will reduce.

   Recall that in the previous chapter, the intersections, which exhibit a multi-axial stress state, are identified and controlled based on their sizes. It has been demonstrated that features showing a multi-axial stress state can be controlled such that the geometrical complexity of the design can be reduced. The same concept is extended here to 3D to eliminate enclosed holes in a ship rudder. The reduced geometrical complexity means that the number of enclosed voids is likely reduced in a design, although the constraint does not directly control this aspect.

   To identify the multi-axial stress state in 3D, the following indicator is used:

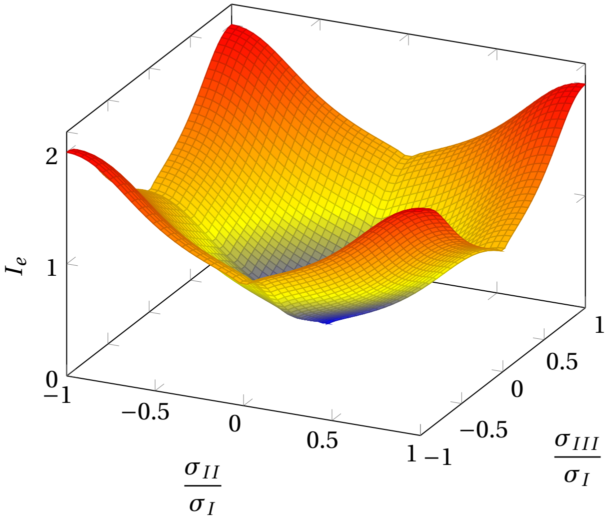

Figure 3.3: Response of 3D intersection indicator (I_e) at various stress states. Here, $|\sigma_I| \geq |\sigma_{II}|$ and $|\sigma_I| \geq |\sigma_{III}|$.

$$H_e^{(12)} = \frac{\sigma_I^2 + \sigma_0^2}{\sigma_{II}^2 + \sigma_0^2} + \frac{\sigma_{II}^2 + \sigma_0^2}{\sigma_I^2 + \sigma_0^2} \tag{3.1}$$

$$H_e^{(13)} = \frac{\sigma_I^2 + \sigma_0^2}{\sigma_{III}^2 + \sigma_0^2} + \frac{\sigma_{III}^2 + \sigma_0^2}{\sigma_I^2 + \sigma_0^2} \tag{3.2}$$

$$I_e = \tilde{\rho}_e^p \left[\frac{1}{\log_2 (H_e^{(12)})} + \frac{1}{\log_2 (H_e^{(13)})} \right]. \tag{3.3}$$

Here, σ_I, σ_{II}, and σ_{III} are the principal stresses. σ_0 is the threshold stress. $H_e^{(12)}$ and $H_e^{(13)}$ are the multi-axiality criteria and I_e is the 3D intersection indicator. The filtered density variable is represented by $\tilde{\rho}_e$. All notations are adopted from the previous chapter. As discussed in the previous chapter, the stress-based formulation enables to calculate the design sensitivities of the intersection indicator for gradient-based optimization. The response of the 3D intersection indicator at all possible stress states is shown in Fig. 3.3. Note that $|\sigma_I| \geq |\sigma_{II}|$ and $|\sigma_I| \geq |\sigma_{III}|$. For single, biaxial, and triaxial stress states the indicator is approximately 0, 1, and 2, respectively. The size of the intersection is evaluated by the material density around the intersection. A spherical domain was used to calculate the intersection size contrary to a circular domain in the 2D case. The thin intersections are penalized during optimization to reduce the geometrical complexity. Note that the intersections encountered in the layers are not explicitly targeted through this formulation.

3.3. SHIP RUDDER OPTIMIZATION

Considering all the design and manufacturing considerations mentioned in the previous section following multi-objective optimization problem similar to the one mentioned in the previous chapter is solved:

$$\min_{\rho} \quad O = \theta c + (1-\theta) I. \tag{3.4}$$

$$\text{s.t.} \quad \mathbf{Ku} = \mathbf{f}. \tag{3.5}$$

$$g = \frac{\sum_{\Omega_N} v_e \tilde{\rho}_e}{V_0} - 1 \leq 0. \tag{3.6}$$

$$0 \leq \rho_e \leq 1, \quad \forall e \in \Omega_N. \tag{3.7}$$

Here, c and I are the normalized compliance and intersection objectives, respectively. The parameter θ determines the contributions from compliance and intersection objectives to the actual objective O. Eq. (3.5) and Eq. (3.6) are the state equation and volume constraint, respectively. The optimization problem was solved on the ship rudder problem shown in Fig. 3.2. The optimized designs obtained from the multi-objective optimization are shown in Fig. 3.4. The only compliance-minimized design with $\theta = 1$ shown in Fig. 3.4a has an enclosed void region. However, the enclosed void space is eliminated when considering the intersection objective with $\theta = 0.5$ as shown in Fig. 3.4b. The weight compared to the original rudder design is 20% lower in each case.

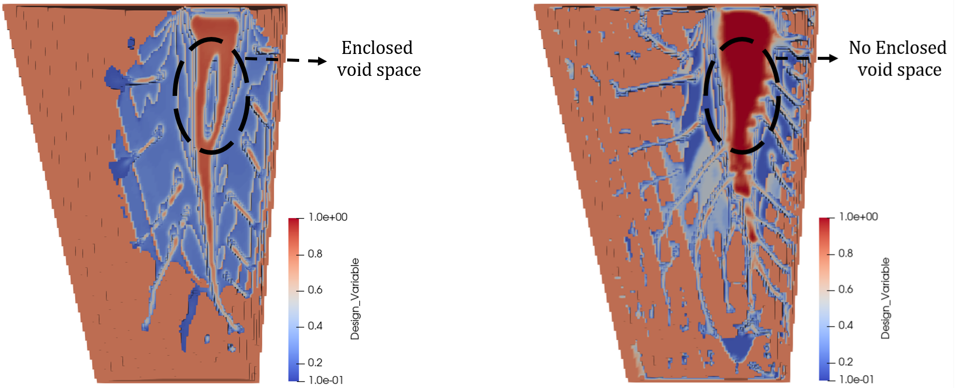

(a) (b)

Figure 3.4: Optimized Ship Rudder Designs: (a) Only compliance minimized design with $\theta = 1.0$ and (b) compliance and intersection objective minimized design with $\theta = 0.5$.

The optimized design shown in Fig. 3.4b was chosen for manufacturing. The optimized design needed certain post-processing steps to generate a design that can be manufactured with WAAM. The disconnected members are connected to allow continuous deposition trajectories and the spacing between the plates is made uniform. Also, the cross-sections of the plates are made uniform to allow the use of constant WAAM process parameters. A series of steps Damen took to reach the final design are shown in Fig. 3.5a. The final design obtained by applying these post-processing steps is shown in Fig. 3.5b. The weight of the final design of the rudder is 30% lower than the original design of the rudder. To evaluate the mechanical performance of the final design, a finite element stress analysis on the final design was performed by Damen. The analysis showed that the final design meets the mechanical performance requirements successfully.

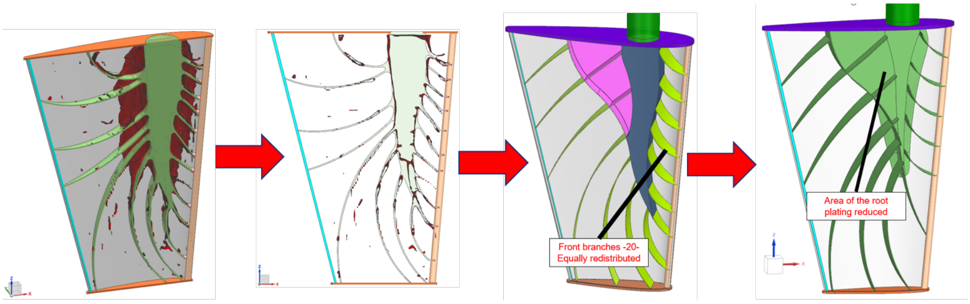

(a)

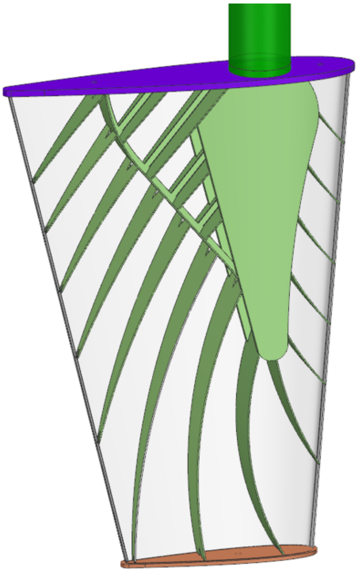

(b)

Figure 3.5: Post-processing: (a) A series of post-processing steps applied to the optimized design shown in Fig. 3.4b. The disconnected branches of the design were joined, they were assigned uniform cross-sections, and the branches were placed equidistantly. (b) The final design obtained that is inspired by the optimized design and will be manufactured using WAAM by MX3D.

3.4. CONCLUSIONS

In this chapter, a ship rudder design is generated using TO with lower weight and equivalent mechanical performance compared to the original ship rudder design by Damen. Various design and manufacturing-related requirements are considered while optimizing the structure for multiple hydrodynamic loading scenarios. The novel intersection control approach is extended in 3D to fulfill a key design requirement of reduced geometrical complexity posed by Damen for the ship rudder. It has been demonstrated that state-of-the-art research in TO is applied to generate a rudder design with 30% weight reduction which is possible to manufacture through WAAM. At the time of writing of this thesis, the rudder is being printed by company MX3D.

BIBLIOGRAPHY

Adam, A. (2023). *Mesh voxelisation* [MATLAB Central File Exchange, Retrieved March 14, 2023]. https://www.mathworks.com/matlabcentral/fileexchange/27390-mesh-voxelisation

Bruns, T. E., & Tortorelli, D. A. (2001). Topology optimization of non-linear elastic structures and compliant mechanisms. *Computer methods in applied mechanics and engineering*, *190*(26-27), 3443–3459.

Liu, K., & Tovar, A. (2014). An efficient 3d topology optimization code written in matlab. *Structural and Multidisciplinary Optimization*, *50*, 1175–1196.

4

SIMULTANEOUS TOPOLOGY AND DEPOSITION DIRECTION OPTIMIZATION FOR WIRE AND ARC ADDITIVE MANUFACTURING

A remarkable elastic anisotropy in plates of austenitic stainless steel produced by the Wire and Arc Additive Manufacturing process is recently reported. The Young's modulus depends on the angle of orientation with respect to the material deposition direction. Here, for the first time, this anisotropy is exploited to maximize structural stiffness by simultaneously optimizing the structural design layout and the local deposition path direction for WAAM. The results obtained indicate deposition that is commonly preferred along the load-path directions for WAAM is sub-optimal and stiffness can be increased at least 53% upon optimizing the deposition directions.

4.1. INTRODUCTION

Wire and Arc Additive Manufacturing (WAAM) is an emerging manufacturing method for large scale engineering structures with applications in maritime, aerospace and automotive industries (Rodrigues et al., 2019; Wu et al., 2018). Material produced by WAAM typically shows anisotropy in strength along and perpendicular to the deposition direction (Biswal et al., 2019; Derekar, 2018; Duarte et al., 2021; Fu et al., 2017; Gordon et al., 2018; Gu et al., 2020; Rafieazad et al., 2019; Sun et al., 2020; Wang et al., 2018). However, very recently, remarkable elastic anisotropy in stainless steel plates, produced by WAAM is observed (Kyvelou et al., 2020; Laghi, Palermo, Gasparini, et al., 2020; Laghi, Palermo, Tonelli, et al., 2020). The Young's modulus observed at 45° to the deposition path direction is 1.5 – 2 times higher than in directions along and perpendicular to the deposition path.

Local fibre orientations of fibre reinforced composite parts have been optimized to enhance performance (Fernandez et al., 2019; Lee et al., 2018; Schmidt et al., 2020). Similarly for WAAM, the deposition path directions can be optimized such that the stiffest directions of the material are aligned with the load-path orientation. The anisotropic nature of WAAM produced stainless steel sheets has already been utilized in design for stiffness improvement or weight reduction (Bruggi et al., 2021). However, the local deposition path directions were not optimized but prescribed before topology optimization. This significantly limits the full exploitation of elastic anisotropy.

The aim here is to include local deposition path directions as additional design variables and optimize for layout and deposition direction simultaneously. A cubic material model is proposed to account for the experimentally observed elastic anisotropy. These WAAM-specific considerations are incorporated into a density-based topology optimization (TO) framework (Bendsoe and Sigmund, 2013). In standard TO, the layout of the design is described by local pseudo-density variables. Here, in addition, independent local deposition direction vectors are introduced.

4.2. PROBLEM FORMULATION

4.2.1. DEFINITION OF DESIGN VARIABLES

Consider an optimization problem shown in Fig. 4.1. The domain is considered as a thin layer to be printed with WAAM with thickness direction perpendicular to the $X-Y$ plane. The continuous design domain is discretized using bilinear plane stress finite elements with pseudo density variable ρ_e and an independent deposition direction vector $\mathbf{v}_e$ assigned to each element e. The density variables ρ_e ranges between 0 and 1, extremes denoting void and material regions, respectively Andreassen et al., 2011. Vector $\mathbf{v}_e$ has components x_e and y_e along the global axes each ranging between -1 and 1. Consequently, the local material orientation makes an angle θ_e

$$\theta_e = \tan^{-1}(y_e, x_e), \tag{4.1}$$

with respect to the positive X-axis. Instead of the orientation angle θ_e, vector components (x_e, y_e) are chosen as design variables because it reduces the likelihood of the solution being a local minimum Nomura et al., 2015.

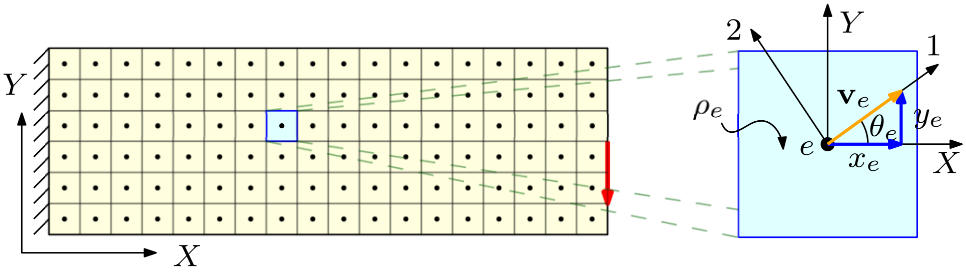

Figure 4.1: Schematic illustration of discretized design domain with load and boundary conditions, and definition of the optimization variables for element e (blue). Here, ρ_e is the density design variable and $\mathbf{v}_e$ is the deposition direction vector with components x_e and y_e along the global axes X and Y, respectively.

4.2.2. MATERIAL MODEL

Kyvelou *et al.* Kyvelou et al., 2020 investigated elastic anisotropy of the 308LSi austenitic stainless steel. Samples cut out from the plates, at 0°, 45° and 90° to the deposition path direction are considered. The corresponding Young's moduli in the plane were 143.3 GPa, 219.5 GPa and 139.6 GPa, respectively (Kyvelou et al., 2020). Here we introduce a cubic material model to account for the elastic anisotropy because of the nearly identical values of the Young's modulus along and perpendicular to the deposition directions. The compliance matrix for cubic material model is

$$\mathbf{Q} = \begin{bmatrix} \frac{1}{E} & \frac{-\nu}{E} & 0 \\ \frac{-\nu}{E} & \frac{1}{E} & 0 \\ 0 & 0 & \frac{1}{G} \end{bmatrix}, \tag{4.2}$$

for plane stress conditions suitable for a plate. The stress $\boldsymbol{\sigma} = [\sigma_{11}, \sigma_{22}, \sigma_{12}]^{\mathrm{T}}$ and strain $\boldsymbol{\varepsilon} = [\varepsilon_{11}, \varepsilon_{22}, \varepsilon_{12}]^{\mathrm{T}}$ given in Voight notation are then related as

$$\boldsymbol{\varepsilon} = \mathbf{Q}\boldsymbol{\sigma}. \tag{4.3}$$

Here, E is the Young's modulus identical in X- and Y-directions, ν is the Poisson's ratio and G is the shear modulus. Note that, E, ν and G are independent of each other for cubic elasticity. To determine E, the average of the Young's moduli along and perpendicular to the deposition direction is evaluated as $E = 141.5$ GPa. The Poisson's ratio is assumed to be 0.30 which is a typical value for austenitic stainless steel Ledbetter, 1984. To determine G, the experimentally measured value of the Young's modulus for a sample cut out at 45° to the deposition direction is used. Following the experiment, the compliance matrix $\mathbf{Q}'(\theta) = \mathbf{T}(\theta)\mathbf{Q}\mathbf{T}(\theta)^{\mathrm{T}}$ is calculated for a coordinate system rotated by $\theta = \pi/4$ in the counter clockwise direction. Here, $\mathbf{T}(\theta)$ is the transformation matrix

$$\mathbf{T}(\theta) = \begin{bmatrix} \frac{1+\cos 2\theta}{2} & \frac{1-\cos 2\theta}{2} & -\frac{\sin 2\theta}{2} \\ \frac{1-\cos 2\theta}{2} & \frac{1+\cos 2\theta}{2} & \frac{\sin 2\theta}{2} \\ \sin 2\theta & -\sin 2\theta & \cos 2\theta \end{bmatrix}. \tag{4.4}$$

Equating the component corresponding to first row and first column of $\mathbf{Q}'(\pi/4)$ to the reciprocal of experimentally measured value 219.5 GPa implies $G = 120.1$ GPa. The implications of cubic elasticity are further detailed in B.1.

4.2.3. OPTIMIZATION PROBLEM

Planar cantilever and bridge optimization problems are considered as shown in Fig. 4.2. These are representative of 3D WAAM cases where the final structure is composed of

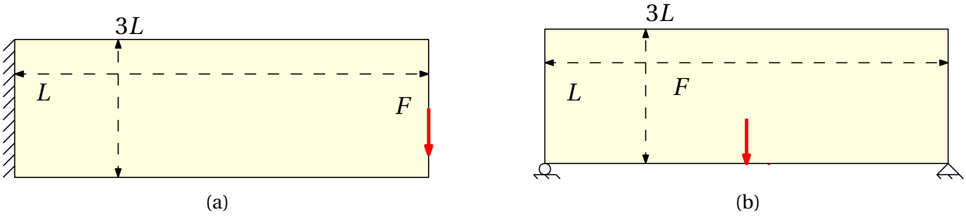

Figure 4.2: Optimization test problems considered for simultaneous design and deposition direction optimization: (a) cantilever, (b) bridge.

identical layers stacked. The cubic material model of deposition-dependent elastic properties is applied. A 50 × 150 structured mesh is used for both problems as schematically represented in Fig. 4.1. The size of a finite element is 10 mm × 10 mm. A concentrated load F is applied in both problems. Because of the linearity, the optimized design layouts do not depend on force magnitude (Bendsoe and Sigmund, 2013).

The global stiffness of both problems is maximized by minimizing the elastic strain energy. The corresponding optimization problem becomes

$$\min_{\boldsymbol{\rho},\mathbf{x},\mathbf{y}} \quad \phi = \frac{1}{2}\sum_{\Omega_N} \mathbf{u}_e^{\mathrm{T}} \mathbf{k}_e(\rho_e, x_e, y_e)\mathbf{u}_e, \tag{4.5}$$

$$\text{s.t.} \quad \mathbf{K}\mathbf{u} = \mathbf{f}. \tag{4.6}$$

$$V(\boldsymbol{\rho}) \le V_0. \tag{4.7}$$

$$0 \le \rho_e \le 1, \quad -1 \le x_e \le 1, \quad -1 \le y_e \le 1, \quad \forall e \in \Omega_N. \tag{4.8}$$

In Eq. (4.5), ϕ is the total elastic strain energy. The arrays of design variables ρ_e, x_e and y_e are represented by $\boldsymbol{\rho}$, $\mathbf{x}$ and $\mathbf{y}$, respectively. Element nodal degrees of freedom and the element stiffness matrix are represented by $\mathbf{u}_e$ and $\mathbf{k}_e$, respectively. Element stiffness matrices depend on the pseudo-density variable ρ_e which will be denoted as density in the remainder, and vector $\mathbf{v}_e$. The design domain comprising N elements is represented by Ω_N. Filtering is applied to density variables to avoid the formation of checkerboard patterns in the design layout and to ensure a minimum feature size in the optimized structure Bruns and Tortorelli, 2001. Filtered densities are denoted as $\tilde{\rho}_e$. A detailed description of the dependence of the element stiffness matrix on the design variables is given in B.2. Eq. (4.6) represents the equilibrium where $\mathbf{K}$, $\mathbf{u}$ and $\mathbf{f}$ are the global stiffness matrix, nodal degrees of freedom and nodal loads, respectively. Eq. (4.7) represents the constraint on material volume $V(\boldsymbol{\rho})$. The allowed material volume in the design domain V_0 is selected as 50% of the design domain for both optimization problems. Eq. (4.8) represents the bounds on the optimization variables. The gradient-based optimization algorithm MMA is used (Svanberg, 1987). The required derivatives of the elastic strain energy with respect to design variables are provided in B.2.

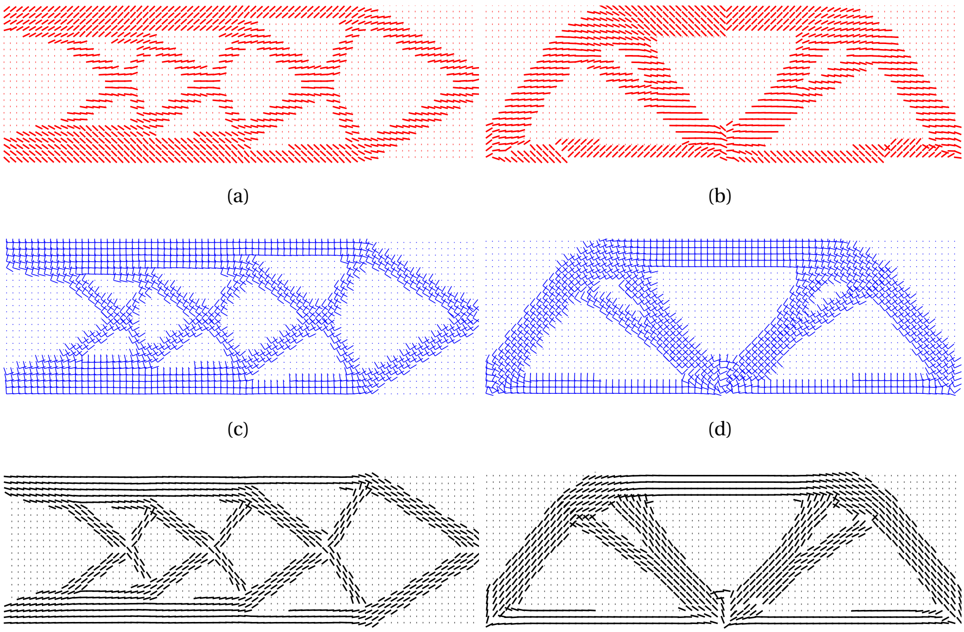

(a) (b)

(c) (d)

(e) (f)

Figure 4.3: Top row: optimized layout with optimized deposition directions for (a) cantilever ($\bar{\phi} = 1.00$) and (b) bridge ($\bar{\phi} = 1.00$) problems. Middle row: two stiffest material directions that are identical in stiffness corresponding to the optimized deposition direction for (c) cantilever and (d) bridge problems. Bottom row: optimized layouts with deposition directions prescribed along the load-path direction for (e) cantilever ($\bar{\phi} = 1.56$) and (f) bridge ($\bar{\phi} = 1.53$) problems.To ensure better readability, directions of every second element are omitted both in X- and Y- directions. $\bar{\phi} = \phi/\phi_{\text{ref}}$ is the normalised strain energy where ϕ_{ref} is the elastic strain energy of optimized design for the problem of interest shown in (a) for cantilever and (b) for bridge problems. ϕ is calculated using Eq. (4.5).

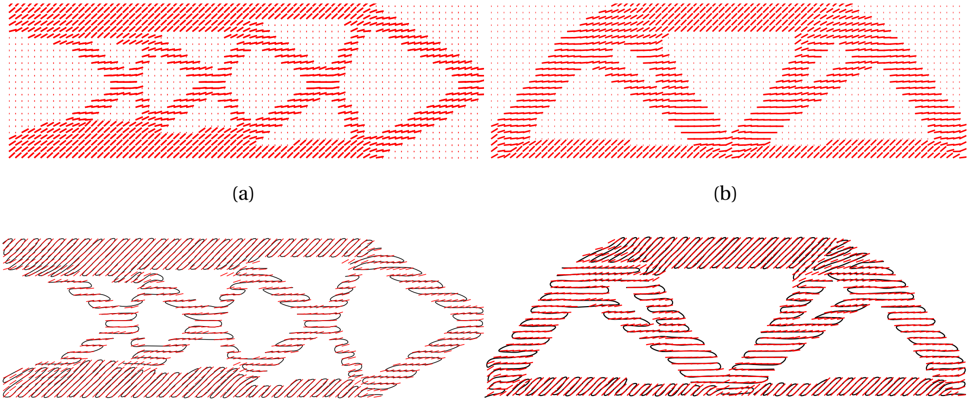

(a) (b)

(c) (d)

Figure 4.4: Top row: post processed optimized deposition directions corresponding to (a) cantilever and (b) bridge problems. Bottom row: an illustration of a possible deposition path (black) along the post processes optimized deposition directions (red) for (c) cantilever and (d) bridge designs, respectively.

4.3. Results

The optimized layouts and optimized deposition directions (red) of the considered structural problems are shown in Fig. 4.3. The deposition directions are only plotted for elements with $\tilde{\rho}_e \geq 0.5$.

The optimized deposition directions for horizontal members are aligned at approximately ±45° with respect to X direction whereas for inclined members this angle is smaller. In Fig. 4.3b horizontal deposition direction becomes optimal for members merging in the middle since these members have an inclination of ±45° with X- direction.

The cubic material stiffness is indifferent to rotation by $\pi/2$ owing to cubic symmetry in elasticity. Therefore the two stiffest material directions (blue), that are identical in stiffness are shown for both problems in Fig. 4.3. It is observed that one of the two equally stiff directions aligns with the straight members' local orientation that corresponds to the load-path of the design. Abrupt discontinuity in the optimized deposition directions (red) are seen in Fig. 4.3b. However, these correspond to a rotation of deposition direction by ±90°. Thus the stiffness of the material remains continuous.

Next, we present a comparison between the optimized and commonly employed deposition directions. The deposition directions (black) shown in Fig. 4.3 are prescribed to be aligned with the local orientation of members and hence the load-path of the corresponding layout. The elastic strain energies obtained when the deposition direction follows the load-path are 1.56 and 1.53 times higher than the direction optimized ones for the cantilever and bridge problems, respectively. This implies at least a 53% higher stiffness in both problems solely by exploiting the elastic anisotropy, which corresponds to the ratio between the extreme values of E-modulus observed experimentally (Kyvelou et al., 2020). Thus, surprisingly, the conventional deposition path strategy results in the worst possible stiffness performance for the anisotropic stainless steel.

In order to extract a WAAM deposition path from the optimized deposition directions, the material orientation θ_e at each element is mapped between 0 and $\frac{\pi}{4}$ because in this range the elastic properties uniquely depend on the orientation of material. Therefore, θ_e is first mapped between 0 and $\frac{\pi}{2}$ as

$$\alpha_e = \begin{cases} \theta_e & \text{if,} \quad x_e \geq 0 \quad \text{and} \quad y_e \geq 0, \\ \pi - \theta_e & \text{if,} \quad x_e \leq 0 \quad \text{and} \quad y_e \geq 0, \\ -\theta_e & \text{if,} \quad x_e \geq 0 \quad \text{and} \quad y_e \leq 0, \\ \pi + \theta_e & \text{if,} \quad x_e \leq 0 \quad \text{and} \quad y_e \leq 0, \end{cases} \tag{4.9}$$

and subsequently α_e is mapped between 0 and $\frac{\pi}{4}$ as

$$\theta_e^{(p)} = \begin{cases} \alpha_e & \text{if,} \quad \alpha_e \leq \frac{\pi}{4}, \\ \frac{\pi}{2} - \alpha_e & \text{if,} \quad \alpha_e > \frac{\pi}{4}. \end{cases} \tag{4.10}$$

The orientation of the post-processed optimized deposition directions $\theta_e^{(p)}$ (red) are shown in Fig. 4.4. The performance (ϕ) of the part is not affected owing to the cubic symmetry of the elasticity. The post-processing is required not only for extracting a viable deposition path but also because the optimized deposition directions θ_e depend upon the initial state of v_e before optimization while the set of $\theta_e^{(p)}$ is unique. The effect of initial state is discussed in B.3. An illustration of a possible deposition path (black) in line with the optimal post-processed deposition directions is shown in Fig. 4.4 for both designs. The convergence behaviour of ϕ is discussed in B.4.

4.4. CONCLUSIONS

Recently observed remarkable elastic anisotropy in WAAM produced stainless steel is exploited in this study to improve structural stiffness through topology optimization. Structural layout and deposition directions are optimized simultaneously to maximize the global stiffness. The results show that the deposition directions align approximately at ±45° with respect to the load-path. It is also shown for both problems that the deposition path following the optimal deposition directions on the optimized design will improve the structural stiffness by more than 53% compared to conventional deposition along the load-path directions.

BIBLIOGRAPHY

Andreassen, E., Clausen, A., Schevenels, M., Lazarov, B. S., & Sigmund, O. (2011). Efficient topology optimization in matlab using 88 lines of code. *Structural and Multidisciplinary Optimization*, *43*(1), 1–16.

Bendsoe, M. P., & Sigmund, O. (2013). *Topology optimization: Theory, methods, and applications*. Springer Science & Business Media.

Biswal, R., Zhang, X., Syed, A. K., Awd, M., Ding, J., Walther, F., & Williams, S. (2019). Criticality of porosity defects on the fatigue performance of wire+ arc additive manufactured titanium alloy. *International Journal of Fatigue*, *122*, 208–217.

Bruggi, M., Laghi, V., & Trombetti, T. (2021). Simultaneous design of the topology and the build orientation of wire-and-arc additively manufactured structural elements. *Computers & Structures*, *242*, 106370.

Bruns, T. E., & Tortorelli, D. A. (2001). Topology optimization of non-linear elastic structures and compliant mechanisms. *Computer methods in applied mechanics and engineering*, *190*(26-27), 3443–3459.

Derekar, K. (2018). A review of wire arc additive manufacturing and advances in wire arc additive manufacturing of aluminium. *Materials science and technology*, *34*(8), 895–916.

Duarte, V. R., Rodrigues, T. A., Schell, N., Santos, T. G., Oliveira, J. P., & Miranda, R. M. (2021). Wire and arc additive manufacturing of high-strength low-alloy steel: Microstructure and mechanical properties. *Advanced Engineering Materials*, 2001036.

Fernandez, F., Compel, W. S., Lewicki, J. P., & Tortorelli, D. A. (2019). Optimal design of fiber reinforced composite structures and their direct ink write fabrication. *Computer Methods in Applied Mechanics and Engineering*, *353*, 277–307.

Fu, Y., Zhang, H., Wang, G., & Wang, H. (2017). Investigation of mechanical properties for hybrid deposition and micro-rolling of bainite steel. *Journal of materials processing technology*, *250*, 220–227.

Gordon, J., Haden, C., Nied, H., Vinci, R., & Harlow, D. (2018). Fatigue crack growth anisotropy, texture and residual stress in austenitic steel made by wire and arc additive manufacturing. *Materials Science and Engineering: A*, *724*, 431–438.

Gu, J., Gao, M., Yang, S., Bai, J., Zhai, Y., & Ding, J. (2020). Microstructure, defects, and mechanical properties of wire+ arc additively manufactured alcu4. 3-mg1. 5 alloy. *Materials & Design*, *186*, 108357.

Kyvelou, P., Slack, H., Mountanou, D. D., Wadee, M. A., Britton, T. B., Buchanan, C., & Gardner, L. (2020). Mechanical and microstructural testing of wire and arc additively manufactured sheet material. *Materials & Design*, *192*, 108675.

Laghi, V., Palermo, M., Gasparini, G., Veljkovic, M., & Trombetti, T. (2020). Assessment of design mechanical parameters and partial safety factors for wire-and-arc additive manufactured stainless steel. *Engineering Structures*, *225*, 111314.

Laghi, V., Palermo, M., Tonelli, L., Gasparini, G., Ceschini, L., & Trombetti, T. (2020). Tensile properties and microstructural features of 304l austenitic stainless steel produced by wire-and-arc additive manufacturing. *The International Journal of Advanced Manufacturing Technology*, *106*(9), 3693–3705.

Ledbetter, H. (1984). Monocrystal-polycrystal elastic constants of a stainless steel. *Physica Status Solidi (a)*, *85*(1), 89–96.

Lee, J., Kim, D., Nomura, T., Dede, E. M., & Yoo, J. (2018). Topology optimization for continuous and discrete orientation design of functionally graded fiber-reinforced composite structures. *Composite Structures*, *201*, 217–233.

Nomura, T., Dede, E. M., Lee, J., Yamasaki, S., Matsumori, T., Kawamoto, A., & Kikuchi, N. (2015). General topology optimization method with continuous and discrete orientation design using isoparametric projection. *International Journal for Numerical Methods in Engineering*, *101*(8), 571–605.

Rafieazad, M., Ghaffari, M., Nemani, A. V., & Nasiri, A. (2019). Microstructural evolution and mechanical properties of a low-carbon low-alloy steel produced by wire arc additive manufacturing. *The International Journal of Advanced Manufacturing Technology*, *105*(5), 2121–2134.

Rodrigues, T. A., Duarte, V., Miranda, R., Santos, T. G., & Oliveira, J. (2019). Current status and perspectives on wire and arc additive manufacturing (waam). *Materials*, *12*(7), 1121.

Schmidt, M.-P., Couret, L., Gout, C., & Pedersen, C. B. (2020). Structural topology optimization with smoothly varying fiber orientations. *Structural and Multidisciplinary Optimization*, *62*(6), 3105–3126.

Sun, L., Jiang, F., Huang, R., Yuan, D., Guo, C., & Wang, J. (2020). Anisotropic mechanical properties and deformation behavior of low-carbon high-strength steel component fabricated by wire and arc additive manufacturing. *Materials Science and Engineering: A*, *787*, 139514.

Svanberg, K. (1987). The method of moving asymptotes—a new method for structural optimization. *International journal for numerical methods in engineering*, *24*(2), 359–373.

Wang, T., Zhang, Y., Wu, Z., & Shi, C. (2018). Microstructure and properties of die steel fabricated by waam using h13 wire. *Vacuum*, *149*, 185–189.

Wu, B., Pan, Z., Ding, D., Cuiuri, D., Li, H., Xu, J., & Norrish, J. (2018). A review of the wire arc additive manufacturing of metals: Properties, defects and quality improvement. *Journal of Manufacturing Processes*, *35*, 127–139.

5

MICROSTRUCTURE ESTIMATION AND VALIDATION OF ER110S-G STEEL STRUCTURES PRODUCED BY WIRE AND ARC ADDITIVE MANUFACTURING

Wire and Arc Additive Manufacturing (WAAM) emerged as a manufacturing process for large scale structures with extensive form and design freedom. WAAM can be fully exploited once the relation between the transient thermal history and its relation to microstructure development and resultant mechanical properties is established. This relation can be further used for computational design tools such as Topology Optimization. This paper presents a model to predict the relation between the thermal history and solid-state phase transformations in a widely applicable High Strength Low Alloy steel ER110S-G*. The transient thermal history of parts manufactured by WAAM is modeled using finite element analysis. The modelled thermal history is validated with thermocouple measurements. Our results show that a critical cooling cycle is responsible for the solid-state phase transformation in an AM part. The cooling rate of this particular cooling cycle is superimposed onto an experimentally constructed Continuous Cooling Transformation (CCT) diagram to determine the local solid-state phase fractions. The predicted phase fractions in three wall samples with different design and processing conditions of AM parts are used to predict the hardness. The predicted hardness is* 10% *higher than the measured hardness of AM samples. The effect of tempering is also considered in the model through JMAK equation. The results show that the tempering is caused in regions with high martensite content and it lowers the hardness by* 8 – 10%*. The micrographs of the AM parts show that the microstructural features are same for the AM parts with similar critical cooling rates.*

5.1. INTRODUCTION

Wire and Arc Additive Manufacturing (WAAM) has recently emerged as a novel manufacturing method with extensive form freedom for large-scale structures, especially in maritime and aerospace applications (J. Ding et al., 2015; Knezović and Topić, 2018). In WAAM, the metal wire is melted by an electric arc and deposited along predefined paths. The deposition typically happens layer-by-layer starting on a substrate, as schematically shown in Fig. 5.1. WAAM has been employed for a wide range of metallic materials including Titanium alloys, Nickel based alloys, Aluminum alloys, and Steels (Wu, Pan, Ding, Cuiuri, Li, et al., 2018). WAAM technology is currently used to manufacture shapes that are not feasible for conventional manufacturing technologies with milling and casting.

Topology Optimization (TO) is a computational design tool through which optimal geometric layout of a component with enhanced mechanical performance is determined (Bendsoe and Sigmund, 2013), and TO designs are typically geometrically complex. Near net shape of complex structures can be realised by WAAM with high dimensional accuracy (D. Ding et al., 2015; Rauch et al., 2021; Song et al., 2021; Venturini et al., 2018; Venturini et al., 2016). TO in conjunction with WAAM can be used to utilise the potential of manufacturing technology (Liu et al., 2018).

The mechanical properties of these metal WAAM parts can vary significantly depending on the microstructural development during the manufacturing process, as a result of the complex thermal history (Aldalur et al., 2020; Su et al., 2019; Wang et al., 2019; Wu, Pan, Ding, Cuiuri, and Li, 2018). The material locally experiences multiple thermal cycles depending on the design features, deposition strategies, process conditions, and material properties. The most common design studied is a simple wall. The thermal history experienced by such a simple wall is numerically evaluated and experimentally measured (J. Ding et al., 2014; Gornyakov et al., 2021; Hejripour et al., 2019; Rodrigues et al., 2019). Even for a simple thin wall, as shown in Fig. **??**, the thermal history experienced by material points is substantially different at different wall locations. For example, near the substrate, multiple heating, and cooling cycles are experienced, whereas the topmost layer of the wall experiences only a single heating and cooling cycle. The material deposited near the substrate exhibits a higher hardness than the material deposited farther away. This is because the substrate acts as a heat sink and facilitates rapid cooling for the material points close to it, leading to a microstructure with a dominant martensite phase (Rodrigues et al., 2019). However, the effect of the substrate for material points further away from it diminishes, causing a reduction in cooling rates and a reduction in the martensite phase fraction (Duarte et al., 2021; Rodideal et al., 2022; Yildiz et al., 2020). Thin walls intersecting at a junction are also studied (McAndrew et al., 2018; Mehnen et al., 2014). These studies conclude that since there is more material in the proximity of the junction local thermal diffusivity is high, which facilitates heat towards the base plate at the junction compared to regions far away. The design-induced thermal inhomogeneity is also partially due to the number of times the junction is in contact with the heat source compared to the material points far away from the junction. Heat accumulation due to local design change also leads to low cooling rates (Mishra et al., 2022).

Apart from the local design features, process parameters that influence the thermal history are wire feed rate, travel speed of the heat source, inter-pass dwell time, and the associated inter-pass temperature. The heat input is proportional to the ratio of wire feed rate and travel speed (Ayed et al., 2020; Rodrigues et al., 2019; Wu, Pan, Ding, Cuiuri, and Li, 2018). Consequently, variation in the heat input can lead to variations in the microstructure (Rodrigues et al., 2019). Inter-pass dwell time is the duration between the end and initiation of two subsequent layers. Increasing the inter-pass dwell time allows more time for the part to cool down. For thin walls, increasing the dwell time can result in a more uniform microstructure because the thermal conditions of the deposited material and pre-deposited material would remain the same for every layer (Foster et al., 2017). However, increasing dwell time increases the duration of manufacturing and therefore implies a higher cost of production (Rocha et al., 2020). Inter-pass temperature is the temperature at which the deposition of the next layer starts. It is observed that a thin wall structure manufactured with high inter-pass temperature, leads to a thermal condition where the material experiences high temperatures for a longer time. For steels, the cooling rates reported at the high inter-pass temperature are low. The low cooling rate results in solid-state phases with lower strength which reduces the overall yield strength of the manufactured part (Müller et al., 2022). The deposition pattern also influences the thermal history experienced throughout the part. Thin wall structures produced by deposition patterns with overlapping and oscillating strategies, shown in Fig. 5.2, show that the oscillating strategy leads to lower cooling rates than the overlapping strategy (Aldalur et al., 2020; Dirisu et al., 2019). This is because, with an oscillating strategy, the frequency of the heat source returning to the same material point is higher than that of the overlapping strategy, consequently leading to higher temperatures and lower cooling rates, hardness, and strength. This could be attributed to the presence of a high fraction of the soft ferrite phase.

Our aim is to establish the relationship between the thermal history obtained from the WAAM process and the resulting mechanical properties. This will pave the way to use this particular relation in TO to generate designs with desired properties. A requirement for TO is that a simulation correlating between a physical quantity and resulting properties should be computationally inexpensive. This is because of the iterative nature of the optimization process typically consisting of hundreds of iterations and the simulation performed for each iteration of the optimization.

We choose to study the effect of the WAAM process on High-Strength Low Alloy (HSLA) steel *ER110S-G*, which exhibits excellent weldability and is suitable for the WAAM process (Xin et al., 2021). Microstructure of HSLA steel encompasses various aspects such as grain size and morphology, crystallographic texture, solid-state phases, and tempering effects, all dictated by the transient thermal history. The combination of thermal gradients in the melt pool and solidification rates determines the grain size and morphologies (DebRoy et al., 2018). After solidification, the formation of predominantly columnar grains of the austenite phase (γ) commences in HSLA steels. Once the austenite is formed, solid-state phase transformations of interest begin. Below the critical temperature Ac_3, the austenite (γ) transforms to a phase mixture containing various morphologies of ferrite (α) (polygonal ferrite, upper bainite, and acicular ferrite) and martensite (α_m). These solid-state phases significantly control mechanical properties such as strength and ductility (Bhadeshia and Honeycombe, 2017; Callister Jr and Rethwisch, 2020). The formation of each of these phases depends on the cooling rate austenite en-

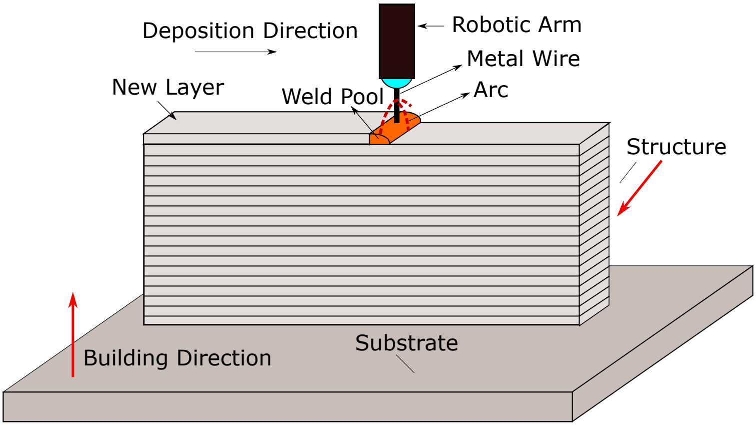

Figure 5.1: Schematic representation of the WAAM process of a thin wall in a layer-by-layer manner.

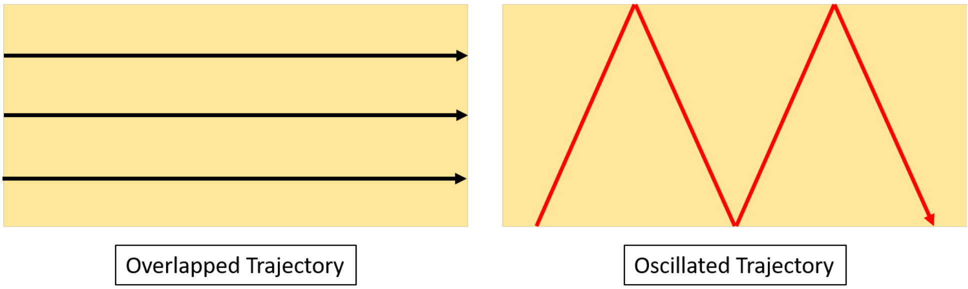

Figure 5.2: Schematic illustration of deposition paths of the overlapping and oscillating deposition strategies used by Aldalur et al., 2020 to investigate their effect on the mechanical properties.

counters. Martensite can further transform into tempered martensite, given it is held above a critical tempering temperature. It has been reported that there is no preferred orientation or strong texture in the WAAM printed HSLA steels resulting in isotropic mechanical properties (Haden et al., 2017; Huang et al., 2022; Rodrigues et al., 2019; L. Sun et al., 2020).

Various modeling approaches can be used to model various aspects of microstructure. To understand microstructure development in detail cellular automata models (Elahi et al., 2023; Lian et al., 2018; Teferra and Rowenhorst, 2021), phase field model (M. Yang et al., 2021), kinetic monte carlo model (Rodgers et al., 2017) and representative volume method (van Nuland et al., 2021) can be used. These models provide a detailed representation of the microstructure development but are computationally expensive, which makes them unsuitable for optimization study. Therefore, we choose a finite element-based model to evaluate the transient thermal history and correlate it to the material properties. Since there are no strict models that can predict the phase transformation and tempering kinetics for HSLA steels, therefore, our objective in this particular study is to model the solid-state phase transformation and the effect of tempering of a WAAM-manufactured HSLA part and validate it through experiments. Thus, we set aside the considerations related to grain size, and morphology for simplicity. Hereon, the terminology microstructure refers to solid-state phases and its their phase fractions. For the powder bed AM process, Zhang et al., 2019 estimated the metallurgical phases of Steel 5140. However, no experimental validation is reported. Also, the effect of tempering is not accounted for in their analysis.

In this study, the deposition process in WAAM is simulated using the finite element activation method, and the heat added to the material is modeled using the Double Ellipsoid Goldak heat source (Goldak et al., 1984). A finite element analysis is performed to determine the thermal history. The thermal history obtained from the simulation is validated by the temperature measured through multiple thermocouples during the actual printing of these parts. The critical cooling rate responsible for the solid-state phase transformation from the thermal history is identified. A Continuous Cooling Transformation (CCT) diagram is constructed from dilatometry experiments and used for estimating the phase fractions of the metallurgical phases due to the corresponding simulated critical cooling rate of the material points for the entire part. After that, the tempering of the martensite phase is accounted for through the Johnson-Mehl-Avrami-Kohnogorov (JMAK) equation. A series of tempering experiments are done in which the samples are placed at isothermal temperatures for a fixed time to calibrate the JMAK equation. This equation is then applied to the transient thermal history obtained from WAAM simulations. Finally, the estimated phase fractions of the metallurgical phases are used to predict the microhardness of the part using empirical relations from the literature (Doane, 1979). These estimated values are compared to the experimentally measured hardness values.

Details on the experimental setup and part geometries studied in this paper are outlined in Section 5.2. Description of the thermal modelling is given in Section 5.3. The procedure for predicting the fraction and morphology of the solid-state phases is explained in Section 5.4. The results obtained are given in Section 5.5. Finally, the most salient points of the study are reiterated in Section 5.6.

5.2. EXPERIMENTAL SETUP

5.2.1. PART GEOMETRIES AND DEPOSITION STRATEGY

The schematic representations of the geometric layouts of the parts are shown in Fig. 5.3. Three walls are manufactured. Simple walls shown in Fig. 5.3a are produced with two different welding conditions. The tapered wall is produced with a single set of welding conditions to study the effect of design on the microstructure. As deposition progresses, the geometric layout of the tapered wall facilitates faster cooling compared to the simple wall. Therefore, the effect of tapering on the microstructure is also investigated. The full description of the process parameters is given in Table 5.1. The deposition strategy for printing is based on bidirectional deposition, i.e. the deposition direction is reversed after completion of a layer as indicated in Fig. 5.3. For each geometry, 20 single bead layers are deposited. The bead height (h) and bead thickness (t) corresponding to each geometry are also given in Table 5.1. During the experiments, four thermocouples are attached to each wall, and the locations of the thermocouples are indicated with black dots in Fig. 5.3. From here on, the three samples are referred to as thick, thin, and tapered walls as given in Table 5.1. Preliminary single bead experiments are performed, and a process parameter window is identified (Kuo-hao WU, 2020). Two sets of process parameters are selected from this process parameter window. Deposition of thick and thin wall structures is achieved with a constant travel speed of 8 mm/s and wire-feed rate of 4.5 m/min and 2 m/min, respectively. The tapered wall comprises bidirectionally deposited 20 layers with a 120 mm long initial layer. A 45 ° tapering is achieved in the tapered wall by offsetting the beads' start and stopping by 1.6 mm in subsequent layers. Each bead for all the walls is deposited with an approximate inter-layer time of 120 s. The inter-layer time of approximately 600 s is taken after the layers in which thermocouples are attached.

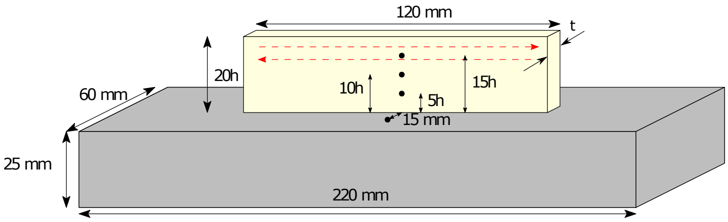

(a) Simple Wall

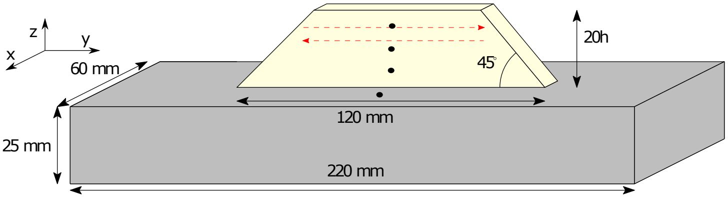

(b) Tapered Wall

Figure 5.3: Schematic illustration of the layout of the parts investigated. The deposition strategy is shown with red arrows. The thermocouples indicated with black dots are attached to the substrate at the 5th layer, 10th layer, and 15th layer.

Table 5.1: Process parameters used for manufacturing the parts.

Specimen	Geometry	WFR (m/min)	TS (mm/s)	h (mm)	t (mm)	# of layers
S1	Thick Wall	4.5	8.0	1.43	8.35	20
S2	Thin Wall	2.0	8.0	1.23	4.73	20
S3	Tapered Wall	4.5	8.0	1.43	8.35	20

5.2.2. SETUP AND MATERIAL

Thick, thin and tapered walls are fabricated by a Fanuc 5-axis robot system integrated with a Fronius 5000CMT-i power source. The first layer of the walls is deposited on an

ER110S-G steel substrate of 250 mm × 80 mm × 25 mm. The composition of the high strength steel wire (LNMoNiVa) with a diameter of 1.2 mm from Lincoln Electric used for the WAAM experiments is provided in Table 5.2. The density ρ, the heat capacity c_p, and the conductivity κ of the steel as a function of temperature are given in Fig. 5.4 Gao, 2018. The peak of specific heat of the material at the transformation temperature is used to model heat dissipation and generation during phase transformation. Pulsed mode deposition is used as the metal transfer mode. A mixture of 82% argon and 18% carbon dioxide is used as the shielding gas with a flow rate of 17 l/min. During welding a contact tip-to-work piece distance (CTWD) of 15 mm is maintained .

Table 5.2: Composition of high-strength steel wire (LNMoNiVa) as provided by the supplier.

Element	C	Mn	Ni	Si	Cr	Mo	Cu	V	Fe
Weight percentage	0.09	1.7	1.4	0.54	0.3	0.24	0.06	0.08	Balance

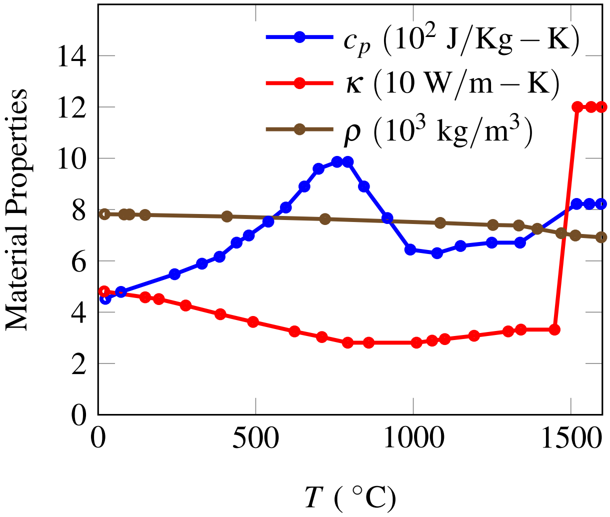

Figure 5.4: Thermal material properties of HSLA *ER110S-G* steel used for thermal simulations (Gao, 2018).

5.2.3. PROCESS MONITORING

Current and voltage characteristics are measured at 5 kHz frequency during the deposition using a Triton 4000 data acquisition system. Linear heat input (HI) corresponding to the process parameters used is determined from the measured current and voltage data according to

$$HI = \frac{\eta \Sigma_{i=0}^{n} V_i I_i n}{TS}, \tag{5.1}$$

where V_i is the instantaneous voltage measured at i^{th} time instance, I_i is the instantaneous current, n is the total number of measurements, TS is the travel speed, and η

is the arc efficiency. The arc efficiency depends upon the processing conditions and is generally in the range of 0.75 – 0.90 (DuPont, Marder, et al., 1995). K-type thermocouples are attached to the substrate and the part during the WAAM process (see also Fig. 5.3a). Time-temperature data from the thermocouples are recorded with a DL75 scope at a sampling rate of 500 Hz. The height of all the 20 layer samples is measured at three locations and then averaged to estimate the layer height. This layer height is further used in the thermal model to simulate the deposition of the individual layers.

5.2.4. DILATOMETRY EXPERIMENTS

Continuous cooling and tempering experiments are performed in a Bahr 805 DIL A/D dilatometer. Samples of 10 mm × 4 mm × 2 mm are extracted from a WAAM deposited *ER110S-G* block by wire electron discharge machining. A K-type thermocouple is attached to the centre of the block, which acts as the control thermocouple for executing the controlled thermal profiles.

CONTINUOUS COOLING EXPERIMENTS

Continuous cooling transformation diagrams (CCT) are generally constructed experimentally by sequentially heating the steel grade of interest to austenitisation temperatures and then subjecting it to controlled cooling rates. Samples are heated to 900 °C at 20 °C/s and held at 900 °C for 120 s for full austenitisation. The samples are subsequently cooled down to room temperature at 5, 10, 20, 30, 40, 50, 75 and 330 °C/s. The dilatometer recorded the change in length of the samples as a result of thermal expansion and phase transformation with temperature. The temperature versus dilation plot is illustrated in Fig. 5.5. During cooling from 900 °C, regions devoid of phase transformations are indicated by linear dilation. Phase transformation temperatures are determined by identifying the temperature at which the temperature versus dilation plot deviates from its linear behaviour. The lever rule is applied to the dilatometry data to assess the phase fraction of the austenite remaining at a particular temperature. The application of the lever rule is based on two assumptions:

- Partitioning of elements during cooling is ignored.
- Volume change associated with the measured dilation is isotropic (Moyer and Ansell, 1975).

As indicated in Fig. 5.5, the relative position of the dilatometric curve between the extrapolated linear regions of austenite and ferrite enables estimation of the transformed austenite fraction with temperature (Suh et al., 2007).

Moreover, we assume that the alloying is homogeneous in our dilatometry sample. The validity of this assumption is confirmed by the Energy Dispersive Spectroscopy (EDS) of the dilatometry samples. The result showed no significant variation in the alloying elements compared to the specified percentage of the alloys in Table 5.2.

TEMPERING EXPERIMENTS

Tempering experiments on WAAM printed *ER110S-G* HSLA are performed to develop a phenomenological model to predict tempering kinetics. Since tempering is associated

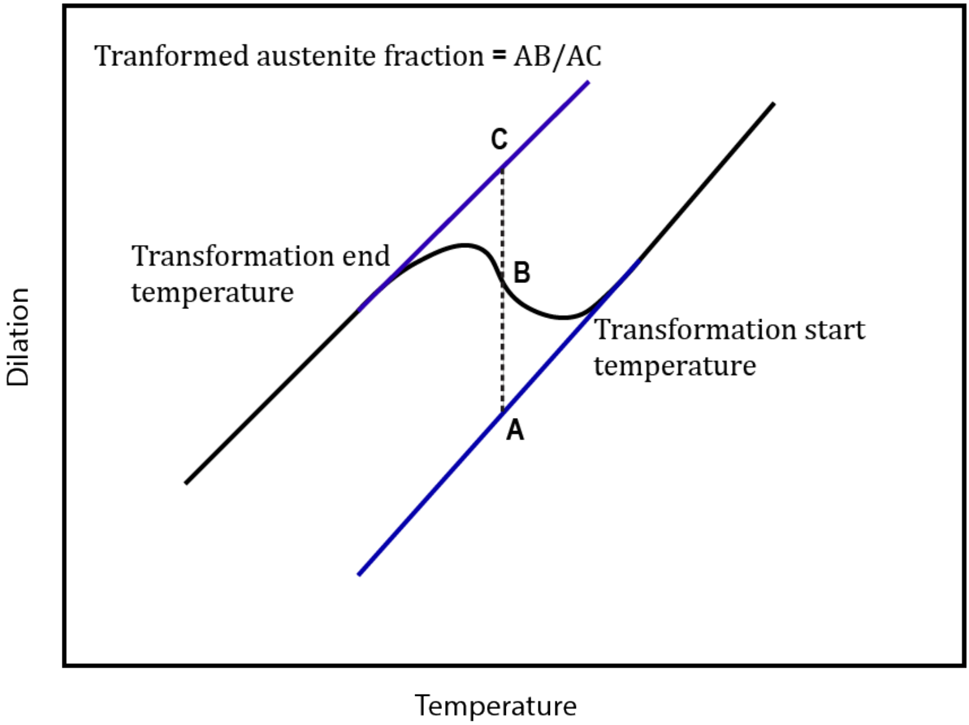

Figure 5.5: Illustration of dilatometry data during austenite decomposition.

with martensite, the sample is heated to the austenitic temperature of 900 °C, held for 120 s, and quenched to room temperature. A high cooling rate during quenching ensures that a fully martensitic microstructure is obtained. The sample is subsequently heated to temperatures such as 700 °C, 550 °C and 400 °C, which lie in the tempering zone. The samples are held at the tempering temperature for 5 s, 120 s and 1800 s and then quenched to room temperature. Due to tempering, the hardness of the samples reduce. The reduction in hardness due to tempering is a function of the tempering temperature and duration and can be modelled using the JMAK equation. To model the tempering kinetics using the JMAK equation, it is imperative to know the hardness of the fully tempered martensite. For this purpose, one dilatometry sample is austenised, quenched to room temperature, and then subjected to a tempering treatment at 700 °C for 5 h.

5.2.5. MICROSTRUCTURAL CHARACTERISATION

Transverse cross-sections are extracted from the centre of thick, thin, and tapered walls for micro-hardness measurements. Samples are prepared by grinding and polishing with colloidal silica paste of 1 μm and 3 μm particle size. A 2% Nital solution is utilised for etching, and microstructural features are observed via optical microscopy. Vickers micro-hardness measurements are made along the build direction of the deposited samples with a load of 1 kg. In the case of the dilatometry samples from the continuous cooling and tempering experiments, hardness measurements with a load of 1 kg are made at 10 points on each sample and averaged.

5.3. THERMAL MODELLING

During the WAAM process, the heat transfer from the newly deposited hot metal to the rest of the part and substrate occurs by conduction. In contrast, heat transfer to the surroundings occurs through convection and radiation. In Section 5.3.1, heat transfer equations solved numerically to simulate the heat transfer during the deposition process are given. As mentioned previously, the WAAM process consists of two aspects, local heating of the part with a moving heat source and material deposition. Heat addition is modelled through the Goldak heat source model (Goldak et al., 1984). The Goldak heat source model is briefly described in Section 5.3.2. The material addition is simulated by the finite element activation method described in Section 5.3.3.

5.3.1. HEAT TRANSFER EQUATION

The governing equation for heat transfer through conduction is given by

$$\frac{\partial(\rho c_p T)}{\partial t} = \nabla \cdot (\kappa \nabla T) + \dot{Q}. \tag{5.2}$$

Here, T and t are the temperature and time, while ρ, c_p and κ are the density, specific heat capacity and thermal conductivity of the material, respectively. $\dot{Q}$ is the power per unit volume added to the part, in this case representing the electric arc, which is modelled using the Goldak heat source model (Goldak et al., 1984) explained in the next section.

The heat flux **j** from the part to the surroundings is governed by

$$\mathbf{n}\cdot\mathbf{j} = h_c(T - T_a) + \epsilon\sigma(T^4 - T_a^4). \tag{5.3}$$

Here, **n** is the unit outward normal of the surface from which heat transfer occurs. h_c is the convective heat transfer coefficient, ϵ is the material emissivity, and σ is the Stefan-Boltzmann constant (5.6703×10^{-8} W/m^{2}K^4). T_a is the ambient temperature of the surrounding.

5.3.2. DOUBLE ELLIPSOIDAL GOLDAK HEAT SOURCE MODEL

The Double Ellipsoidal Goldak heat source model (Goldak et al., 1984) is widely used in welding and WAAM (Y. Yang et al., 2021), to mimic the heat addition. In the Goldak heat source model, the complexity of the weld pool and the heat transfer phenomenon therein are simplified by a double ellipsoidal heat distribution schematically shown in Fig. 5.6.

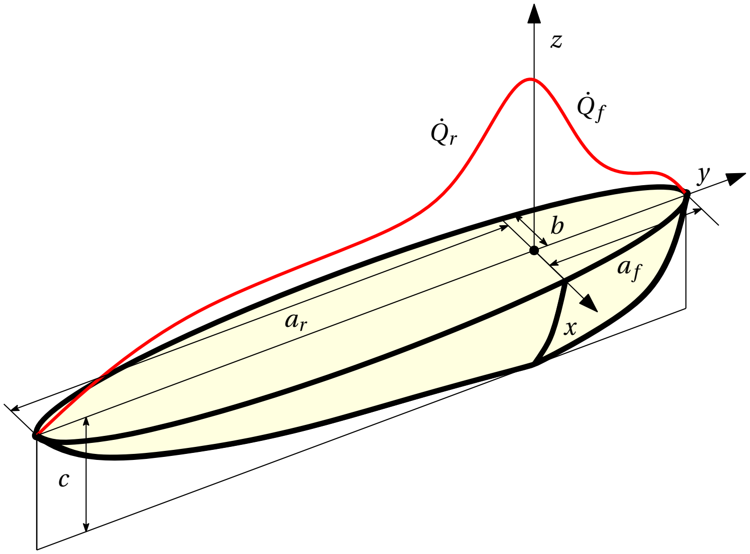

Figure 5.6: Schematic representation of the Goldak heat source (Goldak et al., 1984) to model the heat addition process during WAAM. $\dot{Q}_r$ and $\dot{Q}_f$ is the power per unit volume given in Eq. (5.4) for the rear and front regions with respect to the origin, which is schematically represented by the red curve.

The heat distribution inside a general ellipsoid is given as

$$\dot{Q}(x,y,z,t) = \frac{6\sqrt{3}\eta V I f}{abc\pi\sqrt{\pi}} \exp\left(-\frac{3(y - v_s t)^2}{a^2} - \frac{3x^2}{b^2} - \frac{3z^2}{c^2}\right). \tag{5.4}$$

Here, $\dot{Q}$ is the power per unit volume given for a general ellipsoid where a, b and c are the half-length, half-width and half depth of an ellipsoid. V and I are the voltage and current, respectively. η is the efficiency of the heat source, which typically ranges from 0.8 to 0.9 (Y. Yang et al., 2021). In the Goldak heat source model, the front and rear of the weld pool are approximated by combinations of quarters of two general ellipsoids. The front and rear ellipsoid are of different shapes; therefore, the half-length of the ellipsoid is a_f and a_r representing the front and rear length of the weld pool, respectively. b and c are the same for both ellipsoids. $\dot{Q}_f$ and $\dot{Q}_r$ are the power per unit volume distributed over the front and rear ellipsoids as shown in Fig. 5.6. The dimensions of the front and rear arc are substituted in Eq. (5.4) to calculate the distribution of power per unit volume $\dot{Q}_f$ and $\dot{Q}_r$ over the front and rear end, respectively. The factor f represents the fraction of power attributed to an ellipsoid. f_f and f_r are power factors associated with the front and rear ellipsoid. These factors are calculated as

$$f_f = \frac{2a_f}{a_f + a_r}, \qquad f_r = \frac{2a_r}{a_f + a_r}. \tag{5.5}$$

5.3.3. FINITE ELEMENT ANALYSIS AND ELEMENT ACTIVATION METHOD

The weak form of the heat equation is solved by the finite element (FE) analysis within a time integration scheme (Hughes and Liu, 1978) using the commercial software COMSOL to obtain the temperature distribution of the part. As an example, the FE mesh used for discretising the wall geometry is schematically shown in Fig. 5.7. The elements on the surface are subjected to the convection and radiation boundary conditions given in Eq. (5.3).

A FE activation scheme is used to model the deposition process, i.e., the growing domain. In this FE activation approach, each element e is assigned a variable x_e to scale the associated thermal conductivity. If x_e is equal to 0 or 1, the finite element is deactivated and activated, respectively. The conductivity κ for an element e (κ_e), is given as

$$\kappa_e = \kappa_{min} + x_e(\kappa - \kappa_{min}). \tag{5.6}$$

where, κ_{min} is the minimum conductivity value which is taken as 1×10^{-6} W/mK. The heat source location in Fig. 5.7 is used to determine which elements are active ($x_e = 1$) at a given time. In contrast, the remaining elements of the layer stay deactivated with $x_e = 0$. For each time step, the location of the heat source changes, and new elements are activated until the deposition is complete. After that, the temperature history at each node of the FE mesh is obtained by a post-processing script.

5.4. MICROSTRUCTURE PREDICTION

5.4.1. SOLID-STATE PHASE TRANSFORMATION

As mentioned in the introduction, the transient thermal history experienced by a material point during the WAAM process consists of multiple heating and cooling cycles. The first cycle corresponds to the deposition of the material in which the metal is melted, deposited, and solidified. After solidification, the most critical solid-state transformation occurs when the parent phase of austenite transforms into the child phases of ferrite, bainite and martensite. For a material point that has already been deposited, subsequent heating and cooling cycles depend on the deposition path, i.e. depending on when material deposition occurs close to the material point of interest. For the thin wall structures

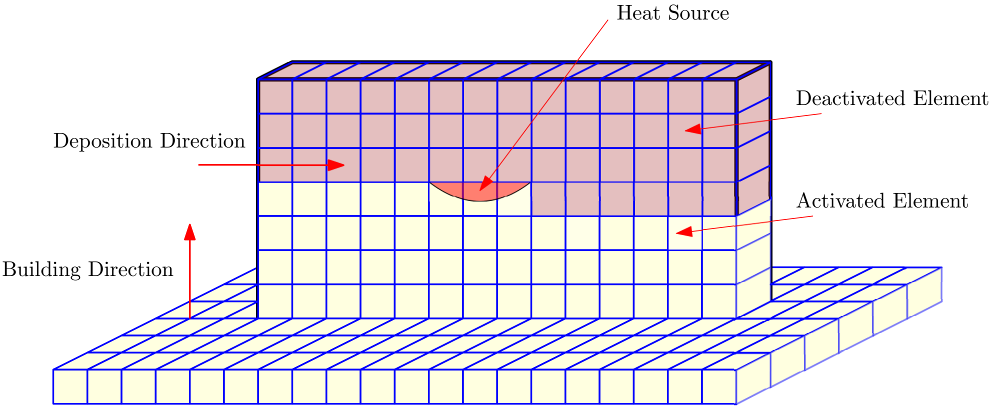

Figure 5.7: Schematic representation of finite element activation method to model material deposition during WAAM. Based on the time and location of the heat source, the deposited elements are activated, represented in yellow. In contrast, the elements of the part that are not yet deposited are kept deactivated, shown in pink.

we investigate, this phenomenon occurs when the material is deposited near the material point of interest during the deposition of the subsequent layers. If the temperature in the already deposited material point exceeds the Ac_3 temperature in any of the thermal cycles, the child phases transform back to the parent phase austenite. Therefore, the cooling stage after heating for which the temperature of the pre-deposited material exceeds the Ac_3 temperature for the last time becomes critical for determining the fraction and morphology of child phases. In this paper, this is termed the critical cooling stage. The cooling rate of the critical cooling stage is superimposed onto a CCT diagram of the *ER110S-G* HSLA grade constructed experimentally from the dilatometry measurements to estimate the child phase fractions. The procedure to calculate the phase fractions of the child phases using the CCT diagram is described in the Results and Discussion section.

5.4.2. TEMPERING OF MARTENSITE

Thermal cycles with a peak temperature lower than Ac_3 are unable to transform child phases back to austenite. Although a partial transformation of ferrite to austenite occurs when steel is heated to a temperature between Ac_1 and Ac_3, this effect is neglected for simplicity in this paper. However, heating a material point below Ac_3 can still induce tempering for the martensite phase. If HSLA steel is heated to a temperature above 250 °C, diffusion of carbon from supersaturated martensite leads to the formation of tempered martensite. Tempered martensite has relatively lower hardness and strength but a higher ductility than pristine (untempered) martensite (Bhadeshia and Honeycombe, 2017). Hence, determining tempered martensite fraction is important for a realistic estimation of hardness in WAAM parts. The tempering ratio increases with the tempering temperature and duration which can be accounted for with the JMAK equation as suggested in (Y. Sun et al., 2019), i.e.

$$X_T = 1 - \exp\left(-\left(D_0 \exp(-Q_t/RT)\, t\right)^N\right). \tag{5.7}$$

Here, t is the tempering duration, T is the tempering temperature, $R = 8.3145$ J/mol/K is the universal gas constant and $Q_t = 1.96 \times 10^5$ J/mol is the activation energy of the tempering process (Y. Sun et al., 2019). D_0 and N are the material constants determined from the tempering experiments described in Section 5.2.4 for HSLA *ER110S-G* steel. The tempering ratio X_T of tempered samples is estimated as

$$X_T = \frac{H_T - H_0}{H_\infty - H_0}, \tag{5.8}$$

where H_T are the measured hardness value of tempered martensite and H_0 and H_∞ are the hardness values measured at $X_T = 0$ and $X_T = 1$, respectively. The tempering ratio of 0 and 1 indicates pure martensite and fully tempered martensite, respectively. The harnesses of the fully tempered martensite and untempered martensite are experimentally determined as $H_\infty = 271.3 \pm 3.3$ HV and $H_0 = 389.6 \pm 3.5$ HV respectively.

5.4.3. HARDNESS ESTIMATION

After the calculation of the phase fractions of all the phases, first using the CCT diagram and then using Eq. (5.7), it remains to estimate the hardness using the rule of mixture given as follows

$$HV = f_F H_F + f_B H_B + f_M H_M + f_{TM} H_{TM}. \tag{5.9}$$

Here, f_F, f_B, f_M and f_{TM} are the phase fractions of ferrite, bainite, martensite and tempered martensite, respectively. H_F, H_B, H_M and H_{TM} are the Vicker hardness of the corresponding individual phases. The hardness of the individual phases is evaluated using slightly modified correlations given in (Doane, 1979). This correlation is used because it is valid for the low carbon steels but developed for the conventional manufacturing processes which exhibit lower cooling rates than WAAM. Therefore, the correlation is modified to account for high cooling rates. In the modified correlation, an average cooling rate is evaluated in a specific temperature range, in contrast to the cooling rate evaluated at a specific temperature (Doane, 1979). The modified correlation is as follows

$$\begin{aligned}
H_M =& 127 + 949\text{C} + 27\text{Si} + 11\text{Mn} + 8\text{Ni} \\
&+ 16\text{Cr} + 21\log(C/C_0), \\
H_B =& 323 + 185\text{C} + 330\text{Si} + 153\text{Mn} + 65\text{Ni} \\
&+ 144\text{Cr} + 191\text{Mo} \\
&+ \log(C/C_0)(89 + 53\text{C} - 55\text{Si} - 22\text{Mn} \\
&- 10\text{Ni} - 20\text{Cr} - 33\text{Mo}) \\
H_F =& 42 + 223\text{C} + 53\text{Si} + 30\text{Mn} + 12.6\text{Ni} \\
&+ 7\text{Cr} + 19\text{Mo} \\
&+ \log(C/C_0)(10 - 19\text{Si} + 4\text{Ni} \\
&+ 8\text{Cr} + 130\text{V}).
\end{aligned} \tag{5.10}$$

Here, the symbols of the elements indicate the weight percentage of the elements in the chemical composition of the steel given in Table 5.2. C is the average cooling rate in °C/h. C_0 is the constant cooling rate equal to 1 °C/h to normalize the units of the quantity on which log(.) is being applied.

5.5. RESULTS AND DISCUSSIONS

In this section, first, the predicted thermal history will be validated in Section 5.5.1 by comparing the thermal model predictions with the thermocouple measurements. Subsequently, in Section 5.5.2 the experimentally constructed CCT diagram is presented. In Section 5.5.3, the solid-state phase fraction fields are determined using the simulated temperature history and the CCT diagram. Tempering ratio calculation procedure of martensite through JMAK equation and tempering experiments are given in Section 5.5.4. The estimated phase fractions and tempering ratios for all three samples are discussed in Section 5.5.5. The optical micrographs of the three wall samples manufactured by WAAM are shown in Section 5.5.6. An empirical relation described in Section 5.5.3 predicts the hardness values associated with a mixture of solid phases and is compared with the experimentally attained hardness values of the printed samples in Section 5.5.7.

5.5.1. THERMAL HISTORY VALIDATION

In the remainder, the thermocouples which are attached to the substrate, 5^{th}, 10^{th} and 15^{th} layers are labeled as $L00$, $L05$, $L10$ and $L15$, respectively. For each specimen $S1$, $S2$ and $S3$ given in Table 5.1, there are 4 thermocouples each of which is uniquely identified as $S\#L\#\#$. For example, the thermocouple attached to layer 15 on the specimen $S3$ is identified as $S3L15$. The locations of thermocouples are shown in Fig. 5.3. The thermal history predicted by the FEA and measured through four thermocouples for specimen $S1$ are superimposed and are shown in Fig. 5.8. For specimens $S2$ and $S3$, the superimposed results are shown in Section C.1. For specimens $S2$ and $S3$, the thermocouple data are only shown for three thermocouples each. It is because $S2L15$ and $S3L05$ thermocouples burned during the experiments in S2 and S3, respectively.

Each peak in the plot indicates the deposition of a new layer. Good agreement is observed between the numerical model predictions and the experiments, especially after the first few layers are deposited (see Fig. 5.8). The peak temperature predictions are well above the thermocouple data ($S1L05$, $S1L10$ and $S1L15$) for the first few peaks. In the first peak temperatures are expected to exceed the melting point, around 1500 °C. However, the maximum temperature measured from the K-type thermocouples used in our study is 1200 °C. Moreover, the thermocouple is carefully placed away from fusion zone to avoid damage to the thermocouple. These factors contribute in not capturing the first temperature peaks. Secondly, in K-type thermocouples, the time it takes to reach the 63% of the value of the temperature it is measuring is equal to 0.02 s. Since the heating rates in the first few layers are typically on the order of 10^3 °C/s, the thermocouple measurements are expected to underestimate the peak temperature. We note in passing that the discrepancy diminishes after a few peaks because the heating and cooling rates and the peak temperatures both decrease. The effects mentioned above are not so dominant

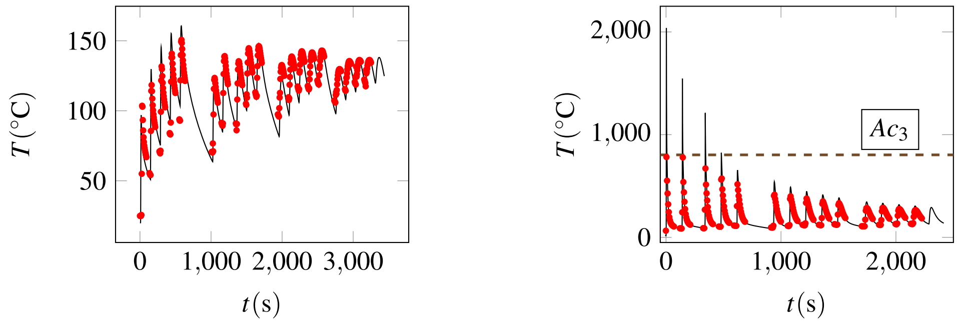

(a) S1L00

(b) S1L05

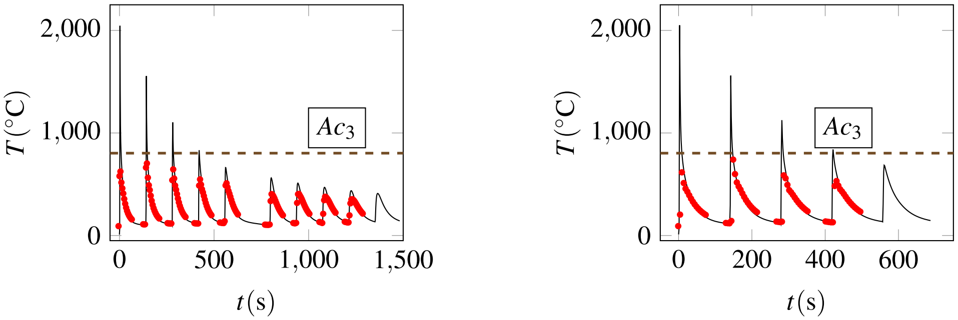

(c) S1L10

(d) S1L15

Figure 5.8: Temperature data from thermocouples at (a) substrate, (b) 5^{th} layer, (c) 10^{th} layer and (d) 15^{th} layer associated with specimen $S1$ (red data points). Temperature predictions calculated with FEA are depicted with a solid black line and thermocouple measurements are illustrated with red points. The black dots denote the thermocouple data points used to calculate the critical cooling rate to compare it with the numerically simulated thermal cooling rates for validation purposes.

for the thermocouple attached to the substrate. Therefore, the superposition of the numerical and experimental data best matches the thermocouple attached to the substrate (see Fig. 5.8a).

The thermal history is post-processed to identify the critical cooling cycle for each material point. The dotted line indicates the Ac_3 temperature in Fig. 5.8. Recall that the cooling rate after the last time, the temperature exceeds Ac_3, is considered the critical cooling rate. The region before the critical cooling cycle is termed the reset region, while the region after the critical cooling cycle is the tempering region. The thermal cycles in the latter region transform martensite to tempered martensite, granted the martensite phase is among the child phases during the critical cooling cycle.

Fig. 5.9a shows the average critical cooling rates between the temperature range 800 °C to 300 °C ($C_{8|3}$), estimated by the numerical thermal model along the line in z direction passing through the thermocouples. The cooling rates are high near the substrate and reduced for layers further away from the substrate. This is because the substrate acts as a heat sink and facilitates rapid heat evacuation for the layers deposited close to it. Actual cooling rates close to the substrate are also measured and reported in the literature, showing similar observations (Rodrigues et al., 2019). A comparison of the cooling rates obtained from the numerical analysis and experimental measurements is shown in Fig. 5.9b. The cooling rates are shown after the first 5 layers for better visualisation. For all the samples, the predicted cooling rates are higher than the measured counterparts, as shown in Fig. 5.9b. The measured cooling rates are 25 – 50% lower than the predicted cooling rates. However, the qualitative trends along the height of the walls are well captured. The lower cooling rate observed in the experimental measurements can be attributed to the before mentioned poor ability of thermocouples to capture the temperature peaks. The discrepancy in the cooling rate measurements and numerically obtained cooling rates becomes less severe once the peak temperature is well captured.

It remains to rationalise the different cooling rates for the various specimens considered in the study. The cooling rates observed in the thin wall are higher than in the thick and tapered walls. This is because the heat input in the thin wall is considerably lower than in the thick and tapered wall promoting a higher cooling rate. Moreover, the predicted cooling rates of the tapered wall for the topmost layers of the specimen are slightly higher than the thick straight wall. As the length of the deposited layer decreases after every deposited layer in the tapered wall, more solid material underneath the deposited layer is available for heat conduction, promoting higher cooling rates at the top layers of the tapered wall compared to the thick wall. This effect is visible both in the experimentally measured and numerically predicted cooling rates. It is also worth noting the effect of tapering is anticipated to be more pronounced near the edges of the specimen than the centre where the thermocouples are situated.

Various parameters are carefully chosen in the numerical thermal model to achieve good agreement with the experimental data. These parameters involve arc efficiency of the heat source ($\eta = 0.8$), heat transfer coefficients through the wall and substrate to the surroundings ($h_c = 5.7\ \mathrm{W/m^2-K}$) and thermal material properties as suggested in Gao, 2018. All of these parameters impact the thermal history obtained from the simulation. The uncertainties in these parameters will cumulatively impact the numerical predictions of the peak temperature and cooling rates. Through the careful selection of the parameters, the thermal history obtained from numerical FE calculations agrees with thermal data measured from multiple thermocouples. Also, the qualitative trends of cooling rates are well captured. Therefore, the numerical thermal history will be used to predict the solid-state phase fractions in the printed part.

5.5.2. DILATOMETRY EXPERIMENTS AND CCT DIAGRAM

The optical micrographs obtained from the dilatometry samples corresponding to various cooling rates are given in Fig. 5.10. A qualitative comparison of the optical micrographs indicates the variation in microstructure caused by cooling from the austenitizing temperature at constant cooling rates ranging from 1 °C/s to 330 °C/s. For low cooling rates, coarse grains of ferrite are dominant in the microstructure. The martensite formation in samples cooled at 1 °C/s could be associated with carbon diffusion. The carbon diffuses to the neighbouring austenite grains during ferrite formation, stabilising austenite and subsequent full or partial transformation of remaining austenite

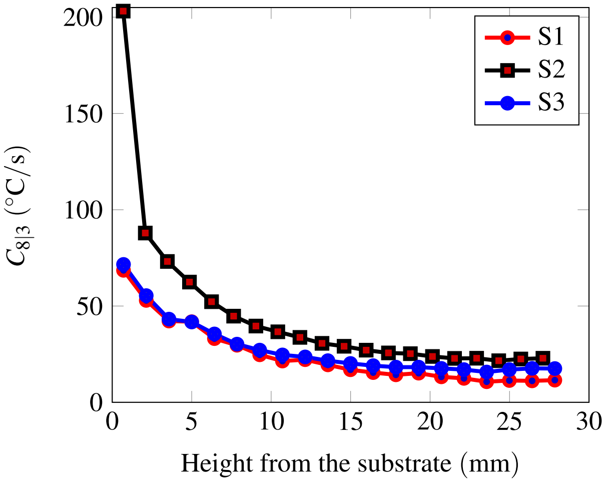

(a)

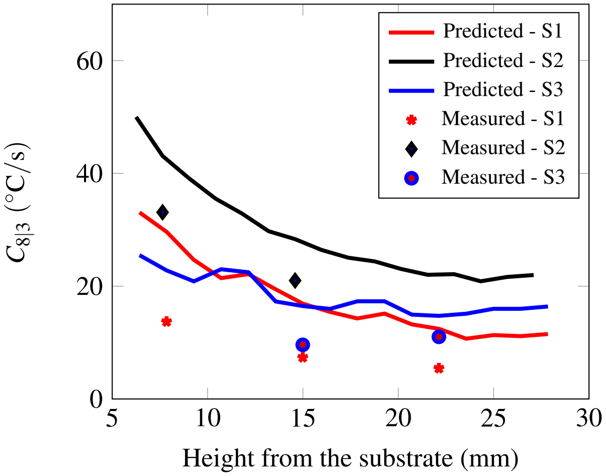

(b)

Figure 5.9: (a) Average cooling rate of the critical cycle obtained from the thermal modelling along with the height of the specimen from the substrate. (b) Comparison of the critical cycle cooling rates measured experimentally and obtained from the thermal modelling.

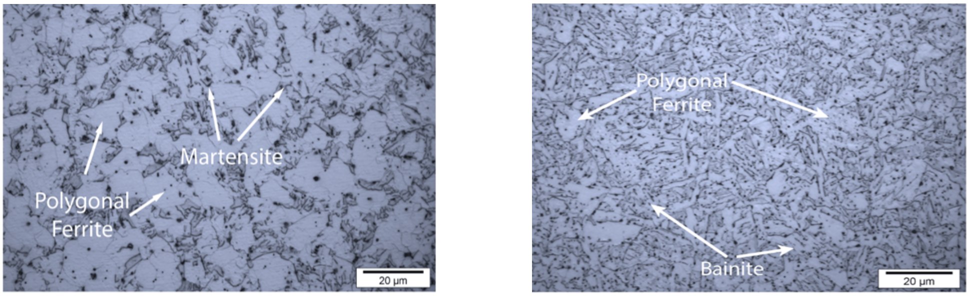

(a) 1 °C/s (b) 10 °C/s

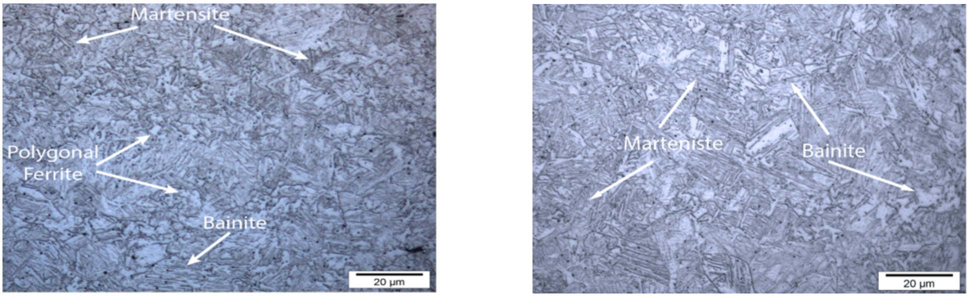

(c) 30 °C/s (d) 50 °C/s

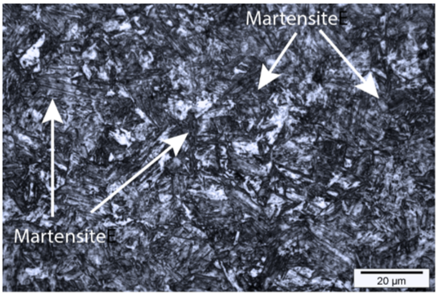

(e) 330 °C/s

Figure 5.10: Optical micrographs obtained from dilatometry samples cooled at different cooling rates from austenitization temperature

to martensite (Thompson et al., 1996). A mixed microstructure of ferrite and bainite can be seen for the sample subjected to a cooling rate of 10 °C/s. Samples cooled at 30 °C/s have a mixed microstructure of ferrite, bainite, and martensite. As the cooling rate increases to 50 °C/s, the microstructure is a mixture of bainite and martensite with traces of grain boundary ferrite. An increase in martensite fractions can be observed in samples cooled at 10 °C/s to 330 °C/s. A fully martensitic microstructure is observed in the sample cooled at 330 °C/s, indicating the complete transformation of the austenitised sample to martensite.

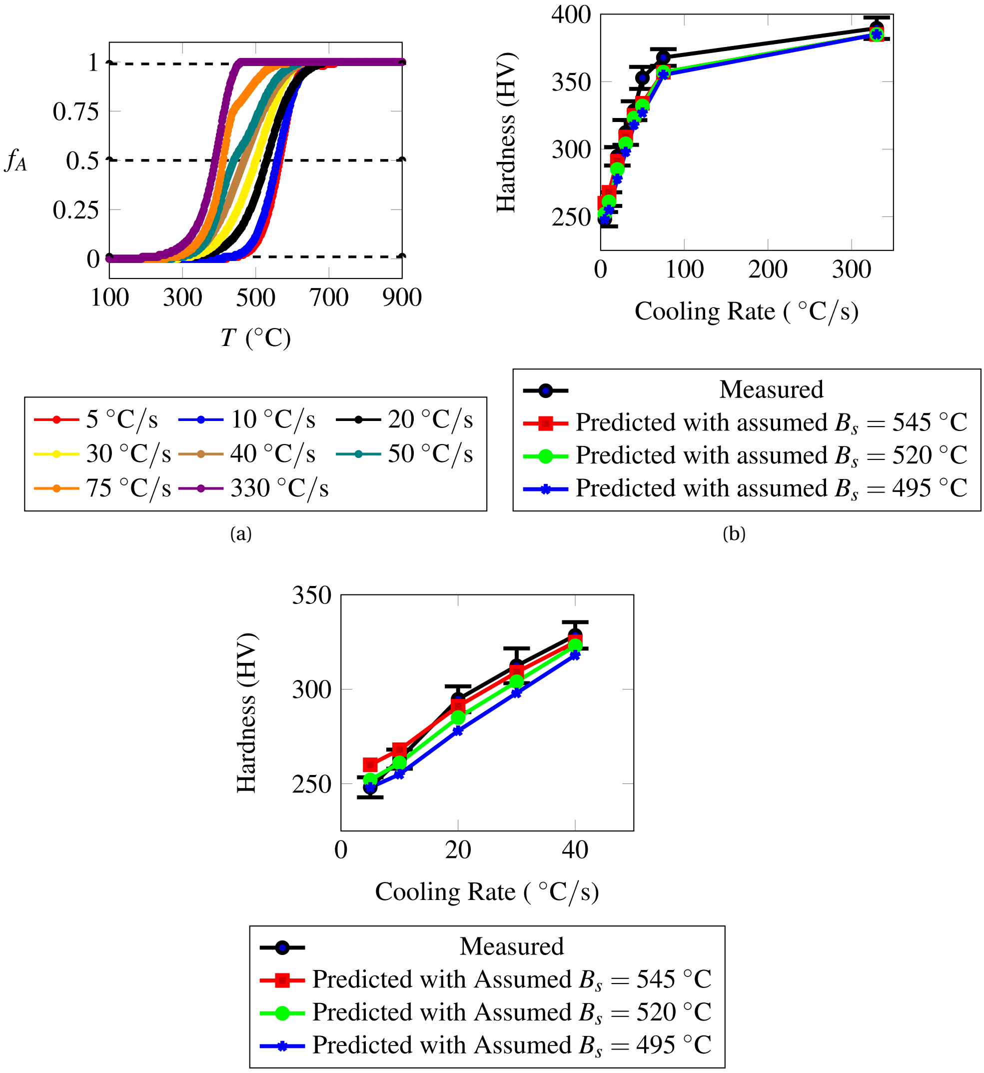

(a) (b)

(c)

Figure 5.11: (a) Curve fitted dilatometry data obtained for sampled cooling rates. (b) Hardness measurements of the dilatometry samples and a comparison with the predicted hardness evaluated using Eq. (5.9).

The raw dilatometry data is shown in Fig. C.3. Each experiment is repeated three times for each cooling rate to ensure repeatability. The resultant fraction of austenite phase (f_A) versus temperature is obtained using the lever rule, discussed in Section 5.2.4, is shown in Fig. C.4. For each cooling rate, a curve fitting operation is performed to evaluate the relation between the phase fraction of austenite and temperature. The curve fitted datasets evaluate the average austenite phase fraction as a function of temperature for the sampled cooling rates, therefore also at a given time, are shown in Fig. 5.11a. The corresponding measured hardness profiles of the samples are shown in Fig. 5.11b by a black line.

To construct the Continuous Cooling Transformation (CCT) diagram, the temperature and time values for a given percent of austenite transformed are evaluated from post-processed dilatometry data. Fig. 5.11a is then converted to a CCT diagram as shown in Fig. 5.12.

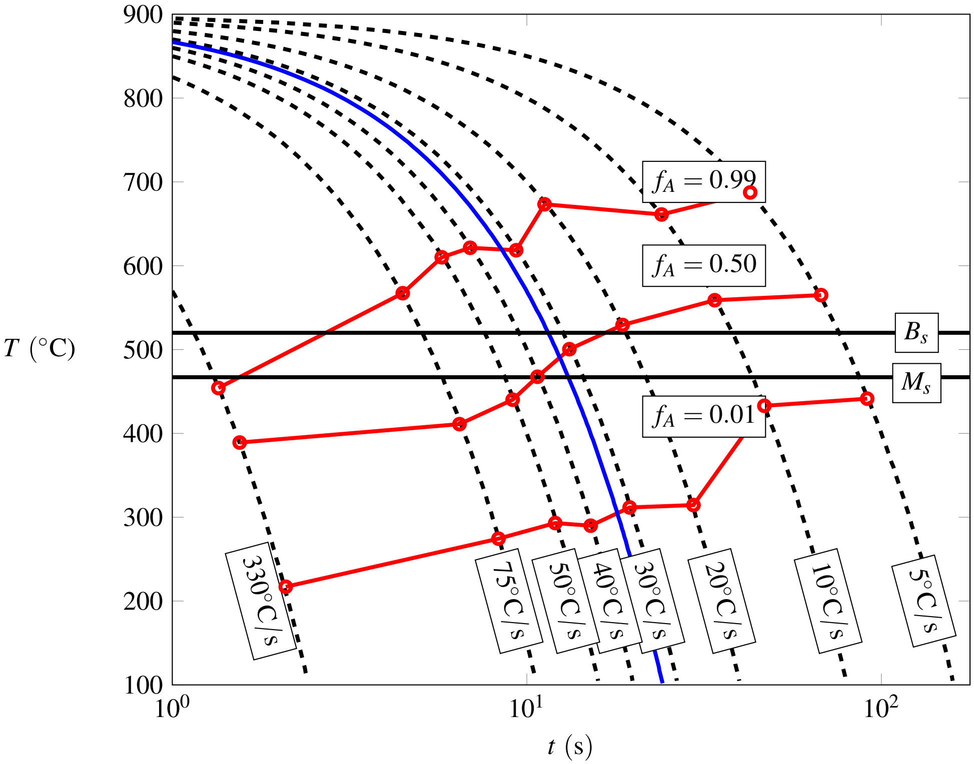

Figure 5.12: Continuous Cooling Transformation (CCT) diagram obtained from the dilatometry experiments. The dashed black lines represent the cooling rates, and the red lines represent the iso-phase fraction lines of the austenite phase. Solid back lines represent the bainite start temperature (B_s) and martensite start temperature (M_s). Start temperatures are assumed to be independent of the cooling rates.

The dotted black lines denote various cooling rates in the experimentally constructed CCT diagram of *ER110S-G* steel. The red iso-phase lines denote the constant phase fractions across these constant cooling rate profiles. The area engulfed by the iso-phase fraction lines represents where the austenite phase transforms into α phases.

The data obtained from dilatometry are also analysed to identify the temperatures at which the transformation of phases such as martensite and bainite start. Martensite start temperature (M_s) is evaluated using the dilatometry data corresponding to the highest cooling rate 330 °C/s. At this cooling rate, there is only a single-phase transformation from austenite to martensite, which is also evident from Fig. 5.10e. Hence, martensite start temperatures can be evaluated by locating the temperature at which the austenite dilatometry curve deviates from linearity. The observed martensite start temperature is 467 °C at 330 °C/s. Also, for cooling rates 75 °C/s and 50 °C/s at approximately the same temperature, a change in slope is observed (see in Fig. 5.11a). This indicates that the martensite starts temperature can be taken as 467 °C and is considered independent of the cooling rate.

To identify the bainite start temperature (B_s), the dilatometry data of intermediate cooling rates such as 20 °C/s, 30 °C/s and 40 °C/s are considered. The dilatometry data of intermediate cooling rates show a plateau type formation in the temperature range where transformation to ferrite and bainite is feasible. The associated micrographs further validate the presence of both ferrite and bainite in Fig. 5.10. A hit and trial method is used to estimate the bainite start temperature. Firstly, the B_s is assumed to be in a temperature range of 490 °C – 550 °C independent of the cooling rate. Thereafter, for the sampled cooling rates, the corresponding H_M, H_B, and H_F are calculated using the relationship given in Eq. (5.10). The phase fractions are calculated from the CCT diagram, assuming a trial value of B_s. Finally, the rule of mixtures is applied to predict the hardness value of a dilatometry sample. These predicted hardness values are compared to the experimentally measured hardness of the dilatometry samples. The full comparison is shown in Fig. 5.11b. Zooming at low cooling rates are shown in Fig. 5.11c. The results also imply that the B_s depends on the cooling rate. However, $B_s = 520$ °C gives the best fit for the broad range of samples. Therefore, $B_s = 520$ °C is assumed for simplicity.

5.5.3. SOLID-STATE PHASE FRACTION ESTIMATION

To calculate the phase fraction of the α phases, the average cooling rate for the critical cooling cycle is calculated between 800 °C and 300 °C. Corresponding to the average critical cooling rate, the phase fraction of the austenite is evaluated at the start temperature of the different α phases according to the CCT diagram. For example, the average cooling rate during the critical cooling cycle of the thermal history shown in Fig. 5.8b is superimposed on the CCT diagram (see Fig. 5.12) in blue. The blue line first intersects the bainite start temperature B_s, and subsequently the martensite start temperature M_s. The remaining phase fractions of austenite are calculated at start temperatures B_s and M_s through interpolation. For interpolation the *interp2* function of MATLAB is used. This interpolation function performs linear interpolation between the actual data points and returns the interpolated values at the query point. The query points in our case are the intersection points of the blue line with B_s and M_s. After calculating the phase fractions at query points, the following relation is used to calculate the phase fractions of individual phases

$$\begin{aligned} f_f &= 1 - f_A(B_s) \\ f_b &= f_A(B_s) - f_A(M_s) \\ f_m &= f_A(M_s) \end{aligned} \tag{5.11}$$

5.5.4. MARTENSITE TEMPERING

To account for the tempering of the martensite phase, the dilatometry samples containing martensite are subjected to different tempering conditions as mentioned in Section 5.2.4. Experimentally measured hardness values and the corresponding tempering ratios calculated using Eq. (5.8) are shown in Fig. 5.13.

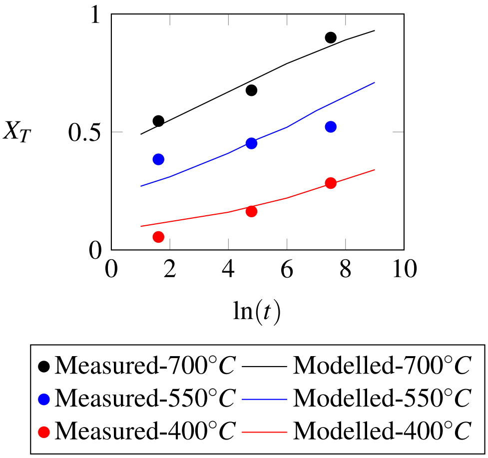

Figure 5.13: Tempering ratio vs. time obtained from experiments for selected values of tempering temperature and the corresponding predictions obtained from Eq. (5.7)

At a constant temperature, Eq. (5.7) can be curve fitted to the experimental data, and the value of D_0 and N can be estimated. For a constant value of $D_0 = 1.179 \times 10^9$ s^{-1} and $N = 0.1695$, Eq. (5.7) is also plotted in Fig. 5.13 which shows a good agreement with the experimental data. It remains to use Eq. (5.7) to predict the degree of tempering in the thermal cycles after the critical cycle. However, the diffusion-based Eq. (5.7) is only applicable for iso-thermal conditions. Therefore, the thermal cycles where tempering occurs are discretised into isothermal steps as shown in Fig. 5.14.

Finally, for tempering cycles, the tempering ratio is calculated from the differential form of Eq. (5.7), which is given as

$$\dot{X}_T = (1 - X_T) N D_0 \exp(-Q_t/RT)(\ln(1/1 - X_T))^{N/(N-1)}. \tag{5.12}$$

We apply a finite difference scheme in the time domain to solve the above differential equation. The tempering ratio at a particular time is then evaluated as follows.

$$X_T(t_{i+1}) = X_T(t_i) + (t_{i+1} - t_i)(1 - X_T(t_i)) N D_0 \exp(-Q_t/RT_i)(\ln(1/1 - X_T(t_i)))^{N/(N-1)}. \tag{5.13}$$

A constant time step of $t_{i+1} - t_i = 1 \times 10^{-6}$ s, is used. The time step for tempering calculation is chosen well below the minimum time step used for numerical thermal history evaluation, which is equivalent to 0.03 s. The tempering ratio is then scaled with the martensite's current phase fraction to predict the tempered martensite's phase fraction.

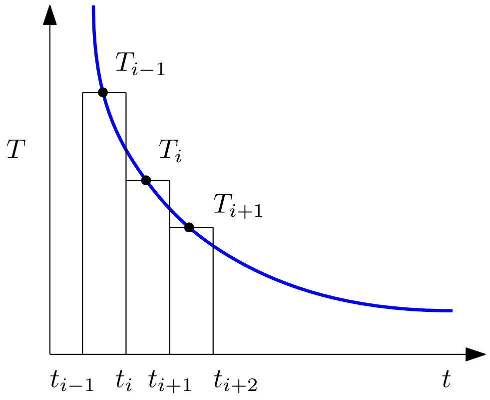

Figure 5.14: Schematic illustration of a thermal history discretised into isothermal steps.

5.5.5. SOLID STATE PHASE FRACTIONS AND TEMPERING RATIO

The phase fraction estimation was performed along the centre line of the specimens along the build direction. This location is selected to minimise the effect of power modulation at the start and stop location during printing. The predicted phase fractions of the α phases are shown in Fig. 5.15 for all three specimens.

It can be observed in Fig. 5.15 that the phase fraction of the martensite decreases as the distance from the substrate increases for all specimens. This effect is due to a reduction in the average cooling rate between the critical range of 800 °C – 300 °C ($C_{8|3}$) as the height of the specimen increases. The average cooling rate for the critical cooling cycle along the part height is shown in Fig. 5.9.

As the cooling rate decreases, the fraction of phases such as bainite and ferrite increases. The phase fraction of the tempered martensite phase also decreases with the decrease in the martensite phase. The tempering is more pronounced in the layers close to the substrate since these layers experience higher number of heating and cooling cycles than the top layers. No tempering occurs on the topmost layers as there are very few or no tempering cycles after the critical cooling cycle. At the same time, the amount of martensite is small as the cooling rates are diminished.

A comparison of the predicted phase fractions of all three samples is shown in Fig. **??** shows that the ferrite phase fraction is lower for the thin wall than others. The thin wall has more martensite phase fraction compared to other samples due to lower heat input and high cooling rates.

5.5.6. OPTICAL MICROGRAPHY

The micrographs obtained from 2nd, 10th and 20th layer are given in Fig. 5.17. The microstructure of 2nd layer is predominantly composed of martensite, even though ferrite and bainite are present in both thick and tapered samples. However, as the build height increases, the observed martensite phase fractions are lower for all three walls due to the reduction in cooling rates endured by the material. The martensite fractions are the lowest at the top layer for all three walls. A combined microstructure of ferrite, bainite

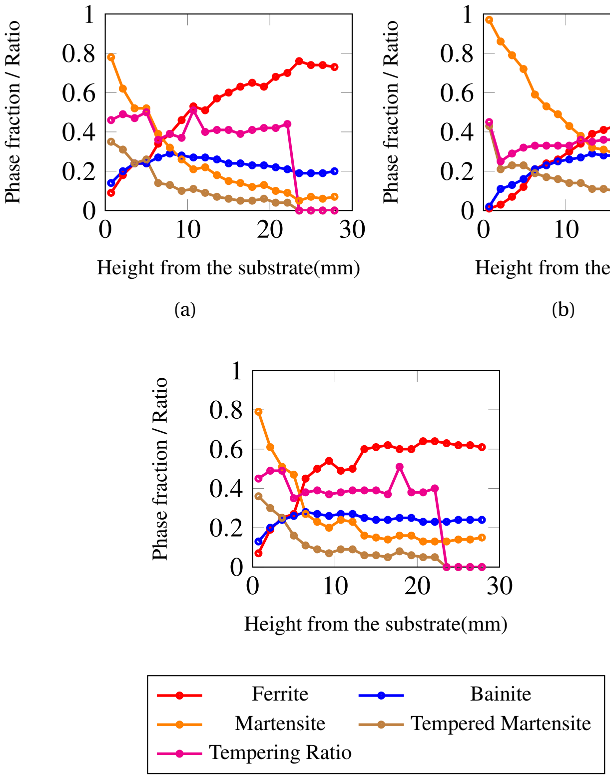

(a)

(b)

(c)

Figure 5.15: Phase fraction predictions of (a) thick (b) thin, and (c) tapered wall along the centre line of the specimens along to the build direction.

and martensite is observed at the 10th layer for all three walls. This could result from the reduced cooling rate observed in the region 10th layer. Similarly, the microstructure of the 20th layer is also comprised of a mixture of ferrite, bainite and martensite. The 20th layer only undergoes a single thermal cycle but has a lower cooling rate due to the lower thermal diffusivity caused by heat accumulation. Therefore, a relatively lower fraction of non-equilibrium phases like bainite and martensite can be observed at 20th layer than at 10th layer.

It can be observed that in Fig. 5.17h the cooling rate is 88 °C/s. This is higher than the critical cooling rate for fully martensitic transformation. Hence the micrograph from Fig. 5.17h is comparable to the micrograph from dilatomtery experiments in Fig. 5.10 corresponding to a cooling rate of 330 °C/s. The micrographs from the 2nd layer of thick and thin samples look similar to the micrographs from dilatomtery corresponding to the cooling rate of 50 °C/s. Additionally the material points from 10th and 20thlayer of the thick, thin, and tapered have undergone cooling rates between 10 °C/s and 20 °C/s. The micrographs from these material points show good comparability with micrographs

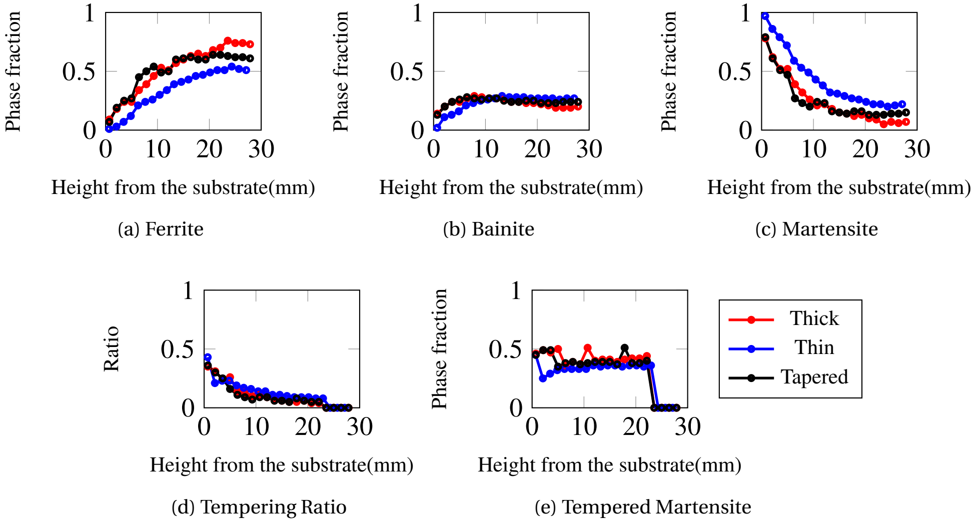

(a) Ferrite (b) Bainite (c) Martensite

(d) Tempering Ratio (e) Tempered Martensite

Figure 5.16: Comparison of predicted solid state phases fraction of (a) ferrite (b) bainite, and (c) martensite between thick, thin and tapered wall along the line in the z direction passing through the thermocouples shown in Fig. 5.3. (d) and (e) compares the tempering ratios and phase fraction of tempered martensite of three samples investigated.

from dilatometry experiments corresponding to cooling rates of 10 °C/s and 30 °C/s. Note that though Fig. 5.17c and Fig. 5.17d have similar cooling rates, the microstructures appear different. The 10th layer undergoes several thermal cycles, remelting, reaustenitization and tempering. However, the material point at 20th layer undergoes only one thermal cycle, resembling the deposition of a single bead and hence gives the microstructure devoid of tempering. The similarity of micrographs with the dilatometry images indicate good correlation of dilatometry samples and the WAAM printed samples. This points to the reliability of the CCT diagram obtained using dilatometry to the WAAM process. Additionally, the optical micrographs indicate good qualitative agreement with predicted phase fractions.

5.5.7. HARDNESS COMPARISON

First, the corresponding hardness for the predicted phase fractions will be evaluated using Eq. (5.9). Subsequently, these hardness predictions are compared with the experimentally measured hardness values as shown in Fig. 5.18.

Hardness measurements are performed at three points at the same build height to quantify the uncertainties on the measured hardness values. Each of these hardness indents was 1.5 mm apart in the x-direction. The standard deviation of three measurements is calculated and indicated as the error bars in Fig. 5.18. The measured hardness value decreases as the height of the specimen increases. This suggests a considerable martensite presence in the layers close to the substrate diminishing towards the top. Predicted hardness values also show a similar trend. Moreover, predicted hardness pro-

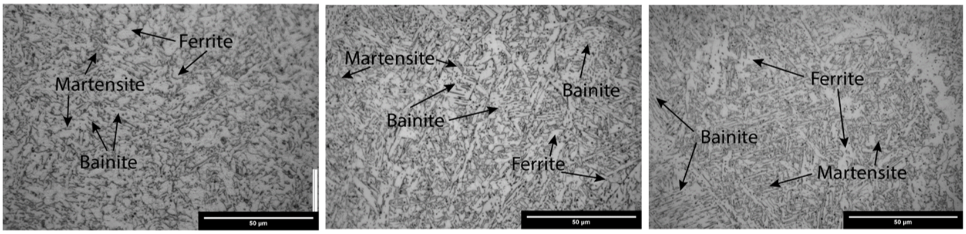

(a) Thick - $C_{8|3} = 12\,^{\circ}\mathrm{C/s}$ (b) Thin - $C_{8|3} = 23\,^{\circ}\mathrm{C/s}$ (c) Tapered - $C_{8|3} = 18\,^{\circ}\mathrm{C/s}$

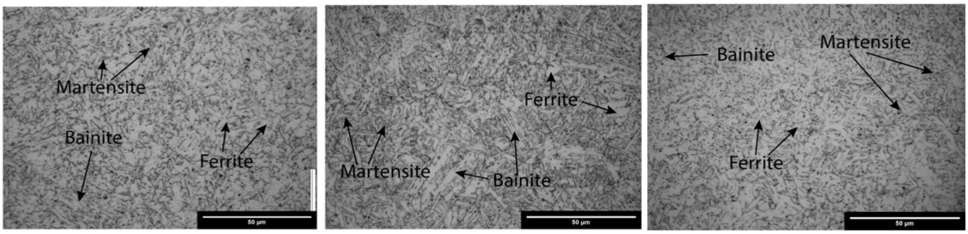

(d) Thick - $C_{8|3} = 18\,^{\circ}\mathrm{C/s}$ (e) Thin - $C_{8|3} = 29\,^{\circ}\mathrm{C/s}$ (f) Tapered - $C_{8|3} = 22\,^{\circ}\mathrm{C/s}$

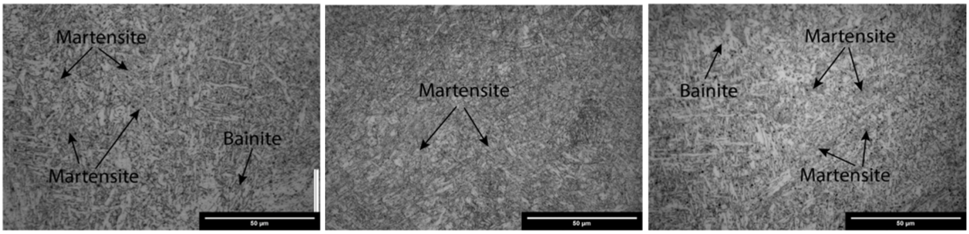

(g) Thick - $C_{8|3} = 53\,^{\circ}\mathrm{C/s}$ (h) Thin - $C_{8|3} = 88\,^{\circ}\mathrm{C/s}$ (i) Tapered - $C_{8|3} = 55\,^{\circ}\mathrm{C/s}$

Figure 5.17: Optical micrographs obtained from the AM manufactured thick, thin and tapered wall. The top, middle and the bottom row represents the 20th, 10th and 2nd layer of the printed sample, respectively. The corresponding calculated critical cooling rates are also given.

files accounting for the tempering show that the effect of tempering is more significant and the degree of tempering is more pronounced in the layers close to the substrate than at the topmost layers as anticipated.

The hardness predictions are in good agreement with the measurements for the layers close to the substrate. Recall that the value of hardness is less sensitive to the high cooling rates as shown in Fig. 5.11b. The predicted cooling rates for the critical cooling cycles for layers close to the substrate are $> 75\,^{\circ}\mathrm{C/s}$ as can be seen in Fig. 5.9. This will result in a complete phase transformation from austenite to martensite. Therefore, the predicted hardness is reasonably accurate for layers close to the substrate. Cooling rates become moderate or low for the layers away from the substrate, as shown in Fig. 5.9. The cooling rates of the critical cooling cycle as predicted by the thermal model, are higher than those observed from thermocouples. Though lack of data points at peaks limits this comparison. Lower cooling rates would promote more ferrite content and a reduc-

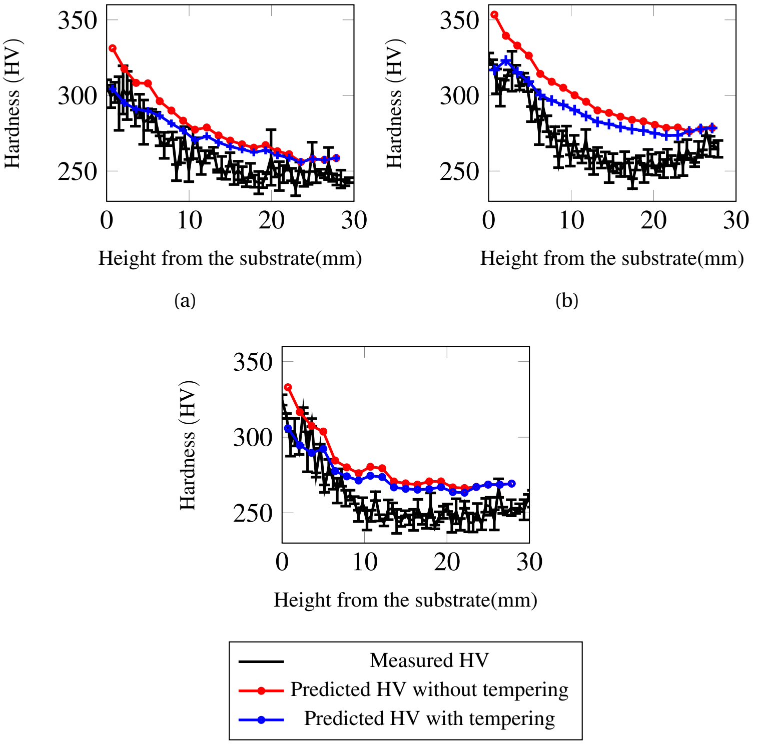

(a) (b)

(c)

Figure 5.18: Hardness comparison of the (a) thick (b) thin, and (c) tapered walls.

tion in hardness. A possible source of error is the constant Ac_3 temperature assumption in our model. In reality, the Ac_3 temperature depends on the heating rates (FG et al., 2003). Depending on the heating rate, the Ac_3 temperature can change. Based on the Ac_3 temperature and peak temperature, the critical cooling cycle might shift, impacting the cooling rates and, consequently, the hardness. The critical cooling cycle for the heating rate dependent cases will be the last cooling cycle with peak temperature exceeding Ac_3 corresponding to the heating rate. Furthermore, the uncertainties in the experimental measurements, such as the dilatometry measurements used in the construction of the CCT diagram, start temperature of various α phases, errors associated with the empirical model for hardness predictions and uncertainties in capturing tempering kinetics also contribute to the mismatch between the predicted and measured hardness values.

The comparison of the hardness of all three samples is shown in Fig. 5.19. The experimental results show that the hardness of the thin specimen is slightly higher than the thick and tapered samples. This can be attributed to the high cooling rates observed in the thin sample due to lower heat input. Comparing the thick and tapered wall shows that the hardness is comparable in the layers close to the substrate. However, top layers of the tapered sample, exhibit a slightly higher hardness than top layers of the thick sample due to a slightly higher cooling rate due to tapering. The comparison of all the samples shows no significant variation in the hardness values due to changes in the process parameters and design.

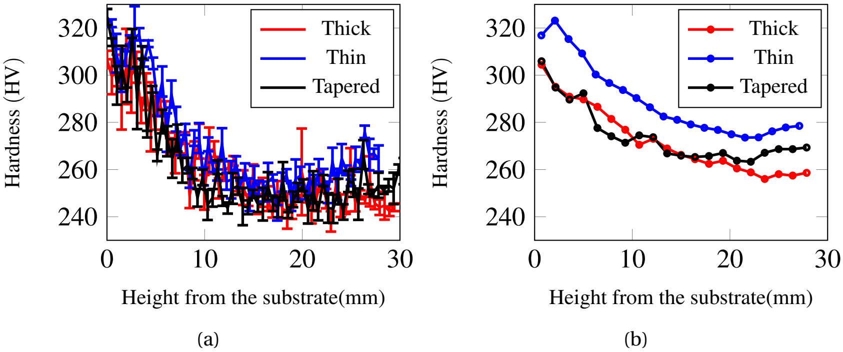

(a)

(b)

Figure 5.19: Comparison of (a) experimental and (b) predicted hardness values of thick, thin and tapered samples.

5.6. CONCLUSIONS

In this study, the correlation between the experimentally validated transient thermal history experienced by the WAAM manufactured HSLA *ER110S-G* steel part is used to predict the composition of resultant solid-state phases and the corresponding hardness response. Following are some salient points of this study:

- The superimposition of the thermal history measured from the thermocouples to the thermal history obtained from the FE modelling shows good agreement for all three wall specimens. The actual cooling rates calculated from the thermocouple data are 25 – 50% lower than the predicted cooling rates.

- Multiple thermal heating and cooling cycles are experienced by WAAM manufactured parts. The thermal cycles for a material point can be divided into three zones. First is the reset zone, in which the peak temperature of cycles are well above the Ac_3 temperature. Consequently, the microstructure resets to the parent austenite phase in this region. The second zone consists of the critical cycle. The critical cycle is the cooling part of the last thermal cycle with a peak temperature higher than the Ac_3 temperature. The solid phase transformation from the parent austenite phase to child phases such as ferrite, bainite and martensite happens due to this critical cycle. The third zone is the tempering zone in which the martensite transforms into tempered martensite.

- The predicted fractions of the solid-state phases in the microstructure depend on the cooling rate of the critical cooling cycle. High cooling rates result in microstructure with a high fraction of martensite phase and low cooling rates result in bainite and ferrite-dominated microstructures. This is validated through the superimposition of the predicted microhardness and measured microhardness of the AM samples. The results show that predicted hardness are in the acceptable limit for regions with high cooling rates. The predicted hardness is 10% higher than the measured hardness which is attributed to the over-prediction of the cooling rates.

- The effect of tempering is significant in the regions where the martensite content is dominant and the regions experience more tempering cycles. The tempering contributed to reduce the microhardness by 8 – 10% in the regions with high martensite percentage.

- Comparison of the AM samples with approximately similar critical cooling rates in the temperature range of 800 °C-300 °C show similar microstructural features. The microstructural features of AM samples are also similar to dilatometry samples which are subjected to constant cooling rates from the austenitization temperature.

- Comparing the hardness of all specimens shows that at the investigated location the effect of the process parameters and design are not significant. This can be attributed to the lack of a significant effect on the cooling rates of the critical cycle.

- In addition, the developed model is very general and applicable across different materials given, the thermal properties of the material and the CCT diagram are available.

BIBLIOGRAPHY

Aldalur, E., Veiga, F., Suárez, A., Bilbao, J., & Lamikiz, A. (2020). High deposition wire arc additive manufacturing of mild steel: Strategies and heat input effect on microstructure and mechanical properties. *Journal of Manufacturing Processes*, *58*, 615–626.

Ayed, A., Valencia, A., Bras, G., Bernard, H., Michaud, P., Balcaen, Y., & Alexis, J. (2020). Effects of waam process parameters on metallurgical and mechanical properties of ti-6al-4v deposits. *Advances in materials, mechanics and manufacturing* (pp. 26–35). Springer.

Bendsoe, M. P., & Sigmund, O. (2013). *Topology optimization: Theory, methods, and applications*. Springer Science & Business Media.

Bhadeshia, H., & Honeycombe, R. (2017). *Steels: Microstructure and properties*. Butterworth-Heinemann.

Callister Jr, W. D., & Rethwisch, D. G. (2020). *Callister's materials science and engineering*. John Wiley & Sons.

DebRoy, T., Wei, H., Zuback, J., Mukherjee, T., Elmer, J., Milewski, J., Beese, A. M., Wilson-Heid, A. d., De, A., & Zhang, W. (2018). Additive manufacturing of metallic components–process, structure and properties. *Progress in Materials Science*, *92*, 112–224.

Ding, D., Pan, Z., Cuiuri, D., & Li, H. (2015). A practical path planning methodology for wire and arc additive manufacturing of thin-walled structures. *Robotics and Computer-Integrated Manufacturing*, *34*, 8–19.

Ding, J., Colegrove, P., Mehnen, J., Williams, S., Wang, F., & Almeida, P. S. (2014). A computationally efficient finite element model of wire and arc additive manufacture. *The International Journal of Advanced Manufacturing Technology*, *70*(1-4), 227–236.

Ding, J., Martina, F., & Williams, S. (2015). Production of large metallic components by additive manufacture–issues and achievements. *Conf. Pap., nov.*

Dirisu, P., Ganguly, S., Mehmanparast, A., Martina, F., & Williams, S. (2019). Analysis of fracture toughness properties of wire+ arc additive manufactured high strength low alloy structural steel components. *Materials Science and Engineering: A*, *765*, 138285.

Doane, D. V. (1979). Application of hardenability concepts in heat treatment of steel. *Journal of Heat Treating*, *1*(1), 5–30.

Duarte, V. R., Rodrigues, T. A., Schell, N., Santos, T. G., Oliveira, J. P., & Miranda, R. M. (2021). Wire and arc additive manufacturing of high-strength low-alloy steel: Microstructure and mechanical properties. *Advanced Engineering Materials*, 2001036.

DuPont, J., Marder, A. et al. (1995). Thermal efficiency of arc welding processes. *Welding Journal-Including Welding Research Supplement*, *74*(12), 406s.

Elahi, S., Tavakoli, R., Romero, I., & Tourret, D. (2023). Grain growth competition during melt pool solidification—comparing phase-field and cellular automaton models. *Computational Materials Science*, *216*, 111882.

FG, C., Capdevila, C., & De Andres, C. G. (2003). An attempt to establish the variables that most directly influence the austenite formation process in steels. *ISIJ international*, *43*(5), 726–735.

Foster, B., Beese, A., Keist, J., McHale, E., & Palmer, T. (2017). Impact of interlayer dwell time on microstructure and mechanical properties of nickel and titanium alloys. *Metallurgical and Materials Transactions A*, *48*(9), 4411–4422.

Gao, H. (2018). *Residual stress development due to high-frequency post weld impact treatments for high-strength steels* (Doctoral dissertation). Delft University of Technology.

Goldak, J., Chakravarti, A., & Bibby, M. (1984). A new finite element model for welding heat sources. *Metallurgical transactions B*, *15*(2), 299–305.

Gornyakov, V., Sun, Y., Ding, J., & Williams, S. (2021). Efficient determination and evaluation of steady-state thermal–mechanical variables generated by wire arc additive manufacturing and high pressure rolling. *Modelling and Simulation in Materials Science and Engineering*, *30*(1), 014001.

Haden, C., Zeng, G., Carter III, F., Ruhl, C., Krick, B., & Harlow, D. (2017). Wire and arc additive manufactured steel: Tensile and wear properties. *Additive manufacturing*, *16*, 115–123.

Hejripour, F., Binesh, F., Hebel, M., & Aidun, D. K. (2019). Thermal modeling and characterization of wire arc additive manufactured duplex stainless steel. *Journal of Materials Processing Technology*, *272*, 58–71.

Huang, C., Kyvelou, P., Zhang, R., Britton, T. B., & Gardner, L. (2022). Mechanical testing and microstructural analysis of wire arc additively manufactured steels. *Materials & Design*, *216*, 110544.

Hughes, T. J., & Liu, W. (1978). Implicit-explicit finite elements in transient analysis: Stability theory.

Knezović, N., & Topić, A. (2018). Wire and arc additive manufacturing (waam)–a new advance in manufacturing. *International Conference "New Technologies, Development and Applications"*, 65–71.

Kuo-hao WU. (2020). *3D Additive Manufacturing: Microstructural Evolution of HSLA Steel in WAAM process* (tech. rep.). http://repository.tudelft.nl/.

Lian, Y., Lin, S., Yan, W., Liu, W. K., & Wagner, G. J. (2018). A parallelized three-dimensional cellular automaton model for grain growth during additive manufacturing. *Computational Mechanics*, *61*(5), 543–558.

Liu, J., Gaynor, A. T., Chen, S., Kang, Z., Suresh, K., Takezawa, A., Li, L., Kato, J., Tang, J., Wang, C. C., et al. (2018). Current and future trends in topology optimization for additive manufacturing. *Structural and Multidisciplinary Optimization*, *57*(6), 2457–2483.

McAndrew, A. R., Rosales, M. A., Colegrove, P. A., Hönnige, J. R., Ho, A., Fayolle, R., Eyitayo, K., Stan, I., Sukrongpang, P., Crochemore, A., et al. (2018). Interpass rolling of ti-6al-4v wire+ arc additively manufactured features for microstructural refinement. *Additive Manufacturing*, *21*, 340–349.

Mehnen, J., Ding, J., Lockett, H., & Kazanas, P. (2014). Design study for wire and arc additive manufacture. *International Journal of Product Development 20*, *19*(1-3), 2–20.

Mishra, V., Ayas, C., Langelaar, M., & van Keulen, F. (2022). Controlling cooling rates through topology optimization for required microstructure in additive manufacturing process. *2022 ASPE and euspen Summer Topical Meeting on Advancing Precision in Additive Manufacturing*, 8–12.

Moyer, J., & Ansell, G. (1975). The volume expansion accompanying the martensite transformation in iron-carbon alloys. *Metallurgical Transactions A*, *6*(9), 1785–1791.

Müller, J., Hensel, J., & Dilger, K. (2022). Mechanical properties of wire and arc additively manufactured high-strength steel structures. *Welding in the World*, *66*(3), 395–407.

Rauch, M., Hascoet, J.-Y., & Querard, V. (2021). A multiaxis tool path generation approach for thin wall structures made with waam. *Journal of Manufacturing and Materials Processing*, *5*(4), 128.

Rocha, P. C. J., Rodrigues, M. B., Pereira, M., Galeazzi, D., et al. (2020). Analysis of interlayer idle time as a temperature control technique in additive manufacturing of thick walls by means of cmt and cmt pulse welding processes. *Soldagem & Inspeção*, *25*.

Rodgers, T. M., Madison, J. D., & Tikare, V. (2017). Simulation of metal additive manufacturing microstructures using kinetic monte carlo. *Computational Materials Science*, *135*, 78–89.

Rodideal, N., Machado, C. M., Infante, V., Braga, D. F., Santos, T. G., & Vidal, C. (2022). Mechanical characterization and fatigue assessment of wire and arc additively manufactured hsla steel parts. *International Journal of Fatigue*, *164*, 107146.

Rodrigues, T. A., Duarte, V., Avila, J. A., Santos, T. G., Miranda, R., & Oliveira, J. (2019). Wire and arc additive manufacturing of hsla steel: Effect of thermal cycles on microstructure and mechanical properties. *Additive Manufacturing*, *27*, 440–450.

Song, G.-H., Lee, C.-M., & Kim, D.-H. (2021). Investigation of path planning to reduce height errors of intersection parts in wire-arc additive manufacturing. *Materials*, *14*(21), 6477.

Su, C., Chen, X., Gao, C., & Wang, Y. (2019). Effect of heat input on microstructure and mechanical properties of al-mg alloys fabricated by waam. *Applied Surface Science*, *486*, 431–440.

Suh, D.-W., Oh, C.-S., Han, H. N., & Kim, S.-J. (2007). Dilatometric analysis of austenite decomposition considering the effect of non-isotropic volume change. *Acta materialia*, *55*(8), 2659–2669.

Sun, L., Jiang, F., Huang, R., Yuan, D., Guo, C., & Wang, J. (2020). Anisotropic mechanical properties and deformation behavior of low-carbon high-strength steel component fabricated by wire and arc additive manufacturing. *Materials Science and Engineering: A*, *787*, 139514.

Sun, Y., Obasi, G., Hamelin, C., Vasileiou, A., Flint, T., Francis, J., & Smith, M. (2019). Characterisation and modelling of tempering during multi-pass welding. *Journal of Materials Processing Technology*, *270*, 118–131.

Teferra, K., & Rowenhorst, D. J. (2021). Optimizing the cellular automata finite element model for additive manufacturing to simulate large microstructures. *Acta Materialia*, *213*, 116930.

Thompson, S. et al. (1996). Continuous cooling transformation behavior in hsla80 steel. *Metallurgical and Materials Transactions*, *27*(6), 1557–1571.

van Nuland, T. F., van Dommelen, J., & Geers, M. G. (2021). Microstructural modeling of anisotropic plasticity in large scale additively manufactured 316l stainless steel. *Mechanics of Materials*, *153*, 103664.

Venturini, G., Montevecchi, F., Bandini, F., Scippa, A., & Campatelli, G. (2018). Feature based three axes computer aided manufacturing software for wire arc additive manufacturing dedicated to thin walled components. *Additive Manufacturing*, *22*, 643–657.

Venturini, G., Montevecchi, F., Scippa, A., & Campatelli, G. (2016). Optimization of waam deposition patterns for t-crossing features. *Procedia Cirp*, *55*, 95–100.

Wang, L., Xue, J., & Wang, Q. (2019). Correlation between arc mode, microstructure, and mechanical properties during wire arc additive manufacturing of 316l stainless steel. *Materials Science and Engineering: A*, *751*, 183–190.

Wu, B., Pan, Z., Ding, D., Cuiuri, D., & Li, H. (2018). Effects of heat accumulation on microstructure and mechanical properties of ti6al4v alloy deposited by wire arc additive manufacturing. *Additive Manufacturing*, *23*, 151–160.

Wu, B., Pan, Z., Ding, D., Cuiuri, D., Li, H., Xu, J., & Norrish, J. (2018). A review of the wire arc additive manufacturing of metals: Properties, defects and quality improvement. *Journal of Manufacturing Processes*, *35*, 127–139.

Xin, H., Correia, J. A., Veljkovic, M., Zhang, Y., Berto, F., & de Jesus, A. M. (2021). Probabilistic strain-fatigue life performance based on stochastic analysis of structural and waam-stainless steels. *Engineering Failure Analysis*, 105495.

Yang, M., Wang, L., & Yan, W. (2021). Phase-field modeling of grain evolutions in additive manufacturing from nucleation, growth, to coarsening. *Npj Computational Materials*, *7*(1), 1–12.

Yang, Y., Zhou, X., Li, Q., & Ayas, C. (2021). A computationally efficient thermo-mechanical model for wire arc additive manufacturing. *Additive Manufacturing*, 102090.

Yildiz, A. S., Davut, K., Koc, B., & Yilmaz, O. (2020). Wire arc additive manufacturing of high-strength low alloy steels: Study of process parameters and their influence on the bead geometry and mechanical characteristics. *The International Journal of Advanced Manufacturing Technology*, *108*(11), 3391–3404.

Zhang, Q., Xie, J., Gao, Z., London, T., Griffiths, D., & Oancea, V. (2019). A metallurgical phase transformation framework applied to slm additive manufacturing processes. *Materials & Design*, *166*, 107618.

6

DESIGN FOR MATERIAL PROPERTIES OF ADDITIVELY MANUFACTURED METALS USING TOPOLOGY OPTIMIZATION

In metal Additive Manufacturing (AM), the deposited material is subjected to a series of heating and cooling cycles. The locally occurring temperature extremes and cooling rates determine solid-state phase fractions, material microstructure, texture, and ultimately the local material properties. As the shape of a part determines the local thermal history during AM, this offers an opportunity to influence these material properties through design. In this paper, we present a way to obtain desired properties by controlling the local thermal history. This is achieved through topology optimization of the printed part while considering its entire transient thermal history. As an example of this approach, this work focuses on high strength low alloy steels, where resulting phase fractions significantly influence mechanical properties such as yield strength and ductility. These solid-state phase fractions depend on cooling rates in a particular critical temperature range. The phase composition and hence the local yield strength in target regions can be controlled by constraining the cooling time in this range. Numerical examples illustrate the capability of the proposed approach in adapting part designs to achieve various desired material properties.

6.1. INTRODUCTION

Metal Additive Manufacturing (AM) processes encompass a wide range of technologies in which the part is manufactured through sequential addition of the molten material, generally in a layer-by-layer manner, with the help of a heat source. Currently, functional metal parts with dimensions ranging from millimeters to several meters can be realized through various metal AM processes from various alloys such as Titanium alloys, Nickel based alloys, Aluminum alloys, and steels (DebRoy et al., 2018). For example, small parts with intricate details can be realized by Laser Powder Bed fusion (LPBF) processes. In contrast, Large-scale parts with dimensions of a few meters can be manufactured by Direct Energy Deposition (DED) processes such as Wire and Arc Additive Manufacturing (WAAM).

The main advantage of AM technologies is that geometrically complex shapes can be realized which is not feasible with conventional manufacturing technologies such as milling and casting. To exploit this form freedom, Topology Optimization (TO) is often used in conjunction with AM. TO is a computational design tool through which the optimal geometric layout of a part is obtained to enhance parts specific performance. The designs obtained by TO tend to be geometrically complex and thus can often only be realized by AM (Liu et al., 2018).

The mechanical properties of a part depend on the microstructure development during the manufacturing process. In addition to this, the microstructure development is related to the thermal history experienced by the part during the process. The microstructure of metal has multiple aspects such as grain size, grain morphology, crystallographic texture, and types and phase fractions of solid-state phases. Once the molten metal is deposited, the thermal gradients and solidification rates in the melt zone determine the grain size and morphology (Kou, 2003). In addition, the crystallographic texture also depends on maximum heat flow directions and crystallographic texture of the already deposited material (DebRoy et al., 2018). These phenomena primarily depend on process parameters such as the power input, travel speed of the heat source, and layer thickness. The type of solid-state phase transformations depends on the cooling rate experienced by the material after the solidification of the metal in a critical temperature range (Callister Jr and Rethwisch, 2020). For example, in HSLA steels, the critical temperature range from 800° to 500°C, determines the phase fraction of solid-state phases (Dornelas et al., 2020; Reisgen et al., 2020; Rodrigues et al., 2019). Similarly, Nickel-based (Tian et al., 2014) and Titanium-based (Kelly and Kampe, 2004; Xu et al., 2015) alloys also exhibit various solid-state phase transformations depend on cooling rates.

The right combination of phase fractions is essential for the mechanical performance of the produced parts. In HSLA steels when cooling rate in the critical temperature range is low, the microstructure is dominated by phases with high ductility and low strength and vice versa. In the AM process, the thermal history experienced by a material region can be influenced by the local design features around that region. This also opens up the possibility to control the cooling rates in a material region or, an alternate representation of cooling rates, cooling time in the critical temperature range. Consequently, solid-state phase fractions can be controlled in a material region through appropriate design changes. In this paper, we consider the situation that AM process parameters are fixed and cannot be manipulated by the user. This implies for AM, a relation holds between the design, thermal history, and resultant yield strength distribution. In this work, this relation is used to locally obtain desired material properties from AM process through TO.

The solid-state phase fractions are dictated by the thermal history that can be predicted with an AM process simulation. Only a few studies have considered transient thermal simulation within TO. However, none of these studies can control the solid-state phase fractions. For instance, maximum temperature minimization over time has been investigated in (Wu et al., 2019). Moreover, to facilitate heat transfer in the AM process, transient thermal compliance is minimized (Wu et al., 2021). Our aim in this paper is to present a novel TO methodology to control the cooling time in local design regions. Consequently, we will be able to generate the part design to obtain a desired mechanical property distribution for the first time through computational design.

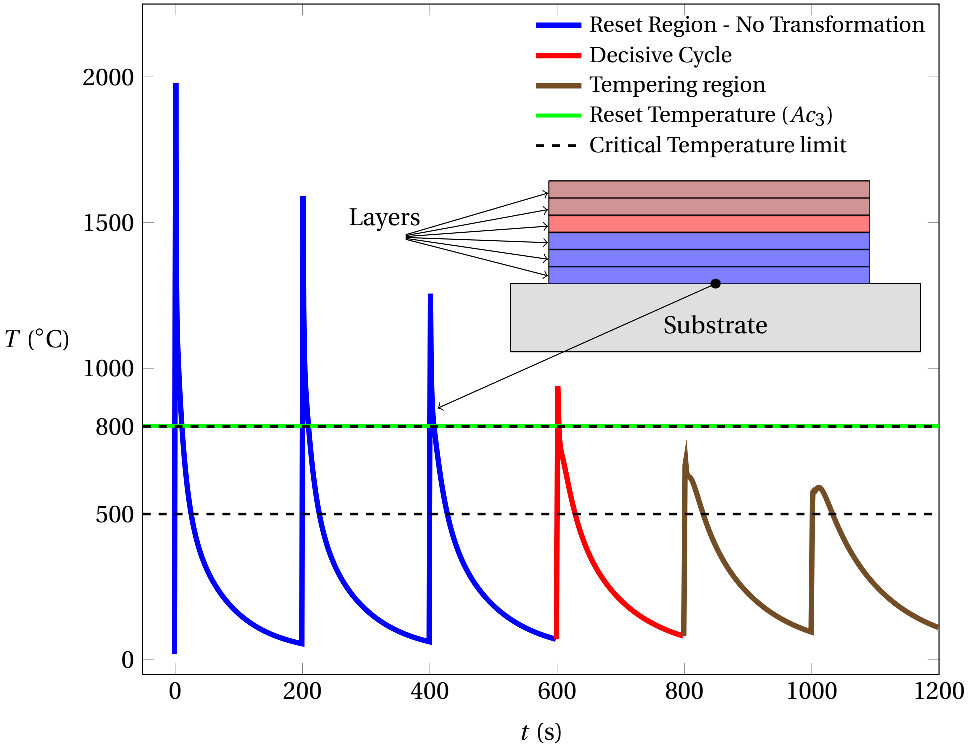

Figure 6.1: The complete thermal history experienced by a material point during deposition of the layers in a layer-by-layer manner in an Additive Manufacturing process. The colors of the transient thermal history correspond to the color of the deposited layer.

It remains to establish the relation between the thermal history of a material point and the microstructure development. Due to the sequential deposition of layers in AM process, deposited material experiences multiple heating and cooling cycles as shown in Fig. 6.1. The first heating and cooling cycle corresponds to its own deposition with a peak temperature above the melting point, which is approximately 1500°C for steels. The subsequent cycles are due to the deposition of successive layers on the pre-deposited material. The peak temperatures observed in these subsequent cycles gradually decrease but can still be substantially high. During cooling in a material-specific critical temperature range, the parent solid-state phase transforms into child phases, e.g., in HSLA steels the austenite phase transforms into ferrite, bainite, and martensite (Callister Jr and Rethwisch, 2020). The subsequent heating cycle and the corresponding peak temperature determine whether these child phases transform back to the parent austenite phase. In steels, the critical Ac_3 temperature is the temperature above which all child phases transform back to the parent phase completely (Gavard et al., 1996; Huang et al., 2022; Mishra et al., 2023). This critical temperature is hence termed the reset temperature in the remainder and is indicated in Fig. 6.1. Consequently, the complete thermal history of a material point can be divided into three parts (Mishra et al., 2023). The first part is the reset region where the parent phase transforms into the child phases but then the child phases completely transform back into the parent phase during the subsequent heating. After the reset region, comes the decisive cycle in which the parent phase transforms to the child solid-state phases for the last time. The time spent by the material during cooling, in the critical temperature range for the decisive cycle determines the solid-state child phase fractions. Controlling this particular cooling rate through design changes would allow us to control the solid-state phase transformations, and therefore an important aspect of the metal microstructure, during the AM process. The thermal cycles after the decisive cooling cycle are the tempering cycles when the martensite phase if present, transforms to tempered martensite (Callister Jr and Rethwisch, 2020). The effect of tempering is currently excluded from this study for simplicity since this is a second-order effect but the methodology developed can be extended to account for the tempering effects.

To evaluate the thermal history during AM, we consider a simplified, finite element-based process model to reduce the computational cost to a level that allows its integration into the TO process. Consequently, material properties are idealized as temperature-independent. Moreover, the material addition is considered in a layer-by-layer manner. This implies the finite elements associated with the deposited material are activated in a sequential manner in time. In line with the material deposition heat is added to the entire layer is heated simultaneously for a particular period and thereafter the part is allowed to cool. Melting and solidification of the metal are not included because during these phenomena temperature remains unchanged and the energy absorption during melting is balanced by energy dissipation during solidification (Ranjan et al., 2020). Moreover, convective/radiative heat transfer through the part is neglected because conduction remains the dominant mode of the heat transfer method in AM processes (Paul et al., 2014). By employing these simplifications we sacrifice the resolution related to the movement of the heat source, but achieve large gains in computational efficiency with limited loss of accuracy (Ranjan et al., 2020). Even with these simplifications, performing a topology optimization including a transient AM process simulation remains a computationally demanding task. For this reason, 3D examples are presently not feasible in our implementation, and instead 2D numerical examples are studied. As a means to study the effectiveness of the method, these are nevertheless deemed adequate. In our numerical examples, we consider a WAAM process but the methodology remains valid for other metal AM processes such as laser powder bed fusion.

A density-based TO framework is used for the design optimization (Bendsoe and Sigmund, 2013). The design is evaluated by solving the compliance minimization problem described in Section 6.2. We consider the AM of the compliance-minimized design. The thermal history of the compliance minimized design is evaluated by the simplified AM process model, detailed in Section 6.3. The relation between the cooling time and the resultant yield strength (σ_y) is also given in Section 6.3. We employ gradient-based optimization, which requires the sensitivities of the cooling time in the critical temperature range with respect to design variables. Therefore, the evaluation of the cooling time spent in the critical temperature range is formulated in a continuous manner. This is done by applying combinations of smooth Heaviside functions, details of which are given in Section 6.4. Moreover, as discussed earlier, during the AM process the decisive cycle dictates the resulting solid-state phase of a material point. To account for this, weights are associated with each heating and cooling cycle. The weight is substantial for the decisive cycle whereas negligible for other cycles. The weighting functions used to emphasize the decisive cycle are detailed in Section 6.4 together with the novel optimization problem considered in this work. As discussed previously that the computational cost to include complete thermal history in TO is very high. In Section 6.5 the computational cost to evaluate the thermal history of a 2D TO design is given. Moreover, Optimized designs obtained by various 2D numerical examples are also presented in Section 6.5. The conclusions drawn from this study and directions for future work are outlined in Section 6.6.

6.2. MINIMUM COMPLIANCE TO PROBLEM

We first introduce a common TO problem, i.e, compliance minimization. The problem description is as follows:

$$\min_{\boldsymbol{\rho}} \quad c = \frac{1}{2}\sum_{\Omega_M} \mathbf{u}_e^{\mathrm{T}}\mathbf{k}_e(\rho_e)\mathbf{u}_e, \tag{6.1}$$

$$\text{s.t.} \quad \mathbb{K}\mathbf{u} = \mathbf{f}. \tag{6.2}$$

$$V(\boldsymbol{\rho}) \leq V_0. \tag{6.3}$$

$$0 \leq \rho_e \leq 1, \quad \forall e \in \Omega_M. \tag{6.4}$$

Here, c is the compliance of the structure in the design domain Ω_M discretized with a structured mesh comprising bilinear finite elements. The array of design variables ρ_e, where $e = 1,\ldots M$ denotes the element number for a total of M elements, is represented by $\boldsymbol{\rho}$. Nodal displacement degrees of freedom and the stiffness matrix of a finite element are represented by $\mathbf{u}_e$ and $\mathbf{k}_e$, respectively. Element stiffness matrices depend on the design variable ρ_e through the commonly used modified SIMP interpolation (Bendsoe and Sigmund, 2013) scheme:

$$E_e(\tilde{\rho}_e) = E_{\min} + \tilde{\rho}_e^{\,p}(E_0 - E_{\min}). \tag{6.5}$$

Here, Young's Modulus of the void and material is given by $E_{\min}$ and E_0, respectively. Young's Modulus is penalized with penalization exponent $p = 3$. E_e is Young's Modulus of an element e with filtered design variable $\tilde{\rho}_e$. Filtering is applied to density variables $\boldsymbol{\rho}$ to avoid the formation of checkerboard patterns in the design layout and to ensure a minimum feature size in the optimized structure. Filtered densities are given as follows:

$$\tilde{\rho}_e = \frac{\sum_{i \in \Omega_e^{\min}} w_i(\mathbf{x}_i) v_i \rho_i}{\sum_{i \in \Omega_e^{\min}} w_i(\mathbf{x}_i) v_i}, \tag{6.6}$$

$$w_i(\mathbf{x}_i) = r_{\min} - ||\mathbf{x}_i - \mathbf{x}_e||. \tag{6.7}$$

Eq. (6.6) defines the density filter applied to the design variable ρ_e at position $\mathbf{x}_e$ with element volume v_i (Bruns and Tortorelli, 2001). Eq. (6.7) represents the weight (w_i) associated with the element i at $\mathbf{x}_i$ for the density filter. $\Omega_e^{\min}$ is the circular region with a radius $r_{\min}$ in which the filter is effective. $\mathbb{K}$, $\mathbf{u}$, and $\mathbf{f}$ are the global stiffness matrix, nodal degrees of freedom, and nodal loads, respectively. Eq. (6.3) represents the constraint on material volume $V(\rho)$. The allowed material volume in the design domain is V_0. Eq. (6.4) represents the bounds on the design variables. The gradient-based optimization algorithm Method of Moving Asymptotes (MMA) (Svanberg, 1987) is used.

As a test problem, a cantilever loadcase is considered. The loading and boundary conditions of the cantilever problem and the optimal design are given in Fig. 6.2. The material constants and parameters used for optimization are given in Table 6.1.

Table 6.1: Default Parameters for the optimization

Modelling and Material Properties		Optimization parameters	
Element size	1 mm × 1 mm	p	3
Element Type	Plane stress Q4	Move limit	0.2
E_0	210 GPa	V_0	$0.6\ \Omega_M$
$E_{\min}$	$10^{-9} E_0$	Initial state	$\rho_e = 0.6\ \forall e \in \Omega_M$
Poisson's ratio (ν)	0.3	Stopping crit.	$\lvert\lvert\Delta\boldsymbol{\rho}\rvert\rvert_\infty \leq 0.01$
Domain thickness	1 mm	$r_{\min}$	2.5 mm
Thermal Properties			
κ_0	45 W/m°C	$\kappa_{\min}$	$10^{-9}\kappa_0$
c_{p_0}	496 J/kg°C	$c_{p_{\min}}$	$10^{-3} c_{p_0}$
ρ_m	7800 kg/m^3		

6.3. AM PROCESS MODEL AND PROCESS DEPENDENT PROPERTIES

6.3.1. SIMPLIFIED PROCESS MODEL

To simulate the AM of the compliance-optimized design, we first fix the building direction. Based on the build direction, the complete design is discretized to L layers which are sequentially deposited in a total time of τ. A layer is represented by l_i, where $i = 1, \ldots L$. Layer l_i is deposited, as shown in Fig. 6.3, in a process interval $(\tau_{l_{i-1}}, \tau_{l_i})$ at once[1].

---

[1] Note that manufacturing of a design through AM is considered even though the design has problematic overhanging features. Our main focus is to control local thermal history through design optimization. For con-

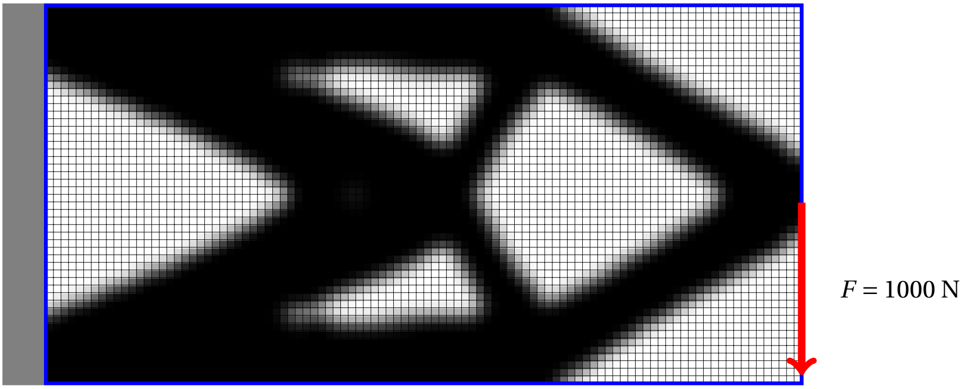

Figure 6.2: Cantilever Beam Problem: The blue rectangular domain (50 mm × 100 mm) is the design domain, discretized with a structured mesh of bilinear quad elements. The displacements at the left boundary of the domain are fixed and a point load is applied indicated with a red arrow. The dark layout is the design obtained from compliance minimization.

Recall that, to every deposited layer, a heat load is applied for a specific period of time, and then the layer is allowed to cool. The amount of heat added to the deposited layer is determined by the process parameters of the AM process. In WAAM, metal wire is melted with an electric arc and deposited. The geometry of the electric arc depends on the wire feed rate and travel speed of the arc. The material point is heated for the time period the electric arc requires to traverse itself. This is the duration, $\Delta\tau^{\mathfrak{h}}$, the heat load is applied to a newly deposited layer in the simplified process model. The duration $\Delta\tau^{\mathfrak{h}}$ is calculated by the ratio of the electric arc length in the deposition direction to travel speed of the electric arc. These parameters are chosen from literature (Mishra et al., 2023). The length of the electric arc in the deposition direction is 12.9 mm and the travel speed of the electric arc is 8 mm. Since the heating time $\Delta\tau^{\mathfrak{h}}$ is kept constant for all the layers, layer l_i, is heated from $\tau_{l_{i-1}}$ to $\tau^{\mathfrak{h}}_{l_i}$, where $\tau^{\mathfrak{h}}_{l_i} - \tau_{l_{i-1}} = \Delta\tau^{\mathfrak{h}}$ and thereafter allowed to cool from $\tau^{\mathfrak{h}}_{l_i}$ to τ_{l_i}.

The following transient heat conduction equation:

$$\mathbf{C}_{l_i}(\boldsymbol{\rho})\dot{\mathbf{T}}_{l_i} + \mathbf{K}_{l_i}(\boldsymbol{\rho})\mathbf{T}_{l_i} = \mathbf{Q}_{l_i}(\boldsymbol{\rho}), \qquad \text{if,} \quad \tau_{l_{i-1}} \le t \le \tau_{l_i}, \tag{6.8}$$

$$\mathbf{T}_{l_i} = \mathbf{T}_0, \qquad \text{at,} \quad t = \tau_{l_{i-1}}, \tag{6.9}$$

is then solved to evaluate the thermal history after the deposition of layer l_i. Here, $\mathbf{C}_{l_i}$ and $\mathbf{K}_{l_i}$ are the heat capacity matrix and thermal conductivity matrix after the deposition of layer l_i, respectively. $\mathbf{T}_0$ is the array of ambient temperatures at which the deposition process starts. $\mathbf{T}_{l_i}$ is the array of nodal temperatures and $\dot{\mathbf{T}}_{l_i}$ is its time derivative. The

---

trolling overhangs in a design several other methods are already present in literature (Gaynor and Guest, 2016; Langelaar, 2017; van de Ven et al., 2018; Zhang et al., 2019).

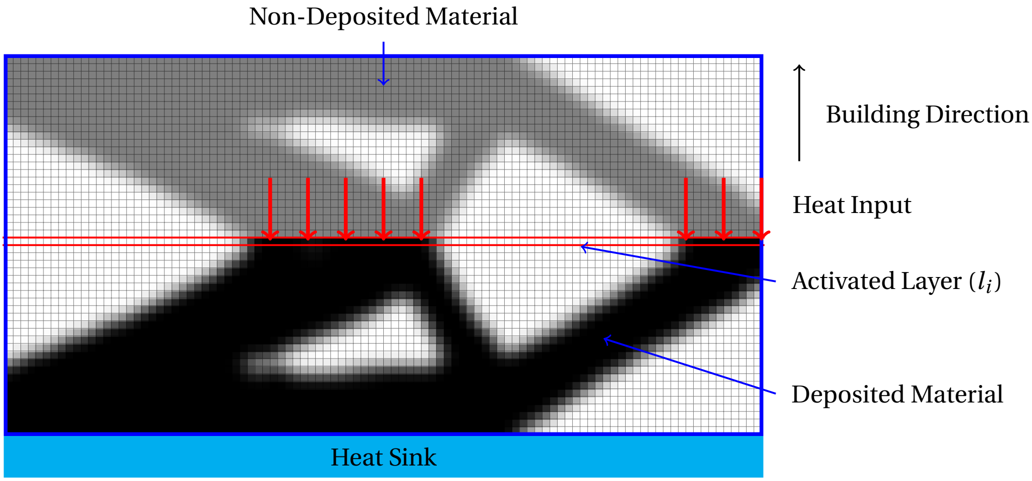

Figure 6.3: Illustration of the simplified process model on the compliance optimized design layout. The cyan region indicates the heat sink condition to simulate the presence of the substrate. Based on the building direction, the complete deposition process is discretized into process intervals. In each process interval, the elements comprising the layer (l_i) are activated at once as shown in the red rectangle. The heat added to the deposited layer is indicated by the red arrows. The heating and subsequent cooling is simulated for each process interval to evaluate the thermal history.

subscript l_i denotes that the nodal values are calculated when layer l_i, is deposited. The $\mathbf{Q}_{l_i}$ is the nodal heat load applied during the deposition of layer l_i. The amount of heat added to the elements in the process model is calculated by the power of the WAAM process. To calculate the heat load for a process interval, the power per unit volume (q_0) is associated with each activated element of the layer l_i. This power density is then scaled by the design variable associated with the element using the SIMP penalization as follows:

$$q_e = \tilde{\rho}_e^p q_0. \tag{6.10}$$

q_e is the power density associated with the activated elements and penalized with the density variable. The penalized power density is then integrated over the top edge of the activated element and assembled into the nodal heat load array. The nodal heat load is applied as follows

$$\mathbf{Q}_{l_i}(\boldsymbol{\rho}) = \begin{cases} \mathbf{Q}_{l_i}(\boldsymbol{\rho}) & \text{if,} \quad \tau_{l_{i-1}} \le t < \tau^{\mathfrak{h}}_{l_i} \\ \mathbf{0} & \text{if,} \quad \tau^{\mathfrak{h}}_{l_i} \le t \le \tau_{l_i}. \end{cases} \tag{6.11}$$

Eq. (6.9) represents the initial condition at the start of a process interval assuming the pre-deposited part cools down to ambient temperature before the deposition of the subsequent layer starts. This particular assumption is realistic for WAAM since, the size of a part is typically 2-3 orders of magnitude larger than the electric arc size. Therefore sufficient cooling time is available during subsequent layer deposition.

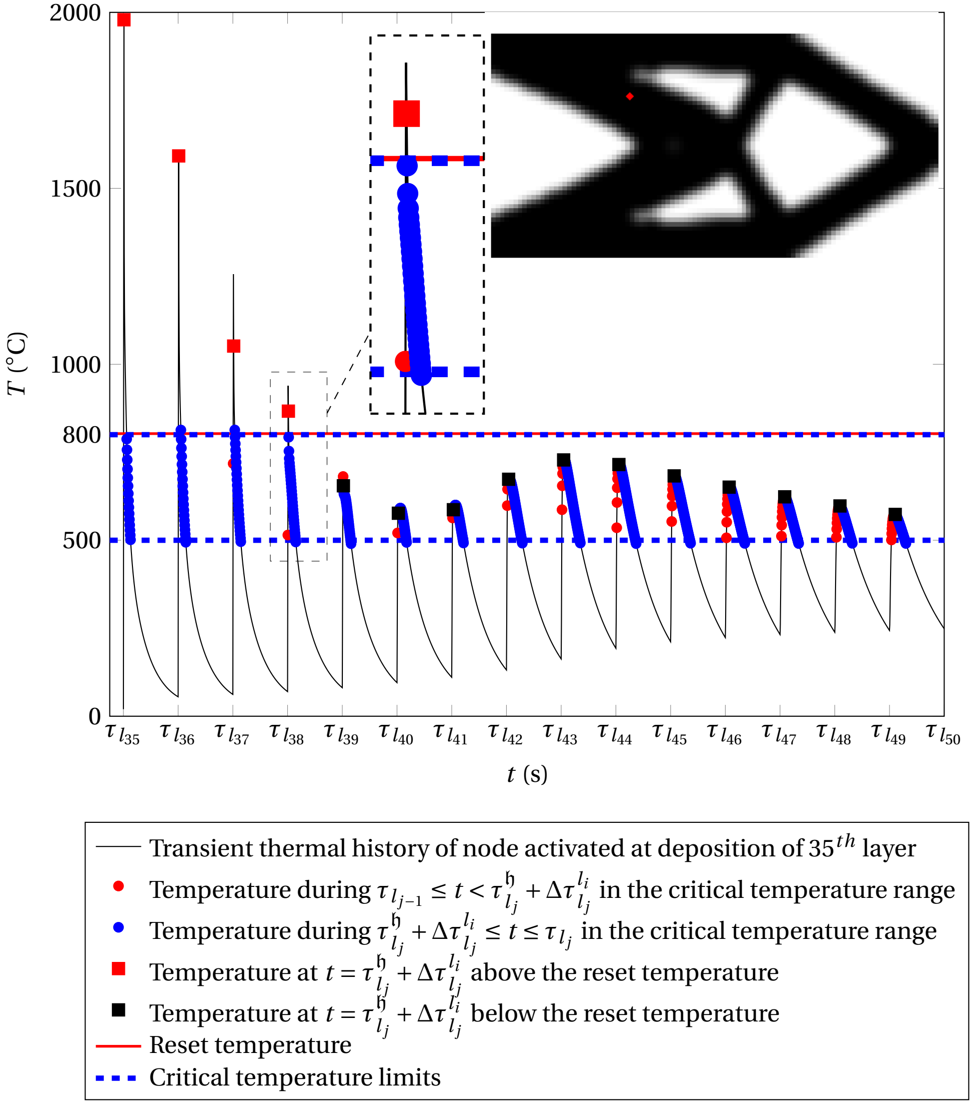

Figure 6.4: Transient thermal history of a node represented by the red in the compliance minimized design obtained by process simulation.

The thermal conductivity and heat capacity matrices are dependent on the design variables as follows:

$$\kappa_e(\tilde{\rho}_e) = \kappa_{\min} + \tilde{\rho}_e^{p_\kappa}(\kappa_0 - \kappa_{\min}). \tag{6.12}$$

$$c_{p_e}(\tilde{\rho}_e) = c_{p_{\min}} + \tilde{\rho}_e^{p_{cp}}(c_{p_0} - c_{p_{\min}}). \tag{6.13}$$

Here, κ_e and c_{p_e} are the thermal conductivity and specific heat capacity of element e. $\kappa_{\min}$ and κ_0 are the thermal conductivity of void and material, respectively. Similarly, $c_{p_{\min}}$ and c_{p_0} are the specific heat capacity of void and material, respectively. The positive penalization exponents on the thermal conductivity and specific heat capacity are p_κ and p_{c_p}, respectively. For the considered heat conduction problem, the cooling rates are governed by the thermal diffusivity, which is given for an element e is given as follows:

$$\alpha_e = \frac{\kappa_e}{\rho_m c_{p_e}}. \tag{6.14}$$

Here, ρ_m is the physical density of the material which is constant. Substituting Eq. (6.12) and Eq. (6.13) in Eq. (6.14), and simplifying we get:

$$\alpha_e = \alpha_0\left(\frac{\kappa_{\min}/\kappa_0 + \tilde{\rho}_e^{p_\kappa}(1-\kappa_{\min}/\kappa_0)}{c_{p_{\min}}/c_{p_0} + \tilde{\rho}_e^{p_{cp}}(1-c_{p_{\min}}/c_{p_0})}\right). \tag{6.15}$$

Here, $\alpha_0 = \kappa_0/(\rho_m c_{p_0})$. If $p_\kappa = p_{c_p} \neq 0$, $\kappa_{\min}/\kappa_0 = 10^{-9}$ and $c_{p_{\min}}/c_{p_0} = 10^{-9}$, then $\alpha_e = \alpha_0$. This means that heat transfer through the void is possible which is physically incorrect. Therefore, we choose $p_\kappa > p_{c_p}$, to make thermal diffusivity design dependent. For $p_\kappa = 3$ and $p_{c_p} = 2$, thermal diffusivity will be linearly dependent on the design variable (Wu et al., 2021). However, for $\tilde{\rho}_e = 0$ with $p_\kappa = 3$ and $p_{c_p} = 2$, $\alpha_e = \alpha_0\left(\frac{\kappa_{\min}}{\kappa_0}\right)/\left(\frac{c_{p_{\min}}}{c_{p_0}}\right)$. Therefore, for $\kappa_{\min}/\kappa_0 = 10^{-9}$ and $c_{p_{\min}}/c_{p_0} = 10^{-9}$, $\alpha_e = \alpha_0$. Again the thermal diffusivity for the void and solid becomes indistinguishable. To circumvent this issue, $\kappa_{\min}/\kappa_0 = 10^{-9}$ and $c_{p_{\min}}/c_{p_0} = 10^{-3}$ are chosen. Through these selected parameters, the thermal diffusivity of the void becomes $10^{-6}\alpha_0$, and heat transfer through the void regions is effectively suppressed.

To solve the transient state equation given by Eq. (6.8), a Backward Euler Scheme is employed in the temporal domain. The motivation to choose this particular scheme is its unconditional stability for linear transient heat conduction problems (Hughes, 1977). The time step used to solve the state equation is chosen sufficiently coarse so that optimization can be realized in a reasonable computational time. The effect of time steps is studied in Section 6.5.1. Even though the time step is kept large the solution time might be high due to number of degrees of freedom. Therefore, a relatively coarse structured mesh of 100 × 50 bilinear quadrilateral elements is chosen for the optimization problem. Note that higher fidelity thermal models can be used to simulate the transient thermal history during the AM process. However, the additional computational costs make the optimization problem computationally intractable.

6.3.2. RELATION BETWEEN COOLING TIME AND YIELD STRENGTH

The relation between the cooling time, hardness, and yield strength (σ_y) is given in Fig. 6.5. The relation between the cooling time in the critical temperature range and the Vickers Hardness is given in Mishra et al., 2023. In Fig. 6.5, the horizontal $t_{8|5}$-axis represents the cooling time between 800°C to 500°C and black data points represent the measured Vickers Hardness (HV). The yield strength is calculated using the empirical relation

$$\sigma_y = 2.876(\mathrm{HV}) - 90.7 \tag{6.16}$$

suggested by Pavlina and Van Tyne, 2008.

σ_y can be directly correlated to the cooling time spent in the critical temperature range 800°C to 500°C through linear regression as:

$$\sigma_y = -198.1 \log\left(t_{8|5}/t_0\right) + 1024. \tag{6.17}$$

Here $t_0 = 1$ s, is a constant to introduce unitless quantity $t_{8|5}/t_0$ before the logarithmic operation is taken.

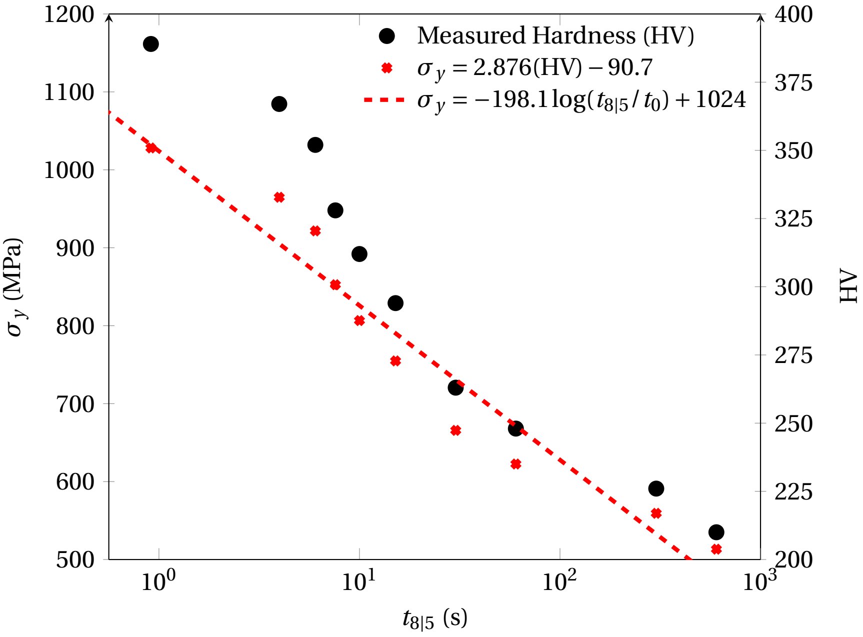

Figure 6.5: Correlation in the cooling time between the critical temperature range 800°C to 500°C, measured Vickers Hardness (HV), and correlated Yield Strength (σ_y).

6.4. COOLING TIME ESTIMATION AND FULL OPTIMIZATION PROBLEM

6.4.1. COOLING TIME SPENT IN THE CRITICAL TEMPERATURE RANGE

We denote the upper and lower bounds of the critical temperature range as $\bar{T}$ and $\underline{T}$, respectively. For HSLA steels, the critical temperature range is between $\bar{T} = 800$°C and $\underline{T} = 500$°C. A typical thermal history for a node of the compliance minimized cantilever design (see Fig. 6.2) obtained by our simplified process simulation is shown in Fig. 6.4. The thermal history of the node has multiple heating and cooling cycles. The first cycle represents the deposition of the layer in which the node indicated by red is activated. The subsequent heating and cooling cycles represent the deposition of the consecutive layers above the node. Each finite element node in the design (apart from the topmost layer) experiences a similar thermal history with multiple heating and cooling cycles. A robust strategy is required to evaluate the cooling time of the decisive cooling cycle.

The entire thermal history of the node n is given by $T_n(t)$. The temperature history of the node n activated at the deposition of layer l_i, after deposition of layer l_j, is represented with ${}^{l_i}_{l_j}T_n(t)$. Here, the index $j = i,\dots,L$. ${}^{l_i}_{l_j}T_n(t)$ represents the thermal history of the node n activated in the interval $(\tau_{l_{i-1}},\tau_{l_i})$, during the process interval $(\tau_{l_{j-1}},\tau_{l_j})$. A combination of Heaviside functions can be used to evaluate the time spent in the critical temperature range in a particular process interval. For a layer l_j deposited after layer l_i, the time spent in the critical temperature range by node n in the process interval $(\tau_{l_{j-1}},\tau_{l_j})$ is evaluated as:

$$ {}^{l_i}_{l_j}\mathrm{t}_n = \int_{\tau_{l_{j-1}}}^{\tau_{l_j}} \bar{H}\Big({}^{l_i}_{l_j}T_n(t)\Big)\underline{H}\Big({}^{l_i}_{l_j}T_n(t)\Big)\,dt \tag{6.18} $$

$$ \text{with,}\quad \bar{H}\Big(T(t)\Big) = \frac{1}{1+\exp\left(\dfrac{-k_W(\bar{T}-T(t))}{\bar{T}}\right)} \tag{6.19} $$

$$ \underline{H}\Big(T(t)\Big) = \frac{1}{1+\exp\left(\dfrac{-k_W(T(t)-\underline{T})}{\underline{T}}\right)} \tag{6.20} $$

The parameter k_W determines the shape of the Heaviside functions, when combined together act as a window function that extracts the time interval where the temperature is in the critical temperature range $[\underline{T},\bar{T}]$. The effect of the parameter k_W is shown in Fig. 6.6, for the temperature range 500 °C to 800 °C. The function $\bar{H}(T)\underline{H}(T) \approx 0$ everywhere except $500\ °\mathrm{C} \le \mathrm{T} \le 800\ °\mathrm{C}$ where $\bar{H}(T)\underline{H}(T) \approx 1$. For $k_W = 100$, this behavior is captured with the desired accuracy as shown in Fig. 6.6. Therefore $k_W = 100$ is chosen in this study. Differentiable, smooth Heaviside approximations are essential in order to allow gradient-based optimization.

For the thermal history shown in Fig. 6.4, the data points labeled with red and blue circles are identified to be within the critical temperature range with $\bar{H}(T)\underline{H}(T) > 0.1$. Note that Eq. (6.18) accounts for the time the node spends in the critical temperature range during both heating and cooling. However, only the cooling phase is relevant for the final microstructure development. In order to isolate the time spent during cooling phase, the time spent during the heating phase should be excluded. It means that for a heating-cooling cycle, the time spent in the critical temperature range for the data points before the peak temperature should be discarded. For this purpose, the estimation of the time instance at which the peak temperature occurs becomes crucial. The time at which the peak temperature occurs for the node n activated during the deposition of layer l_i, during the deposition of l_j has two aspects:

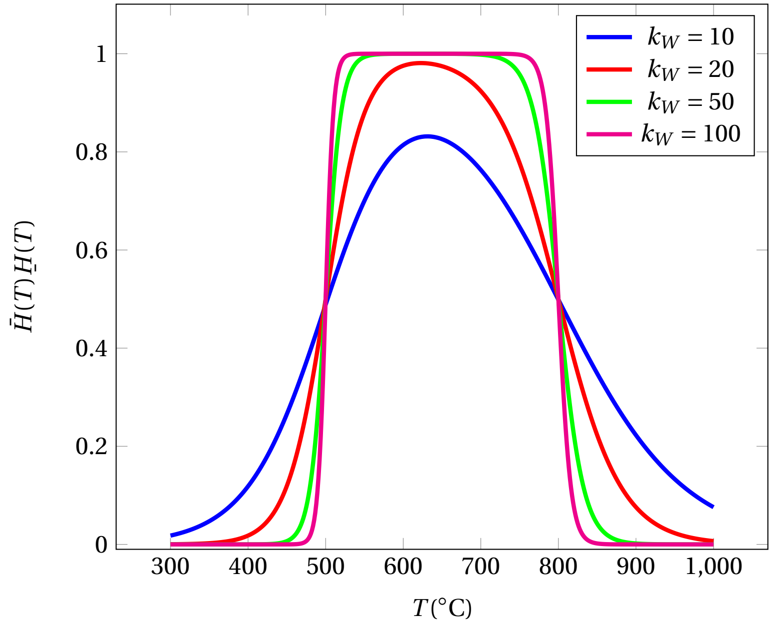

Figure 6.6: The effect of parameter k_W on the combination of Heaviside functions to extract the total time spent in the critical temperature range 800° to 500°C.

1. The duration of heating. In this period heat is added, thus temperature is expected to rise.

2. The time the heat is conducted from layer l_j to node n activated during the deposition of l_i.

An additional Heaviside function, ${}^{l_i}_{l_j}H_n(t)$, is introduced for the node n activated at layer l_i, which is used to filter out the time spent during heating while layer l_j is deposited:

$$
{}^{l_i}_{l_j}H_n(t) = \begin{cases} 0, & \text{if}, \quad \tau_{l_{j-1}} \leq t < \tau^{\mathfrak{h}}_{l_j} + \Delta\tau^{l_i}_{l_j} \\ 1, & \text{if}, \quad \tau^{\mathfrak{h}}_{l_j} + \Delta\tau^{l_i}_{l_j} \leq t \leq \tau_{l_j} \end{cases} \tag{6.21}
$$

Note that the exact Heaviside function is used here since this operation is not design-dependent and consequently is not a part of the sensitivity calculation. Here, $\Delta\tau^{l_i}_{l_j}$ is the time delay required for the heat to diffuse through conduction and reach node n when layer l_j is deposited. This time delay is estimated as

$$
\Delta\tau^{l_i}_{l_j} = \frac{\left(\Delta L^{l_i}_{l_j}\right)^2}{\alpha}. \tag{6.22}
$$

Here, $\Delta L_{l_j}^{l_i}$ is shortest path between layer l_j and node n. This shortest path is design-dependent. During optimization, the design is subject to change in every iteration hence the conduction path is unknown. Therefore, it is complicated to estimate $\Delta L_{l_j}^{l_i}$. For simplicity, it is taken

$$\Delta L_{l_j}^{l_i} = (j - i + 1)\Delta x. \tag{6.23}$$

Here, Δx represents the height of the element which is equivalent to layer thickness shown in Fig. 6.3. Since the optimization starts with a uniform gray design, i.e. $\boldsymbol{\rho}_e = V_0$, and the heat equation (Eq. (6.8)) is scaled by the design variable, the assumption holds valid during the initial optimization iterations. When the optimized design converges to a black-and-white design the assumption does not hold valid. However, it is observed that by using Eq. (6.22) the time instances at which temperature peaks occur can be approximated reasonably well. For the thermal history shown in Fig. 6.4, square-shaped red markers represent temperature at $t = \tau_{l_j}^{\mathfrak{h}} + \Delta\tau_{l_j}^{l_i}$ which captures the temperature peaks at the desired level of accuracy. The time spent by node n in the critical temperature range during cooling, after the layer l_j is deposited is then given as

$${}^{l_i}_{l_j}\tilde{\mathfrak{t}}_n = \int_{\tau_{l_{j-1}}}^{\tau_{l_j}} \left({}^{l_i}_{l_j}H_n(t)\right) \bar{H}\left({}^{l_i}_{l_j}T_n(t)\right) \underline{H}\left({}^{l_i}_{l_j}T_n(t)\right) dt. \tag{6.24}$$

In Fig. 6.4, the temperature data in the critical temperature range during heating and cooling is represented by red and blue colored circles, respectively. It can be observed in Fig. 6.4 that through this approach the time corresponding to heating in the critical temperature range is filtered out. Note that, if $j \approx i$, the heating of node n happens at a much higher rate compared to the cooling, therefore time contribution from the heating phase is negligible. However, if $j >> i$ the heating of node n happens at a slightly slower rate. Therefore a time contribution from the heating phase would be more notable. Still, distant layer additions are not likely to become a decisive cooling cycle that dictates the material microstructure.

6.4.2. IDENTIFYING THE DECISIVE PROCESS INTERVAL

The previous section showed that the time spent in the critical temperature range can be calculated through a continuous function in each process interval. Recall that, a decisive cooling cycle dictates the final solid-state phases. Therefore the cooling time during the decisive process interval should be determined.

To identify the decisive process interval, weights are assigned to each process interval. For the thermal history shown in Fig. 6.4, the cooling time of the fourth cooling cycle is crucial. This is because it is the last process interval where temperatures exceed the reset temperature. The assignment of the weight has two aspects:

1. Determine the process intervals in which the temperature exceeds the reset temperature with a reset weight.
2. From process intervals that are identified with temperatures above reset temperature, extract the last one with a sequential weight.

Recall that the temperatures at $t = \tau^{\mathfrak{h}}_{l_j} + \Delta\tau^{l_i}_{l_j}$ have been observed to approximate the peak temperatures reasonably well. Therefore, in order to identify the process intervals with peak temperatures above the reset temperature, the temperature, ${}^{l_i}_{l_j}\mathrm{T}_n$, at $t = \tau^{\mathfrak{h}}_{l_j} + \Delta\tau^{l_i}_{l_j}$ is extracted from the thermal history. The following smooth Heaviside function is introduced to compute a reset weight depending on this extracted peak temperature:

$$ {}^{l_i}_{l_j}r_n = \frac{1}{1 + \exp\left(\dfrac{-k_R\left({}^{l_i}_{l_j}\mathrm{T}_n - T_R\right)}{T_R}\right)}. \tag{6.25}$$

Here, ${}^{l_i}_{l_j}r_n$ is the reset weight associated with node n activated during layer l_i when layer l_j is deposited. The reset temperature is given by $T_R = 800$°C (Mishra et al., 2023). The reset weight function is 1 if ${}^{l_i}_{l_j}\mathrm{T}_n$ is greater than the reset temperature T_R else reset weight is approximately 0. The parameter k_R controls the shape of the reset weight function. The influence of the parameter k_R on the reset weight function is shown in Fig. 6.7. In this study, $k_R = 100$ is chosen.

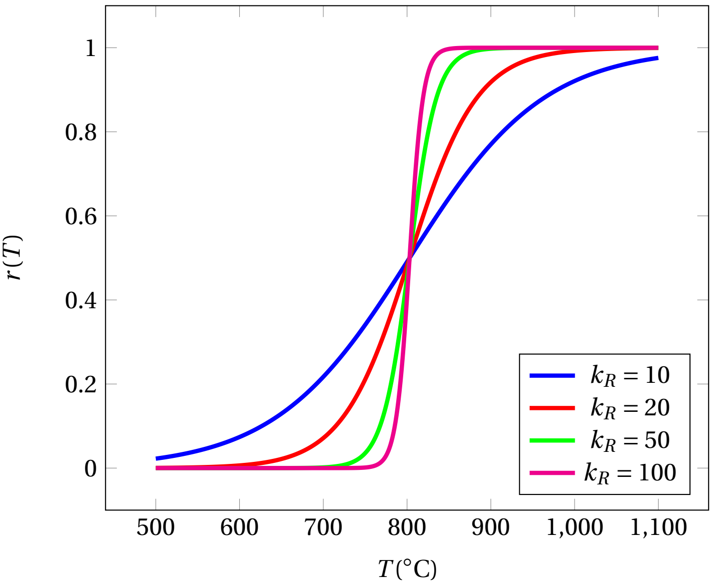

Figure 6.7: The effect of parameter k_R on the reset weight function.

For the thermal history shown in Fig. 6.4 the temperature at time $t = \tau^{\mathfrak{h}}_{l_j} + \Delta\tau^{l_i}_{l_j}$ is shown by the square-shaped markers. The square-shaped markers shown in black and red color indicate the reset weight of 0 and 1, respectively. It can be observed that four process intervals have temperatures above the reset temperature.

The last process interval of these is identified by applying an additional sequential weight to each process interval. The sequential weight is given as:

$$ {}^{l_i}_{l_j}s_n = a^{(j-i+1)} \quad \text{where} \quad a > 1. \tag{6.26}$$

Here, ${}^{l_i}_{l_j}s_n$ is the sequential weight assigned to node n during the deposition of the layer l_j. The condition on base $a > 1$ ensures that the weight grows exponentially and the weight of each subsequent process interval is higher than the previous one. Based on the base a, the relative contribution from the last process interval to the aggregated function can be tuned. This can be understood by comparing the last sequential weight to the sum of all sequential weights:

$$ f = \frac{a^{j-i+1}}{\sum_{j=i}^{L} a^{j-i+1}}. \tag{6.27}$$

Since the sequence in the denominator is a geometric progression, the above equation can be reduced to:

$$ f = \left(1 - \frac{1}{a}\right) \frac{1}{1 - \dfrac{1}{a^{j-i+1}}}. \tag{6.28}$$

For the condition $j >> i$, the term $1/a^{j-i+1} \rightarrow 0$. Thus, the fraction can be approximated as:

$$ f \approx 1 - \frac{1}{a}. \tag{6.29}$$

Thus, for $a = 2$ and $a = 100$ the contribution from the last process interval tends to 50% and 99%, respectively. Using a higher value of a thus makes the contribution of the last process interval more dominant. However, considering higher a values may lead to numerical overflow during computational implementation as the sequential weight function grows exponentially. Therefore, $a = 2$ is considered in this study, which means that the last process interval will contribute 50% in the cooling time estimation.

The reset and sequential weights are combined together to emphasize the cooling time of the decisive process interval as

$$ \tilde{\mathfrak{t}}_n = \frac{\sum_{j=i}^{L} \left[{}^{l_i}_{l_j}\tilde{\mathfrak{t}}_n\right]\left[{}^{l_i}_{l_j}r_n\right]\left[{}^{l_i}_{l_j}s_n\right]}{\sum_{j=i}^{L} \left[{}^{l_i}_{l_j}r_n\right]\left[{}^{l_i}_{l_j}s_n\right]}. \tag{6.30}$$

Through this aggregation, the contribution of the cooling time in the critical temperature range for the decisive cycle will be dominant. For the thermal history shown in Fig. 6.4, the reset and sequential weights corresponding to the first six process interval are given in Fig. 6.8. It can be clearly observed that for the first four cycles, the reset weights are equal to 1. For subsequent thermal cycles, the reset weight is approximately 0. Therefore, reset weight successfully identifies the four cycles with temperatures above reset temperature. The combination of reset and sequential weight shows that the weight on the fourth cycle is the highest. Moreover, the contribution from the fourth cycle is 53%. The cooling times in the critical temperature range for each process interval after deposition of the considered node and their contribution to the aggregated cooling time is shown in Fig. 6.9.

It remains to verify the proposed continuous decisive cooling time identification in the entire domain. For this purpose, the aggregated cooling time field is compared with the actual decisive cooling time field in Fig. 6.10. It is observed that the proposed aggregation scheme captures the decisive cooling times well. A percentage error between the actual and aggregated time is shown in Fig. 6.11. The errors encountered are due to the use of continuous and differentiable mathematical functions to formulate a gradient based optimization problem. The error is low in the region where cooling times are high and vice versa. Moreover, the error is high in the intermediate regions which are dominant at the interface of the solid and void regions.

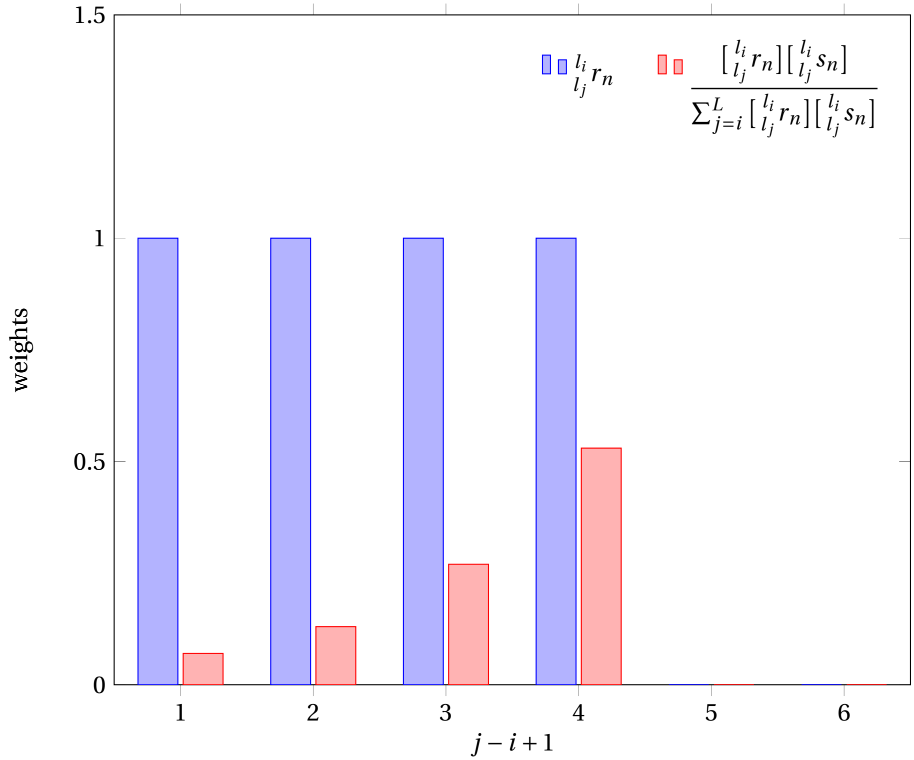

Figure 6.8: Reset weights and aggregated weights assigned to the cooling time of the first six process intervals for the thermal history shown in Fig. 6.4.

6.4.3. OPTIMIZATION PROBLEM

In order to control the cooling times of the decisive cooling cycle in the critical temperature range, we define the following optimization problem:

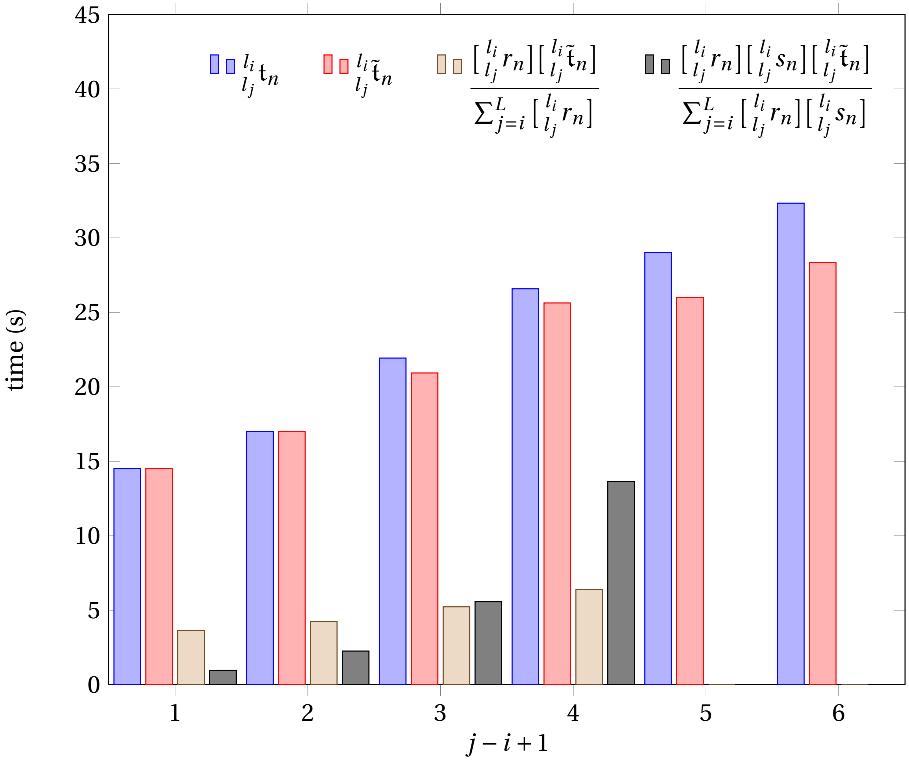

Figure 6.9: The total time and the cooling time in the critical temperature range for the first six process intervals of the thermal history shown in Fig. 6.4. The corresponding contribution to the aggregated weighted cooling time by each process interval is also shown.

$$\min_{\boldsymbol{\rho}} \quad c = \frac{1}{2}\sum_{\Omega_N} \mathbf{u}_e^{\mathrm{T}}\mathbf{k}_e(\rho_e)\mathbf{u}_e, \tag{6.31}$$

$$\text{s.t.} \quad \mathbb{K}\mathbf{u} = \mathbf{f}. \tag{6.32}$$

$$\mathbf{C}_{l_i}\dot{\mathbf{T}}_{l_i} + \mathbf{K}_{l_i}(\boldsymbol{\rho})\mathbf{T}_{l_i} = \mathbf{Q}_{l_i}, \quad \forall l_i \in \Omega_L. \tag{6.33}$$

$$\mathbf{T}_{l_i} = \mathbf{T}_0, \quad t = t_{l_{i-1}}. \tag{6.34}$$

$$\underline{\tau} \leq \frac{1}{N_c}\sum_{\Omega_c}\tilde{\mathfrak{t}}_n \leq \bar{\tau} \tag{6.35}$$

$$V(\boldsymbol{\rho}) \leq V_0. \tag{6.36}$$

$$0 \leq \rho_e \leq 1, \quad \forall e \in \Omega_N. \tag{6.37}$$

In the above problem, the compliance of the structure is minimized considering new constraints regarding the manufacturing process of the design. Eq. (6.35) is the average cooling time constraint imposed during the manufacturing process in a control volume Ω_c. For simplicity, the average is considered instead of a more nonlinear measure such

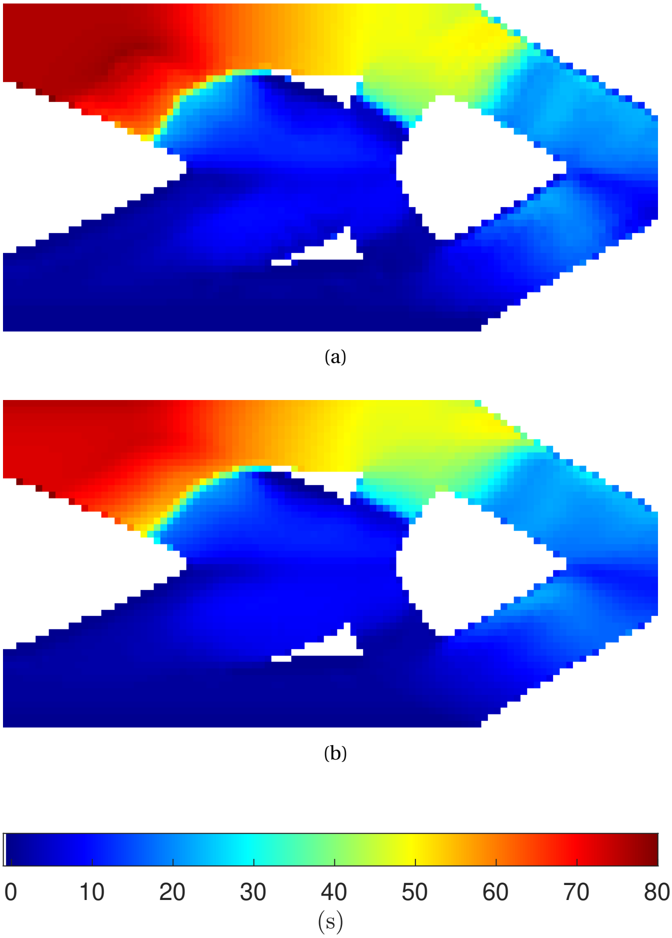
(a)

(b)

Figure 6.10: Comparison between (a) the actual cooling time of the decisive process interval and (b) the aggregated cooling time.

as a (smooth) maximum. $\bar{\tau}$ and $\underline{\tau}$ are the maximum and minimum allowed values of the average time spent by the number of nodes (N_c) in the control volume in the critical temperature range. A gradient-based optimization approach is used for which calculation of the design sensitivities of objectives and constraints is important. The design sensitivities of the compliance objective and volume constraint are well known (Bendsoe and Sigmund, 2013). The design sensitivity of the cooling time constraint with respect to the design variable is given in D.1. A complete flowchart of the optimization framework is given in Fig. 6.13.

The considered loadcase for which the compliance is minimized is shown in Fig. 6.12. Two control volumes and non-design domains, Ω_{c_1} and Ω_{c_2}, are considered in the examples in the next section. Average cooling times are controlled in these control volumes

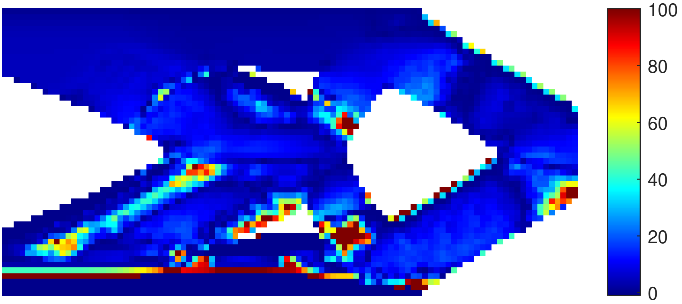

Figure 6.11: The percentage error between the actual time and the aggregated time, shown in Fig. 6.10.

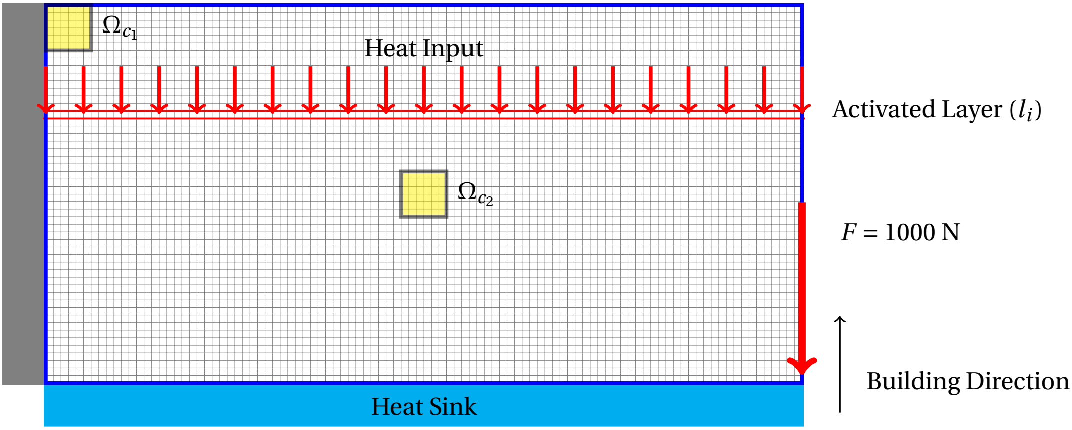

Figure 6.12: Schematic illustration of the cantilever beam problem with Consideration of AM Process induced material properties. The rectangular domain with blue borders is the design domain, discretized with a structured mesh of bilinear quadrilateral elements. The left boundary of the domain is rigidly fixed and a point load is applied indicated with a thick red arrow. The deposition is considered in layer- by-layer manner. The heat input is applied to the deposited layer as indicated by thin red arrows. The translucent yellow regions are the control volumes that remain solid. The decisive cooling times are constrained in these control volumes.

for selected values of $\bar{\tau}$ and $\underline{\tau}$. To demonstrate the degree of control of thermal history and associated microstructure development, initially, the cooling times are constrained in each control volume individually and thereafter, simultaneously.

The constrained cooling time values $\underline{\tau}$ and $\bar{\tau}$ are chosen by considering the standard compliance minimized design Fig. 6.2 as a reference design. For this reference design, the average normalized weighted cooling times in control volume Ω_{c_1} and Ω_{c_2} are approximately 80s and 6s, respectively. The locations of the control volume are selected such that material is only deposited below Ω_{c_1}. In contrast, the material is deposited both above and below of control volume Ω_{c_2}. Thus, for Ω_{c_1}, the heat input has to be fa-

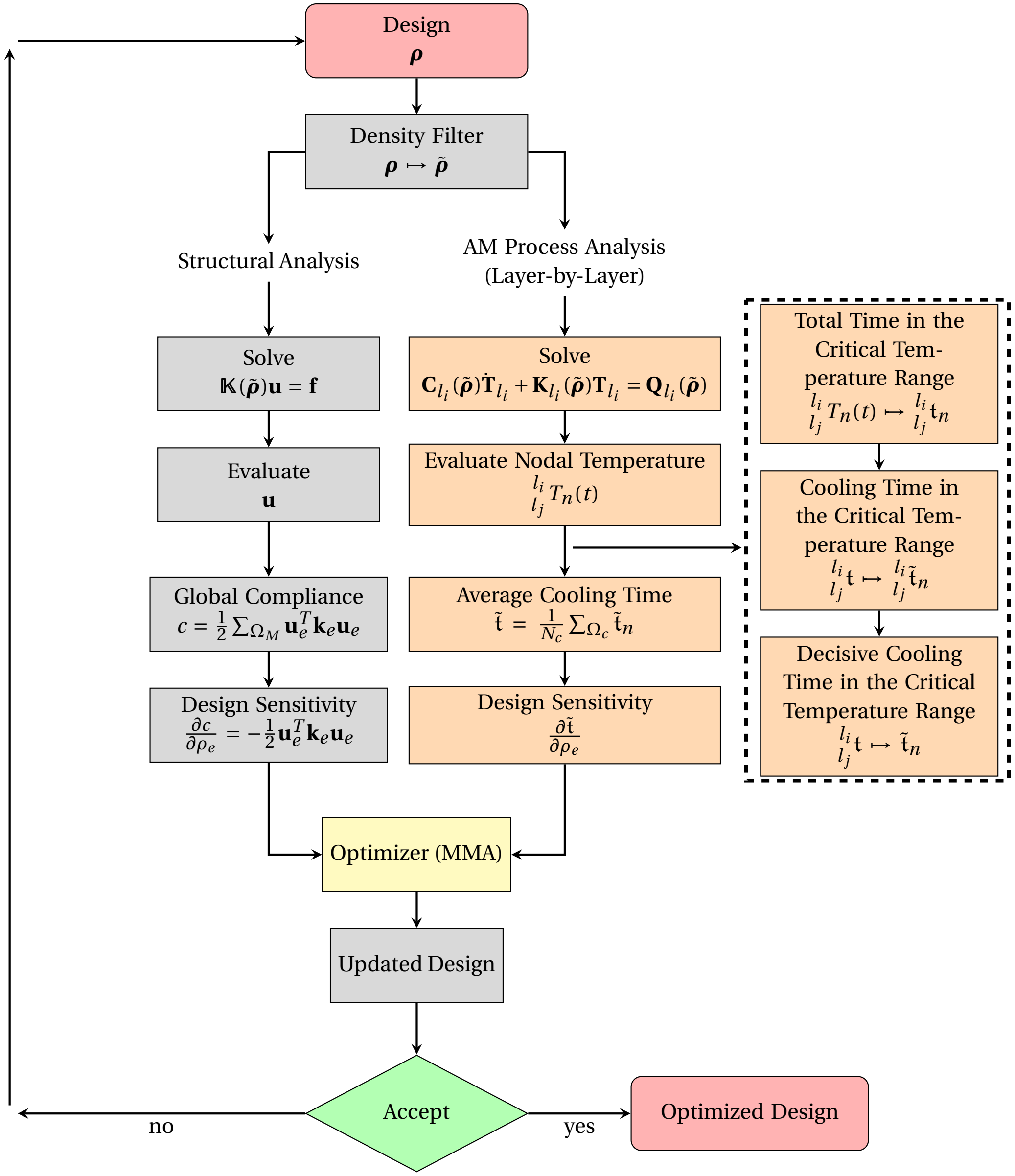

Figure 6.13: Flow chart of the novel design optimization framework for minimum compliance while constraining the average cooling time in the design domain to control the microstructure development during the AM process.

cilitated by the design changes below the control volume, while for Ω_{c_2} design changes are expected above and below the control volume.

6.5. RESULTS AND DISCUSSIONS

As mentioned earlier, first the effect of the time step on the solution of the transient heat conduction equation is examined. Subsequently, the designs obtained by solving the topology optimization problem constraining cooling time in a single control volume and both control volumes simultaneously are presented in this section. Furthermore salient points of the methodology will be discussed along with the results.

6.5.1. EFFECT OF TIME STEPS

The effect of time step Δt on the thermal history of a node of the compliance minimized design is shown in Fig. 6.14. It can be observed that the time step has a distinct effect on the thermal history calculation. By reducing the time step the solution converges to the actual solution of the transient thermal heat conduction problem considered in this study. It is observed that the Forward Euler Scheme (explicit) is not stable when $\Delta t > 0.005$ s. Therefore, the Backward Euler scheme (implicit) is chosen due to its unconditional stability. However, increasing the time step while using an implicit scheme introduces numerical errors in the solution compared to the converged solution as depicted in Fig. 6.14.

Table 6.2: The effect of time step on the total wall clock time to perform the simplified thermal process model. The number of DOFs = 5252, the total time per layer = 200 s, and the Number of layers = 50.

Time Integration Scheme	Implicit	Implicit	Implicit	Implicit	Explicit
Time step	1 s	0.1 s	0.01 s	0.005 s	0.005 s
Number of time steps per layer	200	2000	20000	40000	40000
Total wall clock time for process simulation	240 s	1489 s	14100 s	28120 s	28120 s

The wall clock times to complete the process simulation with MATLAB through Implicit and Explicit schemes with various time steps are given in Table 6.2. The wall clock time to obtain the converged solution is 7.5 hr (28120 s). The same amount of time is also required for the design sensitivities calculation. The number of equations required to calculate design sensitivities, see Section D.1, is the same as of the transient heat transfer problem solved in the process simulation. TO with the converged thermal process simulation solution for a modest 100 iterations takes about two months. This extravagant time required for optimization bounds us to use coarser time steps to get initial results. For instance, by using a time step $\Delta t = 0.1$ to 1.0 s the optimized designs can be obtained in the duration of several weeks to several days. Here we make the pragmatic choice to use $\Delta t = 1.0$ s for our optimization study to obtain results in a few days.

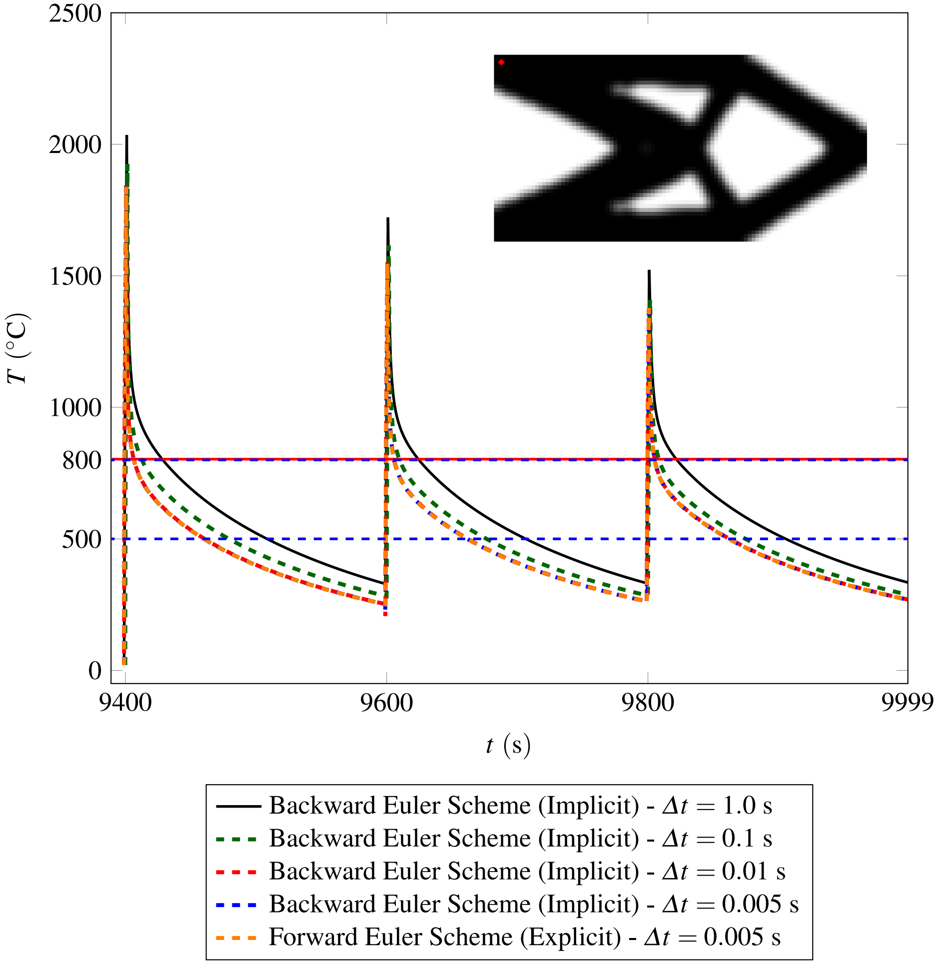

Figure 6.14: Effect of the time step on the thermal history of the indicated node of the compliance minimized design shown as an inset.

6.5.2. OPTIMIZED DESIGNS

Optimized designs with constraints on the average cooling time only in single control volume Ω_{c_1} and Ω_{c_2} are given in Fig. 6.15 and Fig. 6.16, respectively. The results in Fig. 6.15 show that in order to reduce the decisive cooling time in the critical temperature range the optimizer shortens and broadens the path of heat transfer to the heat sink below Ω_{c_1}. The heat transfer is facilitated in a controlled manner and the transient thermal history shows that the decisive cooling time has clearly reduced. The results in Fig. 6.16 show that the decisive cooling time is increased by modifying the design above and below the control volume. The optimizer disintegrates the thick straight bar connected to the control volume into thin features to reduce the incoming heat to the control volume

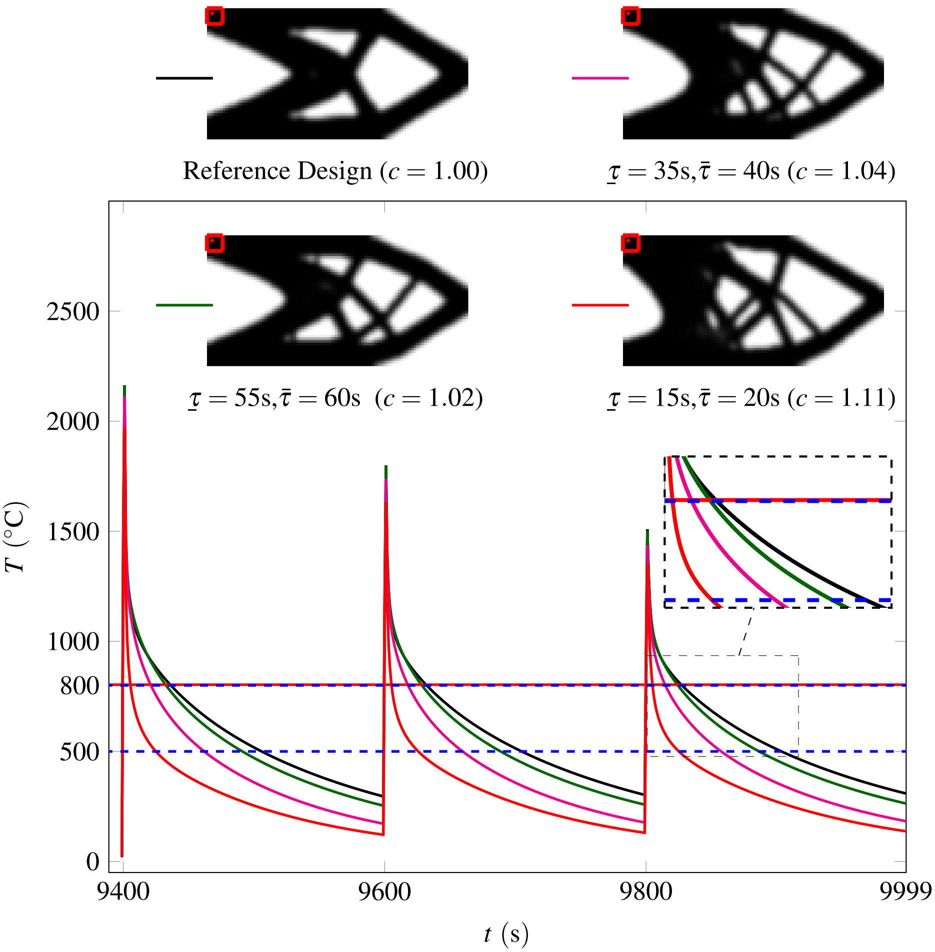

Figure 6.15: The optimized design obtained by controlling the average cooling rate of the control volume Ω_{c_1} and transient thermal history of the node represented by red obtained by process simulation for selected values of $\underline{\tau}$ and $\bar{\tau}$.

during AM. Moreover, the material beneath the control volume is eroded to hinder the heat transfer to the heat sink.

The cooling time of the decisive cycle of the optimized designs and corresponding predicted yield strength are shown in Fig. 6.17 and Fig. 6.18 for control volume Ω_{c_1} and Ω_{c_2}, respectively. The result shows that the cooling time and hence the local yield strength can be increased or decreased through design modifications.

The optimized designs with constraints on the average cooling times on both control volumes simultaneously are shown in Fig. 6.19. For the optimized cases shown in Fig. 6.19 similar observations can be made as in the previous instances in which only

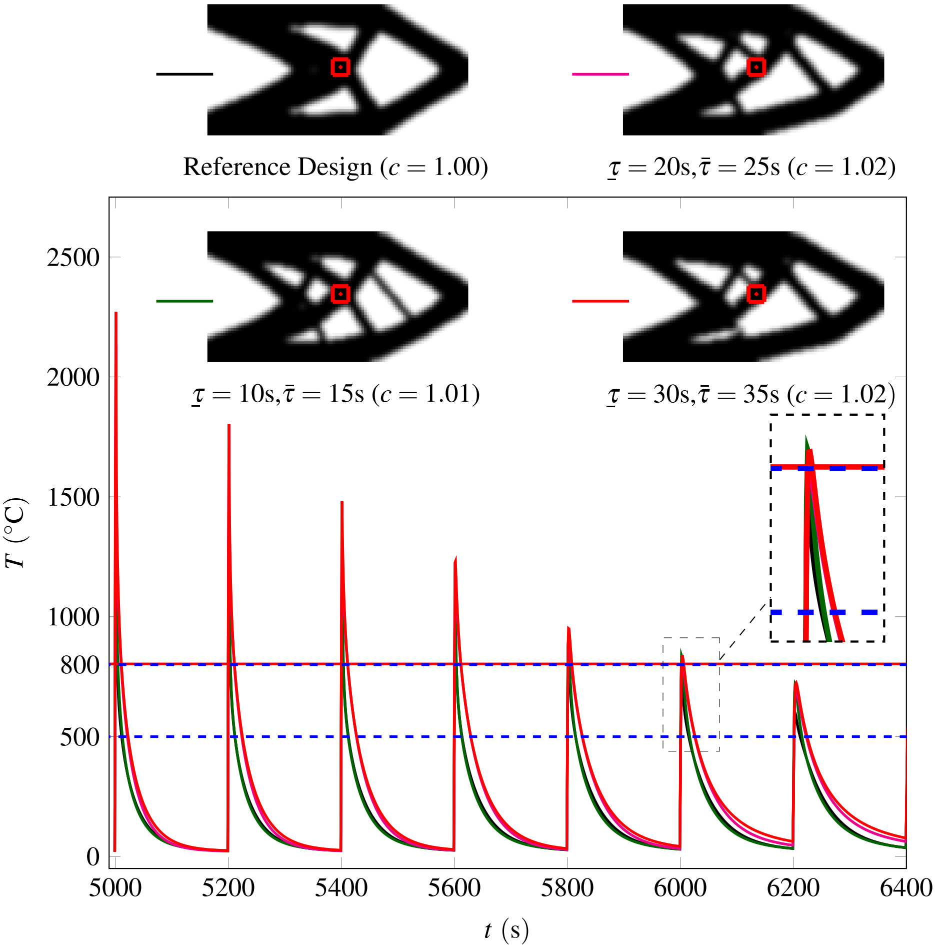

Figure 6.16: Optimized design obtained by controlling the average cooling rate of the control volume Ω_{c_2} and Transient thermal history of the same node represented by red dot obtained by process simulation.

one control volume is controlled. The results in Fig. 6.19 show that the cooling time and the yield strength of different locations in the design domain can be influenced simultaneously.

The compliance of all the optimized designs with average cooling rate constraints has increased compared to the reference design. The increase in compliance is due to the local design changes to fulfill the average cooling time constraint in the local design domain. The increase in compliance ranges from 1 – 11% which is insignificant due to the local design modifications in the design to satisfy the average cooling rate constraint.

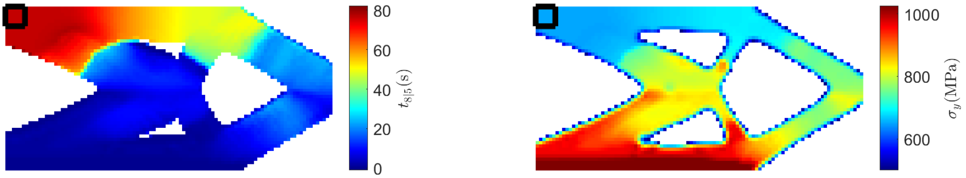

Reference Design

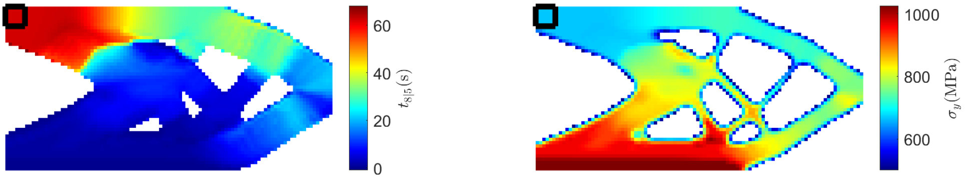

$\underline{\tau} = 55\text{s}$ $\bar{\tau} = 60\text{s}$

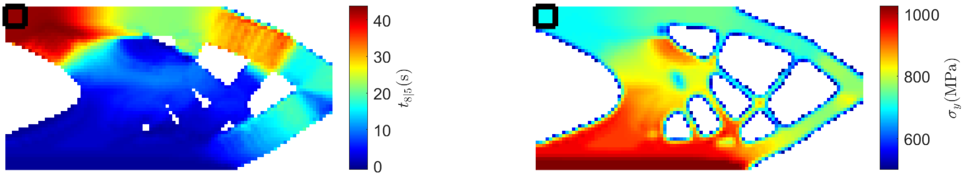

$\underline{\tau} = 35\text{s}$ $\bar{\tau} = 40\text{s}$

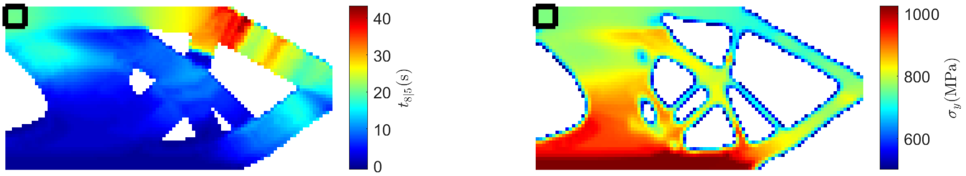

$\underline{\tau} = 15\text{s}$ $\bar{\tau} = 20\text{s}$

Figure 6.17: The left column represents cooling time (in s) of the decisive cooling cycle experienced by the optimized design with a constraint average cooling time in the control volume Ω_{C_1}. The right column is the corresponding predicted Yield Strength estimated by Eq. (6.17).

6.6. Conclusions and Future Work

In this work, a novel TO framework is developed to control an important aspect of metal microstructure, which is solid-state phase fractions by controlling cooling times during the AM process. For AM, the cooling time of a decisive cooling cycle in a critical temperature range is essential. The cooling times directly impact the microstructure and resultant mechanical properties. A novel methodology is presented to isolate the cooling time in the critical temperature range of the decisive cooling cycle from the multiple heating and cooling cycles experienced by the AM parts. The presented method is differentiable

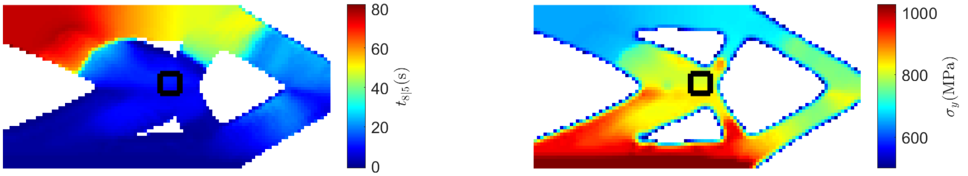

Reference Design

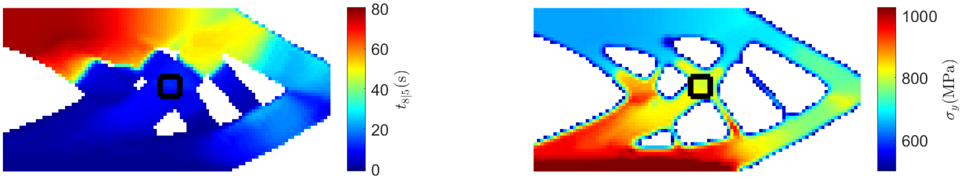

$\underline{\tau} = 10\text{s} \qquad \bar{\tau} = 15\text{s}$

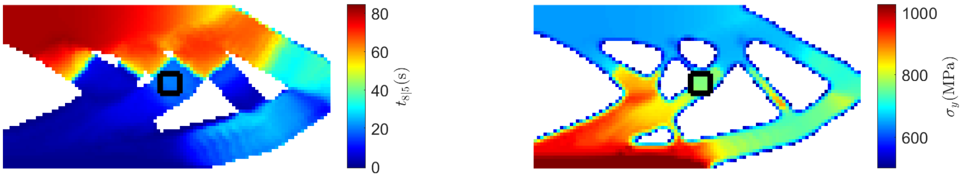

$\underline{\tau} = 20\text{s} \qquad \bar{\tau} = 25\text{s}$

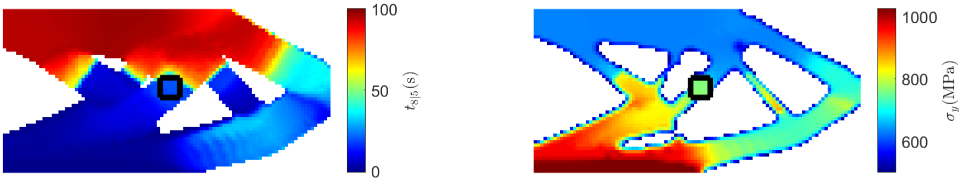

$\underline{\tau} = 30\text{s} \qquad \bar{\tau} = 35\text{s}$

Figure 6.18: The left column represents cooling time (in s) of the decisive cooling cycle experienced by the optimized design with a constraint average cooling time in the control volume Ω_{C_2}. The right column is the corresponding predicted Yield Strength estimated by Eq. (6.17).

and is hence suitable for use in gradient-based topology optimization. The cooling times are constrained at desired design locations during optimization. The results show that the cooling times of the decisive cooling cycle can be increased and reduced to adjust the yield strength in a control volume by facilitating and hindering the incoming and outgoing heat flow toward the heat sink through design optimization.

In this study, the complete transient history of the AM process is evaluated and used for optimization purposes. The computational cost to evaluate the complete transient thermal history and design sensitivities of the cooling time is 960 times higher than the

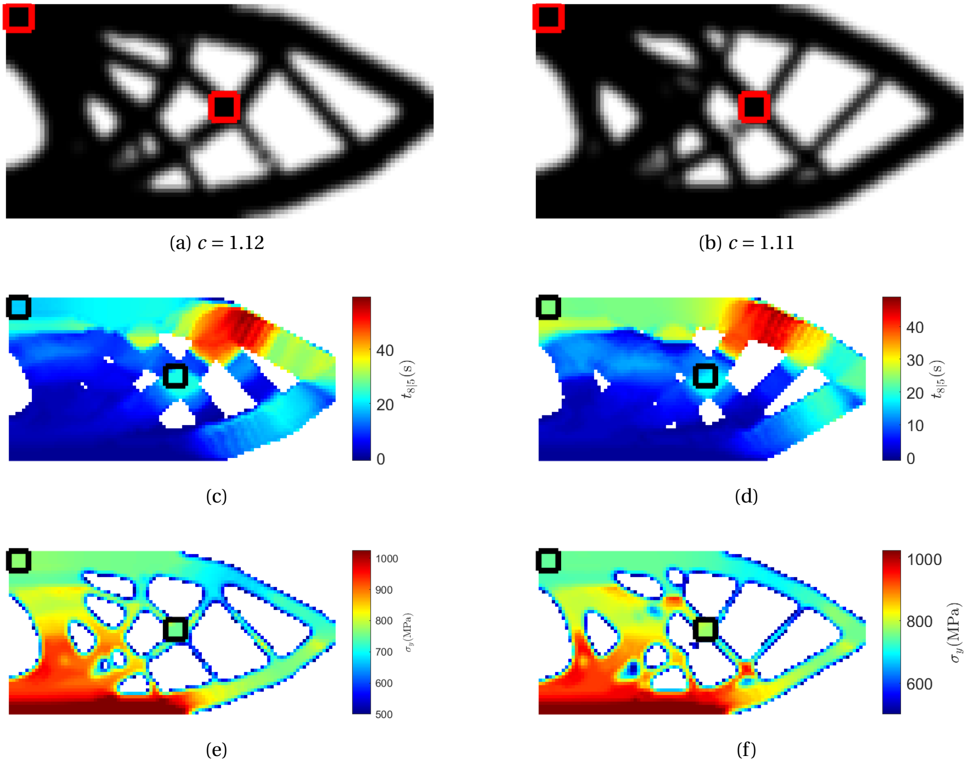

(a) $c = 1.12$ (b) $c = 1.11$

(c) (d)

(e) (f)

Figure 6.19: Optimized design obtained by controlling the average cooling time of the control volumes Ω_{c_1} and Ω_{c_2} simultaneously. (a) For $\Omega_{c_1}: \underline{\tau} = 15\text{s}, \bar{\tau} = 20\text{s}$, For $\Omega_{c_2}: \underline{\tau} = 20\text{s}, \bar{\tau} = 25\text{s}$ (b) For $\Omega_{c_1}: \underline{\tau} = 20\text{s}, \bar{\tau} = 25\text{s}$, For $\Omega_{c_2}: \underline{\tau} = 15\text{s}, \bar{\tau} = 20\text{s}$. (c) and (d) are the corresponding cooling time for both the optimized designs, respectively. (e) and (f) are the predicted Yield Strength obtained by Eq. (6.17).

reference TO problem without AM process constraints in the 2D examples investigated. The computational cost increases with the increase in the spatial resolution of the design, the number of layers required to produce the part through AM process, the number of degrees of freedom constrained during optimization, and the temporal resolution of the time integration scheme.

There are multiple research directions based on the conclusions. The computation cost involve in optimization is immense and there is a need to devise a strategy to lower the computational costs. The computation cost can be reduced by parallel computation of the transient thermal history of each layer which is currently performed sequentially in this study. Consequently, the computation cost of the total process simulation will be factored by the total number of layers in the process. For example, in our case, the wall clock time for the total process simulation of 50 layers is 240 s, see Table 6.2. Through parallel computing, the total wall clock time to evaluate the complete transient thermal history can be reduced to 4.8 s. This enables the transient thermal history to be obtained quickly. Another method to accelerate the process is using an adaptive time-stepping approach. In this approach, the time steps can be reduced in the region of interest and increased elsewhere. For instance, the time stepping in the critical temperature range could be refined, otherwise, it could be coarse. This will enable a reduction of the number of times the system of equations is to be solved in regions other than the critical temperature range. It will pose a requirement to store an array of time steps used in the study which would be used for the design sensitivity calculation. Reducing the computational cost will also allow the extension of this approach to 3D. Once these results get realized in 3D, the design can be manufactured by AM, and validation of the results can be achieved.

Another direction of research is on the mechanics side of the problem. As shown in this work, the yield strength is process dependent and varies locally in the design based on the thermal history. A new stress constraint can be imposed in which the actual stress is evaluated from the loading and boundary conditions, and the local yield strength is estimated from the process simulation. Through this stress constraint efficient designing of the mechanical properties in the entire design domain can be achieved.

Moreover, as discussed in the introduction, in this study effect of tempering is neglected which also has an effect on the mechanical properties. The tempering depends on the amount of time the material experiences in the critical temperature range which is lower than the critical temperature range of solid-state phase transformation for HSLA steels. The window functions used in this study can be used to include the effect of tempering.

Finally, although this work has focused on design changes under the assumption that the AM process cannot be influenced, the proposed approach also applies to problems where the part design is fixed and the process parameters can be optimized. The presented sensitivity analysis remains largely the same, apart from the fact that the heat load becomes dependent on the optimization variables instead of the thermal properties. This variant also presents an interesting direction for future research.

BIBLIOGRAPHY

Bendsoe, M. P., & Sigmund, O. (2013). *Topology optimization: Theory, methods, and applications*. Springer Science & Business Media.

Bruns, T. E., & Tortorelli, D. A. (2001). Topology optimization of non-linear elastic structures and compliant mechanisms. *Computer methods in applied mechanics and engineering*, *190*(26-27), 3443–3459.

Callister Jr, W. D., & Rethwisch, D. G. (2020). *Fundamentals of materials science and engineering: An integrated approach*. John Wiley & Sons.

DebRoy, T., Wei, H., Zuback, J., Mukherjee, T., Elmer, J., Milewski, J., Beese, A. M., Wilson-Heid, A. d., De, A., & Zhang, W. (2018). Additive manufacturing of metallic components–process, structure and properties. *Progress in Materials Science*, *92*, 112–224.

Dornelas, P. H. G., da Cruz Payão Filho, J., Farias, F. W. C., e Oliveira, V. H. P. M., de Oliveira Moraes, D., & Júnior, P. Z. (2020). Fem-thermodynamic simulation methodology to predict the influence of t8/5 on the coarse grain heat-affected zone of a cr-mo low-alloy steel pipe. *Journal of Manufacturing Processes*, *60*, 520–529.

Gavard, L., Bhadeshia, H., MacKay, D., & Suzuki, S. (1996). Bayesian neural network model for austenite formation in steels. *Materials Science and Technology*, *12*(6), 453–463.

Gaynor, A. T., & Guest, J. K. (2016). Topology optimization considering overhang constraints: Eliminating sacrificial support material in additive manufacturing through design. *Structural and Multidisciplinary Optimization*, *54*(5), 1157–1172.

Huang, C., Soliman, M., Treutler, K., Wesling, V., & Spitzer, K.-H. (2022). On the microstructure development under cyclic temperature conditions during waam of microalloyed steels. *Metals*, *12*(11), 1913.

Hughes, T. J. (1977). Unconditionally stable algorithms for nonlinear heat conduction. *Computer methods in applied mechanics and engineering*, *10*(2), 135–139.

Kelly, S., & Kampe, S. (2004). Microstructural evolution in laser-deposited multilayer ti-6al-4v builds: Part i. microstructural characterization. *Metallurgical and Materials Transactions A*, *35*(6), 1861–1867.

Kou, S. (2003). Welding metallurgy.

Langelaar, M. (2017). An additive manufacturing filter for topology optimization of print-ready designs. *Structural and multidisciplinary optimization*, *55*(3), 871–883.

Liu, J., Gaynor, A. T., Chen, S., Kang, Z., Suresh, K., Takezawa, A., Li, L., Kato, J., Tang, J., Wang, C. C., et al. (2018). Current and future trends in topology optimization for additive manufacturing. *Structural and Multidisciplinary Optimization*, *57*(6), 2457–2483.

Mishra, V., Babu, A., Schreurs, R., Wu, K., Hermans, M., & Ayas, C. (2023). Microstructure estimation and validation of er110s-g steel structures produced by wire and arc additive manufacturing. *Journal of Materials Research and Technology*.

Paul, R., Anand, S., & Gerner, F. (2014). Effect of thermal deformation on part errors in metal powder based additive manufacturing processes. *Journal of manufacturing science and Engineering*, *136*(3).

Pavlina, E., & Van Tyne, C. (2008). Correlation of yield strength and tensile strength with hardness for steels. *Journal of materials engineering and performance*, *17*(6), 888–893.

Ranjan, R., Ayas, C., Langelaar, M., & van Keulen, F. (2020). Fast detection of heat accumulation in powder bed fusion using computationally efficient thermal models. *Materials*, *13*(20), 4576.

Reisgen, U., Sharma, R., Mann, S., & Oster, L. (2020). Increasing the manufacturing efficiency of waam by advanced cooling strategies. *Welding in the World*, *64*(8), 1409–1416.

Rodrigues, T. A., Duarte, V., Avila, J. A., Santos, T. G., Miranda, R., & Oliveira, J. (2019). Wire and arc additive manufacturing of hsla steel: Effect of thermal cycles on microstructure and mechanical properties. *Additive Manufacturing*, *27*, 440–450.

Svanberg, K. (1987). The method of moving asymptotes—a new method for structural optimization. *International journal for numerical methods in engineering*, *24*(2), 359–373.

Tian, Y., McAllister, D., Colijn, H., Mills, M., Farson, D., Nordin, M., & Babu, S. (2014). Rationalization of microstructure heterogeneity in inconel 718 builds made by the direct laser additive manufacturing process. *Metallurgical and Materials Transactions A*, *45*(10), 4470–4483.

van de Ven, E., Maas, R., Ayas, C., Langelaar, M., & van Keulen, F. (2018). Continuous front propagation-based overhang control for topology optimization with additive manufacturing. *Structural and Multidisciplinary Optimization*, *57*(5), 2075–2091.

Wu, S., Zhang, Y., & Liu, S. (2019). Topology optimization for minimizing the maximum temperature of transient heat conduction structure. *Structural and Multidisciplinary Optimization*, *60*(1), 69–82.

Wu, S., Zhang, Y., & Liu, S. (2021). Transient thermal dissipation efficiency based method for topology optimization of transient heat conduction structures. *International Journal of Heat and Mass Transfer*, *170*, 121004.

Xu, W., Brandt, M., Sun, S., Elambasseril, J., Liu, Q., Latham, K., Xia, K., & Qian, M. (2015). Additive manufacturing of strong and ductile ti–6al–4v by selective laser melting via in situ martensite decomposition. *Acta Materialia*, *85*, 74–84.

Zhang, K., Cheng, G., & Xu, L. (2019). Topology optimization considering overhang constraint in additive manufacturing. *Computers & Structures*, *212*, 86–100.

7

CONCLUSIONS AND RECOMMENDATIONS

7.1. CONCLUSIONS

WAAM is an upcoming manufacturing technology that is suitable for manufacturing large-scale industrial parts. The technology is maturing rapidly and has found its application in the industry. This thesis is dedicated to develop TO methods to generate designs for WAAM focused on the manufacturability and mechanical performance of the manufactured part. By reflecting on the research questions outlined in the Introduction chapter, this chapter assesses the research output of this thesis and draws the main conclusions.

1. *How to identify and control intersections that are susceptible to WAAM defects in TO?*

Thin intersections are susceptible to WAAM defects. In compliance minimization TO, intersections can be identified by the multi-axial stress state. To control thin intersections an intersection objective is formulated to penalize thin intersections during optimization. Minimizing the thin intersections for WAAM leads to a reduction in the geometrical complexity of the TO design. It can be concluded that stress-based intersection detection was successful in controlling complexity and thin intersections in 2D compliance minimization problem.

The intersection control was also extended in 3D for an industrial case study of Ship Rudder. The method was effective to reduce the geometrical complexity of the rudder design so it is suitable for WAAM. To satisfy key design and manufacturing-related requirements for the ship rudder other TO methods such as density filter and symmetry filter are also applied. The optimized design was 20% lightweight than the original design. Through further post-processing, 10% weight reduction was achieved while achieving the equivalent mechanical performance compared to the original design. It can be concluded that the TO methods can generate early-stage designs which serve as an inspiration for lightweight final designs of mechanical parts for industrial applications.

2. *How to account and exploit for the elastic anisotropy in a TO framework?*

To account for elastic anisotropy, anisotropic material models can be used in the TO framework for instance cubic material model used for the WAAM-manufactured stainless steels parts. The anisotropy induced by WAAM can be exploited by optimizing the part design as well as the process design for the part. It is shown that a stiffness improvement of more than 50% can be achieved by optimizing the deposition direction simultaneously with the part design for WAAM-manufactured stainless steel parts. The optimized directions were oriented such that the highest elastic modulus direction of the material is in line with the load path direction of the part. The improvement in stiffness is proportional to the ratio of the highest and lowest elastic modulus of the anisotropic material. It can be concluded that to achieve maximum overall stiffness due to elastic material anisotropy, the deposition directions over a fixed part design should be oriented such that the highest elastic modulus direction of the material is aligned in line with the load path direction.

3. *How to model and validate the thermal history and phase transformations experienced by WAAM parts and their effect on the resulting microstructure and mechanical properties?*

The part scale thermal history due to the WAAM process can be modeled using the finite element activation method and the Goldak heat source model. The obtained thermal history is validated through comparisons with multiple thermocouple measurements. The phase transformations of the material point during WAAM are dominantly dependent on the cooling rate of a decisive cooling cycle. This is validated by analyzing micrographs and comparing hardness measurements to predictions. The resultant solid-state phases affect the hardness, yield strength, and ductility of the material point. It can be concluded that controlling the decisive thermal cooling cycle will enable control over the phase transformation during the WAAM process.

4. *How to account for the effect of the thermal history in a TO framework to obtain the desired microstructure and mechanical properties during WAAM?*

To account for the transient thermal effects in a TO framework the simplified process model should be used to reduce the computation cost of evaluating the the thermal history during optimization. The proposed weighted approach can be used to identify the decisive cooling cycle and evaluate the cooling time in the critical temperature range in a continuous and differentiable manner. The proposed constraint on the cooling time in the targeted control volume shows that the required cooling time can be achieved and consequently the required yield strength is achieved. The optimized design shows that to decrease the cooling time in the targeted region, material is added beneath it parallel to the build direction. To increase the cooling time the material is removed beneath the control volume and the heat input to the control volume is reduced. It can be concluded material addition and removal beneath the targeted design location can influence the transient thermal history and thus the microstructure development. Through the suggested TO approach required microstructure development can be achieved at the targeted design locations during WAAM, resulting in the required mechanical properties such as yield strength.

As an overall conclusion, the methods developed and presented in this thesis help to generate optimized, WAAM-friendly designs that even exploit the unique characteristics of the process and allow for tailoring of local material properties.

7.2. RECOMMENDATIONS

Based on the conducted research following recommendations for future research can be made:

* The WAAM process generally happens in a layer-by-layer manner. The thin intersection features in each layer may be susceptible to defects. The proposed extension of the intersection control to 3D TO framework does not ensure intersection identification in each layer. Further research is needed to determine if a stress-based planar intersection indicator can be defined for layered fabrication in a general 3D case.

* A series of post-processing steps still needs to be performed to generate the final design from an initial optimized design. For instance, the continuity of the branches, uniform cross-sections, and uniform spacing between branches. The post-processing steps must be formulated in a mathematical formulation to be included in the TO framework to get a manufacturable design from optimization

* For WAAM-manufactured stainless steel structures, optimized part design and process design are presented. These structures should be manufactured using WAAM and their stiffness response should be measured to validate the optimized results. Moreover, from the proposed TO approach the optimized deposition directions can be evaluated. However, the continuous deposition path from the deposition direction is still required. Automated generation of the deposition path from the given deposition direction distribution would be challenging.

* The microstructure estimation and validation are done for HSLA steels. However, these transformations are also observed in other materials. It should be investigated that the decisive cooling cycle from the complete thermal history also results in phase transformations for other WAAM materials. This will enlarge the scope of the presented TO methodology.

* Post-deposition heat treatment operations are essential for WAAM to relieve residual stresses. However, the temperature and cooling time during these operations also affect the microstructure development post-deposition. Accounting for the post-WAAM heat treatment operation on the microstructure development at the part design stage is essential and can be considered by the TO methods presented in this work.

* To account for the transient thermal effects in TO computationally inexpensive thermal models need to be developed. Vital information for microstructure development such as thermal gradients and cooling rate should be evaluated at very low computational cost from these developed thermal models. This could be equally challenging and beneficial to exploit the complete potential of TO for (WA)AM processes. The cooling rates can also be influenced by the modulation of deposition strategy and process parameters such as power input and travel speed. Future research can be in a direction where the part design is kept fixed, and the deposition strategy and process parameters are optimization variables.

Finally, in this thesis, the aspects related to Additive Manufacturing technology (WAAM), Material Science (metal microstructure), Computational Mechanics (Finite Element methods), and Optimization (TO) are combined together to generate optimized part and process design for WAAM. This research utilizes advances in various scientific areas and contributes to generate lightweight designs of mechanical components with required performance that find their application in industry. The author believes that this kind of interdisciplinary research is required to exploit the complete potential of the advances in various scientific areas. For instance, the problem to generate deposition paths through deposition direction requires close collaborative research from a computer scientist and a mechanical engineer. The automated process generated by the computer scientist can be improved by feedback from the mechanical engineer who uses the developed method for WAAM.

ACKNOWLEDGEMENTS

During the course of writing this work, I have received immense support from my support group. This support group has changed from time to time during the course of this thesis. In the initial stage, my family, friends, and fellow workers were the support group. My mother and father supported my stubbornness to pursue a Ph.D. I look back and realize that it was a critical juncture of my life and their support was invaluable. I would also thank *Rajit*, *Ashish*, *Sumit*, and *Nitish* for the great time we had living together and having fun in Delft. Many of them were also pursuing their Ph.D and have successfully defended their thesis. It was encouraging to see their dedication to research and it also inspired me to contribute my best towards research. At work, I would like to thank my fellow workers *Arnoud*, *Stijn*, *Rajit*, *Yong*, *Emiel*, *Lidan*, *Jian*, *Sabiju*, *Sanne*, and *Max* for all their support in solving any problems related to the research, teaching assistance, and office.

In the intermediate stage of the thesis, the world was hit by COVID and so was my life and research. During these difficult times, my wife, *Richa*, was my source of strength. She hoped to visit my hometown for the first time with expectations of a big celebration, however, Corona had other plans for her. The manner in which she showed strength in that situation was inspiring for me. I have no words to express those feelings. Adding to that living with me during my research was not an easy road for her. Adjusting to my work schedule, reading my papers for mistakes, listening to me during my mock presentations, living alone during my conference visits, and much more, while performing her own job was not easy for her. I love you, *Richa* and it is growing stronger. I like to thank you for your support, understanding, and, commitment towards this marriage.

I would also like to thank my supervisors, *Fred van Keulen*, *Can Ayas*, and *Matthijs Langelaar*, for understanding the Corona situation so seamlessly and doing everything in their capacity to provide me with help. I thank my younger brother too, *Aayush*, whose efforts during these times made me more calm than anxious. The support from my friends *Rajit*, *Mohit*, *Ashish*, *Srishti*, *Aviral*, *Pooja*, *Nitish*, *Akanksha*, *Prachee*, *Annant*, *Nakul*, *Prateek*, *Avinash* and others is invaluable. I would also like to acknowledge the support of the extended family members and family-in-law members during this time.

Finally, in the last phase of the thesis, I got immense support from *Aravind* on my collaborative work with him in the Material Science department. I would also thank *Marcel Hermans* for his guidance during the course of the research. A special mention to *Kai* with whom I traveled to a conference and had an amazing trip. I would also like to thank other PME group members, *Nils*, *Aditya*, and *Breno* for the nice lunch talks.

With all of your support, this thesis has become possible. Thank You!

Appendices

A

Appendix A

A.1. Sensitivity Analysis

The sensitivity calculation of the compliance objective and volume constraint is well known (Bendsoe and Sigmund, 2013) and given as follows:

$$\frac{\partial c}{\partial \tilde{\rho}_j} = -p(E_0 - E_{min})\tilde{\rho}_j^{p-1}\mathbf{u}_j^T\mathbf{k_0}\mathbf{u}_j. \tag{A.1}$$

$$\frac{\partial g}{\partial \tilde{\rho}_j} = \frac{v_j}{V_0}. \tag{A.2}$$

The sensitivity of the intersection objective is calculated by applying the quotient, product and chain rules of derivatives. The sensitivity calculation is shown for a single loadcase problem for clarity and it can be extended to multi loadcase problem with minor modification. Firstly, design differentiation of Eq. (2.20),yields:

$$\frac{\partial I}{\partial \tilde{\rho}_j} = -V_0 \frac{\sum_{\Omega_N} \hat{s}_e I_e}{(\sum_{\Omega_N} \tilde{\rho}_e v_e)^2} \sum_{\Omega_N} \frac{\partial \tilde{\rho}_e}{\partial \tilde{\rho}_j} v_e + \frac{V_0}{(\sum_{\Omega_N} \tilde{\rho}_e v_e)} \sum_{\Omega_N} \frac{\partial (\hat{s}_e I_e)}{\partial \tilde{\rho}_j}. \tag{A.3}$$

The term $\dfrac{\partial \tilde{\rho}_e}{\partial \tilde{\rho}_j} = \delta_{ej}$, where δ_{ej} is the Kronecker delta function, thus the above equation reduces to:

$$\frac{\partial I}{\partial \tilde{\rho}_j} = -V_0 v_j \frac{\sum_{\Omega_N} \hat{s}_e I_e}{(\sum_{\Omega_N} \tilde{\rho}_e v_e)^2} + \frac{V_0}{(\sum_{\Omega_N} \tilde{\rho}_e v_e)} \sum_{\Omega_N} \frac{\partial (\hat{s}_e I_e)}{\partial \tilde{\rho}_j}. \tag{A.4}$$

Now the product rule is applied to the later part of the above equation using Eq. (2.18), as shown below:

$$\sum_{\Omega_N} \frac{\partial (\hat{s}_e I_e)}{\partial \tilde{\rho}_j} = \sum_{\Omega_N} \left(-I_e \frac{\partial \hat{\tilde{\rho}}_e}{\partial \tilde{\rho}_j} + (1 - \hat{\tilde{\rho}}_e) \frac{\partial I_e}{\partial \tilde{\rho}_j} \right). \tag{A.5}$$

In the above equation, the term $\frac{\partial \hat{\tilde{\rho}}_e}{\partial \tilde{\rho}_j}$, can be derived from Eq. (2.17) as shown below:

$$\sum_{\Omega_N} -I_e \frac{\partial \hat{\tilde{\rho}}_e}{\partial \tilde{\rho}_j} = \sum_{\Omega_N} -I_e \frac{\sum_{\Omega_e^{\text{int}}} w_i v_i \frac{\partial \tilde{\rho}_i}{\partial \tilde{\rho}_j}}{\sum_{\Omega_e^{\text{int}}} w_i v_i}. \tag{A.6}$$

Now, since filtered densities are independent variables thus, the above equation can be written as:

$$\frac{\partial \hat{\tilde{\rho}}_e}{\partial \tilde{\rho}_j} = \begin{cases} \dfrac{w_j v_j}{\sum_{\Omega_e^{\text{int}}} w_i v_i} & \text{if, } i = j, \\ 0 & \text{if, } i \neq j. \end{cases} \tag{A.7}$$

To calculate the term with $\frac{\partial I_e}{\partial \tilde{\rho}_j}$ in Eq. (A.5), the product rule is applied to Eq. (2.13). With some simplifications and using Eq. (2.8), Eq. (2.9), Eq. (2.12) and Eq. (2.13) the term can be reduced to the following form:

$$\begin{aligned} \sum_{\Omega_N} (1 - \hat{\tilde{\rho}}_e) \frac{\partial I_e}{\partial \tilde{\rho}_j} &= \frac{p \tilde{\rho}_j^{p-1} (1 - \hat{\tilde{\rho}}_j)}{\log_2(H_j)} \\ &\quad - \frac{p \tilde{\rho}_j^{2p-1} (1 - \hat{\tilde{\rho}}_j)}{\ln(2) (\log_2(H_j))^2} \left[\frac{\partial H_j}{\partial \sigma_p} \right] \left[\frac{\partial \sigma_p}{\partial \sigma_j} \right] \mathbf{D}_j \mathbf{B}_j \mathbf{u}_j \\ &\quad - \sum_{\Omega_N} \frac{\tilde{\rho}_e^{2p} (1 - \hat{\tilde{\rho}}_e)}{\ln(2) (\log_2(H_e))^2} \left[\frac{\partial H_e}{\partial \sigma_p} \right] \left[\frac{\partial \sigma_p}{\partial \sigma_e} \right] \mathbf{D}_e \mathbf{B}_e \frac{\partial \mathbf{u}_e}{\partial \tilde{\rho}_j}. \end{aligned} \tag{A.8}$$

where,

$$\left[\frac{\partial H_e}{\partial \sigma_p} \right] = \begin{bmatrix} \dfrac{\partial H_e}{\partial \sigma_I} & \dfrac{\partial H_e}{\partial \sigma_{II}} \end{bmatrix}, \tag{A.9}$$

$$\left[\frac{\partial \sigma_p}{\partial \sigma_e} \right] = \begin{bmatrix} \dfrac{\partial \sigma_I}{\partial \sigma_{xx}} & \dfrac{\partial \sigma_I}{\partial \sigma_{yy}} & \dfrac{\partial \sigma_I}{\partial \tau_{xy}} \\ \dfrac{\partial \sigma_{II}}{\partial \sigma_{xx}} & \dfrac{\partial \sigma_{II}}{\partial \sigma_{yy}} & \dfrac{\partial \sigma_{II}}{\partial \tau_{xy}} \end{bmatrix}, \tag{A.10}$$

$$\left[\frac{\partial \sigma_e}{\partial \tilde{\rho}_j} \right] = \begin{bmatrix} \dfrac{\partial \sigma_{xx}}{\partial \tilde{\rho}_j} & \dfrac{\partial \sigma_{yy}}{\partial \tilde{\rho}_j} & \dfrac{\partial \tau_{xy}}{\partial \tilde{\rho}_j} \end{bmatrix}^T. \tag{A.11}$$

The sensitivity calculation of individual terms is given subsequently as

$$\left[\frac{\partial H_e}{\partial \sigma_p} \right] = \begin{bmatrix} \dfrac{\partial H_e}{\partial \sigma_I} & \dfrac{\partial H_e}{\partial \sigma_{II}} \end{bmatrix} \tag{A.12}$$

where,

$$\frac{\partial H_e}{\partial \sigma_I} = \frac{2\sigma_I}{\sigma_{II}^2+\sigma_0^2} - \frac{2\sigma_I(\sigma_{II}^2+\sigma_0^2)}{(\sigma_I^2+\sigma_0^2)^2} \tag{A.13}$$

$$\frac{\partial H_e}{\partial \sigma_{II}} = \frac{2\sigma_{II}}{\sigma_I^2+\sigma_0^2} - \frac{2\sigma_{II}(\sigma_I^2+\sigma_0^2)}{(\sigma_{II}^2+\sigma_0^2)^2} \tag{A.14}$$

$$\left[\frac{\partial \sigma_p}{\partial \sigma_e}\right] = \begin{bmatrix} \frac{\partial \sigma_I}{\partial \sigma_{xx}} & \frac{\partial \sigma_I}{\partial \sigma_{yy}} & \frac{\partial \sigma_I}{\partial \tau_{xy}} \\ \frac{\partial \sigma_{II}}{\partial \sigma_{xx}} & \frac{\partial \sigma_{II}}{\partial \sigma_{yy}} & \frac{\partial \sigma_{II}}{\partial \tau_{xy}} \end{bmatrix} \tag{A.15}$$

where,

$$\frac{\partial \sigma_I}{\partial \sigma_{xx}} = \frac{1}{2} + \frac{1}{4}\frac{\sigma_{xx}-\sigma_{yy}}{\sqrt{\frac{(\sigma_{xx}-\sigma_{yy})^2}{4}+\tau_{xy}^2}} \tag{A.16}$$

$$\frac{\partial \sigma_I}{\partial \sigma_{yy}} = \frac{1}{2} - \frac{1}{4}\frac{\sigma_{xx}-\sigma_{yy}}{\sqrt{\frac{(\sigma_{xx}-\sigma_{yy})^2}{4}+\tau_{xy}^2}} \tag{A.17}$$

$$\frac{\partial \sigma_I}{\partial \tau_{xy}} = \frac{\tau xy}{\sqrt{\frac{(\sigma_{xx}-\sigma_{yy})^2}{4}+\tau_{xy}^2}} \tag{A.18}$$

$$\frac{\partial \sigma_{II}}{\partial \sigma_{xx}} = \frac{1}{2} - \frac{1}{4}\frac{\sigma_{xx}-\sigma_{yy}}{\sqrt{\frac{(\sigma_{xx}-\sigma_{yy})^2}{4}+\tau_{xy}^2}} \tag{A.19}$$

$$\frac{\partial \sigma_{II}}{\partial \sigma_{yy}} = \frac{1}{2} + \frac{1}{4}\frac{\sigma_{xx}-\sigma_{yy}}{\sqrt{\frac{(\sigma_{xx}-\sigma_{yy})^2}{4}+\tau_{xy}^2}} \tag{A.20}$$

$$\frac{\partial \sigma_{II}}{\partial \tau_{xy}} = \frac{-\tau_{xy}}{\sqrt{\frac{(\sigma_{xx}-\sigma_{yy})^2}{4}+\tau_{xy}^2}} \tag{A.21}$$

Now, in order to calculate the last term of Eq. (A.8), the adjoint method is used by adding the sensitivity of the state equation, given in Eq. (2.22) with Lagrange multiplier ($\boldsymbol{\lambda}$) to above equation. This leads to following equation:

$$\begin{aligned}\sum_{\Omega_N}(1-\hat{\tilde{\rho}}_e)\frac{\partial I_e}{\partial\tilde{\rho}_j} = {} & \frac{p\tilde{\rho}_j^{p-1}(1-\hat{\tilde{\rho}}_j)}{\log_2(H_j)} \\ & - \frac{p\tilde{\rho}_j^{2p-1}(1-\hat{\tilde{\rho}}_j)}{\ln(2)(\log_2(H_j))^2}\left[\frac{\partial H_j}{\partial\sigma_p}\right]\left[\frac{\partial\sigma_p}{\partial\sigma_j}\right]\mathbf{D}_j\mathbf{B}_j\mathbf{u}_j \\ & - \sum_{\Omega_N}\frac{\tilde{\rho}_e^{2p}(1-\hat{\tilde{\rho}}_e)}{\ln(2)(\log_2(H_e))^2}\left[\frac{\partial H_e}{\partial\sigma_p}\right]\left[\frac{\partial\sigma_p}{\partial\sigma_e}\right]\mathbf{D}_e\mathbf{B}_e\frac{\partial\mathbf{u}_e}{\partial\tilde{\rho}_j} \\ & + \boldsymbol{\lambda}^T\left(\frac{\partial\mathbf{K}}{\partial\tilde{\rho}_j}\mathbf{u}+\mathbf{K}\frac{\partial\mathbf{u}}{\partial\tilde{\rho}_j}\right).\end{aligned} \tag{A.22}$$

The Lagrange multiplier can be chosen such that the state sensitivity terms vanish. To this end the following adjoint equation can be solved:

$$\mathbf{K}\boldsymbol{\lambda} = \sum_{\Omega_N}\frac{\tilde{\rho}_e^{2p}(1-\hat{\tilde{\rho}}_e)}{\ln(2)(\log_2(H_e))^2}\mathbf{B}_e^T\mathbf{D}_e^T\left[\frac{\partial\sigma_p}{\partial\sigma_e}\right]^T\left[\frac{\partial H_e}{\partial\sigma_p}\right]^T. \tag{A.23}$$

Finally, Eq. (A.22) is evaluated as follows:

$$\begin{aligned}\sum_{\Omega_N}(1-\hat{\tilde{\rho}}_e)\frac{\partial I_e}{\partial\tilde{\rho}_j} = {} & \frac{p\tilde{\rho}_j^{p-1}(1-\hat{\tilde{\rho}}_j)}{\log_2(H_j)} \\ & - \frac{p\tilde{\rho}_j^{2p-1}(1-\hat{\tilde{\rho}}_j)}{\ln(2)(\log_2(H_j))^2}\left[\frac{\partial H_j}{\partial\sigma_p}\right]\left[\frac{\partial\sigma_p}{\partial\sigma_j}\right]\mathbf{D}_j\mathbf{B}_j\mathbf{u}_j \\ & + \boldsymbol{\lambda}^T\frac{\partial\mathbf{K}}{\partial\tilde{\rho}_j}\mathbf{u}.\end{aligned} \tag{A.24}$$

The sensitivity analysis shown above is for the single load case. For multiple load-cases, the main differences are using the H_e term expressed in Eq. (2.16), and that multiple state equations must be used for the adjoint method and thus, multiple adjoint equations have to be solved to calculate the Lagrange multipliers associated to each state equation. The process of calculating the Lagrange multiplier is the same as shown in this section.

B

Appendix B

B.1. Material Modelling

The compliance matrix for a coordinate system rotated by $\theta = \pi/4$ in the counter clockwise direction with respect to the global coordinates $X - Y$ can be expressed as follows

$$\mathbf{Q}^{'}(\theta) = \begin{bmatrix} Q_{11} & Q_{12} & Q_{16} \\ Q_{21} & Q_{22} & Q_{26} \\ Q_{61} & Q_{62} & Q_{66} \end{bmatrix} \tag{B.1}$$

Each component of the matrix $\mathbf{Q}^{'}(\theta)$ depends upon the amount of rotation θ with respect to the global axes. The subscripts representing the component of the matrix are adopted from (Reddy, 1987) for plane stress conditions. The rotated coordinate system with $1-2$ axes are shown in Fig. 4.1. The Young's Modulus E_1 and E_2 along direction 1 and 2 are equal to $1/Q_{11}$ and $1/Q_{22}$, respectively. The shear modulus G_{12} in $1-2$ plane is equal to $1/Q_{66}$. The variation of E_1, E_2 and G_{12} as a function of θ is given in Fig. B.1. The value of E_1 and E_2 remains identical irrespective of θ. Also, it can be observed cubic symmetry in elasticity is essentially a rotational symmetry by $\pi/2$.

B.2. Sensitivity Analysis

For gradient-based optimization, the sensitivities of the objective function ϕ with respect to the design variables are required. The sensitivities of the objective with respect to the filtered density variable (Bendsoe and Sigmund, 2013) is

$$\frac{\partial \phi}{\partial \tilde{\rho}_e} = -\mathbf{u}_e^{\mathrm{T}} \frac{\partial \mathbf{k}_e}{\partial \tilde{\rho}_e} \mathbf{u}_e. \tag{B.2}$$

Here, $\dfrac{\partial \mathbf{k}_e}{\partial \tilde{\rho}_e}$ is given as follows

$$\frac{\partial \mathbf{k}_e}{\partial \tilde{\rho}_e} = p\tilde{\rho}_e^{p-1} \sum_{i=1}^{2} \sum_{j=1}^{2} w_{ij} (\det(\mathbf{J}))_{ij} \mathbf{B}_{ij}^{\mathrm{T}} \mathbf{T}^{\mathrm{T}} \mathbf{D} \mathbf{T} \mathbf{B}_{ij}. \tag{B.3}$$

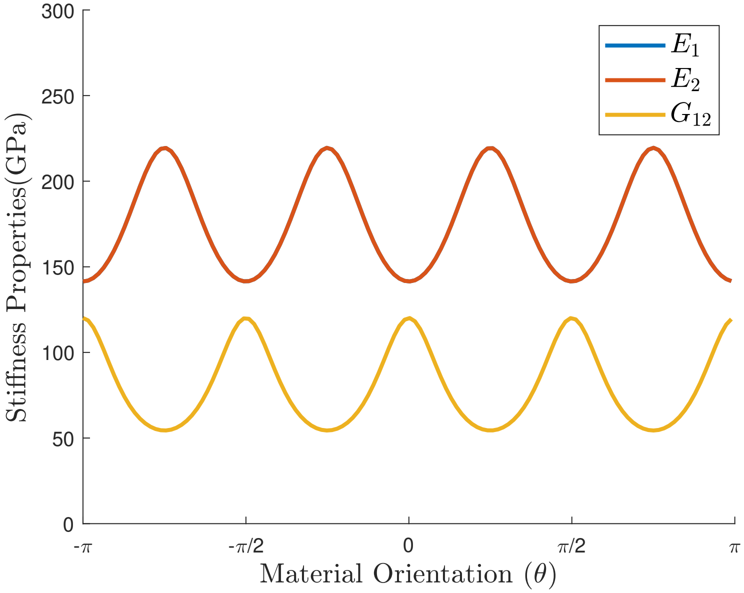

Figure B.1: Variation of the elastic properties with respect to the material orientation (θ)

Similarly, the sensitivities with respect to the deposition direction vector components is calculated by chain rule as shown below

$$\frac{\partial \phi}{\partial x_e} = \frac{\partial \phi}{\partial \theta_e}\frac{\partial \theta_e}{\partial x_e}, \tag{B.4}$$

$$\frac{\partial \phi}{\partial y_e} = \frac{\partial \phi}{\partial \theta_e}\frac{\partial \theta_e}{\partial y_e}. \tag{B.5}$$

Now, $\theta_e = \tan^{-1}(y_e, x_e)$, therefore the terms $\dfrac{\partial \theta_e}{\partial x_e}$ and $\dfrac{\partial \theta_e}{\partial y_e}$ follows

$$\frac{\partial \theta_e}{\partial x_e} = \frac{-y_e}{x_e^2 + y_e^2}, \tag{B.6}$$

$$\frac{\partial \theta_e}{\partial y_e} = \frac{x_e}{x_e^2 + y_e^2}. \tag{B.7}$$

Furthermore, $\dfrac{\partial \phi}{\partial \theta_e}$ is given as

$$\frac{\partial \phi}{\partial \theta_e} = -\mathbf{u}_e^{\mathrm{T}}\frac{\partial \mathbf{k}_e}{\partial \theta_e}\mathbf{u}_e. \tag{B.8}$$

Finally, $\dfrac{\partial \mathbf{k}_e}{\partial \theta_e}$ is calculated as following

$$\frac{\partial \mathbf{k}_e}{\partial \theta_e} = \tilde{\rho}_e^p \sum_{i=1}^{2} \sum_{j=1}^{2} w_{ij} (\det(\mathbf{J}))_{ij} \left[\mathbf{B}_{ij}^{\mathrm{T}} \frac{\partial \mathbf{T}^{\mathrm{T}}}{\partial \theta_e} \mathbf{DTB}_{ij} + \mathbf{B}_{ij}^{\mathrm{T}} \mathbf{T}^{\mathrm{T}} \mathbf{D} \frac{\partial \mathbf{T}}{\partial \theta_e} \mathbf{B}_{ij} \right]. \tag{B.9}$$

B.3. EFFECT OF INITIAL STATE ON OPTIMIZATION

The optimized deposition directions depend on initial state of the design variables. The density variables at the start of the optimization are equal to 0.5 for each element. Three sets of initial deposition states are chosen to investigate the effect on optimized deposition directions. The deposition vectors corresponding to 0° 90° and *random* orientation are chosen for each element at the start of the optimization. The optimized deposition directions corresponding to the three different starting points for Cantilever and Bridge problems are shown in Fig. B.1. It shows that the optimized deposition patterns are highly dependent upon the initial state. This is due to the rotational symmetry in the material model. Fig. B.2 shows for different initial states the stiffest directions corresponding to the optimized deposition directions. It can be inferred that the optimizer is aligning the stiffest direction along the structural members irrespective of the initial state of design variables.

The results post processed by Eq. (4.9) and Eq. (4.10) are shown in Fig. B.3. It can be observed that after post processing the optimized deposition directions are identical for all the three selected initial states.

B.4. CONVERGENCE BEHAVIOUR

The convergence of the elastic strain energy (ϕ) as a function of number of optimization iterations for different initial states is investigated. The convergence behaviour is shown in Fig. B.1 for the cantilever and the bridge problems. It is observed that the elastic strain energies for different initial states converge to the same value for each problem. Moreover, convergence seems to show a same trend for each starting point. This also confirms the finding that the solution to the problem is aligning the stiffest direction to the load path of the structure, however, due to the symmetry of the material the optimized deposition directions are different.

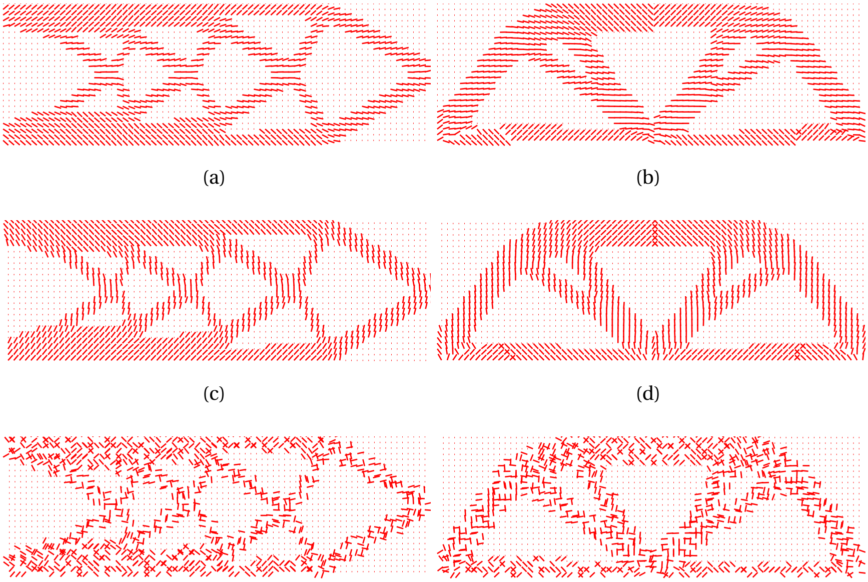

(a) (b)

(c) (d)

(e) (f)

Figure B.1: Effect of initial state on optimized design layout and optimized deposition directions: (a), (c) and (e) provide optimized design layouts and optimized deposition directions with initial states as 0°, 90° and completely random for the cantilever problem. (b), (d) and (f) show optimized design layouts and optimized deposition directions with initial states as 0°, 90° and completely random for the bridge problem.

.

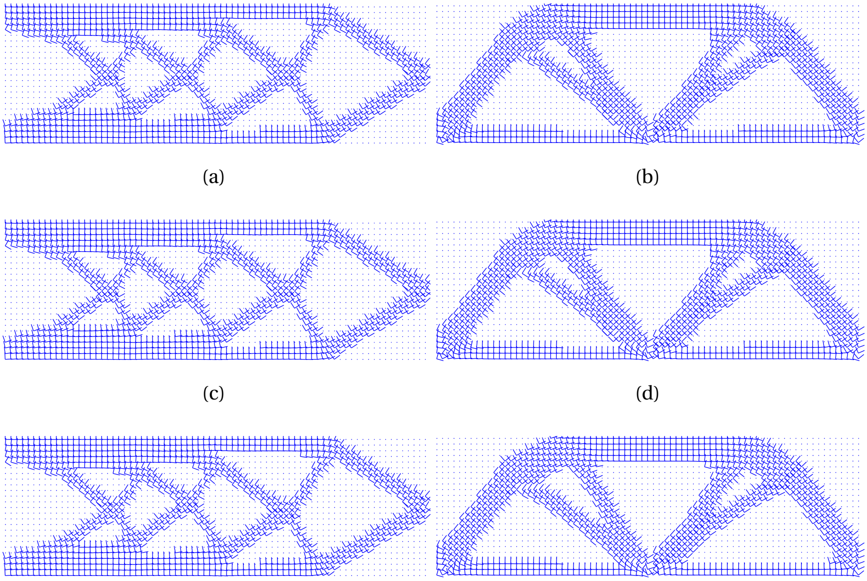

(a) (b)

(c) (d)

(e) (f)

Figure B.2: Effect of initial state on optimized design layout and optimized deposition directions: (a), (c) and (e) show stiffest material directions corresponding to the optimized deposition directions with initial states as 0°, 90° and completely random for the cantilever problem. (b), (d) and (f) depict the stiffest material directions corresponding to the optimized deposition directions with initial states as 0°, 90° and completely random for the bridge problem.

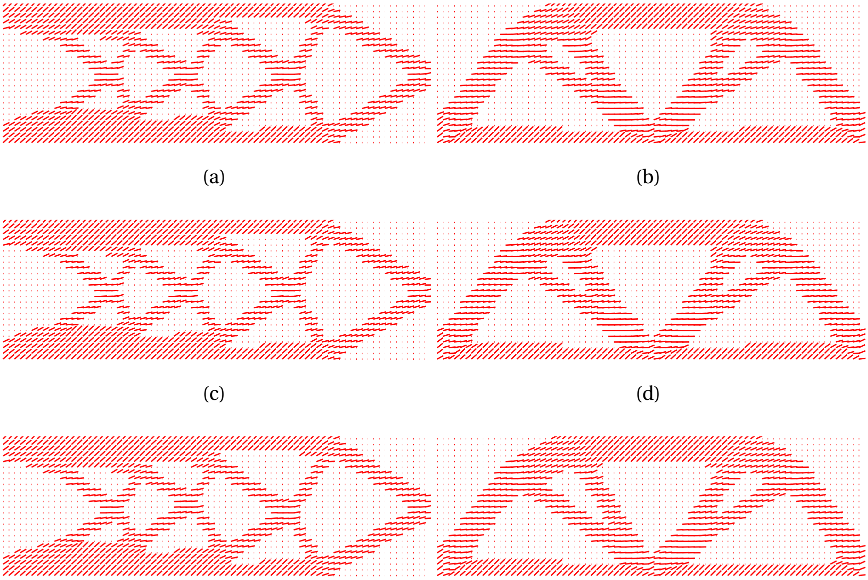

(a) (b)

(c) (d)

(e) (f)

Figure B.3: Effect of initial states on optimized layout and optimized deposition directions: (a), (c) and (e) depict post processed optimized deposition directions with initial states as 0°, 90° and completely random for the cantilever problem. (b), (d) and (f) show post processed optimized deposition directions with initial states as 0°, 90° and completely random for the bridge problem.

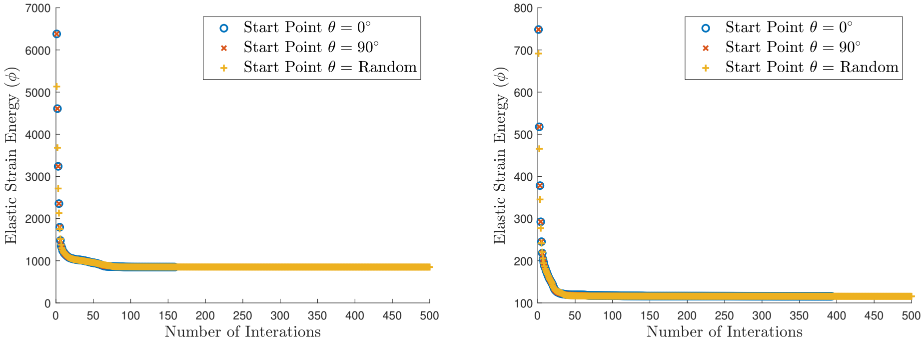

(a) (b)

Figure B.1: Convergence behaviour - Convergence of the elastic strain energy with respect to the number of iteration steps for different initial states for (a) Cantilever and (b) Bridge problem.

C

Appendix C

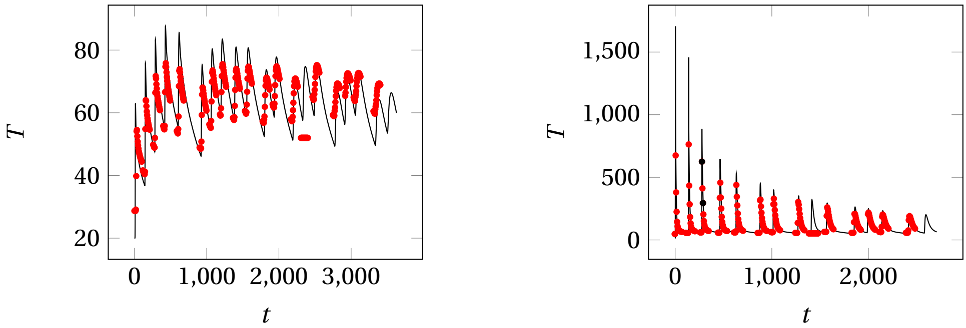

(a) S2L00

(b) S2L05

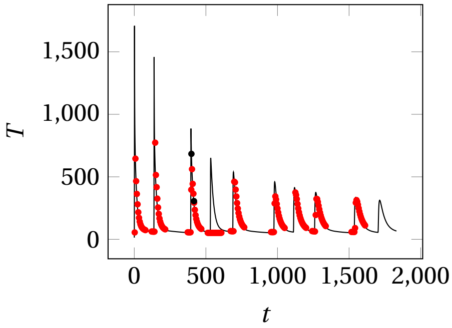

(c) S2L10

Figure C.1: Temperature Data from thermocouple associated to specimen S2 (red data points) compared with the thermal history obtained from the thermal modelling (black solid line). The black dots denote the thermocouple data points which are used to calculate the cooling rate of the critical cycle from the experimental data.

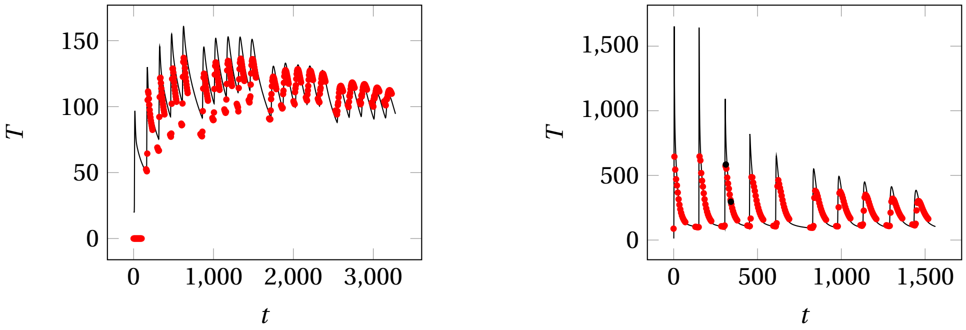

(a) S3L00

(b) S3L10

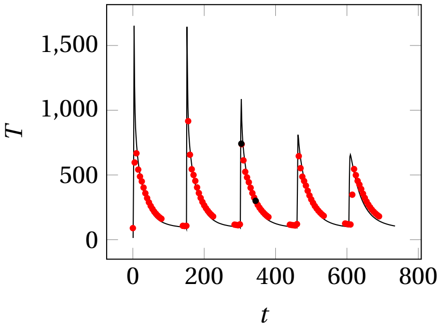

(c) S3L15

Figure C.2: Temperature Data from thermocouple associated to specimen S3 (red data points) compared with the thermal history obtained from the thermal modelling (black solid line). The black dots denote the thermocouple data points which are used to calculate the cooling rate of the critical cycle from the experimental data.

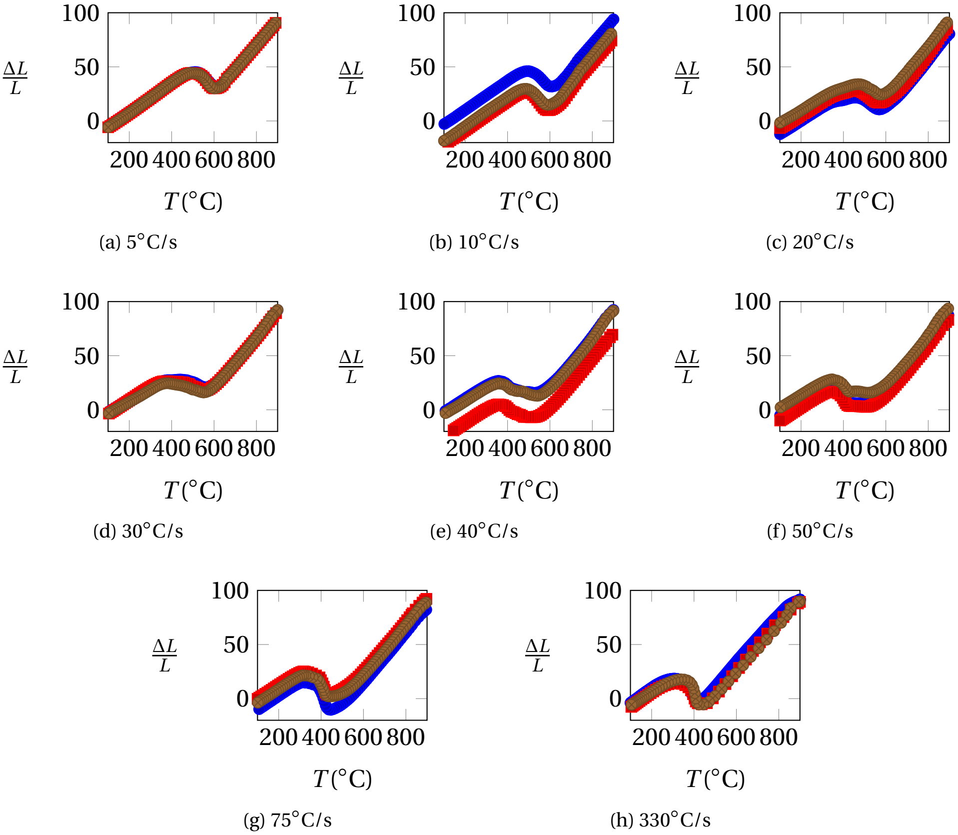

(a) 5°C/s

(b) 10°C/s

(c) 20°C/s

(d) 30°C/s

(e) 40°C/s

(f) 50°C/s

(g) 75°C/s

(h) 330°C/s

Figure C.3: Raw Dilatometry Data for different cooling rate. For each cooling rate 3 sets of data are generated.

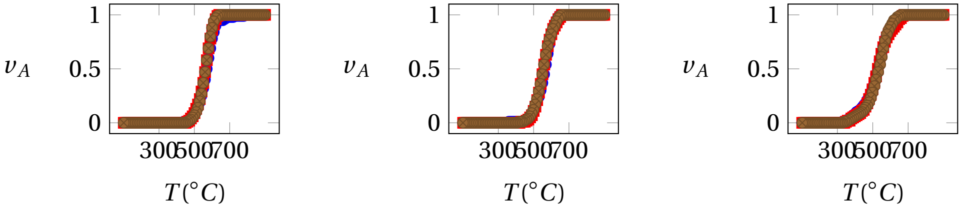

(a) 5$^\circ C/s$ (b) 10$^\circ C/s$ (c) 20$^\circ C/s$

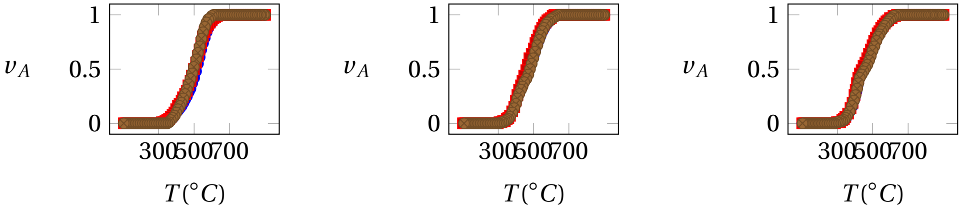

(d) 30$^\circ C/s$ (e) 40$^\circ C/s$ (f) 50$^\circ C/s$

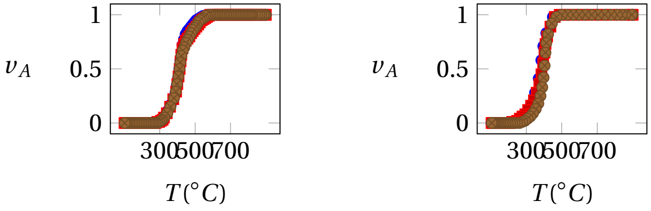

(g) 75$^\circ C/s$ (h) 330$^\circ C/s$

Figure C.4: Austenite volume fraction (v_A) as the function of Temperature calculated from the dilatometry data using the lever rule.

D

APPENDIX D

D.1. SENSITIVITY CALCULATIONS

The design sensitivity calculation of the average cooling time constraint given in Eq. (6.35) is as follows:

$$\frac{\partial}{\partial \rho_e}\left[\frac{1}{N_c}\sum_{\Omega_c}\tilde{\mathfrak{t}}_n\right] = \frac{1}{N_c}\sum_{\Omega_c}\frac{\partial \tilde{\mathfrak{t}}_n}{\partial \rho_e} = \frac{1}{N_c}\sum_{\Omega_c}\frac{\partial}{\partial \rho_e}\left(\frac{\sum_{j=i}^{L}\left[{}^{l_i}_{l_j} r_n\right]\left[{}^{l_i}_{l_j} s_n\right]\left[{}^{l_i}_{l_j}\tilde{\mathfrak{t}}_n\right]}{\sum_{j=i}^{L}\left[{}^{l_i}_{l_j} r_n\right]\left[{}^{l_i}_{l_j} s_n\right]}\right) \tag{D.1}$$

Applying the quotient rule and subsequently, the product rule of derivatives on the above equation will yield

$$\begin{aligned}\frac{\partial \tilde{\mathfrak{t}}_n}{\partial \rho_e} = & \frac{1}{\left(\sum_{j=i}^{L}\left[{}^{l_i}_{l_j} r_n\right]\left[{}^{l_i}_{l_j} s_n\right]\right)^2}\Bigg[\left(\sum_{j=i}^{L}\left[{}^{l_i}_{l_j} r_n\right]\left[{}^{l_i}_{l_j} s_n\right]\right)\Bigg(\sum_{j=i}^{L}\frac{\partial\left[{}^{l_i}_{l_j} r_n\right]}{\partial \rho_e}\left[{}^{l_i}_{l_j} r_n\right]\left[{}^{l_i}_{l_j}\tilde{\mathfrak{t}}_n\right] \\ & + \sum_{j=i}^{L}\left[{}^{l_i}_{l_j} r_n\right]\left[{}^{l_i}_{l_j} s_n\right]\frac{\partial\left[{}^{l_i}_{l_j}\tilde{\mathfrak{t}}_n\right]}{\partial \rho_e}\Bigg) - \left(\sum_{j=i}^{L}\left[{}^{l_i}_{l_j} r_n\right]\left[{}^{l_i}_{l_j} s_n\right]\left[{}^{l_i}_{l_j}\tilde{\mathfrak{t}}_n\right]\right)\left(\sum_{j=i}^{L}\left[{}^{l_i}_{l_j} s_n\right]\frac{\partial\left[{}^{l_i}_{l_j} r_n\right]}{\partial \rho_e}\right)\Bigg]\end{aligned} \tag{D.2}$$

In above equation, $\frac{\partial\left[{}^{l_i}_{l_j}\tilde{\mathfrak{t}}_n\right]}{\partial \rho_e}$ and $\frac{\partial\left[{}^{l_i}_{l_j} r_n\right]}{\partial \rho_e}$ are important terms which need to be evaluated. The sequential weight is independent of the design variable, thus, the design sensitivity of the sequential weight is 0. The calculation of $\frac{\partial\left[{}^{l_i}_{l_j}\tilde{\mathfrak{t}}_n\right]}{\partial \rho_e}$ is done using Eq. (6.24). In subsequent equations, the dependent variable parentheses are dropped to show the calculation in a succinct manner. Applying the product rule and chain rule gives

$$\frac{\partial\left[{}^{l_i}_{l_j}\tilde{\mathfrak{t}}_n\right]}{\partial \rho_e} = \int_{\tau_{l_{j-1}}}^{\tau_{l_j}}\left[{}^{l_i}_{l_j} H_n\right]\left(\bar{H}\frac{\partial \underline{H}}{\partial\left[{}^{l_i}_{l_j} T_n\right]} + \frac{\partial \bar{H}}{\partial\left[{}^{l_i}_{l_j} T_n\right]}\underline{H}\right)\frac{\partial\left[{}^{l_i}_{l_j} T_n\right]}{\partial \rho_e}dt \tag{D.3}$$

Eq. (6.19) and Eq. (6.20) are used to evaluate $\frac{\partial \underline{H}}{\partial [{}^{l_i}_{l_j}T_n]}$ and $\frac{\partial \bar{H}}{\partial [{}^{l_i}_{l_j}T_n]}$. The derivative operations are trivial, therefore, not presented here. However, The evaluation of the term $\frac{\partial [{}^{l_i}_{l_j}T_n]}{\partial \rho_e}$ is not trivial. Adjoint method is employed to calculate $\frac{\partial [{}^{l_i}_{l_j}T_n]}{\partial \rho_e}$. For this purpose, let us introduce following representation for the nodal temperature

$$[{}^{l_i}_{l_j}T_n](t) := \mathbf{R}_n^T \mathbf{T}_{l_j}(t) \tag{D.4}$$

Here, $\mathbf{R}_n$ is the array of length equal to $\mathbf{T}_{l_j}$. The array $\mathbf{R}_n$ has entry 1 at the interested degree of freedom, i.e. node n, and 0 elsewhere. Therefore, the Eq. (D.3) becomes

$$\frac{\partial [{}^{l_i}_{l_j}\tilde{\mathfrak{t}}_n]}{\partial \rho_e} = \int_{\tau_{l_{j-1}}}^{\tau_{l_j}} [{}^{l_i}_{l_j}H_n]\left(\bar{H}\frac{\partial \underline{H}}{\partial [{}^{l_i}_{l_j}T_n]} + \frac{\partial \bar{H}}{\partial [{}^{l_i}_{l_j}T_n]}\underline{H}\right)\mathbf{R}_n^T \frac{\partial \mathbf{T}_{l_j}}{\partial \rho_e} dt \tag{D.5}$$

Note, $[{}^{l_i}_{l_j}H_n] = 0$, if $\tau_{l_{j-1}} \leq t < \tau^{\mathfrak{h}}_{l_j} + \Delta\tau^{l_i}_{l_j}$, therefore the contribution to the sensitivities of the above integration in range $\tau_{l_{j-1}} \leq t < \tau^{\mathfrak{h}}_{l_j} + \Delta\tau^{l_i}_{l_j}$ will be 0.

Similar to $\frac{\partial [{}^{l_i}_{l_j}\tilde{\mathfrak{t}}_n]}{\partial \rho_e}$, $\frac{\partial [{}^{l_i}_{l_j}r_n]}{\partial \rho_e}$ can also be represented in the integral form which includes $\frac{\partial \mathbf{T}_{l_j}}{\partial \rho_e}$ term. To evaluate the design sensitivities of the weight term Eq. (6.25) is used. Applying chain rule we get

$$\frac{\partial [{}^{l_i}_{l_j}r_n]}{\partial \rho_e} = \frac{\partial [{}^{l_i}_{l_j}r_n]}{\partial [{}^{l_i}_{l_j}\mathrm{T}_n]}\frac{\partial [{}^{l_i}_{l_j}\mathrm{T}_n]}{\partial \rho_e}. \tag{D.6}$$

The term $\frac{\partial [{}^{l_i}_{l_j}r_n]}{\partial [{}^{l_i}_{l_j}\mathrm{T}_n]}$ is trivial to calculate. To calculate the non-trivial term $\frac{\partial [{}^{l_i}_{l_j}\mathrm{T}_n]}{\partial \rho_e}$ we re-write the $[{}^{l_i}_{l_j}\mathrm{T}_n]$ as follows:

$$[{}^{l_i}_{l_j}\mathrm{T}_n] = \int_{-\infty}^{\infty} \delta(t - (\tau^{\mathfrak{h}}_{l_j} + \Delta\tau^{l_i}_{l_j}))\mathbf{R}_n^T \mathbf{T}_{l_j}(t) dt \tag{D.7}$$

Now, taking the design sensitivity of the above equation we get:

$$\frac{\partial [{}^{l_i}_{l_j}\mathrm{T}_n]}{\partial \rho_e} = \int_{-\infty}^{\infty} \delta(t - (\tau^{\mathfrak{h}}_{l_j} + \Delta\tau^{l_i}_{l_j}))\mathbf{R}_n^T \frac{\partial \mathbf{T}_{l_j}}{\partial \rho_e} dt = \int_{\tau_{l_{j-1}}}^{\tau_{l_j}} \delta(t - (t^{\mathfrak{h}}_{l_j} + \Delta\tau^{l_i}_{l_j}))\mathbf{R}_n^T \frac{\partial \mathbf{T}_{l_j}}{\partial \rho_e} dt \tag{D.8}$$

Where, δ is the dirac delta function which is equal 1 at $t = \tau^{\mathfrak{h}}_{l_j} + \Delta\tau^{l_i}_{l_j}$.

Both the term $\dfrac{\partial[\,{}^{l_i}_{l_j}\tilde{\mathfrak{t}}_n]}{\partial\rho_e}$ and $\dfrac{\partial[\,{}^{l_i}_{l_j}r_n]}{\partial\rho_e}$ represented in the form of $\dfrac{\partial\mathbf{T}_{l_j}}{\partial\rho_e}$ can be substituted in Eq. (D.2). Firstly, we rewrite the terms in Eq. (D.2) by grouping the terms associated to $\dfrac{\partial[\,{}^{l_i}_{l_j}\tilde{\mathfrak{t}}_n]}{\partial\rho_e}$ and $\dfrac{\partial[\,{}^{l_i}_{l_j}r_n]}{\partial\rho_e}$ together as follows:

$$
\begin{aligned}
\frac{\partial\tilde{\mathfrak{t}}_n}{\partial\rho_e} = \frac{1}{\left(\sum_{j=i}^{L}[\,{}^{l_i}_{l_j}r_n][\,{}^{l_i}_{l_j}s_n]\right)^2}\sum_{j=i}^{L}\Bigg[\Bigg\{\Bigg(\sum_{j=i}^{L}[\,{}^{l_i}_{l_j}r_n][\,{}^{l_i}_{l_j}s_n]\Bigg)[\,{}^{l_i}_{l_j}r_n][\,{}^{l_i}_{l_j}\tilde{\mathfrak{t}}_n]& \\
-\Bigg(\sum_{j=i}^{L}[\,{}^{l_i}_{l_j}r_n][\,{}^{l_i}_{l_j}s_n][\,{}^{l_i}_{l_j}\tilde{\mathfrak{t}}_n]\Bigg)[\,{}^{l_i}_{l_j}s_n]\Bigg\}\frac{\partial[\,{}^{l_i}_{l_j}r_n]}{\partial\rho_e}& \\
+\Bigg\{\Bigg(\sum_{j=i}^{L}[\,{}^{l_i}_{l_j}r_n][\,{}^{l_i}_{l_j}s_n]\Bigg)[\,{}^{l_i}_{l_j}r_n][\,{}^{l_i}_{l_j}s_n]\Bigg\}\frac{\partial[\,{}^{l_i}_{l_j}\tilde{\mathfrak{t}}_n]}{\partial\rho_e}\Bigg]&
\end{aligned}
$$

Now, substituting the design sensitivities $\dfrac{\partial[\,{}^{l_i}_{l_j}\tilde{\mathfrak{t}}_n]}{\partial\rho_e}$ and $\dfrac{\partial[\,{}^{l_i}_{l_j}r_n]}{\partial\rho_e}$ from Eq. (D.5), Eq. (D.6) and Eq. (D.8) in above equation we get:

$$
\begin{aligned}
\frac{\partial\tilde{\mathfrak{t}}_n}{\partial\rho_e} = \frac{1}{\left(\sum_{j=i}^{L}[\,{}^{l_i}_{l_j}r_n][\,{}^{l_i}_{l_j}s_n]\right)^2}\sum_{j=i}^{L}\Bigg[\Bigg\{\Bigg(\sum_{j=i}^{L}[\,{}^{l_i}_{l_j}r_n][\,{}^{l_i}_{l_j}s_n]\Bigg)[\,{}^{l_i}_{l_j}r_n][\,{}^{l_i}_{l_j}\tilde{\mathfrak{t}}_n]& \\
-\Bigg(\sum_{j=i}^{L}[\,{}^{l_i}_{l_j}r_n][\,{}^{l_i}_{l_j}s_n][\,{}^{l_i}_{l_j}\tilde{\mathfrak{t}}_n]\Bigg)[\,{}^{l_i}_{l_j}s_n]\Bigg\}\frac{\partial[\,{}^{l_i}_{l_j}r_n]}{\partial[\,{}^{l_i}_{l_j}\mathrm{T}_n]}\int_{\tau_{l_{j-1}}}^{\tau_{l_j}}\delta(t-(t^{\mathfrak{h}}_{l_j}+\Delta\tau^{l_i}_{l_j}))\mathbf{R}_n^T\frac{\partial\mathbf{T}_{l_j}}{\partial\rho_e}dt& \\
+\Bigg\{\Bigg(\sum_{j=i}^{L}[\,{}^{l_i}_{l_j}r_n][\,{}^{l_i}_{l_j}s_n]\Bigg)[\,{}^{l_i}_{l_j}r_n][\,{}^{l_i}_{l_j}s_n]\Bigg\}\int_{\tau_{l_{j-1}}}^{\tau_{l_j}}[\,{}^{l_i}_{l_j}H_n]\Bigg(\bar{H}\frac{\partial\underline{H}}{\partial[\,{}^{l_i}_{l_j}T_n]}+\frac{\partial\bar{H}}{\partial[\,{}^{l_i}_{l_j}T_n]}\underline{H}\Bigg)\mathbf{R}_n^T\frac{\partial\mathbf{T}_{l_j}}{\partial\rho_e}dt\Bigg]&
\end{aligned}
$$

The above equation can be rewritten as follows:

$$
\begin{aligned}
\frac{\partial\tilde{\mathfrak{t}}_n}{\partial\rho_e} = \frac{1}{\left(\sum_{j=i}^{L}[\,{}^{l_i}_{l_j}r_n][\,{}^{l_i}_{l_j}s_n]\right)^2}\sum_{j=i}^{L}\Bigg[\int_{\tau_{l_{j-1}}}^{\tau_{l_j}}\Bigg[\Bigg\{\Bigg(\sum_{j=i}^{L}[\,{}^{l_i}_{l_j}r_n][\,{}^{l_i}_{l_j}s_n]\Bigg)[\,{}^{l_i}_{l_j}r_n][\,{}^{l_i}_{l_j}\tilde{\mathfrak{t}}_n]& \\
-\Bigg(\sum_{j=i}^{L}[\,{}^{l_i}_{l_j}r_n][\,{}^{l_i}_{l_j}s_n][\,{}^{l_i}_{l_j}\tilde{\mathfrak{t}}_n]\Bigg)[\,{}^{l_i}_{l_j}s_n]\Bigg\}\Bigg\{\frac{\partial[\,{}^{l_i}_{l_j}r_n]}{\partial[\,{}^{l_i}_{l_j}\mathrm{T}_n]}\Bigg\}\Big\{\delta(t-(t^{\mathfrak{h}}_{l_j}+\Delta\tau^{l_i}_{l_j}))\Big\}& \\
+\Bigg\{\Bigg(\sum_{j=i}^{L}[\,{}^{l_i}_{l_j}r_n][\,{}^{l_i}_{l_j}s_n]\Bigg)[\,{}^{l_i}_{l_j}r_n][\,{}^{l_i}_{l_j}s_n]\Bigg\}\Bigg\{[\,{}^{l_i}_{l_j}H_n]\Bigg(\bar{H}\frac{\partial\underline{H}}{\partial[\,{}^{l_i}_{l_j}T_n]}+\frac{\partial\bar{H}}{\partial[\,{}^{l_i}_{l_j}T_n]}\underline{H}\Bigg)\Bigg\}\Bigg]\mathbf{R}_n^T\frac{\partial\mathbf{T}_{l_j}}{\partial\rho_e}dt\Bigg]&
\end{aligned}
$$

The above equation can be condensed to following form:

$$\frac{\partial \tilde{\mathfrak{t}}_n}{\partial \rho_e} = \sum_{j \geq i} \int_{\tau_{l_{j-1}}}^{\tau_{l_j}} {}^{l_i}_{l_j}\mathfrak{B}_n \mathbf{R}_n^T \frac{\partial \mathbf{T}_{l_j}}{\partial \rho_e} dt \tag{D.9}$$

where, ${}^{l_i}_{l_j}\mathfrak{B}_n$ is given as follows:

$$\begin{aligned}
{}^{l_i}_{l_j}\mathfrak{B}_n = \frac{1}{\left(\sum_{j=i}^{L} [{}^{l_i}_{l_j}r_n][{}^{l_i}_{l_j}s_n]\right)^2} & \Bigg[\Bigg\{\Bigg(\sum_{j=i}^{L} [{}^{l_i}_{l_j}r_n][{}^{l_i}_{l_j}s_n]\Bigg)[{}^{l_i}_{l_j}r_n][{}^{l_i}_{l_j}\tilde{\mathfrak{t}}_n] \\
& - \Bigg(\sum_{j=i}^{L} [{}^{l_i}_{l_j}r_n][{}^{l_i}_{l_j}s_n][{}^{l_i}_{l_j}\tilde{\mathfrak{t}}_n]\Bigg)[{}^{l_i}_{l_j}s_n]\Bigg\}\Bigg\{\frac{\partial[{}^{l_i}_{l_j}r_n]}{\partial[{}^{l_i}_{l_j}\mathrm{T}_n]}\Bigg\}\Bigg\{\delta(t - (t^{\mathfrak{h}}_{l_j} + \Delta\tau^{l_i}_{l_j}))\Bigg\} \\
& + \Bigg\{\Bigg(\sum_{j=i}^{L} [{}^{l_i}_{l_j}r_n][{}^{l_i}_{l_j}s_n]\Bigg)[{}^{l_i}_{l_j}r_n][{}^{l_i}_{l_j}s_n]\Bigg\}\Bigg\{[{}^{l_i}_{l_j}H_n]\Bigg(\bar{H}\frac{\partial \underline{H}}{\partial[{}^{l_i}_{l_j}T_n]} + \frac{\partial \bar{H}}{\partial[{}^{l_i}_{l_j}T_n]}\underline{H}\Bigg)\Bigg\}\Bigg]
\end{aligned}$$

To calculate the total sensitivities, the sensitivities of the state equation with the Lagrange multiplier $\boldsymbol{\lambda}_{l_j}(t)$ given as follows can be added to Eq. (D.9).

$$\boldsymbol{\lambda}_{l_j}^T \frac{\partial}{\partial \rho_e}(\mathbf{C}_{l_j}\dot{\mathbf{T}}_{l_j} + \mathbf{K}_{l_j}\mathbf{T}_{l_j} - \mathbf{Q}_{l_j}) = \mathbf{0} \tag{D.10}$$

Eq. (D.9) becomes

$$\frac{\partial \tilde{\mathfrak{t}}_n}{\partial \rho_e} = \sum_{j \geq i} \left[\int_{\tau_{l_{j-1}}}^{\tau_{l_j}} \left[{}^{l_i}_{l_j}\mathfrak{B}_n \mathbf{R}_n^T \frac{\partial \mathbf{T}_{l_j}}{\partial \rho_e} + \boldsymbol{\lambda}_{l_j}^T \frac{\partial}{\partial \rho_e}(\mathbf{C}_{l_j}\dot{\mathbf{T}}_{l_j} + \mathbf{K}_{l_j}\mathbf{T}_{l_j} - \mathbf{Q}_{l_j})\right] dt\right] \tag{D.11}$$

Since, we are free to choose $\boldsymbol{\lambda}_{l_j}(t)$ values, therefore, we choose $\boldsymbol{\lambda}_{l_j}(t) = \mathbf{0}$, if $\tau_{l_{j-1}} \leq t < \tau^{\mathfrak{h}}_{l_j} + \Delta\tau^{l_i}_{l_j}$. This will ensure no contribution to the sensitivities in the range $\tau_{l_{j-1}} \leq t < \tau^{\mathfrak{h}}_{l_j} + \Delta\tau^{l_i}_{l_j}$. Moreover, $\mathbf{Q}_{l_j} = \mathbf{0}$, if $\tau^{\mathfrak{h}}_{l_j} + \Delta\tau^{l_i}_{l_j} \leq t < \tau_{l_j}$, thus the term corresponding to $\mathbf{Q}_{l_j}$ will vanish. With these considerations and expanding the above equation will result in as follows

$$\frac{\partial \tilde{\mathfrak{t}}_n}{\partial \rho_e} = \sum_{j \geq i} \left[\int_{\tau_{l_{j-1}}}^{\tau_{l_j}} \left[{}^{l_i}_{l_j}\mathfrak{B}_n \mathbf{R}_n^T \frac{\partial \mathbf{T}_{l_j}}{\partial \rho_e} + \boldsymbol{\lambda}_{l_j}^T \mathbf{C}_{l_j}\frac{\partial \dot{\mathbf{T}}_{l_j}}{\partial \rho_e} + \boldsymbol{\lambda}_{l_j}^T \frac{\partial \mathbf{C}_{l_j}}{\partial \rho_e}\dot{\mathbf{T}}_{l_j} + \boldsymbol{\lambda}_{l_j}^T \frac{\partial \mathbf{K}_{l_j}}{\partial \rho_e}\mathbf{T}_{l_j} + \boldsymbol{\lambda}_{l_j}^T \mathbf{K}_{l_j}\frac{\partial \mathbf{T}_{l_j}}{\partial \rho_e}\right] dt\right] \tag{D.12}$$

Now, applying the integration by parts for the term $\boldsymbol{\lambda}_{l_j}^T \mathbf{C}_{l_j}\frac{\partial \dot{\mathbf{T}}_{l_j}}{\partial \rho_e}$, to eliminate the term $\frac{\partial \dot{\mathbf{T}}_{l_j}}{\partial \rho_e}$ we get as follows

$$\int_{\tau_{l_{j-1}}}^{\tau_{l_j}} \left[\boldsymbol{\lambda}_{l_j}^T \mathbf{C}_{l_j}\frac{\partial \dot{\mathbf{T}}_{l_j}}{\partial \rho_e}\right] dt = \left[\boldsymbol{\lambda}_{l_j}^T \mathbf{C}_{l_j}\frac{\partial \mathbf{T}_{l_j}}{\partial \rho_e}\right]_{t=\tau_{l_j}} - \left[\boldsymbol{\lambda}_{l_j}^T \mathbf{C}_{l_j}\frac{\partial \mathbf{T}_{l_j}}{\partial \rho_e}\right]_{t=\tau_{l_{j-1}}} - \int_{\tau_{l_{j-1}}}^{\tau_{l_j}} \left[\dot{\boldsymbol{\lambda}}_{l_j}^T \mathbf{C}_{l_j}\frac{\partial \mathbf{T}_{l_j}}{\partial \rho_e}\right] dt \tag{D.13}$$

Since, we assume that the $\boldsymbol{\lambda}_{l_j}(t) = \mathbf{0}$, for $\tau_{l_{j-1}} \leq t < \tau^{\mathfrak{h}}_{l_j} + \Delta\tau^{l_i}_{l_j}$, therefore, $\left[\boldsymbol{\lambda}^T_{l_j}\mathbf{C}_{l_j}\frac{\partial \mathbf{T}_{l_j}}{\partial \rho_e}\right]_{t=\tau_{l_{j-1}}} = \mathbf{0}$. Also, during the manufacturing process we assume that the part cools completely, therefore, $\left.\frac{\partial \mathbf{T}_{l_j}}{\partial \rho_e}\right|_{t=\tau_{l_j}} = \mathbf{0}$. Consequently, $\left[\boldsymbol{\lambda}^T_{l_j}\mathbf{C}_{l_j}\frac{\partial \mathbf{T}_{l_j}}{\partial \rho_e}\right]_{t=\tau_{l_j}} = \mathbf{0}$. Therefore, we are free to choose any $\boldsymbol{\lambda}_{l_j}$ and hence, we choose $\boldsymbol{\lambda}_{l_j}(t = \tau_{l_j}) = \mathbf{0}$. Moreover, if the condition is not satisfied $\left.\frac{\partial \mathbf{T}_{l_j}}{\partial \rho_e}\right|_{t=\tau_{l_j}} = \mathbf{0}$, then $\boldsymbol{\lambda}_{l_j}(t = \tau_{l_j}) = \mathbf{0}$ can be considered and this condition will work as initial condition to calculate complete $\boldsymbol{\lambda}_{l_j}(t)$.

In both conditions, we can write as follows

$$\int_{\tau_{l_{j-1}}}^{\tau_{l_j}} \left[\boldsymbol{\lambda}^T_{l_j}\mathbf{C}_{l_j}\frac{\partial \dot{\mathbf{T}}_{l_j}}{\partial \rho_e}\right] dt = -\int_{\tau_{l_{j-1}}}^{\tau_{l_j}} \left[\dot{\boldsymbol{\lambda}}^T_{l_j}\mathbf{C}_{l_j}\frac{\partial \mathbf{T}_{l_j}}{\partial \rho_e}\right] dt \tag{D.14}$$

Substituting, the above term in Eq. (D.12) we get

$$\frac{\partial \tilde{\mathfrak{t}}_n}{\partial \rho_e} = \sum_{j\geq i}\left[\int_{\tau_{l_{j-1}}}^{\tau_{l_j}} \left[{}^{l_i}_{l_j}\mathfrak{B}_n\mathbf{R}^T_n\frac{\partial \mathbf{T}_{l_j}}{\partial \rho_e} - \dot{\boldsymbol{\lambda}}^T_{l_j}\mathbf{C}_{l_j}\frac{\partial \mathbf{T}_{l_j}}{\partial \rho_e} + \boldsymbol{\lambda}^T_{l_j}\frac{\partial \mathbf{C}_{l_j}}{\partial \rho_e}\dot{\mathbf{T}}_{l_j} + \boldsymbol{\lambda}^T_{l_j}\frac{\partial \mathbf{K}_{l_j}}{\partial \rho_e}\mathbf{T}_{l_j} + \boldsymbol{\lambda}^T_{l_j}\mathbf{K}_{l_j}\frac{\partial \mathbf{T}_{l_j}}{\partial \rho_e}\right] dt\right] \tag{D.15}$$

Now, collecting the contributions with term $\frac{\partial \mathbf{T}_{l_j}}{\partial \rho_e}$ we get

$$\frac{\partial \tilde{\mathfrak{t}}_n}{\partial \rho_e} = \sum_{j\geq i}\left[\int_{\tau_{l_{j-1}}}^{\tau_{l_j}} \left[\left\{{}^{l_i}_{l_j}\mathfrak{B}_n\mathbf{R}^T_n - \dot{\boldsymbol{\lambda}}^T_{l_j}\mathbf{C}_{l_j} + \boldsymbol{\lambda}^T_{l_j}\mathbf{K}_{l_j}\right\}\frac{\partial \mathbf{T}_{l_j}}{\partial \rho_e} + \boldsymbol{\lambda}^T_{l_j}\frac{\partial \mathbf{C}_{l_j}}{\partial \rho_e}\dot{\mathbf{T}}_{l_j} + \boldsymbol{\lambda}^T_{l_j}\frac{\partial \mathbf{K}_{l_j}}{\partial \rho_e}\mathbf{T}_{l_j}\right] dt\right] \tag{D.16}$$

The following set of adjoint equations can be solved to obtain the Lagrange multiplier values such that the term in the brackets always vanishes.

$$\mathbf{C}_{l_j}\dot{\boldsymbol{\lambda}}_{l_j} - \mathbf{K}_{l_j}\boldsymbol{\lambda}_{l_j} = {}^{l_i}_{l_j}\mathfrak{B}_n\mathbf{R}_n \tag{D.17}$$

Subsequently, the design sensitivity of $\tilde{\mathfrak{t}}_n$ is given as follows:

$$\frac{\partial \tilde{\mathfrak{t}}_n}{\partial \rho_e} = \sum_{j\geq i}\left[\int_{\tau_{l_{j-1}}}^{\tau_{l_j}} \left[\boldsymbol{\lambda}^T_{l_j}\frac{\partial \mathbf{C}_{l_j}}{\partial \rho_e}\dot{\mathbf{T}}_{l_j} + \boldsymbol{\lambda}^T_{l_j}\frac{\partial \mathbf{K}_{l_j}}{\partial \rho_e}\mathbf{T}_{l_j}\right] dt\right] \tag{D.18}$$

CURRICULUM VITÆ

Vibhas MISHRA

11-10-1990	Born in Lakhimpur-Kheri, Uttar Pradesh, India.

EDUCATION

2018–2022	Ph.D. Candidate Delft University of Technology Delft, The Netherlands

Thesis:	Computational Design for the Wire and Arc Additive Manufacturing Process
Promotors:	Prof. dr. ir. A. van Keulen Prof. dr. ir. M. Langelaar
Co-Promotor:	Dr. C. Ayas

2015–2017	Master of Science in Aerospace Engineering Delft University of Technology Delft, The Netherlands

Thesis:	A methodology to predict the stiffness properties and buckling load of variable stiffness panels
Supervisors:	Dr. M. Abdalla Dr. D. M. J. Peeters

2008–2012	Bachelor of Technology in Mechanical Engineering Indian Institute of Technology, Banaras Hindu University, Varanasi, Uttar Pradesh, India

Work Experience

2023-Current	Researcher Delft University of Technology Delft, The Netherlands
2012–2015	CAE Engineer Tata Technologies Limited Pune, India
2018–2018	Technical Customer Support Engineer Dassault Systèmes Pune, India

LIST OF PUBLICATIONS

JOURNAL

4. **V. Mishra**, C. Ayas, M. Langelaar *Design for material properties of Additively Manufactured Metals using Topology Optimization*, Material and Design (**Under Review**).

3. **V. Mishra**, A. Babu, R. Schreurs, K. Wu, M.J.M. Hermans, C. Ayas *Microstructure estimation and validation of ER110S-G steel structures produced by wire and arc additive manufacturing*, Journal of Materials Research and Technology **23**, 3579-3601(2023).

2. **V. Mishra**, C. Ayas, M. Langelaar, F. van Keulen *A stress-based criterion to identify and control intersections in 2D compliance minimization topology optimization*, Structural and Multidisciplinary Optimization **65**, 307 (2022).

1. **V. Mishra**, C. Ayas, M. Langelaar, F. van Keulen *Simultaneous topology and deposition direction optimization for Wire and Arc Additive Manufacturing*, Manufacturing Letters **31**, 45-51 (2022).

CONFERENCE

2. **V. Mishra**, C. Ayas, M. Langelaar, F. van Keulen *On controlling microstructure through topology optimization for additive manufacturing*, Proceedings of the ASMO UK12-EU1 Conference Engineering Design Optimization, 147 (2022).

1. **V. Mishra**, C. Ayas, M. Langelaar, F. van Keulen *Controlling cooling rates through topology optimization for required microstructure in additive manufacturing process*, In 2022 ASPE and euspen Summer Topical Meeting on Advancing Precision in Additive Manufacturing, 8-12 (2022).